Dissertation

submitted to the
Combined Faculties for the Natural Sciences and for Mathematics
of the Ruperto-Carola University of Heidelberg, Germany
for the degree of
Doctor of Natural Sciences

Put forward by
Barbara Haller, M.Sc.
Stuttgart, Germany

Oral examination: November 30th, 2018

The Reconstitution of Eukaryotic Architecture and Motility via Microfluidic Technology

Referees:

Prof. Joachim P. Spatz
Institute for Physical Chemistry
University of Heidelberg
Max Planck Institute for Medical Research
Heidelberg

Prof. Reiner Dahint
Institute for Physical Chemistry
University of Heidelberg

Zusammenfassung

In dieser Arbeit wurde das Konzept der Synthetischen Biologie umgesetzt, um minimalistische künstliche Zellen zu konstruieren, welche strukturell und funktionell einer lebenden Zelle ähneln.

In diesem Sinne wurden mittels mikrofluidischer Lab-on-a-Chip Technologie zellgroße Wasser-in-Öl Tröpfchen in hohem Durchsatz hergestellt und mit isolierten Zellbausteinen, wie Membranlipiden, Zellskelett- und Rezeptor-Proteinen, ausgestattet. Die Wasser-in-Öl Tröpfchen wurden über geladene oder ungeladene Tenside stabilisiert. Dadurch konnten Interaktionen zwischen der Tröpfchenwand und dem Tröpfcheninhalt veranlasst oder verhindert werden. Durch das Einkapseln von Membranlipiden konnten so Strukturen in den Tröpfchen aufgebaut werden, welche den Lipidmembranen einer lebendenden eukaryotischen Zelle ähnlich sind: eine äußere Lipidmembran und interne kleinere Kompartimente.

Im Weiteren konnten künstliche Zellen entwickelt werden, die einer lebenden Zelle nicht nur strukturell, sondern auch funktionell ähneln. Hierfür wurden die Zellkompartimente mit Hauptbausteinen des zellulären Bewegungsapparates ausgestattet: ein dynamisches Aktin Zellskelett, Motorproteine und Membranrezeptoren, welche die Zellen auf dem Untergrund adhärieren lassen. Hierbei ist hervorzuheben, dass so erstmals eine multifunktionale künstliche Zelle hergestellt wurde, die sowohl Adhäsions- als auch Zellskelett-Bausteine enthält.

Darüber hinaus wurden autonome Bewegungen der Zellkompartimente gezeigt und dieses Phänomen über einen chemisch-physikalischen Effekt erklärt.

Der hier beschriebene Ansatz ist eine vielseitige Methode, um komplizierte Funktionen einer Zelle in minimalistischen und kontrollierbaren Kompartimenten zu untersuchen. Darüber könnten Mechanismen des frühen evolutionären Lebens – wahrscheinlich ähnlich minimalistisch – erklärt werden.

Abstract

The investigation into how life evolved and cellular complexity developed is an ongoing and highly researched pursuit in science. The central goal of my thesis was to develop a bio-inspired synthetic cell model in order to address this important topic. Towards this end, polymer-stabilized water-in-oil droplets were used as cell-sized compartments for the assembly and testing of specific sets of bioactive components. Moreover, an automated, droplet-based microfluidic technology was implemented for high throughput production of these cell-like compartments and their subsequent manipulation.

To resemble the eukaryotic cell architecture, I established a highly-tunable method for the on-demand creation of synthetic cell systems in the form of 3D-supported lipid bilayers, multicompartment systems or free-standing giant unilamellar vesicles (GUVs). To accomplish this, small unilamellar vesicles were encapsulated into polymer-stabilized water-in-oil droplets. By tuning the charge of the inner droplet interface, adsorption of lipids can either be inhibited, leading to multicompartment systems, or induced, leading to the formation of droplet-stabilized giant unilamellar vesicles (dsGUVs) or a combination of multicompartment systems and dsGUVs. Following assembly, the successful release of free-standing GUVs from the polymer shell and the oil phase into physiological conditions was demonstrated. This paves the way towards future applications in which synthetic cell interactions with a physiological environment are crucial.

Another significant achievement in this thesis was the assembly of a cellular motility module by the reconstitution of actin cytoskeletal networks and adhesion membrane receptors within droplet-based synthetic cells. These disparate cytoskeletal and adhesive elements were united in the lipid membrane structure of dsGUVs. I showed that this module was able to recapitulate key mechanisms in cell migration – namely cytoskeletal pushing and contractile forces. To date, such synthetic cells containing both cytoskeletal and adhesion-associated functional modules capable of self-propulsion has never been demonstrated.

Remarkably, this minimal but functional set of building blocks allowed for the generation of autonomous motion in synthetic cells, and led to the analysis of the mechanism behind this self-propulsion.

The powerful microfluidic technology and synthetic cell-like compartments presented in this thesis have the potential for widespread and diverse employment in synthetic biology as they allow for the use of varied sets of both synthetic and natural building blocks. I believe that the scientific achievements presented in this thesis will be of great interest to researchers in fundamental biology, bioengineering and biochemistry.

Contents

Acronyms

2D	-	two-dimensional
3D	-	three-dimensional
AC	-	alternating current
ADP	-	adenosine diphosphate
AFM	-	atomic force microscopy
ATP	-	adenosine triphosphate
BSA	-	bovine serum albumin
CAD	-	computer animated design
CMC	-	critical micellar concentration
cryo-SEM	-	cry-scanning electron microscopy
DLS	-	dynamic light scattering
DNA	-	deoxyribonucleic acid
dsGUV	-	droplet-stabilized GUV
ECM	-	extracellular matrix
ER	-	endoplasmic reticulum
F-actin	-	filamentous actin
FAK	-	focal adhesion kinase
FRAP	-	fluorescence recovery after photobleaching
FTIR	-	Fourier-transform infrared spectroscopy
G-actin	-	globular actin
GDP	-	guanosine diphosphate
GTP	-	guanosine triphosphate
GUV	-	giant unilamellar vesicle
HRP	-	horseradish peroxidase
IFT	-	initerfacial tension
ILK	-	Integrin-linked kinase
ITO	-	Indium tin oxide
LUV	-	large unilamellar vesicle
MALDI		matrix-assisted laser desorption/ ionization
TOF MS	-	time-of-flight mass spectrometry
NTA	-	nitrilotriacetic acid
PBS	-	phosphate buffer saline
PC	-	phosphatidylcholin
PCR	-	polymerase chain reaction
PDMS	-	polydimethylsiloxane
PE	-	phosphatidylethanolamine
PEG	-	polyethylene glycol
PFO	-	perfluorooctanol
PFPE	-	perfluorinated polyether
PI	-	phosphoinositol
PIP2	-	phosphoinositol posphate

PLL-PEG	-	poly-L-lysine-PEG
PS	-	phosphatidylserine
PTFE	-	polytetrafluoroethylene
QCM-D	-	quartz crystal microbalance with dissipation monitoring
RGD	-	Arginylglycylaspartic acid
Rho6G	-	Rhodamine 6G
RT	-	room temperature
SDS PAGE	-	sodium dodecyl sulfate polyacrylamide gel electrophoresis
SLB	-	supported lipid bilayer
SUV	-	small unilamellar vesicle
THD	-	talin head domain

Introduction

1. Introduction

1.1. Origin of Life

The questions *when* and *how* life first appeared on Earth are amongst the most fundamental questions – prompted by the mesmerizing complexity of each and every organism that are now present on Earth.

It appears that already 3.8 billion years ago, first forms of life had emerged on Earth. This could be evidenced by fossilized mats of stromatolites, formed by the growth of many layers of single-celled microbes.[1] While there are some ideas about *when* life appeared on Earth, *how* it appeared is the more difficult question.

To investigate this question from a scientific point of view, we first of all have to define what life and living matter actually is. One recent definition, which in my opinion suits the best, is phrased by Ruiz-Miarazo *et al.*: "Life is based on the idea of an autonomous system with open-ended evolutionary capacities".[2] Autonomy refers to boundaries between the living entity and its environment as well as to its capacity to use energy and matter for their metabolism and for the synthesis of its own components in order to self-sustain and to replicate. Open-ended evolution refers to the capability to gain new functions and to adapt to distinct situations in an almost unlimited way in order to survive.[2]

With regard to the question of *how* life evolved, most scientists agree, based on experimental evidence, that the creation of life – meaning the creation of first organic building blocks – required very specific environmental conditions.[3] There are two competing theories. In the more conventional one, the primordial soup theory, life has evolved close to the surface due to the oxygen-poor and thus, reactive atmosphere of the early Earth. Hence, simple inorganic molecules could have emerged, fueled by the energy from lightning or from UV rays to form organic building blocks.[4] With the accumulation of these building blocks in the primordial soup, further reactions might have happened leading to the formation of nucleotides or amino acids. These building blocks then formed polymers, like nucleic acids and proteins, that in turn assembled further into units or structures capable of sustaining and replicating themselves.[1] In 1952, Stanley Miller and Harold Urey simulated the early Earth's inorganic conditions in a chemical experiment and ended up with amino acids, supporting the described theory of evolution of life.[5]

However, the fact that today's living organism gaining their energy via a proton gradient across the membrane, favors an alternative theory, where life arose in the deep sea within warm and porous geological structures, so-called hydrothermal vents.[6] Fluids from the Earth's primitive oceanic crust and the more acidic ocean water could have led to a proton gradient in the hydrothermal vent and thus, allowed for chemical reactions driven by a similar energy supply as seen in the living cells today.[7] Later, cells learned how to produce their own gradients and could eventually escape the vents.[6]

Even though these theories are close to bridge the gap between non-living molecules and living cells, synthesis of living matter has not been achieved in the laboratory until now. Approaches towards the creation of an entire cell from scratch are still in their infancy – even though much afford has been made to achieve this major milestone in understanding life in greater detail in the last decades. To recreate what evolution shaped for billions of years in few hours or days in a test tube goes far beyond the grasp of contemporary science. Nevertheless, great results have been achieved towards the creation of functional cellular modules in cell mimetics.[8] The idea here is to start with a minimal system and step-by-step increase its complexity, similarly as it is imagined in the evolution, when cells went from primitive to the complexity they reached now. The use of a minimal set of building blocks, helps to find key players of cellular functions and allows for a better understanding of cellular function and life in general.

In the following, I will introduce relevant functional modules of a eukaryotic cell that have been dissected and studied in the less complex environment of a synthetic cell in my Ph.D. thesis.

1.2. The Complexity of a Living Cell

In this thesis, I will present the eukaryotic membrane architecture and cellular motility based on an *in vitro* synthetic cell approach. Towards this aim, a minimal set of natural building blocks were assembled into cellular mimetic modules within a defined and synthetic environment. To determine the right building blocks to start with, complex cellular functions need to be dissected and fundamental building blocks need to be identified. Thus, before presenting synthetic cell approaches, I will briefly outline the relevant structural and functional modules in a living cell. First, I will introduce eukaryotic lipid membrane structures. Then, I will focus on cellular motility and its major constituents.

1.2.1. Compartments

Compartments are the most basic feature in every cell to maintain the essential difference between cytosol and extracellular environment and to guarantee special reactions to take place. Besides a semipermeable barrier function, the demands on cellular membranes go far beyond.[9] Thus, cellular membranes can be enormously diverse among cells of different species as well as among cells within a multicellular organism, depending on their habitat and their tasks.[10] One thing, however, that all cellular membranes have in common is the 5 nm thick lipid double layer.[11] The most fundamental building block of these membranes are phospholipids. Since the chemical structure of phospholipids and the lipid composition of a membrane can significantly affect crucial biological functions,[9] I will explain the structure and assembly of these building blocks in the following sections.

1.2.1.1. Phospholipids

All lipids of the cell membrane are amphiphilic molecules that possess a polar (hydrophilic) head and a nonpolar (hydrophobic) tail. Among these, most abundant membrane lipids are phospholipids, in animal cells especially phosphoglycerides.[11] As illustrated in Figure 1, these are made from a glycerol backbone that is linked through ester bonds to two fatty acids and to one phosphogroup.[10,12] Typically, one of the fatty acids is unsaturated and thus kinked, and the other one is saturated and straight.[11] The phosphogroup can be linked to several types of head groups e.g. phosphatidyl – ethanolamine (PE), serine (PS) or choline (PC).[11]

Another common lipid is sphingomyelin that have instead of the glycerol backbone a sphingosine and an extra hydroxyl group that increases the polar properties of the head.[13]

Other constituents that play important roles in the cellular membrane in terms of membrane mechanical properties and signaling, are cholesterol and phosphatidylinositol, respectively.[9,14]

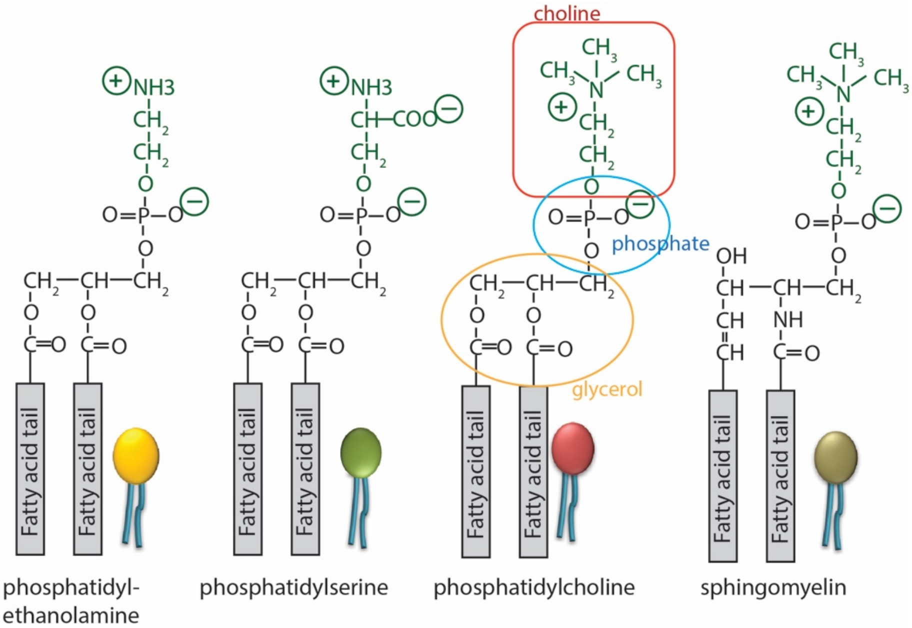

Figure 1: Chemical structure of the major phospholipids in the lipid membrane. Reproduced and modified from [11]*. Copyright © 2002, Bruce Alberts, Alexander Johnson, Julian Lewis, Martin Raff, Keith Roberts, and Peter Walter; Copyright © 1983, 1989, 1994, Bruce Alberts, Dennis Bray, Julian Lewis, Martin Raff, Keith Roberts, and James D. Watson.*

For studying lipid membranes *in vitro*, natural lipids (e.g. isolated from egg or soy)[15] or synthetically derived lipids[16] can be used. In my thesis, I will use lipid compositions made of synthetically derived phospholipids, among these mainly phosphatidylcholine and a varying amount of negatively charged phospholipids, as well as 15% cholesterol; a lipid composition similarly seen in living eukaryotic cells.[12]

1.2.1.2. Lipid Bilayers

Due to the amphiphilic nature of phospholipids, lipids can spontaneously assemble into highly ordered structures, depending on their shape: e.g. bilayers or micelles in the case of cylindrical or cone shaped lipids, respectively.[17] Since thereby the least number of water molecules are exposed to the hydrophobic lipid tails of the lipids, the free energy is minimized. However, one could imagine, that at the edges of planar lipid bilayers the hydrophobic tails are exposed to the water. This would be energetically unfavorable. Thus, lipid bilayers exist in a living cell only as sealed compartments, which is a fundamental principle in the creation of life.[11]

The lipid membranes of a eukaryotic cell can be seen as a two-dimensional fluid at room temperature.[12] This fluidity depends mainly on the composition of the membrane and on the temperature. Whereas straight and long fatty acid tails decrease fluidity, unsaturated and kinky fatty acid tails increase the fluidity.[11] Further cholesterol molecules influence the membrane fluidity in a temperature-dependent manner. Moreover, cholesterol incorporation decreases permeability of the membrane, as it leads to a dense packing of the bilayer.[12]

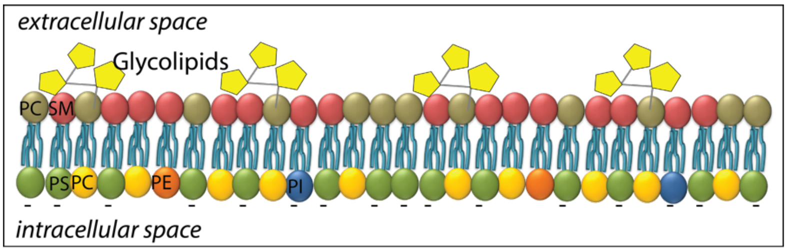

Figure 2: Lipid bilayer of the cellular membrane. Asymmetric lipid composition of the two leaflets. Extracellular leaflet: phosphatidylcholine (PC), sphingomyelin (SM), glycolipids. Intracellular leaflet: phosphatidylserine (PS), phosphatidylethanolamine (PE), phosphatidylinositol (PI). Reproduced and modified from [11] Copyright © 2002, Bruce Alberts, Alexander Johnson, Julian Lewis, Martin Raff, Keith Roberts, and Peter Walter; Copyright © 1983, 1989, 1994, Bruce Alberts, Dennis Bray, Julian Lewis, Martin Raff, Keith Roberts, and James D. Watson.

Besides the diverse lipid compositions and thus varying properties from one membrane type to the other,[10] also the lipid composition in the two leaflets of the bilayer is strikingly distinct (Figure 2). In the inner leaflet, this is especially important for mediating signaling pathways. E.g. the arrangement of functional lipid domains, so-called lipid rafts, are involved in the recruitment and activation of proteins.[17] Further, the negatively charged phosphatidylinositol at the inner leaflet can be modified by an activated lipid kinase to initiate signaling pathways; and another specific phospholipids can be cleaved to generate fragments that subsequently function as signaling molecules.[11] In contrast, the extracellular leaflet contains a lot of glycolipids that are involved in cell-cell or cell-extracellular matrix (ECM) interactions and help to protect the membrane against harsh conditions.[18]

The lipid bilayer membranes are not only found as an outer cell membrane, but also form intracellular smaller compartments, which are a hallmark of the eukaryotic architecture. Since I aim to resemble these eukaryotic structures in my thesis (multicompartment system, see Section 5.1.2), I will explain briefly some of the major intracellular compartments in a living cell in the next section.

1.2.1.3. Intracellular Compartments

In or on lipid membranes many essential biochemical processes take place. The precursors of first eukaryotic cells were simple organisms without internal membranes, however, much smaller, comprising thereby a large surface-to-volume ratio and enough area for all membrane dependent vital functions in the cell.[11] In eukaryotic cells, membrane-enclosed compartments occupy in average around half of the cell volume.[11] This provides additional membrane surface, and allows for specialized separated aqueous space with an own set of enzymes and specialized molecules.[19]

The basic structure of a eukaryotic cell is shown in Figure 3.

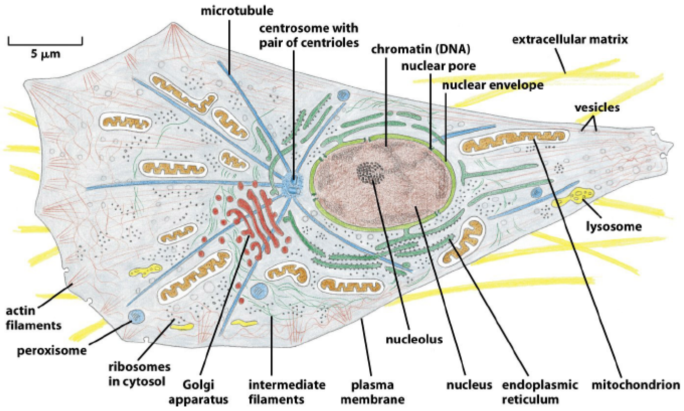

Figure 3: Representative schematic image of a eukaryotic cell. The outer lipid membrane surrounds the internal cytosol, which contains a highly structured internal architecture e.g. nucleus, mitochondria, endoplasmatic reticulum (ER), Golgi apparatus, cytoskeleton etc. Reproduced and modified from [11] Copyright © 2002, Bruce Alberts, Alexander Johnson, Julian Lewis, Martin Raff, Keith Roberts, and Peter Walter; Copyright © 1983, 1989, 1994, Bruce Alberts, Dennis Bray, Julian Lewis, Martin Raff, Keith Roberts, and James D. Watson.

The name Eukaryote is derived from the Greek words "*eu*" meaning "well" or "true", and "*karyon*" meaning "nut" or "kernel". Thus, the most fundamental internal eukaryotic compartment is the nucleus, which houses the genetic material and mediates the protein synthesis.[20] Similar like other internal compartments, the nucleus probably has been evolved from invagination and pinching off specialized membrane structures from the plasma membrane (like Golgi apparatus, endoplasmatic reticulum (ER)) or through the engulfment of bacteria (like in case of mitochondria).[21,20]

Another prominent intracellular structure is the ER, which makes up about half of the total membrane area in a cell.[11] The "rough ER" comprises ribosomes bound to the cytosolic part, here, cytosolic and membrane-bound proteins as well as lipids are synthesized.[22] The "smooth ER" is lacking ribosomes and is mainly involved in sending off the produced lipids and proteins to the Golgi apparatus, where they are covalently modified and further translocated to different destinations in the cell.[22]

Another essential internal compartment – especially concerning the cellular energy supply – are mitochondria.[11] These possess an inner, highly convoluted, and an outer membrane and thereby two separated compartments: the internal matrix and the intermembrane space. Each compartment is equipped with a unique set of proteins that e.g. mediates selective transport or governs the signaling cascade of the respiratory chain, essential to generate ATP.[23] This process is membrane-dependent as it is based on a proton gradient across the membrane. Thus, the highly folded inner membrane is key for large surface-to-volume rations and for an efficient ATP production.[19] These lipid membrane folds are an interesting phenomenon in a living cell. In this regard, membrane folds have been also studied in artificial membrane systems in the past[24–26] and will be further investigated in my thesis in Section 5.1.4.4.4.

I demonstrated in the last section that lipid membranes provide barrier function as well as that they actively participate in cell signaling pathways. Besides this, lipid membranes serve as scaffolds for membrane proteins, which are key to equip the membranes and compartments with complex and sophisticated function as for example the mentioned respiratory chain in the mitochondria. The structure of membrane proteins and how they are assembled at the membrane, will be presented in the following section.

1.2.1.4. Transmembrane Proteins

Around 30% of the encoded proteins in an animal cell are membrane proteins and make up half of the membrane's mass.[27] Membrane proteins promote important membrane functions including, but not limited to, specific transport, catalysis of membrane associated reactions (ATP synthesis) or transduction of signals from the extracellular environment.[19] Proteins interact with the membrane mainly due to amphiphilic properties.[11]

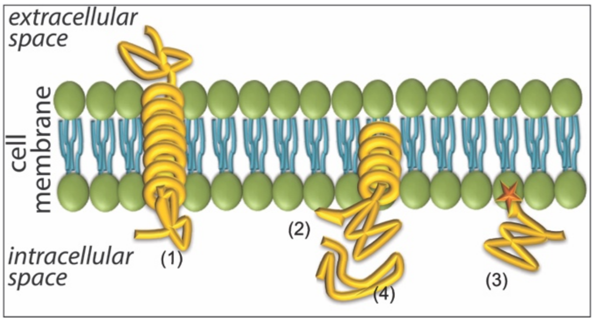

Figure 4: Representative image of membrane proteins in the cellular membrane. (1) transmembrane protein, (2) integral membrane protein with a hydrophobic terminal domain, (3) membrane protein covalently linked to lipid, (4) peripheral membrane protein. Reproduced and modified from [11] Copyright © 2002, Bruce Alberts, Alexander Johnson, Julian Lewis, Martin Raff, Keith Roberts, and Peter Walter; Copyright © 1983, 1989, 1994, Bruce Alberts, Dennis Bray, Julian Lewis, Martin Raff, Keith Roberts, and James D. Watson.

In this regard, Figure 4 shows that depending on the arrangement of their hydrophobic and hydrophilic protein domains, they can either span across the lipid bilayer (transmembrane proteins (1)); or appear only at one side of the membrane (integral membrane proteins (2)) by having one hydrophobic terminal domain; or by being covalently connected to a lipid in one leaflet of the membrane (3). Some other membrane proteins are non-covalently associated to the membrane via interactions to other membrane proteins. These are called peripheral membrane proteins (4).[11]

In my thesis, a transmembrane protein, the so-called integrin-transmembrane receptor, was reconstituted within the lipid membranes of synthetic cells. Thereby, the membrane was equipped with an important building block of the cellular adhesion module that allow the cell to attach onto an extracellular substrate. Moreover, peripheral membrane proteins are addressed in my thesis, which connect the integrin receptors to the cytoskeleton, and thereby coordinate multiple aspects in cell locomotion. However, before these proteins are discussed in more detail in Section 5.3, I will first outline cellular motility more generally in the next section.

1.2.1. Cellular Motility

The phenomenon of cell migration is seen in many animal cells. For example cells of the immune system migrate to the site of infection, osteoclasts crawl over bone, or fibroblasts migrate through connective tissues, rebuilding damaged structures.[28]

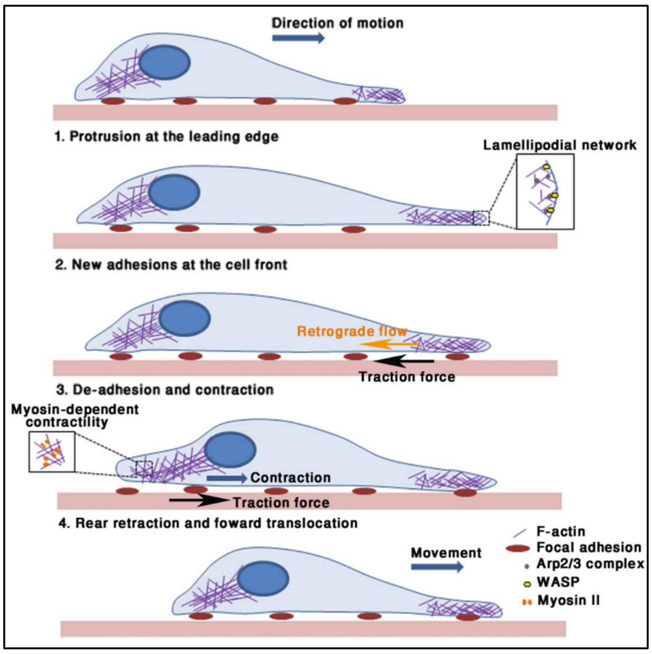

Figure 5: Schematic illustration of major steps of a cell migration on a 2D substrate. Locomotion is mediated by: 1. cellular protrusions at the leading edge, 2. formation of new adhesions to the substrate, 3. contraction of the cell body and 4. the forward translocation of the cell. Reprinted with permission from [28].

The migration process is highly complex, as it has to integrate the dynamic interplay between cytoskeletal filaments, filament regulators, motor proteins and membrane flows.[11]

Nevertheless, it can be condensed into few major activities presented in Figure 5: protrusion at the front of the cell; attachment onto the substrate; and traction, in which the rear of the cell is drawn forward.[29]

Major constituents that mediate this migration are actin cytoskeletal filaments together with contractile motor proteins, like the myosin motor II, as well as for the attachment of the cell body the already mentioned integrin transmembrane receptors. These building blocks will be outlined in the following sections, starting with cytoskeletal building blocks.

1.2.1.1. The Cytoskeleton

In a eukaryotic cell, the cytoskeleton governs many cellular processes. It mediates the cell's shape, its mechanical robustness and its internal structure.[30] Moreover, the cytoskeleton is crucial for chromosome segregation during mitosis, it splits the cell in two during division, guides the intracellular transport of organelles and allows the cell to crawl across surfaces.[19]

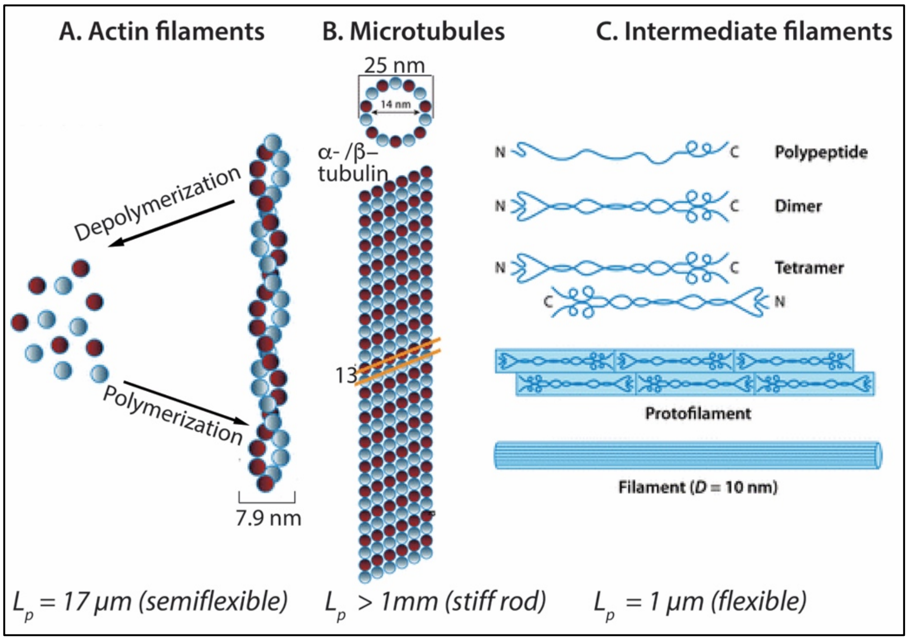

Figure 6: Primary constituents of the cytoskeleton: (A) actin filaments, (B) microtubules, (C) intermediate filaments with their persistence lengths. Reprinted with permission from [31] © Copyright 2009 ANNUAL REVIEWS, INC.

There are three kinds of cytoskeletal filaments depicted in Figure 6: actin filaments that shape dynamically the cell surface, build the contractile ring to round up the cells before division and that are further responsible for cell locomotion (A);[32] microtubules that direct intracellular transport and location of membrane enclosed organelles (B); and intermediate filaments that provide mechanical strength and align around the inner part of the nuclear envelope (C).[11]

These three cytoskeletal constituents comprise a polymer-like structure made of subunits that assemble based on different intermolecular attractive forces. Intermediate filaments, for example, form strong lateral contacts between their fibrous subunits, thus, possessing strong rope-like properties that can tolerate stretching and bending.[33] Microtubules are built from globular subunits, the α and β tubulin, each of them bound to a GTP. These subunits form dimers before being assembled into a protofilament by hydrolyzing the GTP, which is bound to the β tubulin. 13 of these protofilaments are then used to build a hollow cylindrical structure. This structure makes the microtubule stiff and difficult to bend, possessing a persistence length (length before filament bends due to random thermal fluctuations) of several millimeters.[34] Filamentous actin ("F-actin") is made of only one kind of ATP or ADP-bound globular monomer ("G-actin") and only two of the protofilaments twist around each other in a right-handed helix. This makes the filaments relatively flexible and easy to bend, thus, actin filaments possess a persistence length of around 17 µm.[35] However, actin-binding proteins as crosslinkers and bundling proteins (

Table 1) can combine individual actin filaments to filament structures with adaptable properties.[36]

Table 1: actin-binding proteins and the effect on actin filaments.

Actin-binding protein	Effect on actin
Arp2/3, WASP	Branch formation
Fascin, α-actinin	Filament bundling
Filamin, spectrin	Filament crosslinking
Cortactin	Sidebinders
Gelsolin, villin	Severing and Capping
ADF/cofilin	Depolymerisation
WASP	Nuclelators
Profiling, profilin	Monomer delivery and polymerization

In my thesis, I will reconstitute actin cytoskeleton networks in a synthetic cell. Thus, I will address next solely actin-related cytoskeletal features, especially regarding pushing and contractile forces during cell migration.

Pushing Forces generated by Actin Treadmilling

The protrusion of the leading edge during cellular locomotion relies primarily on forces of elongated filaments that push during actin polymerization against the plasma membrane.[37] This can result in different shapes of protrusive structures, including filopodia (spiky structures), lamellipodia (sheet-like structures) or pseudopodia (stubby 3D- projections).[11]

Polymerization of actin is basically initiated by a local monomer concentration above a critical value. This critical concentration depends critically on the presence of ATP or ADP. In this regard, the monomer concentration needs to be significantly higher when the monomers are bound to the diphosphate state (ADP). Thus, actin polymerization happens mainly when the monomers are bound to ATP.[11] After the incorporation of actin monomers into the filament, the ATP is hydrolyzed to ADP in a time-dependent manner (Figure 7). Thus, the longer the subunits have been in the polymer lattice the more likely they hold the ADP.[38]

Much of the free energy from the ATP-hydrolysation reaction is stored within the polymer lattice. This drives the dissociation of monomers when bound to ADP and the incorporation when bound to ATP.[39] Thus, the ends of the actin filaments are often described as a "plus" and a "minus end" with distinct kinetic rate constants for association and dissociation. This can lead to a simultaneous shrinkage and elongation of the filament at the according sides, so-called treadmilling.[40]

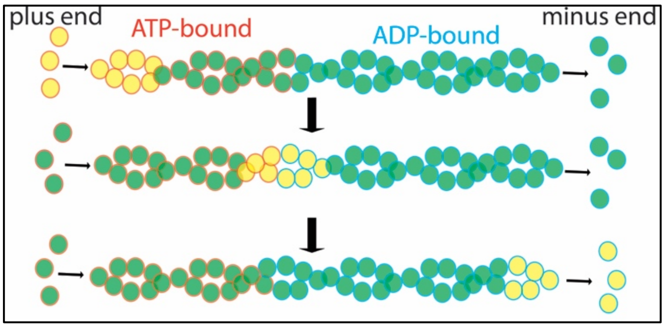

Figure 7: Illustration of actin treadmilling. ATP-bound (orange stroke) actin monomers polymerize at the "plus end". ATP will be hydrolyzed to ADP (blue stroke) and actin monomers again depolymerize at the "minus end". Reproduced and modified from [11] *Copyright © 2002, Bruce Alberts, Alexander Johnson, Julian Lewis, Martin Raff, Keith Roberts, and Peter Walter; Copyright © 1983, 1989, 1994, Bruce Alberts, Dennis Bray, Julian Lewis, Martin Raff, Keith Roberts, and James D. Watson.*

Besides the critical monomer concentration and the binding of ATP / ADP, the polymerization and depolymerization of actin filaments is further regulated by many accessory proteins that are in turn controlled by extracellular or intracellular signal. The ARP complex, for example, is a nucleation regulator associated to the leading edge of migrating cells and forms a treelike filament web at the cell cortex, thus assist the actin cytoskeleton to regulate cell shape and movement.[41,29] Other proteins, e.g. cross linkers or bundling proteins lead to parallel bundles of actin filaments. A list of actin-binding proteins and their function is listed in

Table 1.[29] The recruitment of these proteins and its complex interplay with actin filaments allow for rapid and coordinated network transformation during cell cycle or locomotion.[19,29]

Contraction Forces through Molecular Motors

The most remarkable cytoskeleton-binding proteins are motor proteins. These proteins bind with one part to a cargo (e.g. organelles or other filaments) and with another part to the filament track. While changing their conformation under ATP hydrolysis, the cargo is then translocated along a filament.[42] The motor proteins in a cell differ depending on the type of filament they bind to, which direction they move in and which cargo they carry.[11]

The motor protein, myosin II, is the most relevant motor for cell motility, as it leads to the contractile force that retracts the cell rear during cell migration.[28]

Myosin II is a homodimer (Figure 8), with each monomer consists of a light and a heavy chain that builds a long α-helix tail and a globular head region.[43] The two long tails form a coiled-coil that further interact tail-to-tail with other dimers, resulting in thick bundles exposing several hundred heads.[44] The heads bind to a filament and under ATP hydrolysis each head undergoes a conformational change. Cycles of filament binding, conformational change, filament release, conformational relaxation and filament rebinding lead then to a pushing or pulling force.[45]

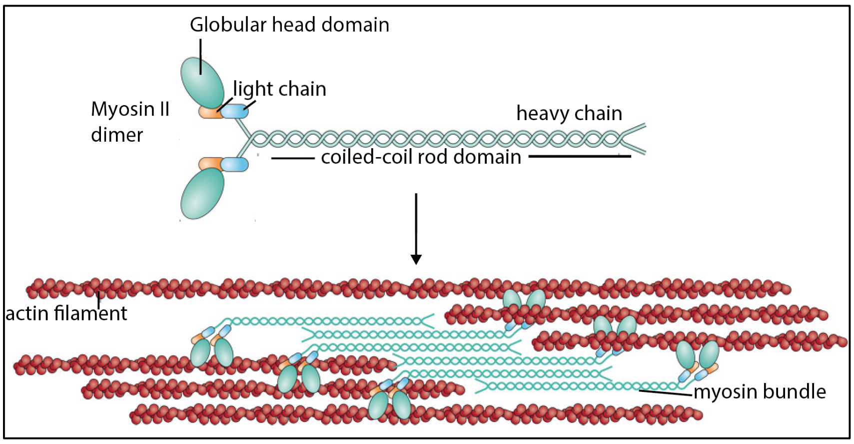

Figure 8: Schematic illustration of myosin II motor as a dimer and as a myosin bundle interacting with actin filaments. Reprinted from [43].

The contraction of the actin networks upon myosin II activity is based on the symmetry breaking of actin filaments severing: actin filament buckling is much more prone under compression (already at 3-4 pN) than actin rupture under tension (round 400 pN).[46] This allows the cell to contract its rear and to move forward.

Besides the cytoskeleton pushing and contractile forces, the third crucial element in cell locomotion is the cell adhesion to the substrate. When moving forward, the cell has to create new attachment sites that serve as anchor points. This only allows the cell to apply the traction force to the substrate and to pull the cell body forward.[28] The crosstalk between the dynamic cell adhesion machinery and cytoskeletal assembly is thereby particularly important and makes the whole locomotion process considerably complex.[47]

The adhesion of the cell to the extracellular matrix (ECM) via integrin transmembrane receptors and its important linkage to the cytoskeleton will be addressed in the following section.

1.2.1.2. Cell-Extracellular Matrix (ECM) Interactions

The extracellular matrix (ECM) consists of a variety of protein fibers in a hydrated gel of glycosaminoglycan chains.[11] It does not only provide a mechanical support for cells but also influences their behavior in multiple ways.[48]

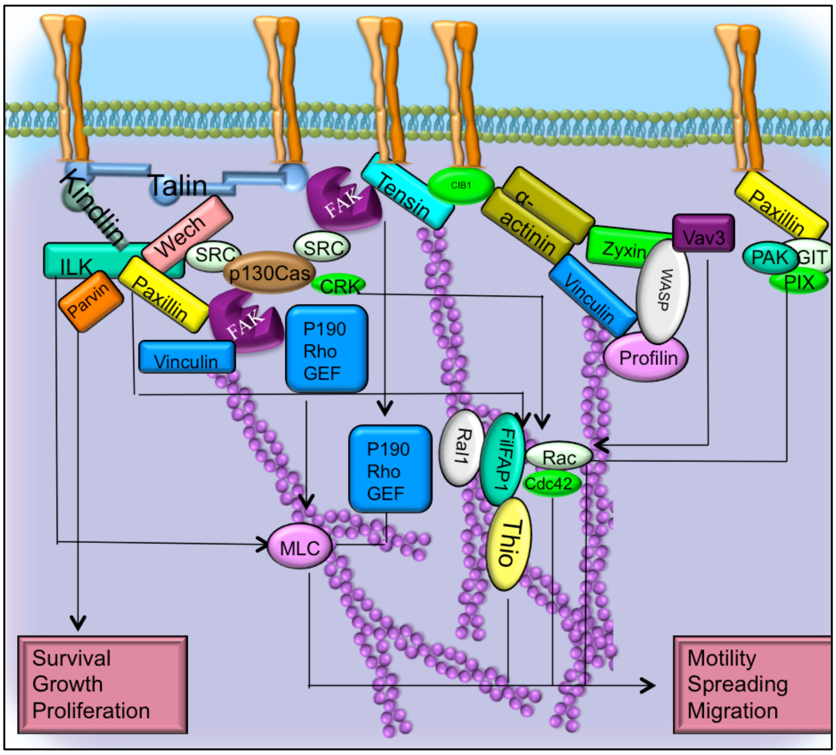

Figure 9: Schematic representation of integrins that are bound to the extracellular matrix and linked to the actin cytoskeleton through multiple peripheral anchoring proteins, including, but not limited to, talin, vinculin and α-actinin. Other proteins, like focal adhesion kinase are also recruited and trigger the downstream activation of signaling pathways that influence e.g. myosin II motor activity. Adapted from [49].

The protein fibers e.g. collagen, fibronectin and fibrinogen provide binding sites on the ECM substrate that allow cells to attach via integrin transmembrane receptors.[50] The integrin family includes at least 24 different integrins, composed of two non-covalently associated α and β subunits that both span across the cell membrane.[51] Their extracellular tail specifically recognizes certain ligands of extracellular matrix proteins. These ligands are small peptide sequences within the ECM proteins e.g. the tripeptide RGD found in fibrinogen or fibronectin, or more complex ones, as the GFOGER peptide that is found within collagen.[52] With the intracellular part integrins are connected to actin filaments via a set of intracellular anchoring proteins (Figure 9).[53] During migration, the cell rapidly creates and breaks adhesion interactions with the ECM accompanied by the prompt assembly and disassembly of actin filaments.[28] This interplay is governed by an activated or inactivated conformation state of integrin, which can be triggered by the mentioned anchoring proteins or by extracellular cues.[54]

This in turn influences major signaling pathways regulating for example cell proliferation, differentiation, survival or cell death (Figure 9).[55]

The assembled protein complexes can be quite heterogeneous, either small and transient or large and durable.[47] Very strong attachments are for example focal adhesions.[43] Characteristic proteins involved in this complex include for example vinculin, talin, paxillin or tyrosine-phosphorylated proteins, as the focal adhesion kinase (FAK).[43,53]

Since talin and FAK will be addressed in my thesis, I will explain only these two adhesion-associated proteins in more detail:

Talin is a 270 kDa protein that links, beside others, the actin cytoskeleton to the integrin β subunits and triggers the affinity of integrin to ECM proteins.[56]

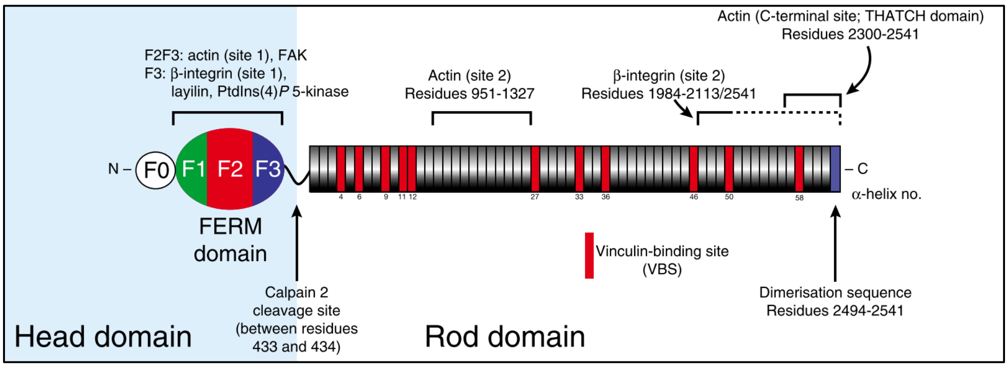

Figure 10: Domain structure of talin with binding sites for e.g. integrin, actin, vinculin. Reprinted from [56].

It comprises a globular head (talin head domain (THD)) and a flexible rod domain as depicted in Figure 10.[54] The FERM-domain (F for 4.1 protein, E for ezrin, R for radixin and M for moesin), which is a wide spread domain in adhesion-associated proteins, at the globular head includes binding sites to the cytoplasmic domain of β-integrins as well as for actin.[57] The talin rod contains additional binding sites for – among others –integrin and at least two more for actin.[56,58]

FAK is a signaling protein that is one of the major and initial proteins recruited to the adhesion sites at the intracellular integrin domain.[52,59] Further due to its tyrosine kinase activity it can phosphorylate other proteins and thus, regulates adhesion dynamics.[60] It is supposed to have a talin binding site as well as a FERM-domain for integrin binding.[59]

This is only a very brief description of the cell-ECM interaction and its regulation during cell migration. In fact, many aspects of the regulatory mechanism of cell adhesion and migration is not yet elucidated as it is incredibly complex. In this regard, a review of Zaidel-Bar and colleagues describes the “integrin adhesome” as a network comprising up to 156 linked components modified by up to 690 interactions.[53] This emphasizes the advantages of the bottom-up approach presented in my thesis, where cellular function is first dissected into its basic structure before moving to more complex systems.

1.2.1.3. Membrane Flow in Cell Migration

Besides cytoskeletal pushing and contractile forces, the adhesion to the substrate and its ECM-cell crosstalk many more minor elements contribute to cell locomotion e.g. the cell membrane flow. Clearly, by extruding the cell body in the front of the cell, the membrane needs to be enlarged.[61] Towards this aim, the additional membrane surface can be provided for example by exocytosis of internal vesicles at the front of the cell body and the according endocytosis at the rear of the cell.[62] This generates a lateral flow of the lipids in the membrane from the front to the rear (see Figure 11).[61]

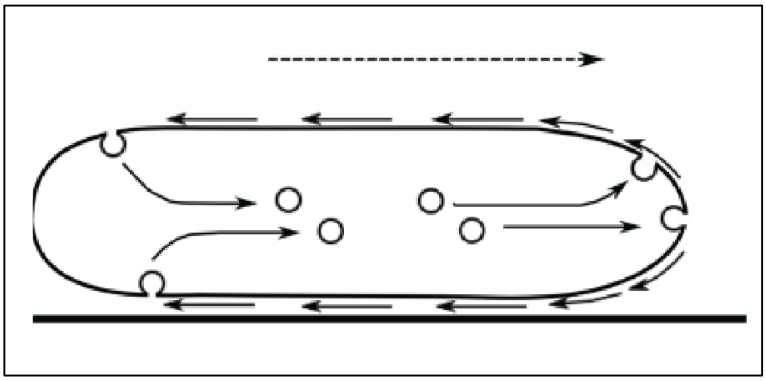

Figure 11: Schematic representation of membrane flow through exocytosis of internal vesicles at the front of the cell body and the according endocytosis at the rear of the cell. Reprinted from [61].

Moreover, in the amoebae *Dictyostelium discoideum,* this membrane flow is speculated to be directly linked to locomotion.[63] This assumption is based on the observation that peripheral cytoplasmic vacuoles as well as externally bound particles flow in the same velocity as the forward movement of the amoebae.[64] It was further shown that migration was impaired in mutants lacking an exocytosis-relevant protein.[65] Nevertheless, if the membrane flow is indeed a key driving force in the locomotion of this primitive eukaryotic cell, is still controversially discussed in literature.[62,63]

A possible route towards understanding and elucidating cellular function in greater detail is by means of synthetic biology. In this regard, I investigated in my thesis the influence of such tangential membrane flows on self-propulsion of synthetic cells (see Section 5.2.6).

Primarily, in the following section, I will explain the concept of synthetic biology and will present in detail the state of art regarding the reconstitution of eukaryotic architecture and cellular motility in synthetic cells.

1.3. Bottom-up Synthetic biology

Synthetic biology is an interdisciplinary field of biology and engineering. Research in this field is dealing with the fundamental question how life has evolved in order to understand it in greater detail. The question is addressed in two ways: Through a bottom-up and a top-down approach. In the top-down strategy, living organisms are compared in order to find similarities and a universal ancestor. Furthermore, living organisms are used for engineering and modification approaches, e.g. integrating modules with designed properties or modifying genomes by deleting or inserting genes encoding for proteins of interest.[66] The effects of these approaches might then be microscopically visible through a gain or loss of function or an altered response to an incoming signal.[67,68]

However, today's living organisms are the result of billions of years of evolution, hence, even the simplest cell has achieved a high degree of complexity that limits the understanding of all the processes and its synergistic interactions. This is very challenging for the top-down approach.

In contrast, the philosophy behind the bottom-up approach is often summarized with a quote from the physicist Richard Feynman "What I cannot create, I do not understand" – meaning we can only fully understand a living cell when we build it from scratch.[69] Hence, to circumvent the complexity of living cells, the bottom-up approach relies entirely on new building blocks and functional modules that are created and used to construct a minimal artificial cell (Figure 12). These simplified systems provide well-understood starting points to elucidate complicated cellular functions and life in general.[70]

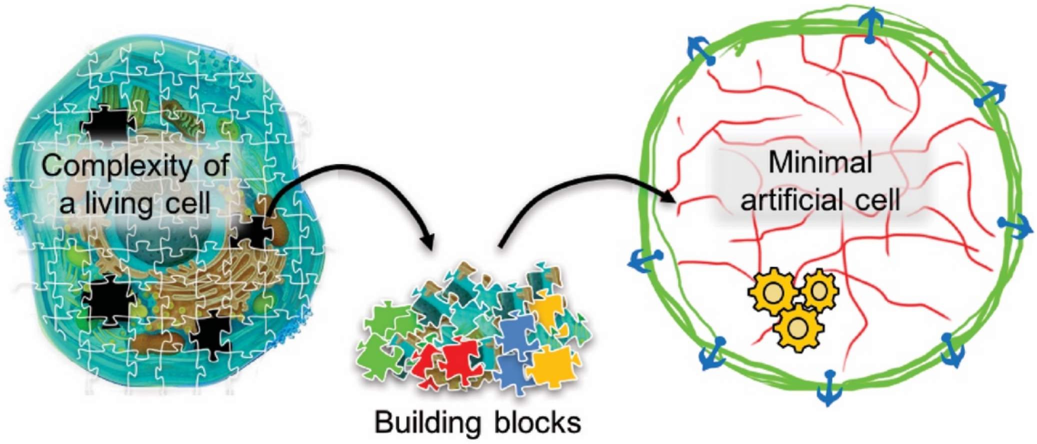

Figure 12: Schematic representation of a bottom-up synthetic cell approach. The dissection of a living cell into building blocks and the reconstruction of functional modules within an artificial compartment.

One of the most basic features of life are the boundaries between the environment and the internal space, where metabolic reactions take place. In this regard, many compartment-based model systems have been developed in synthetic biology.[71] In the following, I will give an overview of different compartment systems used in synthetic biology, including water-in-oil droplets and lipid-based compartment systems, which I used in my thesis.

1.3.1. Compartmentalization

Base of all life is formed by compartments, which create an enclosed space for controlled biochemical reactions. In particular, eukaryotic life is characterized by the coexistence of a larger outer compartment and internal smaller ones. It provides segregated internal reaction volumes that enable spatial and temporal assembly of biological processes.[11]

An adequate compartment system is thus indispensable for the bottom-up construction of synthetic cells. One of the current challenges in synthetic biology is the creation of cellular membrane mimetics, providing chemical and physical stability while allowing for further functionalization with biological components. Moreover, the manufacturing process should be bio-compatible and the system should be transferable into physiological conditions.[72]

Even though they may not yet fulfill all these prerequisites, various compartment systems have been developed and used as model systems in the past decades. These include natural membrane-based lipid vesicles,[73] but also capsules of other amphiphilic molecules like coacervates,[74] polymersomes,[75] proteinosomes,[76] and water-in-oil droplets.[16,77]

1.3.2. Cell-sized Compartments

The advantage of synthetic membranes is the possibility to employ a nearly unlimited toolbox of building blocks, with properties designed by means of chemical synthesis. Moreover, bio- and synthetic molecules can be combined merging the potency of chemical as well as biological systems.[78,79] In this regard, the first concept of an artificial cell was developed already in 1960's by Thomas Chang. His artificial cells were based on semipermeable nylon microcapsules containing lysate from red blood cells.[80] Remarkably, these artificial red blood cells were capable of oxygen[81] and carbon dioxide transport,[82] and had antioxidant functions.[83] This is not only one of the oldest examples of artificial cells, but simultaneously also one of the most successful ones, as a blood substitute based on this nanotechnological assembly of red blood cell constitutes has been approved in 2009 for routine use.[84] This proves the valuable potential of synthetic cells, not only in helping us to understand evolution of life but also for medical applications.

Nowadays, the widely used **water-in-oil emulsion droplets** are considered to be one of the simplest cell-sized compartments. They can be produced with high yield by manually mixing of an aqueous phase comprising the biological material and an oil phase,[85] or – with more precise control - by means of microfluidic technology.[77] To prevent coalescence, the water-in-oil droplets are stabilized by amphiphilic molecules, that can be either synthetic block copolymers[86] or phospholipids[87] forming a monolayer around droplets. Due to their chemical and physical stability and their high throughput production, these droplets are used widely in studies concerning cell-free gene expression or PCR applications[88] as well as in synthetic cell studies.[16,77,89] Therefore, in my thesis, I will make use of the advantages of surfactant-stabilized water-in-oil droplets. I implement them as compartments for the assembly of artificial cells.

A drawback of water-in-oil droplets in implementation as a synthetic cell is the continuous oil phase that lacks the physiological relevance and biocompatibility.

Water-in-water **polymersome-based compartments**, comprising a bilayer of amphiphilic block copolymers, are promising candidates for the assembly of artificial cells in physiological conditions.[75] Moreover, polymer chemistry provides the ability to tailor the properties of the polymersome's building blocks depending on the application the vesicles are produced for. Hence, their properties are diverse, resulting in stable compartments with capabilities such as drug encapsulation, targetability, stimuli-responsive release, and biodegradability.[90,91] Towards this end, Langowska *et al.* for example created permeable polymersomes by the insertion of a bacterial pore-forming protein into the membranes, for the *in-situ* production and release of antibiotics by an encapsulated antibiotics-producing enzyme.[92] A similar polymersome approach has been shown to act as an artificial organelle – an artificial peroxisomes – demonstrating activity in cells by the uptake and conversion of superoxide radicals and H_2O_2.[93]

Besides the usage of synthetic polymers, natural polymers as Deoxyribonucleic acid (DNA) and proteins can be found as building blocks for synthetic cell compartments.[94] In this regard, there are polymersomes that consist of protein building blocks, thus, are called **proteinosomes**. In order to achieve their self-assembly into compartment structures, proteins can be rendered amphiphilic by being chemically linked to synthetic hydrophobic segments.[80] Similarly, like in case of synthetic polymersomes, the proteinosome function can be tailored by encapsulating a variety of enzymes and active compounds. In this regard, Huang *et al.* designed a proteinosome based on amphiphilic BSA-polymer hybrid molecules, featuring controlled membrane disassembly and release of entrapped material.[95]

Further, also DNA has been used to construct compartments.[96] However, the field of synthetic biology benefits in a much broader way from DNA nanotechnology, as it can be used to create robust building blocks with new functions and features[97] e.g. membrane ion channels,[98] or molecular motors.[99] Even though natural building blocks as proteins and DNA are intrinsically biologically relevant, the best way to mimic cellular compartments is by means of phospholipids, since they also make up the cellular membranes in living cells.

1.3.3. Lipid-based Model Systems

In my thesis, I will combine polymer-stabilized water-in-oil droplets with lipid-based vesicles. Thereby, the mechanical and chemical stability of polymersomes and the physiological relevance of phospholipid bilayers is exploited. Lipid membranes have been studied intensively in the last decades, as they are considered as the best mimetics of the cellular membranes.[100,101] Important parts in this research are planar lipid membranes. These include so-called black lipid membranes, lipid bilayers spanned over a hollow device, and **solid supported lipid bilayers** (**SLB**, see Figure 13A). Both are valuable models for studying membrane physics,[100] cell-cell interface interactions,[102] or lateral mobility of adsorbed macromolecules.[103]

In addition to adaptation of SLB for various light microscopy techniques, SLBs allow analysis by means of very sensitive surface techniques, such as surface plasmon resonance, Quartz crystal microbalance (QCM, for more details see Section 4.8.1) or atomic force microscopy (AFM).[104] The most common way to create such lipid bilayers are the Langmuir Blodgett technique or the direct fusion technique, that was pioneered by McConnell *et al.* in the early 80s.[101] The fusion of lipid vesicles on hydrophilic supports is easy to implement, however, the process is not fully understood, yet. The driving force of the fusion process is suggested to be governed by van der Waals forces and electrostatic interactions with the substrate. The process begins with the adsorption of the vesicles, what can result then to the fusion of the vesicles with each other and to the support once a certain surface coverage is reached.[100] Vesicle fusion depends on the gain in adhesion energy and the energy cost for the vesicles' curvature,[105,106] however, can be influenced by many factors, e.g. vesicle properties (bending rigidity, lipid composition, size, surface charge, osmotic pressure), nature of the surface (charge, roughness, cleanliness), as well as buffer conditions (pH, ionic strength).[100]

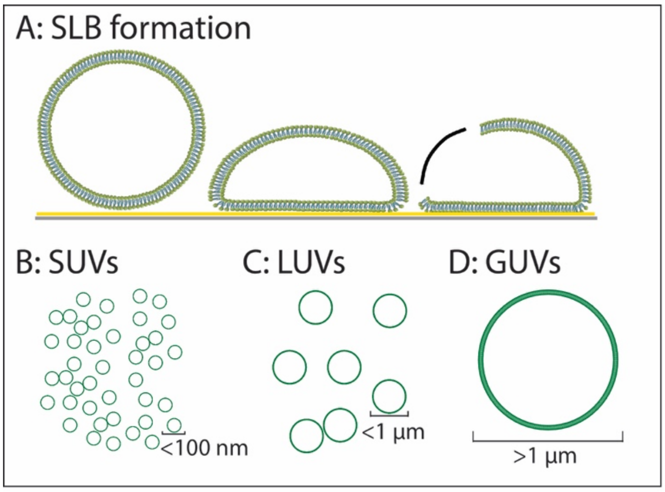

Figure 13: Illustration of lipid-based model systems. A) Supported lipid bilayer (SLB) formation, B) Small unilamellar vesicles (SUVs), C) Large unilamellar vesicles (LUVs) D) Giant unilamellar vesicles (GUVs)

Despite the fact that valuable knowledge has been gained by studying planar lipid membranes, spherical lipid compartments are considered as favorable model system for cell mimetics. **Lipid vesicles** are classified into small (SUVs, <100 nm, see Figure 13B), large (LUVs, 100 to 1000 nm, Figure 13C) or giant unilamellar vesicles (GUVs, 1 µm – 100 µm, Figure 13D)[107] and, depending on the number of bilayers, into uni-, oligo- and multi-lamellar. An additional important parameter is the phospholipid charge.[108]

The production of SUVs and LUVs is a high yield and straight forward process. In the production process, the desired lipids are mixed in organic solvent in a glass vial. After the solvent is dried off, a lipid film remains. This film is then hydrated by the addition of an aqueous buffer and vigorous shaking. This results in multilamellar vesicles, that can be downsized and transformed into mainly unilamellar vesicles by a variety of techniques, such as sonication, or extrusion.[109] In the extrusion technique, the vesicles are pressed through a bicarbonate filter with a pore size of 50 – 400 nm.[86,110] Another way to create lipid vesicles is the detergent removal method. Here the dried lipid film is dissolved in an aqueous buffer, containing detergents above their critical micelles concentration. Upon removal of the detergent, the micelles enrich in phospholipids, and finally form lipid vesicles. The detergent can be removed e.g. by dialysis or by adsorption to porous hydrophobic beads. This method of detergent removal allows for reconstitution of membrane-associated proteins. It also allows for a good encapsulation efficiency of soluble material[109,111,112] rendering the lipid vesicles a good model system to investigate cellular processes.[4,113,114]

Even though they are too small to be observed with optical tools, SUVs can be analyzed in bulk by means of dynamic light scattering (DLS), AFM, quartz crystal microbalance with dissipation monitoring (QCM-D), or electron microscopy.[115] Moreover, lipid vesicles play an important role as carriers for numerous molecules in drug delivery, cosmetics, and food industries.[116]

1.3.4. GUVs

Cell-sized GUVs possess significant advantages when used as synthetic cell compartments. This is due to cell-like membrane curvature and the possibility to be easily observed and manipulated under optical microscopes. Therefore, GUVs remain the gold standard in synthetic biology and are used widely to imitate cellular processes.[117] Moreover, GUVs gained much attention as biochemical reactors for macromolecule synthesis.[118]

For the preparation of GUVs several techniques have been developed (Figure 14). Currently, electroformation (Figure 14a)[119] and gentle hydration[120] are the most commonly used methods to create GUVs. Similar as for SUV or LUV preparation, the procedure starts with the formation of a dried lipid film on a substrate. For the gentle hydration method, a pre-swelling step in water-saturated atmosphere is followed by the introduction of aqueous buffer into the swelling chamber. The gentle hydration can take up to a couple of days until the process is completed and the GUVs can be harvested. For electroformation, the vesicle swelling is accelerated by applying an AC field. For this purpose, the lipid film has to be deposited on conductive indium tin oxide (ITO) coated glass slides.[121] The advantage of electroformation is that it is much faster (few hours) than the hydration method and the vesicles are usually larger, unilamellar and have fewer defects in the membrane. Nevertheless, it also brings along several drawbacks: Low yield in physiological buffer solutions, heterogeneity in lipid composition and size, the limitation that only small amounts of charged lipids can be used, as well as low efficiencies when encapsulating biomolecules.[107,122,123] Other methods like microfluidic jetting (Figure 14d),[124] or emulsion transfer (Figure 14b),[72] overcome these limitations to some extent but compromise the GUV yield.

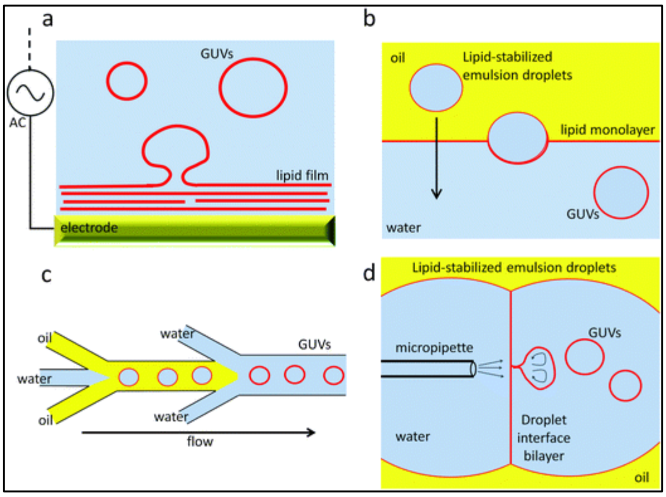

Figure 14: Overview of most common GUV formation methods. (a) Electroformation or gentle swelling (without electrical field); (b) emulsion-transfer method; (c) microfluidic double emulsions; (d) microfluidic jetting. Reprinted from [125] *- Published by The Royal Society of Chemistry.*

For the microfluidic jetting approach (Figure 14d), a black lipid membrane is formed in aqueous solution. By applying a microfluidic jet across the membrane, GUVs are blown from the planar lipid film.[124] In the droplet transfer method[126] aqueous buffer is dropwise introduced into an oil-solution containing lipids. These lipid-stabilized water-in-oil droplets are subsequently transferred by means of centrifugation through another lipid monolayer into an aqueous phase, thereby receiving a second lipid leaflet.[127] Both processes allow for efficient encapsulation of macromolecules and ensure that the content is distinct from the continuous aqueous phase.

In recent years, microfluidic technologies for the high throughput production of monodisperse GUVs have been developed (Figure 14c), most of them based on water-in-oil-in-water double emulsions. Here the critical point is the residues of organic solvents in the bilayer. This limitation could be solved by Deshpande *et al.* by generating double emulsion droplets with an organic phase, consisting of lipid-carrying octanol. The excess octanol in the bilayer is – within few seconds after production – dewetted from the droplet as a pocket, which is pinched off by outer fluid streams. This leaves a pure lipid bilayer-enclosed vesicle behind.[128] Further, Elani *et* *al.* optimized the droplet transfer method by incorporating the procedure within a microfluidic device.[129]

A different microfluidic approach to generate GUVs in a high throughput manner was developed in our group.[16] These GUVs are initially stabilized by a block copolymer layer in an oil phase, therefore named droplet-stabilized GUVs (dsGUVs). In this stabilized environment, the dsGUVs can be loaded sequentially with biomolecules via high throughput picoinjection technology.[130] After loading, the dsGUVs can be released as free-standing GUVs from the surfactant shell and the oil phase into a physiological environment. This method will be discussed in more detail in Section 4.5.5 and 5.1.4 of this thesis.

1.3.5. Multicompartment Systems

To date most of the artificial cell research has been focused mainly on single-compartment structures with homogenously distributed internal content. However, the natural architecture of eukaryotic cells features smaller vesicular compartments inside the external lipid membrane. These smaller vesicular compartments – like organelles and transport vesicles – provide a physical boundary between specialized microenvironments, and allow for a multitude of vital processes e.g. energy production or material transport (see Sections 1.2.1.3). Thus, to achieve multiple distinct reactions in a single artificial cell, compartments that incorporate organelle-like structures have to be designed.[71,131,132]

The idea of a multicompartment system within water-in-oil droplets has been implemented in my thesis in Section 5.1.2. Thus, I want to give an overview how multicompartment systems have been realized in other groups, thereby addressing also multivesicular system, that mimic multicellularity.

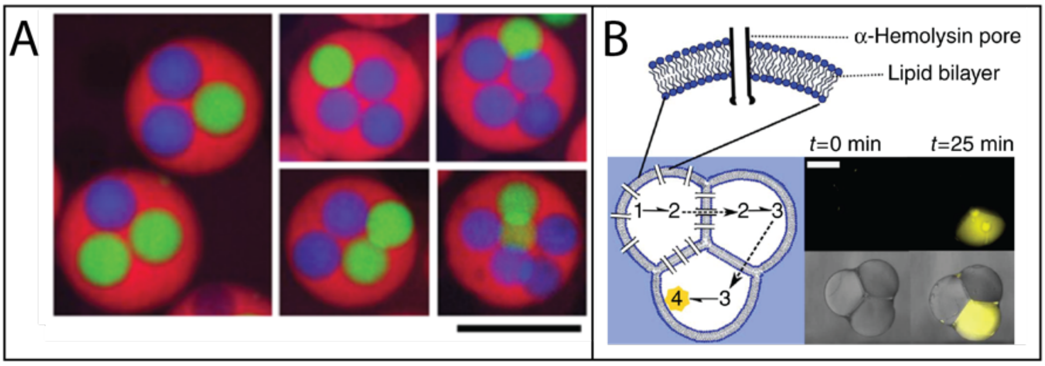

Figure 15: Synthetic multicompartment and multivesicular systems. (A) Confocal fluorescence images of GUVs with different numbers and ratios of internal liposomes. Scale bar 100 µm. Reprinted with permission from [133]. Copyright 2018 American Chemical Society. (B) Multivesicular structure allowing for multi-step enzyme reactions through α-hemolysin pores. Scale bar 250 mm. Reprinted with permission from [72].

GUVs containing smaller lipid vesicles exhibit the required topological feature to mimic the basic organelle-like structure in eukaryotic cells. These structures can appear as a result of endo-budding or during morphological changes of the GUVs under osmotic stress or temperature changes.[134]

In a different approach, so-called vesosomes have been developed, comprising of aggregated vesicles with distinct content, that were encapsulated by unrolling bilayers from spirally twisted lipid cylinders.[135] More advanced, monodisperse vesosome structures have been recently produced by the microfluidic approach of Deng *et al.*, in which single or a defined number of liposomes have been encapsulated into larger double emulsion droplets (Figure 15A).[133] Thereby, multicompartment vesicles, capable of performing sophisticated reactions, including RNA synthesis and transport between the encapsulated liposomes, were realized.[133]

Bolinger *et al.* trapped SUVs inside LUVs by hydrating a dried lipid film with an SUV solution. Based on different phase transition temperatures of the encapsulated SUVs, distinct chemical reactions could be performed in a controlled and successive way through the rupture of SUVs once a particular phase transition temperature is reached.[136]

To achieve multivesicular structures, which mimic multicellular organisms, Villar and colleagues surrounded several water-in-oil emulsion droplets by a monolayer of phospholipids.[137] Thereby a droplet network was created allowing for communication between the vesicles via membrane pores. Elani *et al.* constructed similar structures, with internal lipid bilayer divisions, to perform a multi-step enzymatic cascade by transferring the products from one to the adjacent compartment (Figure 15B).[72] More recently, the same group achieved a multistep reaction cascade between living cells and co-encapsulated enzymes within microfluidic water-in-oil droplets.[129] These results can relate to the evolutionary milestone of eukaryotic cells, originated – based on the endosymbiotic theory – through endocytosis of formerly free-living organisms.[20]

These recent works show the importance of segregated space to allow for sophisticated reactions to happen. Moreover, internal compartments increase the cellular membrane area, a place where major cellular function takes place in eukaryotic cells (e.g. proton gradient for ATP synthesis, protein and lipid synthesis, transport etc.).[11] A way to further increase surface-to-volume ratio in eukaryotic structures is through membrane folds. This is for example seen in organelle structures as the mitochondria or the endoplasmic reticulum.

In the next section, I will discuss how the surface-to-volume ratio can be increased in artificial compartments. I will focus thereby only on the membrane folds in GUVs as this will be part of my thesis in Section 5.1.4.4.4.

1.3.6. Organelle Structures with Increased Surface-to-Volume Ratio

GUVs are normally spherical vesicles, but – due to the low bending rigidity – GUV's lipid membrane can be adapted to various shapes with increased surface-to-volume ratio.[121,138] These shape changes can be mediated e.g. by osmotic stress or by encapsulated macromolecules (like PEG) leading to a depletion effect between the membrane and the crowding polymers.[134] Under such conditions the morphology of GUVs can deviate from the spherical shape and resemble eukaryotic organelles like the mitochondria, the Golgi apparatus, or the smooth endoplasmic reticulum with increased surface-to-volume ratio (Figure 16A).[139]

In this regard, it has been achieved that GUVs display cristae-like morphology (Figure 16B), and thus, provide a good model system to mimic the inner membrane morphologies of mitochondria.[24] This cristae structure evolved due to certain mitochondria-typical and cardiolipin-rich lipid composition and a local pH gradient created by exposing the outer lipid monolayer to an acidic buffer solution. It was assumed that the negatively charged cardiolipin functioned as a proton trap, leading to an area reduction of the exposed monolayer and thus, to an area mismatch between the inner and outer monolayers of the membrane. This created mechanical stress and induced tube-like membrane invaginations.

In another work by Bilal *et al.* (Figure 16C), endoplasmic reticulum networks were mimicked, based on nanotube networks, that rolled up from of multilayered lipid films upon Ca^{2+} depletion.[140]

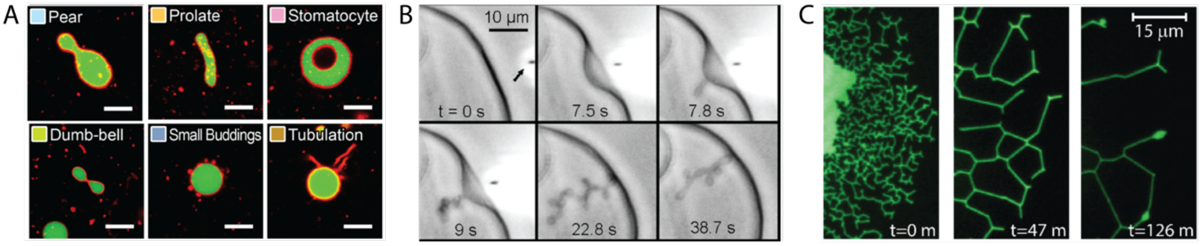

Figure 16: Lipid-based systems with increased surface-to-volume ratio. (A) Confocal fluorescence images of different GUV shape categories, evolved through interactions with macromolecules and deflation. Scale bar 10 µm. Reprinted with permission from [139]. Copyright 2018 American Chemical Society. *(B) Various bright-field time-lapse images of dynamic cristae-like membrane invaginations due to a local pH gradient at a cardiolipin-containing membrane. Reprinted with permission from [24]. Copyright © 2008 The Biophysical Society. (C) Fluorescence images showing the formation of lipid nanotube networks by retraction of lipid bilayer membranes from the surface. Reproduced from [140] with permission from The Royal Society of Chemistry.*

This shows that lipid membrane systems alone can create specialized cellular structures. Nevertheless, in a living cell, proteins are key to equip the cellular membranes with sophisticated and complex functions. Therefore, in the following sections I will discuss the contributions of membrane proteins towards the creation of functional modules within a synthetic cell.

1.3.7. Functional Modules

A living cell constantly needs to fulfill different tasks including, but not limited to, protein expression, endo- and exocytosis, cell-cell or cell-matrix interaction, and locomotion. All these tasks are based on a specialized set of building blocks and regulatory molecules, which can be grouped into functional modules.

To create cellular functional modules in a synthetic system, first, the complex machinery of a living cell has to be dissected. Major building blocks have to be identified and reconstituted within the artificial system. Towards this end, some approaches involve cell lysate extracts to ensure optimal conditions for the machinery of interest.[89] However, the content of such cell extracts is poorly defined and limits experimental control. Thus, for bottom-up assembly of functional modules it is advantageous to use synthetic or purified building blocks, isolated or engineered proteins, or DNA constructs.

In my thesis, I focused on reconstituting cellular motility, that can be subdivided into the functional modules of actin dynamics (elongation and contraction), and adhesion-associated membrane proteins. Thus, in the following sections, I will present an overview of different works that addressed the reconstitution of membrane proteins into cell-sized vesicles, followed by the state of art regarding cytoskeletal network reconstitution.

1.3.8. Reconstitution of Membrane Proteins

Nearly one third of the proteins in a living cell are embedded in cellular membranes and mediate important biological reactions, such as transport, adhesion, signal transduction, and the generation of energy.[141,142] In this concern, it is crucial to include transmembrane proteins when constructing cell mimetics.

In the following, I will discuss the most common methods for reconstituting membrane proteins into SUVs and GUVs.

First studies of reconstituted membrane proteins in artificial cells have been done in liposomes and date back to the 70's.[143] Here ATPase activity and ATP exchange could be achieved in SUVs by isolating and reconstituting membrane fragments from mitochondria.[143] Since then, many more membrane proteins have been reconstituted within SUVs, ranging from proteins for selective transport (e.g. ion channels[144], H^+/K^+-ATPase[145]) to integrin adhesion receptors as presented in Figure 17.[15,146]

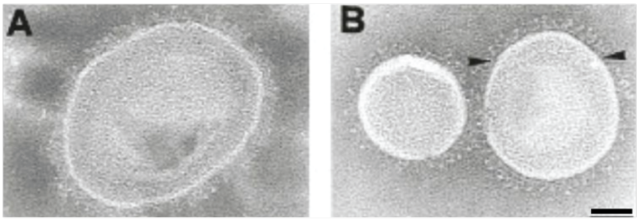

Figure 17: Cryoelectron micrographs of vesicles containing reconstituted integrin $\alpha_{IIb}\beta_3$ in high(A) and low (B) density. Scale bar 100 nm. (Reprinted with permission from [15]. Copyright (1997) American Chemical Society.

Towards this end, first, the active protein has to be isolated from a recombinant source, or in case of larger proteins, membrane fractions have to be obtained from cells of interest or from specific organelles. Then they need to be purified from other components of the natural membrane by means of differential centrifugation and detergent-mediated solubilization.

For the reconstitution of the isolated membrane protein into an artificial membrane, it can be either directly embedded into the lipid membrane or, if the hydrophobic domain is too large, the transfer of the protein needs to be assisted by the presence of a detergent that is removed after reconstitution.[109]

Whereas the reconstitution of transmembrane proteins into small lipid vesicles is straight forward, the reconstitution into GUVs comes along with challenges and thus is not as prevalent. Due to the GUV's fragility and harsh preparation conditions, the reconstitution of transmembrane proteins is more complicated, however, not less important. GUVs resemble a eukaryotic cell in terms of size, and thus, a wider range of optical analysis methods can be used. In standard GUV preparation methods, a dehydration step is involved. This may lead when a protein is included to the loss of its activity. A gentler dehydration step, however, in the presence of e.g. agarose, can help to prevent complete dehydration.[147] Doing so, the reconstitution of e.g. a functional voltage-gated ion channel has been achieved.[148] Further, the droplet transfer method has been used for transmembrane protein reconstitution. The pitfall here is that most proteins do not assemble into a lipid monolayer, which limits its application.[149]

To bypass the mentioned problems, some approaches involve a prior step of proteoliposome formation and subsequently their fusion with GUVs through the help of detergents,[150] fusogenic peptides,[151] DNA,[152] or complementary charges.[153] Nevertheless, while being favorable for protein activity, these methods come with their own challenges, due to GUV instabilities.[117]

Thus, transmembrane proteins have been embedded as well into membranes of mechanically stable polymersomes, by means of detergent-mediated reconstitution. In this concern, however, the polymersomes need to meet certain criteria e.g. a membrane thickness and fluidity comparable to the ones of typical lipid bilayers. Fulfilling this, the reconstitution of e.g. quinol oxidase or bacteriorhodopsin and the F1FO ATP synthase into polymersomes, was achieved.[154,155]

Nevertheless, all these methods for reconstituting membrane proteins into cell-sized compartments, come along with limitations. In this regard, a stable and fast method, to fuse protein-containing SUVs into one big GUV, would be highly desirable. The first method, achieving this goal, was developed here and will be presented in Section 5.1.3 of this thesis.

1.3.9. Towards Artificial Motility

Many processes in the cell, including but not limited to, embryonic development, immune response, tissue formation and wound healing, are based on cellular motility. Eukaryotic cells move mostly by migration on a substrate. This movement is accomplished in - simply put - three major steps: 1) Extension of the leading edge. 2) New adhesions to the substrate at the front and 3) detachment of adhesion sites at the rear and the contraction of the cell body (see Section 1.2.1).[28]

Thus, towards the reconstitution of cellular motility, an active cytoskeleton as well as cell adhesion receptors are key players. Therefore, reconstitution of these building blocks in synthetic cells was the major goal in my thesis. To date, no cell mimetics have been reported that include adhesion capability as well as cytoskeletal function. The state of art in this field will be presented in the following.

1.3.9.1. Artificial Cytoskeleton

The cytoskeleton consists of three major filament types (see Section 1.2.1.1). To date, the encapsulation of actin and microtubule networks is a similarly straight forward procedure.[156,157] However, the encapsulation of intermediate filaments into artificial cells is clearly absent as its reconstitution is relatively complex.[8] Therefore, I will only introduce the reconstitution of microtubules and actin networks in the following sections.

Microtubules

The first studies that encapsulated microtubules into artificial cells were performed in the early 90's.[156,157] Here, the impact of microtubules on cell shape could be resembled by the deformation of vesicles upon microtubule polymerization due to their intrinsic stiffness (persistence length 1-2 mm[158]) and their capability to apply a significant pushing force onto the compartment boundaries.[156,157]

More recently, Hayashi *et al.* showed the dynamic control of microtubule polymerization and depolymerization via compression force. It was demonstrated that while microtubule polymerization led to GUV protrusions at ambient pressure, the application of hydrostatic pressure led to the shrinkage of the protrusions, as a result of microtubule depolymerization (Figure 18A).[159] This dynamic process resembled the organization of the cytoskeleton in a living cell, which is not static but permanently reassembles in response to internal and external environmental factors. In a living cell, this dynamic organization is mainly mediated by motor proteins like kinesin.[11]

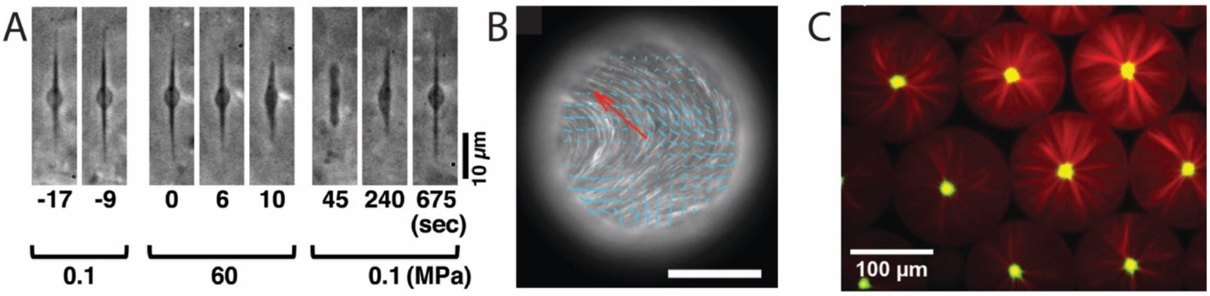

Figure 18: Microtubules reconstituted in artificial cell systems (A) Phase contrast images of microtubules polymerized in liposomes. Reversible shrinkage of vesicle protrusions by applied pressure. Reprinted with permission from [159] *Copyright © 2016 American Chemical Society. (B) Fluorescence image of active microtubule bundles in a water-in-oil droplet. Pushing microtubules induced streaming flows, indicated with blue arrows; red arrow indicates direction of droplet velocity. Scale bar 100 mm. Reprinted with permission from* [161] *Copyright © 2012, Springer Nature (C) Confocal image of microtubule asters (labeled in red) in surfactant-stabilized water-in-oil droplets, organized by kinesin (labeled in green).*[77] *- Published by The Royal Society of Chemistry.*

In 2012, it was demonstrated in a synthetic cell that upon kinesin activity microtubule bundles showed highly ordered collective network dynamics, orchestrated by a hydrodynamic connection between the bundles and a resulting directed fluid flow (Figure 18B).[161] Most remarkably, an autonomous motion of water-in-oil droplets could be observed when the droplets comprised microtubules and kinesin networks.

Recently, water-in-oil droplets were used by our group and others,[77,85] to investigate the microtubule aster organization (Figure 18C) depending on kinesin motor concentration and confinement size. Whereas in smaller droplets, microtubules bent in bundles at the droplets boundary, in droplets larger than 100 μm microtubule aster formation appeared.[77,85]

Actin

The actin cytoskeleton is involved in the elongation force, contraction force and the connection to the membrane receptors. These are major features of cellular motility and will be implemented in the synthetic cell approach, presented in my thesis in Section 5.2. However, first I will introduce what have been done so far in the field of actin dynamics in synthetic cells.

Actin networks have been studied intensively in the past.[162–164] First incorporation of actin networks within cell mimetics was achieved in the late 80's by Cortese *et al.*,[162] followed by a more sophisticated approach of Bärmann *et al.*[163] Bärmann and colleagues used the hydration method to incorporate actin monomers in the GUV's lumen and polymerized them by increasing ion concentrations through ionophores in the GUV membrane. Similar to encapsulated microtubules, a deformation of the flexible compartment upon filament polymerization was observed. However, this was dependent on the compartment size. Thus, deformation was observed only, when actin filaments were encapsulated in vesicles, that were smaller than the filament's persistence length.[163]

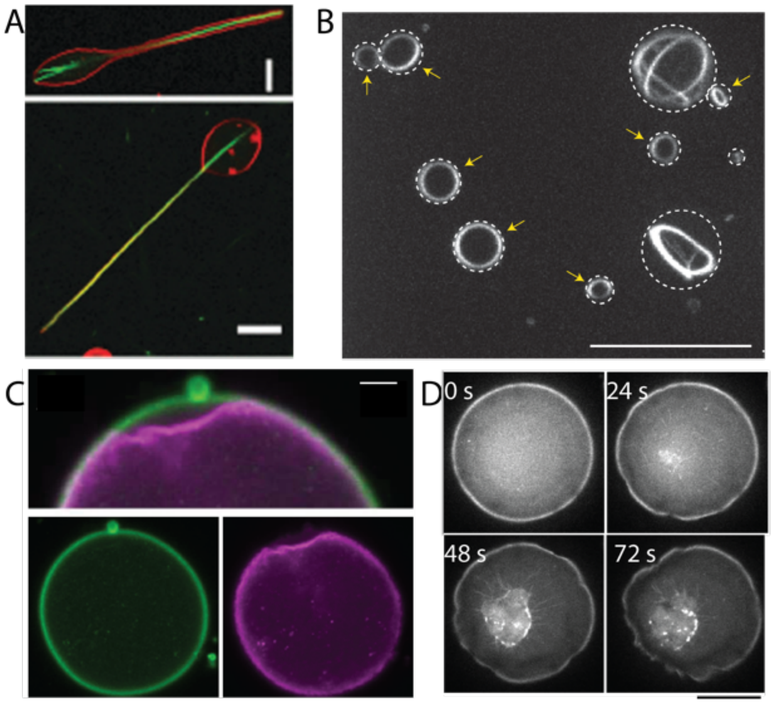

Figure 19: Examples of actin and actomyosin networks within artificial cell systems. (A) Confocal fluorescence images of actin networks polymerized in liposomes. Presence of the crosslinker fascin (actin-to-fascin ratio 5:1) leads to long protrusions of vesicles. Scale bar 5 µm. Reproduced from [165] with permission from The Royal Society of Chemistry. (B) Actin filaments encapsulated within water-in-oil droplets surrounded by a phospholipid monolayer. Actin forms thick and rigid bundles in the presence of methylcellulose. Filaments are forced to adapt to the spherical shape of the droplet and organize into cortical rings in order to minimize filament bending, Scale bar 20 µm. Reprinted with permission from [166] Copyright © 2015, Springer Nature (C) Fluorescent image of actomyosin cortex (labeled in magenta) assembly within water-in-oil droplets stabilized by an amphiphilic actin-binding protein (labeled in green). Through myosin's contraction force, the network detaches from the droplets interface. Scale bar 10 µm. Reprinted with permission from [89] Copyright © 2014, Abu Shah and Keren. (D): Confocal fluorescence image of actomyosin within water-in-oil droplets. Contraction leads to non-periodic oscillatory deformation of the lipid interface. Scale bar 50 µm. Reprinted with permission from [167] Copyright © 2016, Springer Nature.

In similar studies, it was shown that the deformation of actin-containing vesicles can be triggered by changing the length and mechanical properties of the actin filaments through co-encapsulation of capping proteins as gelsolin,[162] or bundling proteins as fascin (see Figure 19A).[165] Further, membrane deformation could be suppressed by increasing the bending rigidity of the membrane. Hereby, actin bundles were forced to adapt to the spherical shape, and organize into cortical rings in order to minimize the elastic energy costs, associated with filament bending.[165]

Similar effects could be seen in water-in-oil droplets by modelling the actin bundling through the presence of methylcellulose (see Figure 19B).[166] The bundling is based on the depletion effect that leads to the exclusion of macromolecules from the surface of actin filaments. The total free energy is minimized, when the depletion volume is at its maximum.[168]

These works show that rigid actin filaments can generate a considerably amount of pushing force between the confinement and the network, depending on the filament bending elasticity and membrane curvature.

In a living cell, the actin networks are constantly reassembled. Thereby, dynamic actin forces are generated based on directional polymerization and depolymerization of the actin filaments, the so-called treadmilling. A popular model system, showing the motor-free force generation of actin networks through polymerization, is the intracellular pathogen *listeria*, which uses the actin cytoskeleton of its host to be propelled throughout the cell body. Thereby, *listeria* recruits actin monomers to its rear and by inducing actin polymerization the bacterium is pushed forward.[169] Towards recreation of this phenomenon *in vitro,* polystyrene beads, or small lipid vesicles, were coated with the *listeria*'s pathogenic protein ActA, that acts as nucleation sites for actin polymerization. [169]

In cell motility, the pushing forces at the front of the cell have to be orchestrated with the contraction of the rear. In this regard, myosin motor proteins, associated to the actin cytoskeleton, so-called actomyosin networks, play a critical role.[170]

Actomyosin dynamics have been studied intensively on 2D substrates, investigating the effects of e.g. different actin-to-myosin ratios, the presence and critical concentrations of actin crosslinkers, ionic conditions, and ATP concentrations on network contraction.[164,171] Further stability of actomyosin filaments were tested under compressive and tensile stresses,[172] explaining the break of symmetry between myosin-mediated forces, that leads finally to a net contractile force.[46]

In order to create cytoskeletal dynamics within a cell-like confinement, several studies encapsulated actomyosin networks into lipid vesicles or water-in-oil droplets.[87,171,173]

In a living cell, the actomyosin network forms a dynamic cortex, linked via several complex tethering proteins to the membrane.[170] Hence, actomyosin linkage to the membrane was reconstituted artificially, e.g. via electrostatic interaction to positively charged lipids in the membrane,[87,171] via biotin-streptavidin interactions,[174] or via natural anchoring proteins.[173]

In this regard, Shah *et al.* encapsulated cell extracts into water-in-oil droplets and linked the actomyosin cortex via an amphiphilic protein to the lipid monolayer at the oil-water interface. With this system, they could show spontaneous, myosin-driven symmetry breaking of the assembled actomyosin cortex, resulting either in an asymmetric organization of the cortex and a deformation of the droplet, or in a detachment of the cortex from the droplets interface (see Figure 19C).[89]

In other studies, encapsulated and membrane-linked actomyosin contraction led to membrane oscillation (see Figure 19D),[171] membrane blebbing,[175] or even to a collapse[171] of the compartment membrane, depending on the bending rigidity of the compartment's membrane and the connection to it.

To balance the applied cytoskeletal forces, major steps in motility involve, besides the described cell shape changes, the adhesion to the substrate.[170] How the functional module of adhesion can be implemented in an artificial cell will be described in the following section, and is further described in context of the droplet-stabilized GUV approach in my thesis in Section 5.3.

1.3.9.2. Adhesion Receptors

In a living cell, adhesion to certain proteins of the extracellular substrate is mediated by the transmembrane protein integrin. To study cellular adhesion in artificial systems, integrins have been reconstituted in SLB in 2D.[176] By doing so, GUVs, comprising the RGD peptide on their surface, showed a specific binding to the integrin proteins embedded in the SLB.[176] Even though, this shows the functionality of reconstituted integrin proteins, the fact that the integrin proteins are reconstituted in 2D has several drawbacks. First, it is lacking cell-like geometry and second, it does not provide the possibility to include a cytoskeletal connection.

Towards adhesion studies in spherical liposomes, the reconstitution of $\alpha_{IIb}\beta_3$ integrin into SUVs (see Figure 20) has been shown together with their specific interaction to various ECM proteins by means of QCM-D.[146,15] This proves the functionality of the reconstituted integrin proteins, however lacks cell-like dimensions.[146]

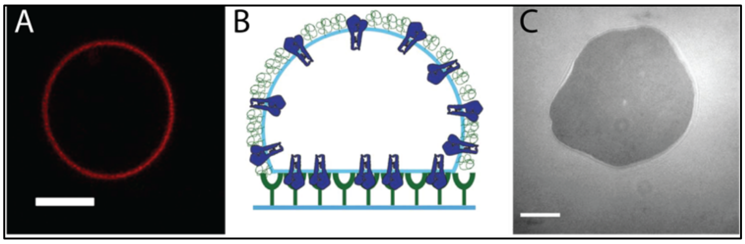

Figure 20: Integrin reconstituted in GUVs. (A) Confocal image of a GUV containing 5% of the integrins fluorescently labeled. (B) Scheme of a GUV containing integrins interacting with a fibrinogen-coated surface. (C) Adhesion is detected with reflection interference contrast microscopy (black patch). Scale bar 10 µm. (Reprinted with permission from [177]. Copyright (2009) Elsevier Ltd.

In this regard, Streicher *et al.* showed the successful incorporation of functional integrin proteins into GUVs (Figure 20A), and further, their biological activity by specific adhesion of these GUVs to substrates comprising RGD motifs (Figure 20B, C).[177]

Besides the work of Streicher *et al.* there is only one more study to my knowledge, showing the reconstitution of integrins into GUVs: it is the before mentioned droplet-stabilized GUV approach, that involves the fusion of proteoliposomes to a cell-sized vesicle, and the subsequent release of integrin-GUVs out of the stabilizing droplet and oil phase into an aqueous and physiological phase. Whereas the protocol of Streicher *et al.* involves a dehydration step, which can potentially affect protein activity, the dsGUV approach is performed in mild conditions and under high throughput performance, providing thereby the possibility to implement the integrin-GUVs in versatile follow-up adhesion studies.[16] This method will be implemented in this thesis in Section 5.3.3.

As described above, previous synthetic cell studies have investigated the functional modules of adhesion and cytoskeleton separately, however to my knowledge, none have reported a combined approach. Thus, another milestone to achieve would be to combine adhesion and cytoskeletal proteins in one artificial cell and further introduce proteins to anchor the actin cytoskeleton to integrin receptors. Such an approach will be addressed in my thesis in Section 5.3.4.

Prior to this, I will characterize the compartment system that is implemented in my thesis: microfluidic block copolymer stabilized water-in-oil emulsion droplets. The according technical and theoretical background will be described in the following.

1.4. Technical Background

In my thesis, I will use a microfluidic approach to create water-in-oil emulsion droplets as compartments for the assembly of synthetic cells. In this regard, I will introduce in the following the general concept of emulsions and their stabilization through surface active molecules, namely emulsifiers or surfactants. In addition to the reduction of the interfacial tension at the water-oil interface, surfactants may induce the interactions of encapsulated molecules with the interface layer. These surfactant-based functions play a crucial role in the generation of droplet-stabilized GUVs as well as in actin network dynamics (see Section 5.1 and 5.2.3.2, respectively). Further, I will describe adsorption models to give an idea about the dynamics at the droplets interface. Moreover, I will describe, how water-in-oil droplets are implemented through precise and high throughput microfluidic technology.

1.4.1. Emulsions

An emulsion is a colloidal mixture of substances that are insoluble in each other and thus, form a two-phase system with a continuous and a dispersed phase.[178] In emulsions, both substances are liquids e.g. mayonnaise or homogenized milk are emulsions where, respectively, water is dispersed in oil, thus a water-in-oil emulsion, or *vice versa*. These two emulsions are called single emulsions. Double or multiple emulsions are also possible and include for example water-in-oil-in-water systems.[179]

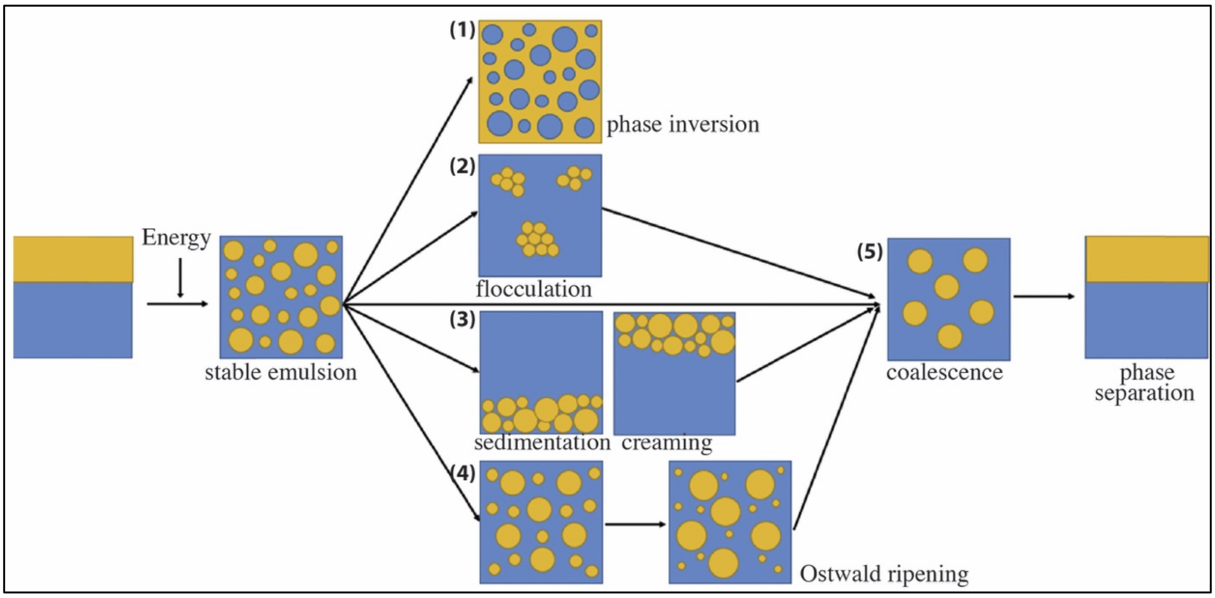

Figure 21: Schematic representation of mechanisms in emulsions. Adapted and reprinted with permission from [184]*. Copyright (2017) Elsevier Ltd.*

The fact that the phases are not soluble in each other is governed by distinct intermolecular interactions between molecules of each phase. This means that the energy costs of enthalpy and entropy of mixing counteract.[180] In this sense, emulsions do not form spontaneously and are intrinsically unstable.[181] Thus, to create an emulsion energy is required. Energy can be provided for example in the form of vigorously stirring, ultrasound sonication or by means of microfluidics. Eventually, the emulsion phases tend to separate again in the two primary phases.[178] The instability or aging of an emulsion is described by the time how long it takes before the emulsion changes its properties due to e.g. phase inversion (1), flocculation (2), sedimentation or creaming (3), Ostwald ripening (4) or coalescence (fusion of two droplets) (5) (see Figure 21).[182–184]

Ostwald ripening is a process based on differently sized droplets in the emulsion. As the Laplace pressure (see Section 1.4.3) is lower in large droplets than in small droplets, the large droplets grow in expense of smaller droplets.[185] Flocculation describes the process when the droplets form grape-like structures due to attractive interactions between each other.[178] Creaming is the effect when the dispersed phase rise up due to buoyancy. This happens for example when the two phases have a large difference in their density.[186] The instability of an emulsion can be influenced by e.g. temperature or mechanical methods like centrifugation.[187]

The stability of emulsion is of great importance in industry and particularly in biotechnological applications,[188] when emulsion droplets are used as microreactors or – like in this thesis – as synthetic cells, where the components are required to maintain stably encapsulated to well-controlled biochemical conditions.[189–191] Thus, in the following I will explain how emulsifiers or surfactants counteract the aging effects of emulsions.

1.4.2. Surfactants

A surfactant is a compound word describing surface-active agents. As the name implies, surfactants adsorb at interfaces of two insoluble fluids (Figure 22), as they possess typically a hydrophobic tail and a hydrophilic head.

Since emulsions are metastable systems, they require surfactants for stabilization.[192] In this regard, surfactants can increase stability from minutes to weeks, which is suitable for the approach of water-in-oil droplets in synthetic cell assembly.[193]

The mechanisms behind stabilization can be thermodynamically driven by decreasing the interfacial tension and thus, the free energy or by repulsive interaction or steric barrier (activation energy) between the surfactant layer of two adjacent droplets.[194,195]

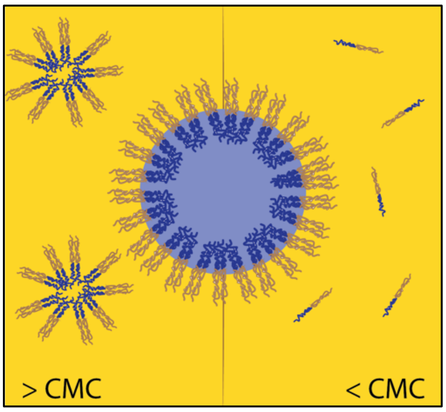

Figure 22: Schematic representation of emulsion stabilization through surfactants in concentration above critical micellar concentration (CMC) and below CMC.

1.4.2.1. Surfactant Adsorption

The adsorption of the surfactants to the interface is mediated by the Gibbs free energy[195] and can be described by the Gibbs Adsorption Equation.[180]

$$d\gamma = -\sum_i \Gamma_i \, \mathrm{d}\mu_i$$

with γ is the interfacial tension, μ the chemical potential of each compound i (which is in case of surfactant adsorption to the interface the surfactants and the solvents), and the surface coverage Γ (Figure 23) (which is the concentration per area of the compound at the interface). The Gibbs convention says that Γ of the solvent is 0 and for surfactants $\Gamma_S \neq 0$,[180] resulting in

$$d\gamma = -\Gamma_S \, \mathrm{d}\mu_S$$

The chemical potential of the surfactant $d\mu_S$ can be described as

$$d\mu_S = RTdlnC_{Bulk}$$

with C_{Bulk} as the surfactant concentration in the bulk, R the ideal gas constant and T the absolute temperature.

This leads in equilibrium condition to

$$\Gamma_{eq} = -\frac{1}{RT}\frac{d\gamma_{eq}}{dlnC_{bulk}}$$

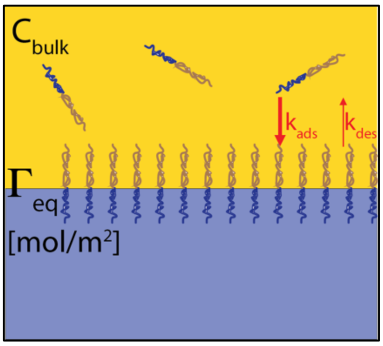

Figure 23: Schematic representation of surfactant surface coverage Γ_S at a water-oil interface with the adsorption and desorption constant k_{ads} and k_{des} and the bulk concentration of the surfactant C_{bulk}.

We can derive that the surface tension γ is directly related to the surface coverage Γ_{eq}, meaning the more surfactant molecules are adsorbed at the interface the lower the surface tension. The surface coverage is in turn dependent on the chemical and physical properties of the surfactant, e.g. charge or size of the head group and tail and their interaction with the according phase. In this regard, surfactants with a charged head group cannot form a dense packing in pure water interfaces due to electrostatic repulsion.[196] This can, however, be reversed by adding a counterion resulting in a possibly even denser packing as the charge of the head group is screened.[197]

These considerations will be of great importance to understand the formation of lipid-based compartment systems inside our water-in-oil droplets that are stabilized by a mixture of charged and uncharged surfactants (see Section 5.1.3).

1.4.2.2. Critical micellar concentration

The Gibbs adsorption equation holds only for surfactant solutions below a critical concentration.[198] This concentration is called the critical micellar concentration (CMC, see Figure 22). Above this CMC, the surfactant monomers assemble into micelles and thus, the linear relation between interfacial tensions and surfactant concentrations is no longer valid. The micelle formation of the surfactant is mediated by decreasing the contact area of the hydrophobic or hydrophilic part to the solvent, thus also depends on the properties of the solvents.[199] A typical CMC for fluorosurfactants at water-oil-interfaces is 4 µM.[181]

1.4.3. Interfacial tension

Two immiscible liquids experience an unbalanced force of attraction at their interface, due to distinct interactions with the second phase. This leads to the accumulation of free energy, the surface free energy. To reduce surface free energy, the area of the interface is always minimized.[200] The force needed to increase the area is the interfacial tension; it has the dimension of an energy per area, in other words a force per length.[201]

The surface tension of an interface between two liquids can be measured by different methods. One method is the pendant drop method (see Figure 24) that is based on the shape of a hanging drop. The drop is suspended from a needle into a bulk liquid and the contour of the drop is detected.[202]

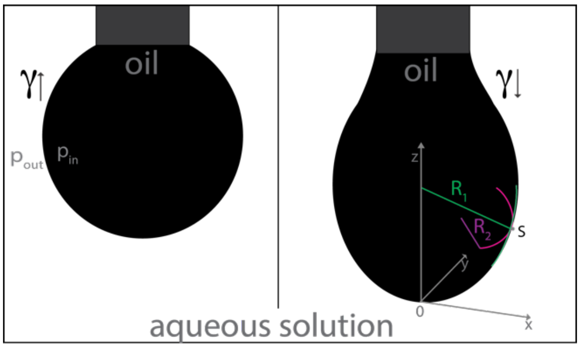

Figure 24: Droplet shapes of oil-in-water pendant drop measurements. Left: spherical droplet indicates high surface tension γ at the water-oil interface. Right: An elongated droplet indicates lowered surface tension γ at the water-oil interface. R1 and R2 are the principal radii of curvature at point S on the surface. Figure adapted from [205,206].

The shape or the radii of the pendant drop is dependent on both, gravity and the surface tension. Whereas the surface tension seeks to get the drop into a spherical shape to minimize the surface area, gravity stretches the drop to the characteristic pear shape.[203] Thus, how much the shape deviates from a sphere is dependent on the density difference of the two phases and the surface tension. This is described in the Bond number Bo

$$Bo = \frac{\Delta\rho g R^2}{\gamma}$$

where $\Delta\rho$ is the density difference between the phases, g is the gravity constant, R the droplet's radius and γ the surface tension. In pendant drop experiments the Bond number of a droplet is then used for the Young-Laplace fit.[201,204]

The Young-Laplace equation describes the increased pressure Δp within a drop as a result of the interfacial tension between the inner and the outer phase and relates the radii of the curvature of the surface to the interfacial tension[183,207]:

$$\Delta p = p_{in} - p_{out} = \gamma \cdot \left(\frac{1}{R_1} + \frac{1}{R_2}\right)$$

where R_1 and R_2 are the radii of curvature, Δp the Laplace pressure and γ the interfacial tension.

As in this thesis, different kinds of surfactants in mixtures are used to stabilize the water-in-oil droplets, the measurement of interfacial tension helps to characterize the system and gives a hint, what kind of surfactant is most prevalent at the interface (see Section 5.1.1.4). To further understand molecular processes associated with the stabilization of water-in-oil droplets, I will introduce in the following the kinetics of surfactant assembly at water-in-oil interfaces.

1.4.4. Adsorption Kinetics

Adsorption kinetic models describe the coverage of an interface in a time dependent manner, starting at time 0, when the interfacial tension is given by the interface of the pure liquids, until the equilibrium coverage is reached.

The kinetics of surfactants is governed by their properties (electrostatic repulsion or attraction, steric hindrance) in relation to the two phases. Further, adsorption kinetics depends critically on the length scales. In this regard, the models are either limited only by diffusion (Figure 25A, macro scale) or limited by adsorption due to an adsorption barrier (Figure 25B, micro scale).[181,190]

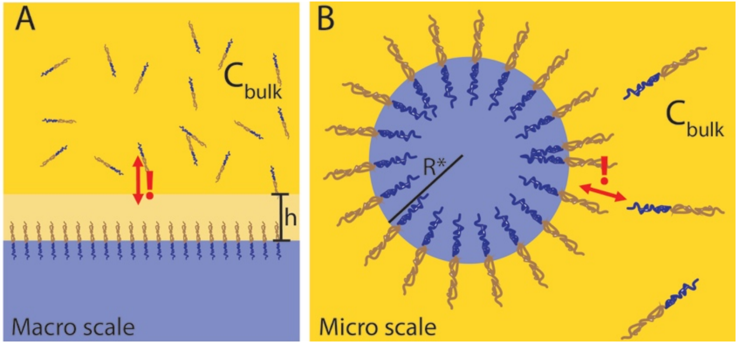

Figure 25: Schematic representation of adsorption kinetics in (A) macro scale, where kinetics is limited by diffusion of surfactants from the bulk to the depletion area (with the depth h) and (B) microscale (R<50 µm), where kinetics is limited by adsorption. Here the diffusion is much faster than the adsorption process.*

(A) Macro scales:

In larger scales (Figure 25A), the diffusion is generally slower than the adsorption process itself. This means that the time τ_{2D} a surfactant molecule needs to adsorb on a flat interface is directly related to the Fickian diffusion laws.[208] Thus, when a planar interface (2D) is considered τ_{2D} is described as

$$\tau_{2D} = \frac{h^2}{D}$$

with D the diffusion coefficient and h the depletion depth (Figure 25B) of the layer where all molecules adsorb to a planar interface

$$h_{2D} = \frac{\Gamma_\infty}{\mathrm{C}_{bulk}}$$

with Γ_∞ the maximal interfacial coverage and C_{bulk} the concentration in the bulk. [208,209] For surfactant concentrations below CMC h_{2D} is in the order of tens of centimeters and for concentrations above CMC in the order of mm or µm.[203]

A time dependent surface coverage can be described at flat interfaces[197,210] with

$$\Gamma(t) = 2\sqrt{Dt}\mathrm{C}_{bulk}$$

(B) Micro scales

For small dimensions, as in the case of the water-in-oil droplets of my thesis, kinetics is usually limited by the adsorption mechanism. Here, the diffusion in a system is much faster than the adsorption of the molecule to the interface. This effect is referred to as an adsorption barrier, which could be e.g. electrostatic repulsion.[203]

This counts for systems below the cutoff radius R* (Figure 25B), that is described by

$$R^* = \frac{D}{k_{ads}\Gamma_\infty}$$

with D the diffusion constant, k_{ads} the adsorption rate and Γ_∞ the maximal interfacial coverage. For surfactants at water-oil interfaces R* is in the range of 50 µm.[203]

A model describing the adsorption of molecules to an interface is the Langmuir adsorption isotherm.[180] This model includes the following assumptions: There is a fixed number of adsorption sites that are all similarly in favor. That means that when there are no interactions between surfactant molecules, adsorption is independent on the presence of already adsorbed surfactants. All adsorption sites can hold only a maximum of one surfactant molecule.[180] This in turn means that in the Langmuir model the adsorption of molecules at an interface is only dependent on the concentration in the bulk C_{Bulk}, the maximum number of adsorption sites Γ_∞ and the adsorption k_{ads}.[211]

$$\frac{d\Gamma}{dt} = k_{ads} C_{Bulk} \Gamma_{\infty} \left(1 - \frac{\Gamma}{\Gamma_{\infty}}\right)$$

When the coverage of the interface is in a steady state, this results in the Langmuir isotherm:

$$\Gamma_{eq} = \Gamma_{\infty} \left(\frac{\kappa C_{Bulk}}{1 + \kappa C_{Bulk}}\right)$$

with $\kappa = k_{ads}/k_{des}$.

This is only valid for surfactant concentrations below the CMC.[211]

Indeed, most of the microfluidic experiments are performed above the CMC, where Γ_{eq} should be constant for all C_{Bulk}.

In this regard, significant deviations from this model have been observed by Riechers *et al.*, when the model was applied on experimental data.[181] Moreover, they observed a C_{Bulk} dependency of interfacial processes, even though surfactant concentration was above the CMC. This was explained by the additional desorption and adsorption processes of surfactant at the interface in equilibrium, showing that water-in-oil droplets cannot be considered as a stable capsule but that the surfactants at the interface are dynamically exchanged.[181]

This demonstrates that the interfacial processes in water-in-oil droplets may be considerably complex. Especially, in case of surfactant mixtures, like it is used in this thesis, more complex adsorption kinetics may happen due to competitive adsorption of the different surfactants or due to a synergistic adsorption behavior based on coupling or electrostatic repulsion.[196]

Nevertheless, the discussed dynamical arrangement of molecules at the water-in-oil interface brings up a phenomenon that has to be considered when studying artificial motility. This phenomenon, the Marangoni effect, will be explained in the following and will be further investigated in Section 5.2.6 in my thesis.

1.4.5. Marangoni effect

The Marangoni effect appears at liquid-liquid interfaces, e.g. water-in-oil droplets, when the surface coverage is out of equilibrium and there are local variations in the surface tensions (Figure 26A).[212,213] These differences in the surface tension, $\nabla \gamma$, create a surface stress that needs to be balanced by viscous stresses. These in turn lead to a flow tangential to the surface, the Marangoni flow, towards the interfaces with higher surface tension. This can lead then to a propulsion of droplets towards lower surface tensions (Figure 26B).[214]

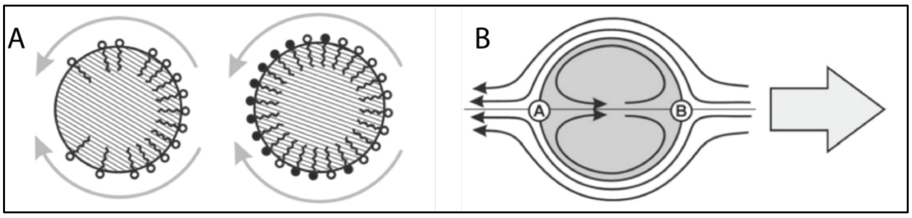

Figure 26: A schematic representation of Marangoni flow fields on water-in-oil droplets with a local heterogeneity of surface tension. (A) Two possibilities to generate Marangoni flow at the surface of the droplet: a concentration gradient of surfactants along the droplet interface or black/white surfactants have distinct surface tension and are not homogeneously distributed, e.g. through a local chemical reaction at the interface. Arrows indicate that Marangoni stresses point in direction of higher surface tension. (B) Marangoni stresses at the surface inside and outside of a droplets emerging due to surface tension differences (γ(A)> γ(B)). Large arrow to the right indicates motion of the droplet due to flow around the droplet. Reprinted with permission from [215] *- Published by The Royal Society of Chemistry.*

In a glass of wine, the Marangoni effect can be observed by the naked eye. Here the “tears of wine” result from the fact that the alcohol evaporates faster than the water, especially, at the corners of the glass. This leads to a local decrease in alcohol concentration and thus, to an increase in surface tension, what results in stresses that can lift the liquid upwards against gravity.[215]

Various other factors could be responsible for a non-uniform surface tension (Figure 26A). For example, the simplest scenario can be imagined at a surfactant-free water-in-oil droplet that is then exposed to a surfactant micelle that adsorbs asymmetrically somewhere at the interface.[212] Further variances in the surface tension could be achieved due to a surfactant mixture created by a chemical reaction[216] at the interface e.g. through shining a laser on light-switchable surfactants.[217]

Droplet propulsion continues until equilibrium conditions are reached. This can happen very fast in case of a surfactant micelle adsorbing to a surfactant-free interface, or when the movement is coupled to a chemical reaction, the movement continues until the precursors that sustained a heterogeneity of the interface (“stagnant cap”[219]) are used up.[218]

This effect was used already in several studies to create so-called microswimmers that were capable of spontaneous motion.[216,220]

Thus, the influence of this kind of surfactant kinetics and surfactant interactions with encapsulated components need to be considered, when working with water-in-oil droplets, especially, when investigating artificial motility modules, as presented in this thesis.

So far, I introduced the physico-chemical characteristics of water-in-oil emulsions. Now, I would like to introduce the concept behind the production of the mentioned water-in-oil droplets. In this regard, microfluidic technology and its characteristic features will be discussed in the following sections.

1.4.6. Microfluidics

Microfluidics is a technology to manipulate small amounts of fluid (nano- to atto-liters) in channels with micrometer dimensions.[221,222]

Whereas first applications of microfluidics have evolved in chemical analysis e.g. gas-phase chromatography or high-pressure liquid chromatography,[223] the most common and well-developed field of microfluidics today are lab-on-a-chip devices that first appeared in the early 90's.[224] This concept of microfluidic devices has benefitted from the photo- and soft-lithography technology[225] that was originally developed by the semiconductor industry.[226] Thus, the field of microfluidics could grow rapidly towards versatile and successful applications in research and economics. Moreover, lab-on-a-chip devices gained more and more importance concomitant to the progression in the field of genomics and molecular biology, where sensitive methods for high throughput analysis and synthesis are requisite for e.g. DNA sequencing approaches.[227] Further, in recent years, the microfluidic technology was exploited to develop sophisticated devices for biomedical applications[222] e.g. a portable insulin delivery device.[228] Moreover, microfluidics is also applied in research applications, as in my thesis, where I use microfluidic lab-on-chip devices to provide an automated assembly line for synthetic cells.

Obvious advantages of microfluidic technology are the reduced costs and consumption volumes of expensive reagents and the possibility for analysis and fast diagnostics without specialized laboratory equipment. Further hallmarks of the microfluidic concept lay in physical characteristics that come along with small dimensions. This will be explained in the following sections.

1.4.7. Macroscopic versus Microscopic Force

The behavior of liquids at microscopic or macroscopic scale are quite distinct from each other. Whereas in macroscopic scale, gravity dominates fluid dynamics, in microfluidics these fundamental concepts change. As the volume decreases and the surface-to-volume ratio increases, surface tension or interfacial tension (see Section 1.4.3) plays a more dominant role than gravity.[222,229] This results for example in the phenomenon of the capillary action, the movement of liquids through a narrow constriction. It can be explained by the fact that when an interface between a solid and a liquid is energetically more favorable (resulting in a lower surface energy) than the liquid-liquid interface, the interface between liquid and solid is increased e.g. water rises in a tube. At micro scales, this capillary force is more prevalent as gravitational forces have less impact.[230,231] Thus, the effect can be exploited to manipulate fluids in microfluidic applications e.g. capillary electrophoresis[232] or at-home pregnancy tests.[205]

In respect to flow or swimming of cells or objects in micrometer scale another aspect is crucial to keep in mind: Viscous forces are here much more prevalent than inertial forces.[234] Thus, a swimming movement of a microorganism is very different to that of a swimmer in the macro-world, where the mechanism of swimming forward is based on inertia. In contrast, microorganisms make use of the viscous drag of the surrounding fluid and mainly swim through a cyclic distortion of the cell body (e.g. through flagella), which does not retrace its path as reciprocal motion would not lead to forward movement.[235]

The self-propulsion of non-living objects in micro scale will be further discussed in the results part of my thesis (Section 5.2.4).

Connected to that another important feature concerning flow regimes in small constraints is the laminar flow that will be introduced next.

1.4.8. Laminar Flow

The flow of a fluid through channels can be characterized by the (dimensionless) Reynolds number Re,

$$Re = \frac{\rho v l}{\eta}$$

with ρ is the density, v the velocity, l the characteristic length and η the dynamical viscosity. Fluids with high Re numbers (> 3000) possess flow profiles that are turbulent. In microfluidic length scales (l is small) the Re number is low (<< 2000) and thus, fluids normally exhibit laminar flow.[231] This results for example in the phenomenon that co-flowing fluids do not necessarily mix (Figure 27).[236] This is extremely useful in microfluidic devices when two liquids should not be mixed within the microfluidic channel, e.g. polymer precursor and activator can co-flow separately in one channel until mixing is desired. Mixing can be achieved through separating the continuous phase into segments by applying a vertical flow of a different immiscible fluid phase, e.g. production of water-in-oil droplets, (see Figure 28 "T-junction" or "flow focusing junction") or through curved geometries (see Figure 28 "mixing").[233] Due to the resulting convective flow within the segments rapid mixing evolves.

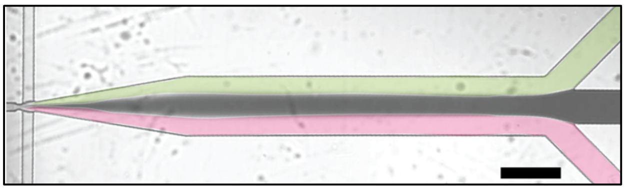

Figure 27: Colored bright-field image of a microfluidic channel showing laminar co-flow of three solutions. Scale bar 100 µm.

The concept of segmented flow is applied in microfluidic water-in-oil-droplets, which I will use as a basis for synthetic cell assembly. In this regard, I will address in the following section how microfluidic water-in-oil emulsions are implemented.

1.4.9. Droplet-based Microfluidics

In droplet-based microfluidics, the reactants, usually in the aqueous phase, are separated into individual segments or droplets by an immiscible phase, usually an oil solution (water-in-oil emulsion droplets).[237] In that condition, the liquid within the droplets does not wet the channel walls and thus, prevents an axial dispersion of components between different droplets.[233]

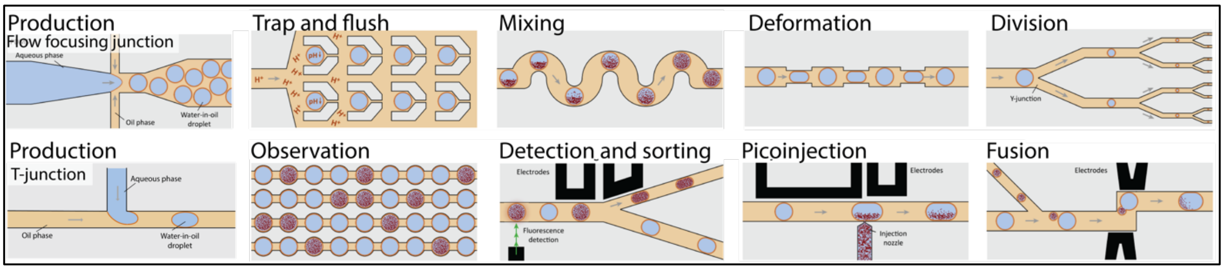

Figure 28: Droplet-based microfluidic modules. Adapted and reprinted with permission from [97]*. Copyright © 2018 Göpfrich et al.*

Droplet generation is typically achieved by certain geometries in the microfluidic device, either a T-junction[238] or a flow focusing junction[239] (see Figure 28), where the two immiscible liquid phases meet. Here, the continuous oil phase applies shear forces to the aqueous phase leading then to the formation of monodisperse droplets. Besides the diameter of the channels, droplet size can be controlled by adjusting the applied flow rates and the flow ratio between aqueous and continuous oil phase. By the addition of surfactants, droplets are stabilized and coalescence is prevented, allowing for storage of the droplets over several weeks.[189]

Further, the droplets can be manipulated by implementation of various active microfluidic units. Figure 28 shows the summary of various microfluidic units that allow for example merging or splitting of droplets or picoinjection of aqueous components into the droplets.[97]

As each droplet contains the same content and production happens at kilohertz rates, the technology is a great tool for high throughput analysis or for the generation of microreactors. This is for example exploited in the well-established emulsion polymerase chain reaction (ePCR).[88] Here every droplet contains not more than one template and can be amplified within the droplet without any competition between other templates. The fact that systems for microfluidic ePCR technology are now commercially available[240] shows that microfluidic water-in-oil droplets have also great economic potential. Moreover, they bear great potential for assembly, manipulation and analysis of synthetic cells. This, I will demonstrate in my thesis, and further I will show, how the here outlined lab-on-chip functions can be employed for the bottom-up construction of synthetic cells.

In the introduction section I have described the complexity of a living cell especially regarding cellular membranes and motility. Further, I gave an overview about how synthetic biology dissects and simplifies functional modules of a living cell in artificial systems. Thereby, I especially focused on cell-like compartment systems based on lipid vesicles and water-in-oil droplets. In the case of water-in-oil droplets, I moreover gave an introduction into the mechanisms behind their stabilization and their microfluidic production.

In the following section, I will address the aims of my research and further explain the methods, how I created biologically relevant membrane systems within water-in-oil droplets and how I assembled functional cellular motility modules.

Motivation

2. Motivation

Even though Life Sciences provide fast and big steps towards elucidating life in its diversity and complexity, yet, we are lacking a detailed understanding. Thus, mankind still fails to beat functional deficits as e.g. cancer or autoimmune diseases.

Towards learning about vital function and life in general, in my opinion, it is best to start from scratch and first understand the building blocks and the assembly of these building blocks into functional modules before investigating more complex and synergistic effects in living systems. This idea exactly describes what bottom-up synthetic biology is based on.[68]

In my thesis, I will use this concept of synthetic biology to build an artificial cell that is comprised of a minimal set of building blocks. Towards this aim, I will implement emulsion-based microfluidic technology, thereby creating a powerful approach to study the assembly of these building blocks into functional modules.

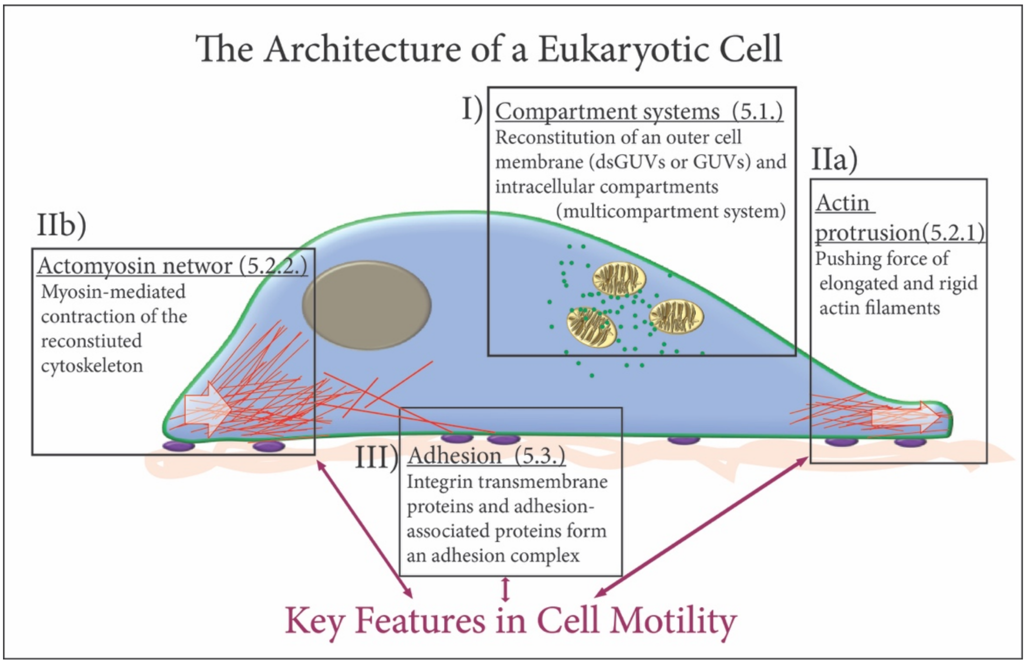

Figure 29: Main elements addressed in my thesis: The membrane-based architecture of eukaryotic cell (Section 5.1) as well as the key features of cell motility (Section 5.2 and 5.3).

The most basic functional unit of a cell is the outer membrane, formed by an entropy-driven self-assembly of phospholipids to a bilayer vesicle in aqueous solution.[11] The reconstitution of these membranes in an artificial system provides not solely a confined reaction space but can be also used to study fundamental membrane physics[144] and to create further structures as membrane tethers and internal smaller compartments to conjecture how **eukaryotic architectural structures** may have evolved. This will be described in the first Part of my thesis (Section5.1), depicted in Figure 29.I.

The second functional module I want to address in my thesis is **cellular motility** (Section 5.2 and 5.3). In this regard, I want to assemble most basic building blocks within the synthetic cell to create simple force generating modules that principally resembles the locomotion machinery in a living cell. The required building blocks are:[28]

- Actin filaments that apply a pushing force onto the membrane in order to protrude the cell body (depicted in Figure 29.IIa).
- Motor proteins that lead to a contraction of the cell body (depicted in Figure 29.IIb).
- An attachment to the substrate to balance these two forces: an integrin adhesion receptors (depicted in Figure 29.III).

After reconstituting and analyzing each building block separately it would be another great achievement to move one level up in complexity and combine multiple functional modules in one artificial cell to allow for a synergistic interplay of the building blocks.

Clearly, the ultimate goal, when reconstituting building blocks of the cellular motility machinery, is the creation of locomotion. This may then elucidate mechanisms governing locomotion is its most basic form.

Materials and Methods

3. Materials

Having introduced the idea of reconstituting structural and functional modules in an artificial compartment system, I will explain now the materials and methods I used in my thesis. Experiments. I will start with the description of the materials I used and then I will continue describing the methods.

3.1. Lipids

Lipids used in this thesis: L-α-phosphatidylcholine (Egg, chicken, eggPC), L-α-phosphatidylglycerol (Egg, chicken, eggPG), 1,2-dioleoyl-sn-glycero-3-phosphocholesteroline (DOPC), 1-palmitoyl-2-oleoyl-sn-glycero-3-phosphocholesteroline (POPC), 1,2-dioleoyl-*sn*-glycero-3-phospho-(1'-*rac*-glycerol) (DOPG) and 1,2-dioleoyl-3-trimethylammonium-propane (DOTAP) were purchased from Avanti (Avanti Polar Lipids, USA), ATTO 488 1,2-dioleoyl-sn-glycero-3-phosphoethanolamine (ATTO 488 DOPE) was purchased from ATTO TEC (Siegen, Germany). All lipids were stored in chloroform at -20 °C and used without further purification. Cholesterol C8667 were purchased from Sigma-Aldrich (Sigma-Aldrich, Germany).

3.2. Surfactants

To stabilize the water-in-oil droplets, non-ionic amphiphilic and ionic block copolymer surfactants were used. These diblock or triblock copolymer surfactants consisted of hydrophobic perfluorinated polyether (PFPE) blocks and Polyethylene glycol (PEG) hydrophilic blocks. The PFPE blocks, which were exposed to the oil phase provide stability by preventing coalescence of the droplets and the PEG blocks provide biological compatibility and inertness to the water encapsulated biomolecules.[189] Dr. Jan-Willi Janiesch (postdoc, MPI, Prof. Spatz Department) synthesized the surfactants that I used at the beginning of my research. However, most of the experiments described in this thesis were based on a commercial fluorosurfactant from RANbiotechnologies, USA. In the following, I will describe the PFPE polymer that is by itself already interfacially active, then the synthesis of custom-made triblock surfactants and further I will introduce the commercial surfactants that I used in this research.

3.2.1. Krytox

The perfluorinated acid, Krytox 157 FS(H), was purchased from DuPont, Netherlands and is basically an perfluoropolyether oil that comprises a carboxylic acid end group (Figure 30), thus can serve as an interfacially active surfactant in water-in-oil-systems. [189] Krytox 157 FS(H) will be hereinafter simply named as Krytox.

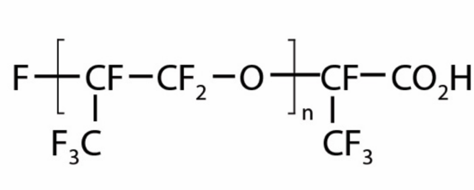

Figure 30: Carboxylic acid terminated perfluoropolyether. Trade name Krytox 157 FS(H) and here referred to as Krytox.

Through its long fluorocarbon tail, Krytox offers long-term stabilization of water-in-oil droplets, however its charged headgroup may interact with biomolecules (e.g. in presence of cations with DNA, RNA, proteins, and lipids) what may be desirable, as in the case of droplet-stabilized GUV formation (see Section 5.1.3) but may also lead to the loss of activity of the encapsulated biomolecules [206]. Moreover, the pH change due to the carboxylic head group might also have an effect on the encapsulated biomolecules. Therefore, water-in-oil droplets for most biological application demand for non-ionic fluorosurfactant. The most widely used surfactant is a block copolymer comprising a hydrophobic Krytox part and an inert PEG hydrophilic part.[193] The synthesis is based on a condensation reaction of the carboxylic acid group of Krytox and the functional group of PEG or PEG-diamine to an ester- or amide bond [189,241], respectively, as will be described in the following section.

3.2.2. PFPE-PEG-PFPE triblock

The synthesis of the PFPE-PEG-PFPE triblock-copolymer surfactant was based on a protocol published earlier[189] and modified as described in Platzman *et al.*[241]. In short, the reaction was carried out under argon atmosphere in dry Tetrahydrofuran (THF) solvent (Acros Organics, Germany) in a heated Schlenk-flask. PEG1400 (1400 mg, 1 mmol, molecular weight 1400 g/mol, Fluka, Germany) was solved in 80 ml dry THF and cooled down to -78 °C, followed by the dropwise addition of N-butyl lithium (1.22 ml of a 1.6 M solution in hexane, 2 mmol, Sigma-Aldrich, Germany) over a period of 60 min. Subsequently, the solution was stirred for additional 30 min and was then slowly heated to RT, and allowed to be stirred for another 30 min. Following this the PFPE7500-carboxylic acid (5 g, 2 mmol, molecular weight 7500g/mol, DuPont, Netherlands) was added dropwise over a period of 30 min and stirred for another 12 h to allow the condensation reaction to happen (Figure 31). Afterwards, to remove the unreacted PEG from the product, the crude was washed with dry THF solvent for three times by means of a separatory funnel. Next, to separate the unreacted PFPE-carboxylic acid the product was dissolved in methanol (Carl Roth GmbH, Germany), in which mainly the PFPE-PEG-PFPE product but not the PFPE-carboxylic acid educt is soluble. Finally, the PFPE-PEG-PFPE product dissolved in the methanol was dried in a rotary evaporator at 40°C and subsequently on a vacuum line. The purity of the product was analyzed by NMR and IR measurements. This is shown esleweher.[241] For reasons of simplicity this costom-made synthesized surfactant is hereinafter referred to as “costum-made triblock surfactant”.

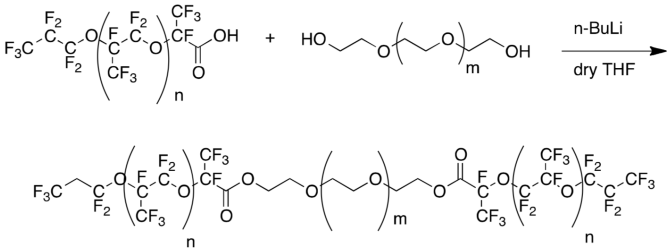

Figure 31: Synthesis of PFPE7500-PEG600-PFPE7500 triblock-copolymer surfactant, referred to in this research simply as custom-made triblock surfactant. Reprinted from [241].

3.2.3. Gold-linked Surfactant

The synthesis of the gold nanoparticle-linked surfactant was performed by Dr. Jan-Willi Janiesch as shown in Figure 32 in a one step process. PFPE7000-carboxylic acid (2.1 mg, 0.3 µmol, molecular weight 7000 g/mol, DuPont, Netherlands) and KOH (5N, 10 µl, Sigma Aldrich, Germany) were added to the (11-Mercaptoundecyl)tetra(ethylene glycol) functionalized gold nanoparticle solution (2% w/w solution in water, 5 ml, Sigma Aldrich, Germany) and stirred for 1 h leading to a flocculation of the PFPE-PEG-gold product and the unreacted PFPE [241].

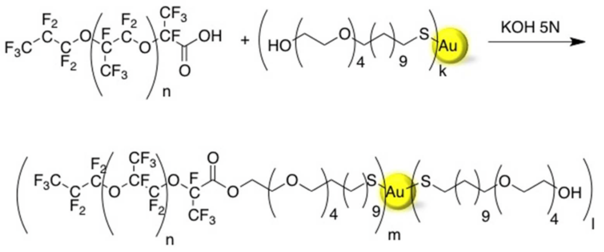

Figure 32: Synthesis of PFPE7000-PEG-gold polymer surfactant. Reprinted from [241].

Afterwards the crude product was washed three times with water to remove remaining KOH, and the water was finally removed by freeze-drying the product for 24 h. Then it was dissolved in 1 ml FC-40 oil (Acros Organics, Germany) followed by a filtration step through a hydrophobic filter (PTFE 0.2 µm, Carl Roth GmbH, Germany) to remove unreacted (11-Mercaptoundecyl)tetra(ethylene glycol) functionalized gold nanoparticles.

3.2.4. Amine Surfactant

The synthesis of the PFPE-PEG-NH_3 diblock-copolymer surfactant was done by Dr. Jan-Willi Janiesch and followed a procedure reported earlier[242] but with several modifications. Krytox 157-FSH (7500 g/mol) was mixed in an equal volume of HFE-7100 oil and the carboxylic groups were activated with a 10x molar excess of oxalyl chloride (Sigma-Aldrich). Following the activation, the solvent and unreacted oxalyl chloride was evaporated and neutralized by bubbling the vapors through 2 M KOH. For the hydrophilic part, distinct to the above described triblock surfactant, a diamine Jeffamine was used (Jeffamine ED600: O,O'-bis(aminopropyl) polypropylene glycol-b-polyethylene glycol-b-polypropylene glycol, Huntsman, USA), which comprises an amino group at each end of the molecule. A stock solution was prepared in anhydrous dichloromethane and HFE-7100 and a 10 x molar excess (in regard to Krytox) of Jeffamine was added - under continuously stirring - to the activated Krytox to initiate the amide reaction. Due to the significant molar excess of Jeffamine, the reaction of a diblock was in favor. Following the reaction, the crude product was diluted in HFE-7100 and centrifuged overnight. A clear bottom phase product was separated from a white top layer consisting of the unreacted Jeffamine. The solvent was evaporated at 65°C for 2 days. This surfactant is hereinafter referred to as "amine surfactant".

3.2.5. Hydrophobic PFPE(7000)-PEG-Beads

In order to break the symmetry of water-in-oil droplets hydrophobic beads that are supposed to bind from the oil phase to the droplets have been synthesized by Dr. Jan-Willi Janiesch according to a protocol described in Kim *et al.*[243] Therefore polystyrene beads (d=2:077 µm, Polyscience Inc, USA) were incubated for 5 h with PEG-PPG-PEG (Pluronic F-127) solution (Sigma-Aldrich, Germany). 50 µL of toluene was added and subsequently removed after 2 h by heating up the solution to 98°C. The beads are then washed with milli-q water and dried under vacuum. Next, these functionalized beads were coupled to Krytox (PFPE7000-carboxylic acid) by mixing the Krytox with the beads, 1.5 ml water and 10 µl of 5N KOH. The resulting hydrophobic beads precipitated and finally could be dried under vacuum before they were dissolved in HFE-7500 oil.

3.2.6. Commercial PEG-based Surfactant

Besides the custom-made triblock surfactant, I made use of a commercially available PFPE-PEG block copolymer from RAN biotechnologies (USA). As the company provides only few information about the chemical and physical properties of the surfactant, the surfactant was characterized in my thesis by FTIR, MALDI-TOF and by means of a partitioning experiment (see Section 5.1.1.1 and 5.1.1.2). To distinguish in the following from the custom-made triblock surfactant, the commercial surfactant is hereinafter referred to as “PEG-based fluorosurfactant”.

3.3. Oil-Phase

The fluorosurfactants used in my thesis are soluble only in fluorinated oil. While for experiments performed with the custom-made triblock surfactant mainly FC-40 oil was used, HFE-7500 (3M, USA) was used when experiments were performed with commercially available PEG-based fluorosurfactant. For stable droplets production, the surfactants were dissolved to a final concentration ranging from 3 to 15 mM.

3.4. Proteins

The proteins used in this research were partly extracted and purified in our lab. Thus, the protocols for their purification is described shortly in the following sections.

3.4.1. Actin

Actin was purified by Christine Mollenhauer or Cornelia Weber (technical assistants, MPI, Prof. Spatz Department) based on a previously published protocol.[244] In short, actin was extracted from rabbit skeletal muscle acetone powder by stirring the acetone powder in actin storage buffer (see Section 3.5.) on ice for 30 min following a centrifugation step at 16 000 rpm for 30 min (Sorvall RC6 centrifuge, SS-34 rotor). The supernatant was resuspended in actin storage buffer and then adjusted to 50 mM KCl and 2 mM $MgCl_2$, which leads to the polymerization of actin. While stirring for 30 min the KCl concentration was increased to 0.8 M KCl to dissociate tropomyosin and subsequently stirred for another 15 min followed by a centrifugation step of 2 h at 35 000 rpm (Optima L-80 XP ultracentrifuge Beckman Coulter, Ti 42 rotor). The supernatant was discarded and the pellet resuspended in actin storage buffer followed by a dialysis against actin storage buffer (see Section 3.5.). Afterwards it was centrifuged again for 2 h at 35 000 rpm and the upper 2/3 of the supernatant was finally purified by gel filtration with Ge-column Hi Load 26/60 Superdex 200 prep grade (General Electric, USA) and then aliquoted, snap frozen in liquid nitrogen and stored at -80°C. Phalloidin and fluorescently labeled actin was purchased from Life Technologies (Alexa Fluor 568, and Alexa Fluor 647 actin conjugate).

3.4.2. Actin-binding proteins

Human recombinant fascin was purchased from Novubio (Bio-Techne) and α-actinin was purchased from Cytoskeleton. The proteins are bundling or crosslinking proteins, respectively, that help to connect the actin network.[35]

3.4.3. $\alpha_{IIb}\beta_3$ Integrin

Integrin $\alpha_{IIb}\beta_3$ was purified from outdated human blood platelets (Katharinenhospital Stuttgart) based on a protocol described in Fritzgerald *et al.*[245] and further optimized by Stojan Perisic (Ph.D. student, MPI, Prof. Spatz Department). In short, to remove other cells from the platelets a differential centrifugation step was applied at RT for 20 min at 1400 rpm (Sorvall RC6 centrifuge, SLA 3000 rotor). Following centrifugation, the platelets were washed three times by pelleting the platelets at 4000 rpm for 30 min and resuspending in 100 ml platelet lysis buffer 1 (see Section 3.5). Platelets were broken with a Turrax homogenizer (IKA, Germany). The lysate was afterwards centrifuged for 30 min at 39 000 rpm (Optima L-80 XP ultracentrifuge, Beckman Coulter, 45 Ti rotor) at 4°C followed by the resuspension of the pellet in 150 ml lysis buffer 2 (see Section 3.5.). Then another two lysis steps with the Turrax in platelet lysis buffer 2 were performed. After 1 h incubation at 4 °C the solution was centrifuged for 15 min at 4°C at 19 000 rpm (Optima L-80 XP ultracentrifuge, Beckman Coulter, 45 Ti rotor). This supernatant was then loaded for affinity chromatography onto an equilibrated Concanavalin A column (GE Healthcare Life Sciences, USA) using an ÄKTA protein purification system. The bound glycoproteins were eluted the next day by adding 100 mM mannose to the equilibration buffer. Fractions containing integrin (tested by SDS PAGE) were pooled and loaded on a heparin column (GE Healthcare Life Sciences, USA). The eluted fractions were again checked for integrin content by SDS PAGE and the pure fractions were pooled. As a next step, the integrin containing fractions were concentrated by a filter step through an Amicon Ultra-15 filter (50 kDa MWCO, Merck, Germany). Following this step, the integrin was loaded onto a Superdex 200 column (GE Healthcare Life Sciences, USA) and eluted overnight. The most pure and concentrated fractions were further sterile filtered, aliquoted, snap frozen and stored at -80°C. The biological activity of the purified integrin was tested by ELISA using AB1967 anti-integrin α_{IIb} antibodies (Merck, Germany). Further the purified integrin was partly used for fluorescence labelling by means of a NHS (succiniminidyl) ester –conjugated Alexa Fluor 568 fluorescent dye (Life technologies) that reacts with primary amines (R-NH2) on the integrin and create a stable amide bond. Aiming so, 50 µg of NHS ester-dye was dissolved in dimethyl sulfoxide (DMSO, Sigma Aldrich), then added to 1 ml of 1 mg/ml integrin solution and allowed to react under stirring for 1 h at RT. The protein was separated from unbound dye via an equilibrated PD-10 desalting column (GE Healthcare Life Sciences, USA), aliquoted, snap frozen and stored at -80°C.

Besides this purified native integrin protein also a recombinant intracellular fragment of the β_3 integrin was used in my thesis. This was a gift from Prof. Geiger, Weizmann institute Israel.

3.4.4. Adhesion-Associated Proteins

Talin protein was extracted and purified from chicken gizzards by Christine Mollenhauer based on a protocol described in Halloran *et al.*[246] and kept in -80 °C until used.

The FAK protein used here was a gift from Prof. Geiger, Weizmann institute Israel. It was shipped to Germany on dry ice and kept at -80°C until usage.

3.4.5. Myosin Motor

Myosin II was isolated by Christine Mollenhauer from rabbit skeletal muscle according to the purification protocols published before.[247] In short, muscle tissue from a freshly sacrificed rabbit was collected, grinded in a meat grinder and mixed with three volumes of extraction buffer for exactly 10 min with constant stirring at 4°C. Afterwards, the muscle tissue residues were separated by a centrifugation step for 15 min at 12 000 rpm (Sorvall RC6 centrifuge, GSA rotor) at 4°C. The pH of the supernatant was adjusted to 6.6 and then diluted very slowly with 10 volumes of cooled milli-q water, leading to a precipitation of myosin. The pellet could be collected by centrifuging for 15 min at 7 000 rpm (Sorvall RC6 centrifuge, GSA rotor) followed by the resuspension of the pellet in 0.25 ml per gram pellet in buffer M1 and the dialysis overnight against buffer M2 (see Section 3.5.). The next day, the dialysed myosin solution was diluted slowly with an equal volume of cold milli-q water and stirred on ice for 30 min. Then a centrifugation step followed at 18 000 rpm (Sorvall RC6 centrifuge, SS34 rotor) for 30 min at 4°C to separate the actomyosin from the myosin. The supernatant containing the myosin was diluted with 7 volumes of milli-q water and centrifuged for 15 min at 12 000 rpm (Sorvall RC6 centrifuge, GSA rotor) at 4 °C. The pellet was resuspended in 2 M KCl to bring it to the final KCl concentration. Following resuspension, the solution was salted out with two steps of 40% and 50% saturated ammonium sulfate, respectively, and centrifugation steps for 10 min at 13 000 rpm (Sorvall RC6 centrifuge, SS34 rotor) at 4°C. The freshly purified myosin II was aliquoted in Buffer D (see Section 3.5), snap frozen and stored at -80°C.

3.4.6. ATP Sensor

The PercevalHR was developed by Tantama *et al.* by mutagenesis of the original Perceval sensor.[248] Dr. Amelie Benk (postdoc, MPI, Prof. Spatz Department) and Christine Mollenhauer performed the protocol to produce the PercevalHR sensor, which is described in details somewhere else.[249] The plasmid pRsetB-PercevalHR was a gift from Gary Yellen (Addgene plasmid # 49081). The protein was expressed in 150–200 ml *E.coli* cultures overnight at 37 °C and then allowed for additional growth for 2–3 days at RT. The cell pellets were collected and lysed in three freeze–thaw cycles followed by agitation in lysis buffer. The lysate was further purified by centrifugation at >15,000 *g* for 10 min at 4 °C and by nickel-affinity low-pressure chromatography (HiTrap Chelating HP, 1 ml bed volume, GE Lifesciences). Protein concentration was determined by the BCA method (Pierce) and aliquots were snap frozen and stored at −80 °C.

3.5. Buffers

All buffers were prepared with ultra-pure milli-q water (R = 18 MΩ, milli-Q filtered) and stored at 4°C.

3.5.1. Buffers for dsGUV Formation

Table 2: Buffers for dsGUV formation.

Lipid charge	Surfactants	Buffer
neutral/negative	PEG-based surfactant plus Krytox	30 mM TrisHCl, pH 7.4 10 mM $MgCl_2$
neutral	PEG-based surfactant plus Krytox	30 mM TrisHCl, pH 7.4 50 mM or 100 mM KCl
positive	PEG-based surfactant plus Krytox	30 mM TrisHCl, pH 7.4
neutral/negative	PEG-based surfactant plus amine surfactant	30mM TrisHCl, pH 7.4 and 9.5

3.5.2. Buffers for Actin and Actomyosin Experiments

Table 3: Buffers for actin and actomyosin experiments.

Buffer				
M1	1 M KCl pH 6.5	0.025 M EDTA	60 mM KH_2PO_4	
M2	0.6 M KCl pH 6.5	0,025 M KH_2PO_4	10 mM EDTA	
D-Buffer	50 M K_2HPO_4	600 mM KCl	pH 6.5	
Actin storage buffer	2.0 mM TRIS pH 7.4	0.2 mM CaCl2	0.2 mM ATP	1 mM TCEP
Actin polymerization buffer	50 mM KCl	10 mM $MgCl_2$	1 mM ATP	± 0.4% methyl-cellulose
ATP recovery buffer (a)	10 mM HEPES 1 mM TCEP	0.12 mM DABCO	0.13 mM KCl	0.1% BSA
ATP recovery buffer (b)	10 mM HEPES	5 mM Creatine-phosphate	Creatine kinase 0.5 mg/ml	
	1 mM TCEP 3 mg/ml glucose 10 mM DTT	Creatine kinase 0.5 mg/ml 0.1 mg/ml glucose-oxidase	5 mM Creatine-phosphate 0.02 mg/ml glucose-catalase	pH 7.4
Motility assay "AB buffer"	25 mM Hepes pH 7.4 25 mM DTT 0.1 mg/ml glucose-oxidase	25 mM KCl 0.02 mg/ml glucose-catalase	25 mM $MgCl_2$ 0.5 wt% methylcellulose	25 mM EGTA 3 mg/ml glucose
Motility assay "Motility buffer"	AB buffer	5 mM ATP		
PercevalHR assay buffer	100mM MOPS pH 7.4	50m M KCl	5mM NaCl	15 mM $MgCl_2$

3.5.3. Buffers for Integrin Experiments

Table 4: Buffers for integrin experiments.

Buffer				
Platelet washing buffer	20 mM TrisHCl pH 7.4	150 mM NaCl	1 mM EDTA	0.01 wt% acetylsalicylic acid
Platelet lysis buffer 1	50 mM TrisHCl pH 7.4	1 mM CaCl2	1 mM $MgCl_2$	
Equilibration buffer	20 mM TrisHCl pH 7.4	100 mM NaCl	1 mM CaCl2	0.1 wt% Triton X-100
Column buffer	20 mM TrisHCl pH 7.4 0.1wt% Triton X-100	150 mM NaCl 0.02 wt% NaN3	1 mM CaCl2 2 mg/l Aprotinin	1 mM $MgCl_2$,
Integrin buffer A	20 mM Tris HCl pH 7.4	50 mM NaCl	1 mM $CaCl_2$	
Integrin buffer B	Integrin buffer A	0.1% Triton X 100		
Integrin activation buffer	Integrin buffer A	1 mM $MgCl_2$	1 mM $MnCl_2$	

3.5.4. Buffers for Protein-Binding Experiments:

Table 5: Buffers for protein-binding experiments.

Buffer			
Talin buffer	50 mM Tris HCl, pH 8		
FAK buffer	20 mM Tris HCl pH 8	0.1 M NaCl	5 mM BME
TBS	20 mM Tris HCl pH 7.5	500 mM NaCl	

3.5.5. Buffers for SDS-PAGE and Western Blot

Table 6: Buffers for SDS-PAGE and Western blot.

Buffer				
6x Loading buffer	300 mM Tris HCl	12% SDS	36% Glycerol	30 mM DTT
Running buffer	25 mM TrisHCl	192 mM glycerine	1% SDS	
Transfer buffer	25 mM Tris pH 8.3	192 mM glycine	20% Methanol	

4. Methods

In the following part, I will explain which methods I used in my thesis. I will first describe the methods towards characterization of surfactants. Then I will introduce the microfluidic technology. In this regard, I will describe the soft and photolithography methods and will continue, in particular, with illustration of different functional microfluidic units. Then I will describe how to generate lipid-based compartment systems and functional modules within water-in-oil droplets.

4.1. Surfactant Characterization

In the following section, I will describe the analytical methods that were implemented to characterize the block-copolymer surfactants used in this thesis.

4.1.1. Infrared (IR) and MALDI Mass Spectrometry (MS) Measurements

IR and MALDI MS measurements were performer to assess the purity of the commercially available PEG-based fluorosurfactant by Dr. Jan Willi Janiesch and Martin Schröter, respectively (Ph.D. Student, MPI, Prof. Spatz Department). IR measurements were conducted on a Nicolet Nexus 870 Fourier transform infrared spectrophotometer (Thermo Electron GmbH, Dreieich, Germany).

MS measurements were performed using a MALDI-TOF MS system (AXIMA Performance, Shimadzu, Japan). Spotting was done by overlaying one spot of a stainless-steel plate with 0.5 µl 1,8,9-trihydroxyanthracene (THA; 10 mg/ml in 1,1,1,3,3,3-hexafluoro-2-propanol (HFIP). Immediately after drying at ambient temperature, the spot was covered with 2 µl of a mixture of surfactant (1 mg/ml in HFIP), THA (10 mg/ml in HFIP) and LiTFA (100 mM in HFIP) in a volume ratio of 10:1:1 and left to dry at ambient temperature. Afterwards, the spot was lined with 1 µl THA (10 mg/ml in HFIP).

4.1.2. Partitioning Experiment

Partitioning experiments were performed to examine the accumulation of Krytox molecules at the water-oil interface.[28] Towards this end, 1 ml of HFE-7500 oil that contained Krytox concentrations between 0 and 1 mM (with and without 1.4 wt% PEG-based fluorosurfactants) was added to a 3.5 ml cuvette. A Tris buffer (30 mM Tris and 10 mM $MgCl_2$) containing Rhodamine 6G (Rho6G 1 mM, Sigma Aldrich, Germany) was gently pipetted on top of the oil solutions. Due to the 1:1 chemical interaction between the Krytox molecules and Rho6G and adsorption and desorption processes of Krytox at the interface, a partitioning of Rho6G molecules to the oil phase was observed.[250] Following 48 h of incubation, samples from the oil and the aqueous phases were carefully collected and transferred into a 96 well plate. Rho6G content was determined in a plate reader (infinite 200, Tecan) by measuring the absorbance at 500 nm.

4.1.3. Interfacial Tension Measurements

A contact angle system OCA (DataPhysics, USA) equipped with a CCD high-speed camera HS for pendant drop measurement, was used to determine the interfacial tension (IFT) between water and HFE-7500 oil droplets containing PEG-based fluorosurfactants and Krytox or amine surfactant. The Young-Laplace equation was chosen to fit the droplet shape in order to determine the IFT values (Section 1.4.3).[209] To investigate the effect of ions on the IFT values, 0 or 1 mM $MgCl_2$ was added into freshly deionized water and was filled into a glass cuvette. A stable oil droplet was generated manually into this aqueous solution using a syringe. IFT values were recorded until a stable value was reached. When IFT values fell below 1 mN/m and stable droplet creation was not possible, values were set to 0 mN/m.

4.2. Microfluidic Device Production

The microfluidic devices used in this research were made of polydimethylsiloxane (PDSM) (Sylgard 184, Dow Corning, USA) and prepared by standard photo- and soft lithography methods (Figure 33) as described in the following sections.

4.2.1. Photolithography

The wafers for the microfluidic devices used in this thesis were produced by Christoph Frey (Ph.D. student, MPI, Prof. Spatz Department). The procedure is described in more detail elsewhere.[251] In short, primarily, the designs of the devices were created with QCAD-pro a computer-aided design (CAD) software. These designs were then used to create chromium photomasks by means of reactive ion etching of the channels into chrome-coated soda lime glass (JD-Photodata, U.K.). In order to create a master with a positive relief of the channels a negative photoresist (SU8−3025, MicroChem, U.S.A.) was spin-coated (Laurell Technologies Corp., U.S.A.) onto silicon-wafer at 2500 rpm in order to get a uniform coating of 30 µm thickness. Next, a prebaking step followed to remove air bubbles and excess photoresist solvent (5 min soft bake at 65 °C then ramped slowly to 95 °C and held for 15 min). Afterwards, the resist was covered with the chromium mask and exposed to UV light for 7.5 s using a mask aligner (MJB4, SUSS MicroTec, Germany). This lead to the photoresist polymerization, where the channel structure was etched into the chromium mask and the UV light could pass through. Following baking steps for 1 min on a hot plate at 65°C and 5 min at 95 °C to solidify the photoresist, the part of the photoresist that was covered with the chromium was washed away with a developing agent (mr-DEV 600 developer (MicroChemicals, Germany)), disclosing the positive relief of the channel structure. The hard bake was carried out in an oven at 150 °C for 15 min.

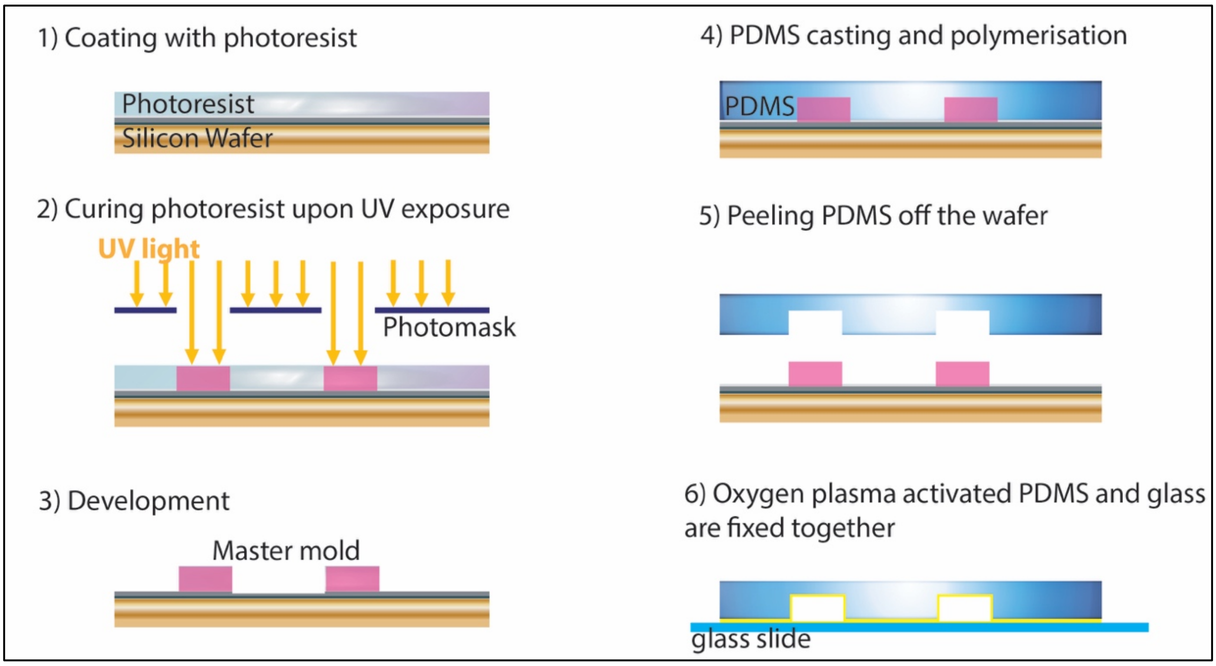

Figure 33: Principle steps to manufacture microfluidic PDMS devices by means of photo- and soft lithography.

All photolithography procedures were performed under clean room conditions (class 100). A profilometer (DektakXT, Bruker, Germany) was used to analyze the heights of the created structures. These master molds were used to produce PDMS devices by the soft lithography method.

4.2.2. Soft Lithography

The first step in soft lithography was to prepare the polydimethylsiloxane (PDMS; Sylgard 184, Dow Corning, U.S.A.) elastomer. Towards this end, a liquid oligomer and the polymerization catalyst was mixed together in a 1:10 ratio (w/w) and was then poured into the mold of the master wafer. To remove air bubbles the polymer was degassed in a desiccator under vacuum and then crosslinked at 65°C for 2 h. Following polymerization, the replica can be peeled off the mold and holes for in- and outlet channels were punched into the PDMS device with a biopsy puncher (0.5 mm diameter, Biopsy Punch, World Precision Instruments, U.S.A.). Afterwards, the devices and 25 x 60 mm cover slips (#1, Carl Roth, Germany) were cleaned with isopropanol and ethanol, blow dried and activated with oxygen plasma (PVA TePla 100, PVA TePla, Germany; 0.45 mbar, 200 W, 20 s) to produce polar groups on the PDMS and the glass. Upon contact of the glass with the PDMS device, a condensation reaction happens of silanol groups with the functional groups of alcohol,[233] leading to a tight fixation of the PDMS to the glass and thus, to the sealing of the microfluidic channels. To improve stability of the contact, the devices were kept in 65 °C for at least 2 h.

Pico-injection devices were additionally equipped with electrodes. In this concern, the devices were heated up on a hotplate to 85°C and Indalloy 19 (51% indium, 32: 5% bismuth, 16: 5% tin, Indium Cooperation, USA) was melted into the inlets of the electrode channels and connected to striped wire tips (MC6A-1, Farnell, UK) that were fixed to the device with the glue Loctite 352 (Henkel, Germany).

Before the use, devices were flushed with sigmacoat® (Sigma-Aldrich, Germany) to render the channels fluorophilic. After around 1 min incubation the channels were flushed with HFE-7500 oil. Devices can be used several times if not contaminated or clotted.

4.3. Different Microfluidic Devices

Most of the designs described in the following were adapted from literature and were further optimized and adjusted for the needs of the research. Figure 34 shows representative sketches of the microfluidic device designs implemented in this research. The bright-field images are colored for clarity (brown, violet: oil phases / blue, red, green: aqueous phases).

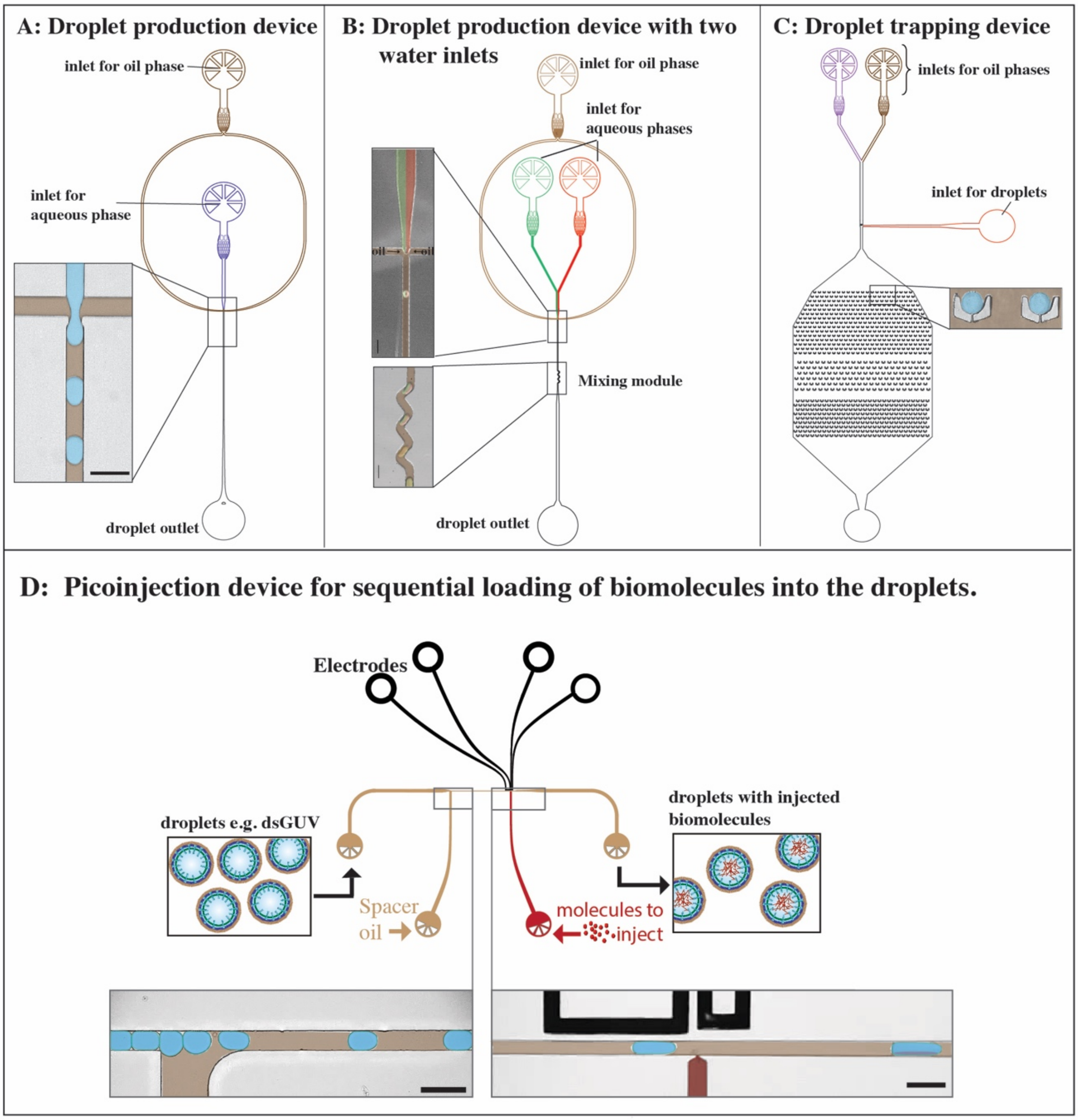

Figure 34: Schematic representations of different droplet-based microfluidic units. (A) droplet production device with one aqueous inlet (colored in blue), (B) droplet production device with two aqueous inlets (colored in red and green) and a zick-zack mixing unit to mix the two aqueous phases after droplet production, (C) droplet trapping device. Droplets are introduced via the red-colored droplet inlet channel and captured in the cavities. Then, the trapped droplets can be exposed to 2 different oil phases applied from the oil inlets (violet and brown). (D) Picoinjection device for sequential loading of biomolecules into the droplet. Electrodes apply an AC electric field at the injection inlet allowing for injection of biomolecules into the passing droplets. Scale bars 50 µm.

4.3.1. Droplet Production Device

A droplet-production device (Figure 34A) comprising of an aqueous inlet and an oil inlet was connected to 0.5 ml or 1 ml syringes (Omnifix-F, B.Braun, Germany), respectively, via PTFE tubing (0.4 x 0.9 mm, Bola, Germany) and cannulas (Sterican, 0.4 x 20 mm, BL/LB, B.Braun, Germany). Monodisperse water-in-oil emulsion droplets were produced with flow rates in the range of 200 to 2000 µl/h and 50 to 200 µl/h of oil and aqueous phases, respectively, controlled via syringe pumps (Pump11Elite, Harvard Apparatus, USA) (see setup in Figure 35).

The oil channel within the device was designed as such that it encounters the aqueous phase at the flow focusing junction (inset Figure 34A) from two opposite direction. When the flow rates of aqueous and oil phases are well adjusted, the aqueous phase will form a droplet-producing nozzle. Immediately, surfactants from the oil phase diffuse to the water-oil interface and hence stabilize the droplets. The size of the produced droplets depends on the dimension of the channel at the flow focusing junction and on the applied flow rates. To create 30 µm droplets, a channel width at the flow focusing junction of 20 µm and an oil/aqueous phase ratio of 10:1 were used. The outlet of the device was connected via a PTFE tubing to a micro tube, where the produced droplets can be collected.

In some biological applications, it is important to avoid interactions between different bio molecules prior to their encapsulation within the droplets (e.g. actin monomers and its polymerization buffer). Towards this end, a droplet production device with two aqueous inlet channels (Figure 34B) was implemented. Due to the laminar flow in the micrometer sized channels (Section 4.3), the mixture between the parallel-flowing solutions is minimized. Subsequently, after the droplet formation, the aqueous phases are then mixed by a zick-zack pattern of the production channel. Finally, the produced droplets can be analyzed in an observation chamber (Figure 36) or introduced into a picoinjection or trapping device.

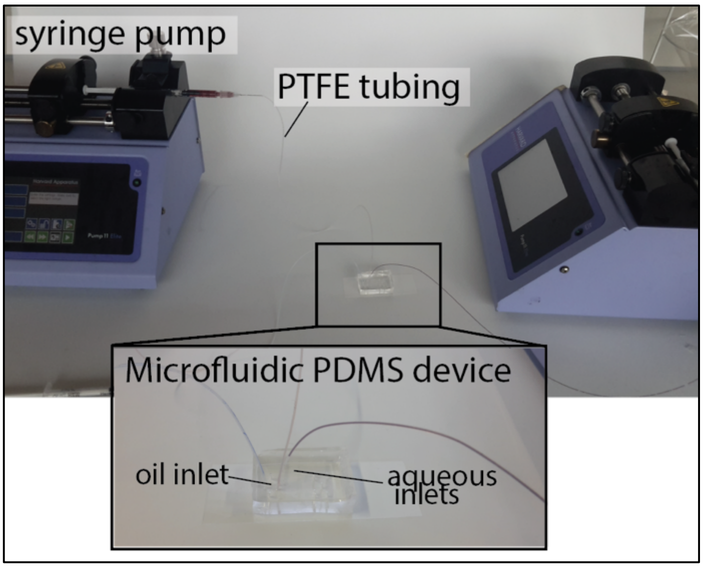

Figure 35: Image of the setup for the microfluidic production of water-in-oil droplets. The inlets of the microfluidic PDMS device (inset) are connected via PTFE tubing to the syringes containing the oil and aqueous buffers. Flow rates were controlled by syringe pumps.

4.3.2. Droplet Observation Chamber

For observation, droplets were collected at the outlet of the device and then transferred into an observation chamber (Figure 36). This chamber consisted of two cover slips (60 x 24 mm (bottom) and 20 x 20 mm (top), Carl Roth, Germany) glued together by a double sided sticky tape (Tesa, Germany), providing thereby a spacing between the two slips of around 90 µm. The chamber was filled up with oil/surfactant solution and, finally sealed with a two-component dentist glue (Twinsil, Picodent GmbH, Germany).

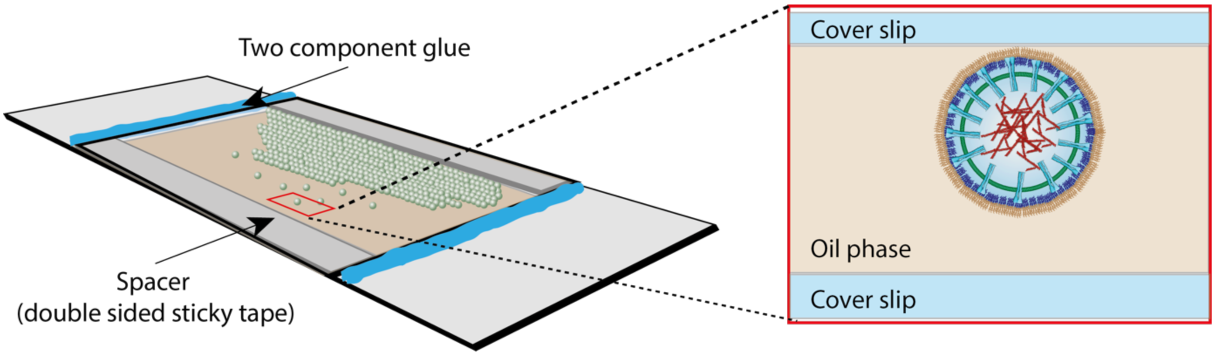

Figure 36: Sketch of observation chamber containing the water-in-oil droplets. The chamber is made of two cover slips glued together by a double sided sticky tape and is sealed with a two-component dentist glue. Inset shows the cross-section through the observation chamber with a water-in-oil droplet that floats to the upper glass of the chamber due to the difference in the density between the HFE-7500 oil (ρ = 1614 kg/m3) and the water phase (ρ = 998 kg/m3). Image modified from [16].

4.3.3. Trapping Device

Microfluidic trapping device was used for time-lapse observation of immobilized droplets under distinct oil phase conditions (Figure 34C). This trapping device comprises of an inlet to introduce the droplets and inlets to apply constant oil flow. In V-shaped cavities the droplets are trapped and hold in place by the applied oil flow.

4.3.4. Picoinjection Device

To further manipulate and sequentially load biomolecules into water-in-oil droplets, a picoinjection device, developed by Abate *et al.*[130] was applied here. The picoinjection device (Figure 37, Figure 34D) consists of an inlet channel where the produced droplets are introduced using a MFCS-EZ flow control system (Fluigent, France). To prevent fusion of the passing droplets under the electrical field, droplets were separated by a stream of surfactant-containing oil from a second oil channel before approaching the injection unit. The injection unit comprises of two electrode channels filled with Indalloy 19 (51% indium, 32.5% bismuth, 16.5% tin, GPS Technologies, Germany). Here an alternating electrical (AC) field in the opposite to the injection channel is applied in order to achieve the poration and destabilization of the surfactant shell and the lipid bilayers. This allows for controlled picoinjection of biomolecules into the droplets that are passing the injection channel. Electrical field (frequency 1 kHz, potential 250 V) was generated by HM 8150 signal generator (HAMEG, Germany) and amplified by a 623B-H-CE amplifier (TREK, USA). Dependent on the applied pressure, the injection volume can be precisely controlled between 1 to 100 picoliter.

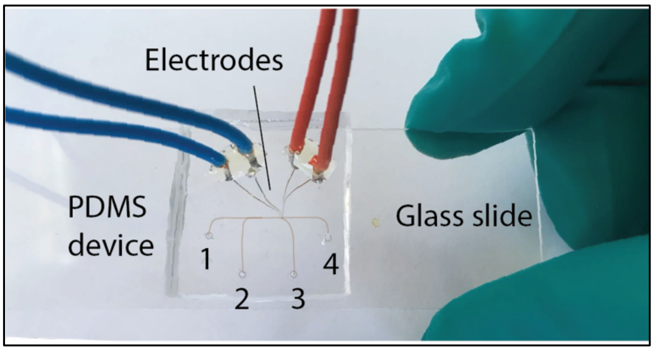

Figure 37: Photo of a microfluidic PDMS device with electrodes glued on a glass slide. Fluid channels are colored in brown for better visibility. 1: inlet for droplets, 2: inlet for spacing oil, 3: injection inlet, 4: outlet.

4.4. Analysis of the Droplets

In the following section, I will describe which methods I used to analyze the microfluidic water-in-oil droplets.

4.4.1. High Speed Camera

In order to observe the droplet-production and picoinjection, an Axio Vert.A1 (Carl Zeiss AG, Germany) inverse microscope equipped with a 20x objective (LD A-Plan 20x/0.35 Ph1, Carl Zeiss AG, Germany) was used. High-speed videos were recorded with a Phantom 7.2 (Vision Research, USA) CCD camera in bright-field with 80 µs exposure time and 10 000 pps.

4.4.2. Confocal Imaging

Confocal fluorescence microscopy was performed with an inverted confocal Laser-Scanning-Microscope (SP5, Leica Germany) equipped with an argon and a white light laser (WLL). Imaging was carried out using a 63x oil-immersion objective (HCX PL APO 63x/1.40-0.60; Leica Microsystems GmbH, Germany). The pinhole for data acquisition was set to 1 Airy unit, which corresponds to an Airy disk diameter of 96 µm and a 0.9 µm thickness of the optical slice. Fluorophores were exited at 488, 558 and 647 nm and the detection windows were set at 500-540 and 568-610 nm and 657-700 nm in case of ATTO 488, Alexa Fluor 568 and Alexa Fluor 647 -labeling, respectively.

Further a LSM 880 confocal microscope (Carl Zeiss, Germany) using a C-Apochromat 40 × /1.2 W water-immersion objective (Carl Zeiss, Germany) was used for fluorescence intensity measurements of flowing droplets. The pinhole was fully opened, to maximize photon collection.

4.5. Lipid-based Compartment Systems

In the next sections I will explain how the surfactant stabilized water-in-oil droplets were tuned to create lipid-based compartment systems, namely multicompartment systems or droplet-stabilized GUVs, or free-standing GUVs. Further I will describe how I characterized these lipid-based compartment systems.

4.5.1. Microfluidic Formation of Multicompartment System and dsGUV

For the formation of multicompartment systems and dsGUVs, solutions of SUVs with different lipid compositions were generated according to previously reported protocols.[16] In brief, the lipids were mixed at desired ratios in a glass vial and dried under a gentle stream of nitrogen. To remove traces of the solvent, the lipids were kept under vacuum in a desiccator for at least 2 h. The dried lipids were resuspended to a concentration of 2.2 mM in 30 mM Tris buffer at pH 7.4 (storage buffer) and the resulting SUV solution was then extruded 7 times through a polycarbonate filter with a pore size of 50 nm (Avanti Polar Lipids, Inc.). The mean SUV diameter was determined using dynamic light scattering (DLS, Malvern Zetasizer (Nano ZS)). Solutions containing SUVs were stored at 4 °C for up to 48 h or encapsulated into microfluidic droplets immediately.

A microfluidic droplet production device (Figure 34A) made of PDMS was utilized to form multicompartment systems or dsGUVs. For this purpose, the flow rate of the water and oil phase was set to 200 µl/h and 2000 µl/h, respectively. These conditions allowed production of phospholipids-containing droplets with a diameter of 30 µm at a rate of 4.2 kHz.

The SUV solution was diluted to a final lipid concentration of 1.1 mM (equivalent to 26.5 µM SUVs / 1.6 x 10^{16} SUVs/ml) in 30 mM Tris and 10 mM $MgCl_2$, so as to form a continuous lipid bilayer within the droplets that were 30 µm in diameter (see Section 4.5.2). To create dsGUVs containing free-floating SUVs in the droplet volume, a lipid concentration of 2.2 mM (equivalent to 53 µM SUVs / 3.2 x 10^{16} SUVs/ml) was used. Finally, the SUVs were introduced into the aqueous channel of the microfluidic device for droplet formation. The oil phase consisted of HFE-7500 oil including 1.4 wt% PEG-based fluorosurfactant and Krytox at concentrations ranging from 0.15 to 15 mM. Droplets were collected in a micro tube, transferred into observation chambers (Figure 36) and observed after compartment formation and after 7 days of storage at 4 °C by confocal fluorescence microscopy to assess compartment formation and stability. Moreover, fluorescence recovery after photobleaching (FRAP) (see Section 4.5.3) and cryo-SEM analysis (see Section 4.5.4) was carried out to characterize bilayer formation. Additionally, droplets sealed in a microfluidic trapping device were imaged under the same conditions.

4.5.2. Minimal Lipid Concentration Required for a Formation of dsGUVs

To ensure a complete coverage of the droplet's inner interface with a lipid bilayer the necessary amount of lipids was calculated according to a droplet with a diameter of 30 µm, the volume $V_{droplet}$ and the surface $A_{droplet}$.

$$V_{droplet} = \frac{4}{3}\pi r^3 = 1.4 \text{ x } 10^4 \text{ µm}^3$$

$$A_{droplet} = 4\pi r^2 = 2.8 \text{ x } 10^3 \text{ µm}^2$$

The area A_{lipid} that a single lipid occupies in a lipid bilayer was assumed to be

$$A_{lipid} = 0.7 \text{ nm}^2 = 7 \text{ x } 10^{-7} \text{ µm}^2$$

Thus, the amount of lipids N_{lipids} necessary to create a lipid bilayer of a size of $A_{droplet}$ is

$$N_{lipids} = A_{droplet}/A_{lipid} \text{ x } 2 = 8 \text{ x } 10^9 \text{ lipids}$$

This corresponds to a minimal concentration c_{min} of

$$c_{min} = N_{lipids} \frac{N_{lipid}}{N_{Avogadro} V_{droplet}} = 950\ \mu M$$

as the minimal amount of lipids necessary to create dsGUVs with a diameter of 30 µm. To compensate possible loss of lipids during SUV extrusion or droplet production a 15% lipid excess was used in the experiments (1.1 mM).

4.5.3. Fluorescence Recovery after Photobleaching (FRAP) Measurements

FRAP measurements were performed to assess the diffusion coefficients of the fluorescently labeled lipids close to the periphery of the droplet. To that end, the droplets were scanned in z-direction until reaching the bottom slice that was not in contact with the glass surface of the observation chamber. This was chosen as the confocal plane to perform FRAP measurements. A circular spot of 5 µm in diameter was used as a bleaching spot (7 cycles, until fluorescence of bleaching spot vanished). Further, 10 pre-bleaching images and 30 post-bleaching images were recorded from the bleaching spot and from the whole droplet base (as a reference). FRAP measurements were performed at least for 20 droplets per condition. The analysis followed the protocols proposed by Axelrod *et al.*[252] and Soumpasis.[253] In this regard, first, the background noise I_{bg} of the detector, measured in the oil phase, was subtracted from all measured intensity values of the bleached spot. Next, average intensity values of the bleaching spot, I(t), and of the whole droplet base, T(t), were extracted from the recorded images and their post bleaching values were normalized by the averages of the prebleaching values, I_{pb} and T_{pb}, leading to I_{nor}.

Photofading was corrected by multiplying the intensities of the bleached spot with the reciprocal, normalized intensities of the droplet base, T(t).

$$I_{nor} = \frac{I(t)-I_{bg}}{I_{pb}-I_{bg}} \cdot \frac{T_{pb}-I_{bg}}{T(t)-I_{bg}}$$

To fit the normalized intensities I_{nor} to an exponential function a nonlinear-square fit (Figure 53A und B) was applied using MATLAB R2015a SP1 (as further described in Weiss *et al.*[20]) resulting in the coefficient values λ

$$f(t) = a(1 - \exp(\lambda \cdot t)$$

The coefficient values λ were then applied to calculate the half time recovery $\tau_{1/2}$ of the bleached spots.

$$\tau_{1/2} = \frac{-\log(0.5)}{\lambda}$$

Based on the half time recovery $\tau_{1/2}$ and the square radius of the bleaching spot, the diffusion coefficient D can be calculated, assuming a Gaussian bleaching profile:

$$D = 0.32\ \frac{r^2}{\tau_{1/2}}$$

4.5.4. Cryo-Scanning Electron Microscopy (cryo-SEM)

For cryo-SEM sample preparation, the droplet emulsion solution (3 µl) was dropped on 0.8 mm diameter gold specimen carriers assembled on a freeze fracture holder (Leica Microsystems, Wetzlar, Germany) and immersed immediately in liquid nitrogen. Next, the droplets were transferred by an evacuated liquid nitrogen-cooled shuttle Leica EM VCT100 (Leica Microsystems, Wetzlar, Germany) into a Leica EM BAF060 (Leica Microsystems, Wetzlar, Germany) freeze fracture and etching system. For cryo observations, the droplets were fractured in the 10^{-6} - 10^{-7} mbar vacuum chamber at -160 °C with a cooled knife. To allow the water in the fractured droplets to sublimate, the sample holder stage was heated to -90 °C for 60 min. Following sublimation, the freeze fractured droplets were coated with 4 nm of Pt-C by electron beam evaporation. For image acquisition, the samples were transferred via an evacuated liquid nitrogen cooled shuttle into the imaging chamber of a Zeiss Ultra 55 field emission electron microscope (FE-SEM) equipped with in-lens, secondary electron (SE) and angle selective backscattered electron (ASB) detectors (Zeiss SMT, Oberkochen, Germany). Top-view imaging was performed under low temperature conditions (Top = -115 ± 5 °C), and with a working distance between 3 to 5 mm. Due to the low conductivity of the emulsion droplets low acceleration voltages of 1.5-2.0 kV were used. Signals were detected with the in-lens detector.

4.5.5. GUVs Release into a Physiological Environment

After formation, dsGUVs were collected from the outlet of the microfluidic chip in a micro tube. The collected droplets were stored at 4 °C overnight for equilibration of the lipid and the ionic conditions within the droplets.

To release the GUVs from the oil phase and from the stabilizing polymer shell into an aqueous environment, 50 µl of 30 mM Tris buffer supplemented with 10 mM $MgCl_2$ (matching the osmolarity of the encapsulated aqueous phase) was pipetted onto the droplet emulsion (Figure 38). To destabilize droplets, 10 – 100 µl of 30 vol% perfluorooctanol (PFO)-containing HFE-7500 oil (de-emulsifier) was slowly added until the milky emulsion turned into a clear aqueous phase (detected by eye). Following de-emulsification, the released GUVs were carefully removed with a pipette and transferred into observation chambers passivated with BSA (Bovine serum albumin, SERVA Electrophoresis GmbH). For this end, cover slides were incubated with PBS containing 1 mg/ml BSA for 2 h at RT and then washed twice with PBS and with milli-q water. Confocal imaging was performed after 1 h to allow for the GUVs to sediment to the bottom of the chamber. For statistical analysis (see next section), GUVs were counted, but only GUVs with diameters > 20 µm were taken into account.

4.5.5.1. Calculation of Release Efficiency

To quantify the success rate of the release, GUVs were transferred into a BSA coated observation chamber and allowed to sediment to the bottom of the observation chamber for 1 h. An area of 246.5 x 20,000 µm within the observation chamber was screened for released GUVs and the amount of GUVs (N_{count}) in that area was counted. Assuming that all GUVs have sunk to the bottom of the observation chamber, N_{count} can be referred to the number of GUVs in the volume $V_{aq\_count} = 246.5 \times 90 \times 20{,}000$ µm.

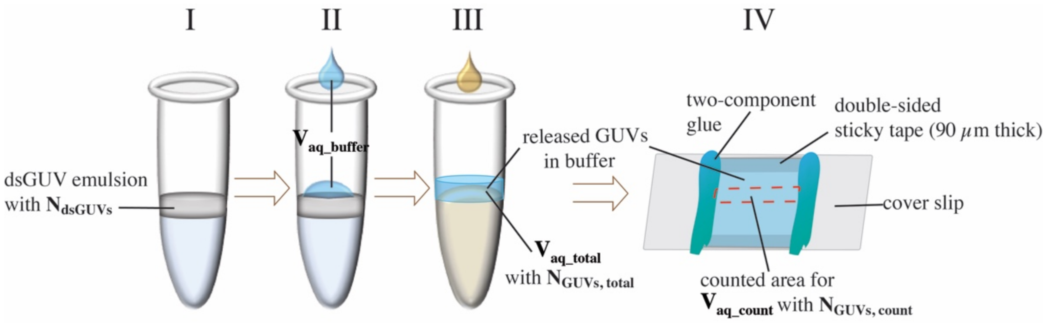

Figure 38: Schematic representation of bulk release approach. I. Collection of dsGUVs for 10 min with production rate of 4.2 kHz lead to 2.52 x 10^6 *dsGUVs. II. Addition of aqueous buffer* V_{buffer}*. III. Addition of de-emulsifier to release GUVs into the aqueous phase. IV. Observation chamber made from two BSA-coated cover slides and a double-sticky tape as a spacer. Edges are sealed with two component glue. In a volume of 246.5 x 20000 x 90 µm (*V_{aq_count}*, marked in red) released GUVs were counted (*$N_{GUVs,\ count}$*) and total number of GUVs in* V_{aq_total} *was extrapolated.*

To get the total number of released GUVs ($N_{GUVs,total}$) in the total aqueous volume of the micro tube (V_{aq_total}) V_{aq_total} was calculated by the sum of the added release buffer ($V_{release\ buffer}$) and the encapsulated aqueous volume within the emulsion:

$$V_{aq\_total} = V_{release\ buffer} + V_{aq\_encapsulated} = 83.3\ \mu l$$

The total number of GUVs can be calculated as

$$N_{GUVs,total} = N_{GUVs,count} * (V_{aq\_total} / V_{aq\_count}) = N_{GUVs,\ count} * 187.8$$

The efficiency of the release $E_{release}$ is then gained by dividing $N_{GUVs,total}$ with the initial amount of dsGUVs in the micro tube.

Efficiency of release: $E_{release}$ [%] = $(N_{GUVs,total} / N_{dsGUVs}) * 100$

4.5.5.2. Osmotic Manipulation of GUVs

For manipulation of the released GUVs, a release buffer was used that did not match the osmolarity of the buffer within the GUV. To achieve hypoosmotic or hyperosmotic conditions 30 mM Tris without $MgCl_2$ or with 15 mM $MgCl_2$ was used. For hyperosmotic conditions 35 µl of the GUV solution could be also placed on the bottom cover slip of the BSA coated observation chamber and allowed to partly evaporate for 10 min before the observation chamber was closed with the second cover slip on top. GUVs were observed after ½ h equilibration time.

4.5.5.3. Purity Assessment of the Released GUVs: Raman Microscopy

For Raman spectra collection released GUVs or dsGUVs were transferred into an observation chamber. Using a confocal Raman microscope (Alpha300RA, WITec GmbH, Germany) GUVs or dsGUVs were observed via a 100x oil objective (NA 1.2, Zeiss, Germany). The same objective was used for focusing a 532 nm laser (20 mW, spot size 350 nm) onto single GUVs or dsGUVs to collect Raman scattered light. Acquisition time was set to 2.14 seconds with five accumulations for each collection window. After the spectra collection, the location of the GUV or the dsGUV was checked again and, in case the GUV or dsGUV stayed in the same location the collected data was saved.

4.6. Functional Cellular Modules in Droplets

After having introduced how to produce the lipid-based compartment system, I will now describe how I assembled functional units in bulk and inside of the water-in-oil droplets towards the reconstitution of cellular motility: namely actin networks adhesion-associated proteins.

4.6.1. Actin-based Dynamics

In this section, all methods related to the assembly of functional actin networks will be described. Thereby, I will explain how actin dynamics were studied in bulk as well as in water-in-oil droplets.

4.6.1.1. Actin Polymerization in Bulk

Actin monomers (G-actin) and ATP solutions were rapidly defrosted and then placed on ice. For the polymerization of G-actin to actin filaments (F-actin) in bulk, G-actin (1% was conjugated with Alexa Fluor 568 or Alexa Fluor 647) was diluted to a concentration of 10.1 µM in actin storage buffer (see Section 3.5). Then a 10x concentrated actin polymerization buffer supplemented with freshly thawed ATP was added in order to achieve polymerization conditions for actin. Actin in polymerization buffer was allowed to polymerize at RT for 30 min. Afterwards 25 µl of the polymerized actin was transferred onto a PLL-PEG coated cover slip (see next section) and observed by means of confocal fluorescence microscopy.

4.6.1.2. Piranha Cleaning of Cover Slips

In order to remove organic residues from glass and render it hydrophilic, the glass was treated with a highly oxidative acid bath. Towards this end, cover slips were placed in a Teflon holder in a beaker under the fume hood and 75 ml sulfuric acid was poured into the beaker followed by slowly adding 15 ml H_2O_2 (1:5). After 45 min incubation, the Teflon holder with the glass cover slips were carefully removed from the solution. Subsequently, cover slips were rinsed in a beaker with deionized water for 5 min before the glasses were dried with a flow of nitrogen and then treated with oxygen plasma for 10 min at 150 W and 0.4 bar.

4.6.1.3. PLL-g-PEG Passivation

In order to passivate the glass surfaces with PLL-g-PEG (SuSoS, USA) cover slips were first cleaned with piranha solution (see previous section) and then activated with oxygen plasma for 10 min, 0.4 bar at 150 W. PLL(20kDa)-g[3.5]-PEG(2kDa) was diluted to a concentration of 0.25 mg/ml in a 10 mM HEPES buffer at pH 7.4 and was pipetted on the freshly activated glass surfaces and allowed to incubate in a moist chamber for 45 min at RT. Afterwards the glass surfaces were rinsed with milli-q water and dried under a nitrogen flow.

4.6.1.4. Actin Network Assembly within Microfluidic Droplets

To create water-in-oil droplets containing actin networks a microfluidic production device with two aqueous inlets was used. One of the aqueous solutions comprised 20 μM G-actin (1% Alexa Fluor 568-labeled) in storage buffer, the other aqueous phase contained a double concentrated polymerization buffer (see Section 3.5.). In some cases, both aqueous phases were substituted with 0.4 wt% methylcellulose. Prior to the encapsulation experiments all aqueous solutions were kept on ice. For droplets production HFE-7500 oil containing 1.4 or 1 wt% PEG-based fluorosurfactant was used. After droplet production, droplets were transferred into an observation chamber that was thoroughly sealed to prevent an directed oil flow in the chamber. Network and droplet dynamics were analyzed at RT using confocal fluorescence microscopy.

4.6.1.5. Actomyosin Network Formation in Bulk

G-actin, myosin and ATP solutions were rapidly defrosted and then placed on ice. G-actin (1% was conjugated with Alexa Fluor 568) was diluted to a concentration of 10.1 μM in actin storage buffer supplemented with 0.75 mM KCl. Then 0.5 μM myosin II was added slowly to the solution to prevent precipitation of myosin clusters and allowed to sit for 30 min on ice. Then a 10x concentrated actin polymerization buffer supplemented with freshly thawed ATP was added in order to achieve polymerization conditions for actin. Actomyosin networks were afterwards transferred onto a PLL-PEG coated cover slip (see Section 4.6.1.3) and was then observed by means of confocal fluorescence microscopy.

4.6.1.6. Actin Motility Assay

For the actin motility assays flow cells (Figure 39) have been fabricated. Towards this aim, a cover slip was coated with a thin layer of nitrocellulose (Zaponlack, Clou, Germany) diluted with ethylacetate (Carl Roth, Germany) in a 1:3 ratio. The two sides were not sealed in order to flush it with liquid samples. In this regard, 40 μl myosin II solution (1 mg/ml in D-buffer, for buffers see Section 3.5.) was introduced into the flow chamber to allow the myosin to be immobilized on the nitrocellulose coating. After 3 min, unbound myosin was washed with 40 µl AB Buffer containing 1 mg/ml BSA to block free nitrocellulose binding sites. Prepolymerized F-actin (see Section 4.6.1.1) was labeled and stabilized with Atto488-phalloidin (Thermo Fisher Scientific, Germany), fragmented with a syringe and dissolved to 0.5 µM with AB buffer. 40 µl of this F-actin solution was pipetted into the flow chamber and allowed to bind to the myosin heads. The flow chamber was mounted on a confocal fluorescence microscope and 40 µl of ATP-containing motility buffer was added into the flow chamber. The movement of actin filaments running over myosin was recorded and then tracked with the help of a manual tracking plugin in ImageJ.

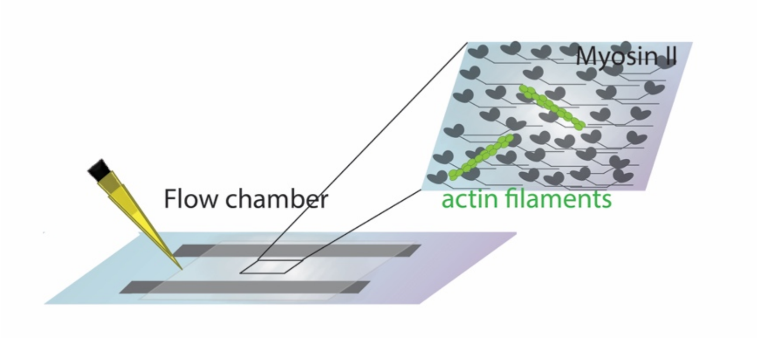

Figure 39: Sketch of a flow chamber to perform a motility assay of F-actin filaments gliding over immobilized myosin II heads.

4.6.1.7. ATP Sensor Experiment

The PercevalHR was developed by Tantama *et al.*[249] and purified and characterized by Dr. Amelie Benk and Christine Mollenhauer (see Section 3.4.6). Fluorescence characterization was performed in a multi-well plate (96 well microplates black, flat clear bottom, VWR) in a plate reader (Infinite 200 PRO, Tecan) in a ATP / ADP (both Sigma Aldrich, Germany) dependent manner (Figure 40B).

To assess the activity of the actomyosin system, the PercevalHR assay buffer (see Section 3.5.) was adjusted to actomyosin conditions (100 MOPS, 75 KCl, 5 NaCl, 0.5 $MgCl_2$; pH 7.4 plus 15 mM $MgCl_2$). Further, 10 µM of F-actin, 0.5 µM of myosin II and 0.1 mM of PercevalHR sensor were dissolved in the buffer and then split into 3 micro tubes. Following splitting, 0 or 100 µM Mg-ATP or 100 µM ADP was added, respectively, and 100 µl of each solution was pipetted into a 96-well plate (Figure 40A). A plate reader was used to collect excitation spectra (from 350 to 520 nm excitation, emission from 545 with a bandwidth of 20 nm) immediately after sample preparation, after 25 min, 1 h and 1.5 h incubation at RT. Accordingly, a control was performed comprising 100 µM Mg-ATP and F-actin but no myosin II.

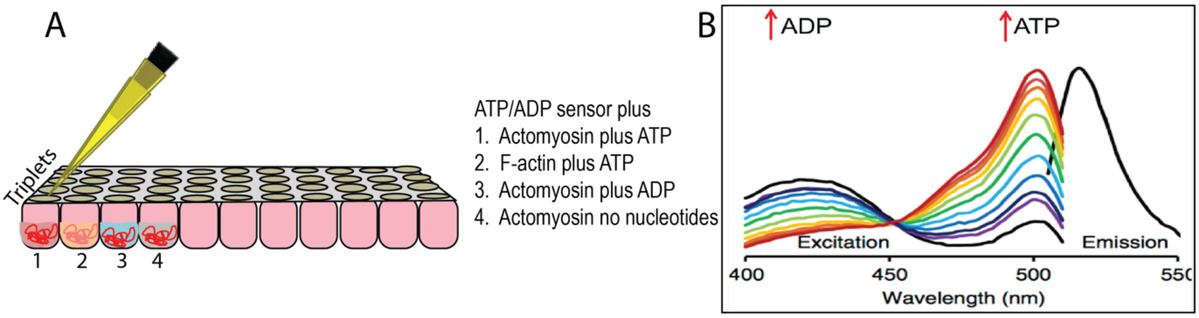

Figure 40: ATP sensor approach. (A) Sketch of sample preparation in a multi-well plate to test ATP hydrolysis of the actomyosin system. (B) Excitation spectra (350 nm – 520nm, emission: 545 nm) of samples containing 100 µM PercevalHR sensor and ATP and ADP in different ratios (black: ADP 100%, red: ATP 100%, 1 mM). Reprinted with permission from Tantama et al.*, 2013. Copyright © 2013, Springer Nature.*

4.6.1.8. Actomyosin Network Formation within Water-in-Oil Droplets

In order to create an active actomyosin network within the water-in-oil droplets, a microfluidic production device with two aqueous inlets was used (Figure 34B) Therefore, two aqueous solutions were prepared: The 1st solution contained: G-actin (20 µM, 1% Alexa Fluor 568-labeled) in storage buffer as well as the ATP recovery buffer ‘a’. The 2nd solution contained: myosin II (mainly 1 µM, when not mentioned explicitly), the double concentrated polymerization buffer including the ATP for myosin activity (1 mM) as well as a ATP recovery buffer ‘b’ (see Section 3.5.) and the F-actin crosslinking protein fascin (0,5 µM, Novus Biologicals, USA). Since size of myosin clusters is depending on the KCl concentration both aqueous solutions were substituted with KCl to reach a final concentration of 75 mM. Myosin was adjusted to KCl conditions for 30 min before encapsulated into the droplets. Further an oxygen scavenger system was included in both solutions to prevent photo-bleaching. As control experiments blebbistatin (0.1 mM, Sigma-Aldrich, Germany) was added to inhibit myosin activity. To track the motility of the droplets fluorescently labeled beads (1µm, Thermo Fisher Scientific, Germany) were included in the aqueous phase.

As an oil phase for droplet production HFE-7500 oil containing 1.4 or 1 wt% PEG-based fluorosurfactant or FC-40 oil containing 5 to 10 mM custom-made triblock surfactant were used. In some experiments, 100 µM gold-surfactant or hydrophobic polystyrene beads (d= 2 µm) were added to the oil phase in order to create actin filament interaction or to label the droplets from the oil phase, respectively.

After droplet production, actomyosin-containing droplets were transferred into an observation chamber that was thoroughly sealed to prevent an oil flow in the chamber. Network and droplet dynamics were analyzed using confocal fluorescence microscopy.

4.6.2. Evaluation of Marangoni Effect on Droplets Motility

To test for droplet dynamics in a millimeter length scale based on the Marangoni effect, 3.5 ml of HFE-7500 oil containing 1.4 wt% PEG-based fluorosurfactant and 0 mM, 1.5 mM or 10.5 mM Krytox was pipetted into petri dishes (35 mm in diameter, VWR International GmbH, Germany). F-actin was prepared as described in Section 4.6.1.1 and allowed overnight at 4 °C to be polymerized completely. A 10 µl droplet of the polymerization buffer labeled with red ink with and without substitution of F-actin (10 µM) was pipetted carefully on top of the oil phase and droplet motion was recorded for 2 min using a simple smart phone camera (Samsung A3). The motion of the droplet swimming on top of the oil was then tracked with ImageJ and velocities were extracted to compare droplet movement of samples with and without F-actin in presence of different Krytox concentrations.

4.6.2.1. Synthesis and Encapsulation of $CaCO_3$ Microspheres

The $CaCO_3$ microspheres were fabricated by Dr. Ilia Platzman following a previously published protocol.[254] In brief, ≈6 µm microspheres were prepared by colloidal crystallization from supersaturated solution. Towards this end, equal volumes of 0.33 mM solutions of $CaCO_3$ and Na_2CO_3 were rapidly mixed and agitated on a magnetic stirrer for 40 min in RT. Following agitation, the mixture was left without stirring for another 15 min. Finally, the microspheres were thoroughly washed with pure water and acetone and dried in air. To encapsulate dextran-FITC (4k, Sigma-Aldrich, Germany) into $CaCO_3$ microspheres by physical adsorption, 400 µl of dextran-FITC dissolved in water (2.5 mg/ml) was added into solution of preformed $CaCO_3$ microspheres.

A microfluidic approach failed to deliver efficiently the microspheres into the droplets due to the blockage of channels by the $CaCO_3$ microspheres. Therefore, to encapsulate the microspheres into water-in-oil droplets, a simple emulsification approach through shaking was applied. In this concern, the $CaCO_3$ beads were dissolved in milli-q water in a concentration of 20 mg/ml and 20 µl were pipetted on top of 100 µl of HFE-7500 oil containing 1.4 wt% PEG-based fluorosurfactant with 10.5 mM Krytox in a micro tube. Following this step, the solution was vortexed vigorously for 15 s until the aqueous phase turned into a milky emulsion. Droplets were transferred into an observation chamber and investigated by bright field and fluorescence microscopy.

4.7. Functional Modules within dsGUVs

The ultimate aim of this thesis is to assemble motility functional modules in a cell-like architecture. In this regard, actin networks as well as adhesion-associated modules were implemented within dsGUVs. The methods how to encapsulate these functional modules within dsGUVs, will be explained in the following.

4.7.1. Actin Polymerization within dsGUVs

Two methods were tested to polymerize actin inside the dsGUVs, a pre-mixed approach and a picoinjection approach. For the pre-mixed approach, actin-containing dsGUVs were produced by means of a droplet production device with two aqueous inlets (Figure 34B). To avoid the actin monomers to polymerize prior to droplet formation one aqueous phase contained the polymerization buffer and the SUVs (2.2 mM) and the other aqueous phase 20 µM actin monomers (1% Alexa 568-labeled actin) in actin storage buffer. Due to the $MgCl_2$ in the polymerization buffer the SUV (70% DOPC, 29,5% DOPG, 0,5% Atto 488 –DOPE) were dragged to the droplet's interface.

For the second approach, two experimental steps were performed. First the dsGUVs were produced as described in Section 4.5, containing actin polymerization buffer and an excess amount of SUV (1.3 mM, 70% DOPC, 29,5% DOPG, 0,5% Atto 488 –DOPE) to allow for maintenance of a continuous lipid bilayer after picoinjection. Following their production, dsGUVs were introduced into the picoinjection device (Figure 34D) and, subsequently, actin monomers (10 µM final concentration, 1% Alexa 568-labeled actin) in storage buffer was injected into these droplets.

4.7.2. Actin Linkage to dsGUV via Biotin-Streptavidin

In order to link actin to the lipid bilayer of the dsGUVs 20% of biotinylated lipids (Avanti Polar Lipids, Inc.) were used to generate SUV (59.5% DOPC, 20% DOPG, 20% biotinylated DOPE, 0.5% Atto488-DOPE). 1.3 mM of these SUVs plus 50 µM streptavidin were dissolved in the actin polymerization buffer and encapsulated into water-in-oil droplets. The dsGUVs were further introduced into a picoinjection device (Figure 34D) and actin monomers containing 1% biotinylated actin and 1% Alexa Fluor 568 labeled actin was injected into the dsGUVs. As an oil phase FC-40 containing 5 mM custom-made triblock surfactant was used.

4.7.3. Integrin Reconstitution into dsGUVs

The reconstitution of $\alpha_{IIb}\beta_3$ integrin into the liposomes was based on a previously published protocol[255] (see also Figure 17). In brief, 435 µM eggPC and 435 µM eggPG was dried under a gentle stream of nitrogen and then placed in a desiccator under vacuum for 2 h or overnight. Next, the dried lipids and Alexa Fluor 568-labeled $\alpha_{IIb}\beta_3$ integrin (see Section 3.4.3) were dissolved in 1 ml of integrin buffer B (see Section 3.5.) to a final ratio of 1:1,000 integrin : lipid. Then the solution was incubated on a Thermomixer (Eppendorf, Germany) for 2h at 37 °C and 600 rpm shaking. Afterwards, 50 mg/ml BT Bio-Beads SM-2 (BIO-RAD, Germany) was added into the micro tube and was stirred on a magnetic stirrer for 3.5 h. This step was repeated once in order to remove the Triton X-100 completely. The proteoliposome solution was used immediately for dsGUV formation or stored up to 48 h at 4°C.

In order to create integrin-reconstituted dsGUV, the integrin proteoliposomes were mixed 1:10 with SUVs (27.25% DOPC, 27.25% POPC, 30% DOPG, 15% cholesterol and 0.5% Atto 488 DOPE) to a final lipid concentration of 1.1 mM in integrin buffer A and 10 mM $MgCl_2$. This liposome mixture was used as an aqueous phase for dsGUV formation. Reconstitution of integrins within the dsGUVs was controlled by monitoring fluorescence colocalization of the Atto 488 labeled lipids and the Alexa Fluor 568 labeled $\alpha_{IIb}\beta_3$ integrin proteins with a confocal fluorescence microscope.

4.7.4. Incorporation of Actin into Integrin-Reconstituted dsGUVs

In order to incorporate both, $\alpha_{IIb}\beta_3$ integrin proteins and actin networks, into dsGUVs a two-step or a premix approach was used. For the two-step approach, the integrin-dsGUVs were created comprising the integrin buffer A (see Section 3.5.) and additionally 15 mM $MgCl_2$. In a second step actin monomers were picoinjected (Figure 34D) into these dsGUVs (final concentration 10 µM actin, Phalloidin Alexa fluor 647 labeled).

For the premix approach, actin-containing integrin-dsGUVs were produced by means of a droplet production device with two aqueous inlets (Figure 34B). 1st aqueous phase contained the integrin buffer A and 30 mM $MgCl_2$, the proteoliposomes and the SUVs (in total 2.2 mM lipids). The 2nd aqueous phase contained 20 µM actin monomers (Phalloidin Alexa fluor 647 labeled) in integrin buffer A. After droplet formation at the flow-focusing junction the two aqueous phases were mixed and the assembly of the actin network as well as the dsGUV formation was controlled by means of confocal fluorescence microscopy.

4.8. Protein Binding Studies

Protein binding studies have been performed in bulk based on QCM-D analysis as well as pull-down assays in order to identify a linker between $\alpha_{IIb}\beta_3$ integrin and actin networks.

4.8.1. QCM-D Analysis

The quartz crystal microbalance (QCM) is a sensitive label-free technique based on an oscillating piezoelectric, crystal quartz plate.[256] Upon adsorption of mass on the crystal, the frequency of the oscillating crystal is changed and can thus be monitored (Figure 41). A QCM with dissipation monitoring (QCM-D) allows further for measuring the energy loss or dissipation of the system, thus the viscoelastic properties of the adsorption layer.[257]

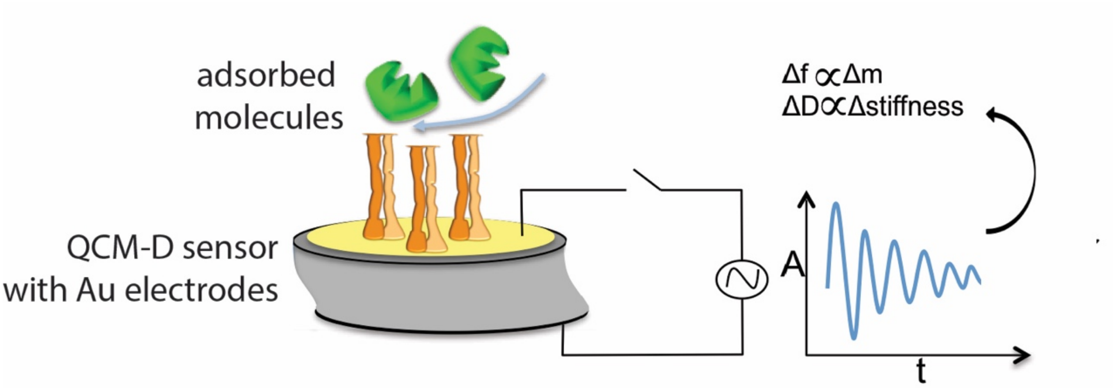

Figure 41: Schematic representation of the QCM-D setup. A QCM-D sensor coated with 2 Au electrodes that apply an alternating current and lead to an oscillation of the piezo element. Upon adhesion of molecules on the sensor the frequency of the oscillating crystal is decreased related to the mass adsorbed on the surface. The energy dissipation is related to the viscoelastic properties of the adsorbed mass.

QCM-D is used here for evaluation of protein-protein interactions, namely to identify a potential protein linker between $\alpha_{IIb}\beta_3$ integrin and actin networks. In this regard, SiO_2 coated sensor crystals (QSX 303, Q-Sense AB, Sweden) were first cleaned by detergent treatment (2% Hellmanex solution, Hellma, Germany) and oxygen plasma (150 W with 0.4 mbar, 45 min, Gigabatch, PVA TePla Ag., Germany) and then mounted in the flow module of a QCM-D (Q Sense Analyzer, Biolin Scientific). Then a constant flow of 25 µl/min through a peristaltic pump (Ismatec IPC, IDEX, Germany) with the according buffer was applied and the air-buffer exchange was recorded until the frequency and dissipation signal reached a stable value again. After this equilibration step, both signals were set to 0 and the data collection window was renewed. Six harmonics (15 – 65MHz) were measured simultaneously, however, for reasons of simplicity in the results only the 7th overtone (35 MHz) is shown. Next, the crystals were either coated with the extracellular matrix protein, fibrinogen (purified from human plasma, Calbiochem, USA), by applying integrin buffer A with 50 µg/ml fibrinogen or a supported lipid bilayer (SLB) was assembled on the crystals. For the SLB assembly SUVs were created (see Section 4.5) (eggPC lipids and 5% NTA-Ni^{2+} linked DOPE) and applied in integrin buffer A into the QCM-D flow chamber. The NTA-Ni^{2+} functional groups were used to immobilize His-tagged focal adhesion kinase (FAK) proteins. On fibrinogen-coated sensors, $\alpha_{IIb}\beta_3$ integrin was applied to bind to fibrinogen, exposing thereby their intracellular tail to further binding partners. Table 7 contains a summary of the experimental steps performed in the QCM-D experiments.

Table 7: Experimental steps of buffers and proteins, introduced in the QCM-D.

Experiment I Integrin-FAK			
Equilibration	Integrin buffer A		30 min
	fibrinogen	50 µg/ml in Buffer A	60 min
Washing step	activation buffer		30 min
	Integrin	50 µg/m in activation buffer	45 min
Washing step	activation buffer		20 min
	FAK	50 µg/ml in activation buffer	45 min
Washing step	activation buffer		90 min
Experiment II SLB-FAK-Integrin			
Equilibration	Integrin buffer A		30 min
	liposomes	0.5 mM, eggPC plus 5% NTA-Ni^{2+} linked DOPE in FAK buffer	30 min
Washing step	FAK buffer		30 min
	FAK	50 µg/ml in FAK buffer	15 min
Washing step	activation buffer		60 min
Washing step	activation buffer		40 min
	Integrin	50 µg/ml	45 min
Washing step	activation buffer		30 min
Experiment III Integrin - Talin			
Equilibration	Integrin buffer A		30 min
	fibrinogen	50 µg/ml in Buffer A	20 min
Washing step	activation buffer		20 min
	Integrin	50 µg/m in activation buffer	45 min
Washing step	activation buffer		20 min
	FL talin	50 µg/ml in activation buffer	90 min
Experiment IV Integrin - THD			
Equilibration	Integrin buffer A		30 min
	fibrinogen	50 µg/ml in Buffer A	20 min
Washing step	activation buffer		20 min
	Integrin	50 µg/m in activation buffer	45 min
Washing step	activation buffer		20 min
Washing step	Talin buffer		15 min
	THD	20 µg/ml in talin buffer	60 min
Washing step	Talin buffer		15 min

Between the introductions of different proteins, washing steps with buffer were performed. For further details of the buffer components see Section 3.5.

The mass m of the adsorbed protein layers on the crystal was estimated according to the Sauerbrey relation by means of the software QTools (Q-Sense, Sweden) which is

$$\Delta m = -(C \cdot \frac{\Delta f_n}{n})$$

with C = mass sensibility (for a 5 MHz quartz crystal) = 17.7 ng*Hz^{-1}*cm^{-2}, Δf the frequency change and n = 1, 3, 5, 7 is the overtone number.

4.8.2. Bead Pull-Down Assay

A pull-down assay was implemented as an additional method to assess the integrin-THD interactions. The first step in the pull-down assay was to immobilize the intracellular fragment of the β_3 integrin (a kind gift from Prof. Geiger, Weizmann institute Israel) on beads to allow for separation of unbound material through centrifugation.

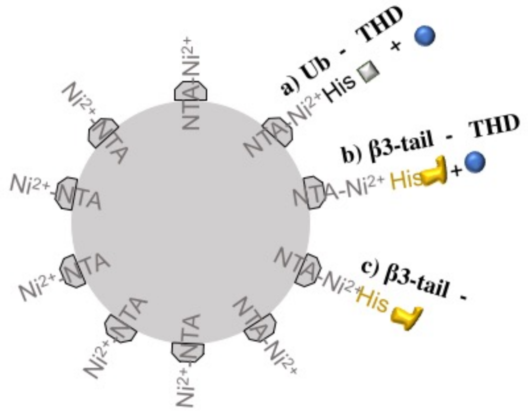

Figure 42: Schematic representation of a NTA-Ni^{2+} bead incubated either with (a) His-Ubiquitin and THD, (b) His-β_3 integrin, His-Ubiquitin and THD or (c) His-β_3 integrin and His-Ubiquitin.

In this regard, 50 µl of NTA-Ni^{2+} resins (HisPur™Thermo Fisher Scientific) was incubated with the His-tagged β3 fragment (100 µg/ml) at RT for 45 min in TBS plus 3 mM $NiCl_2$. Then the beads were separated by centrifuging for 10 min at 1,000 g (Eppendorf table top centrifuge). The supernatant was discarded and the pellet washed twice with TBS plus 3 mM $NiCl_2$ (see Section 3.5.). Following this step, free NTA-Ni^{2+} binding sites were blocked with His-Ubiquitin (100 µg/ml, a kind gift from Prof. Geiger, Weizmann Institute, Israel) in TBS plus 3 mM $NiCl_2$

and 0.5 mg/ml BSA for 1 h at RT. After centrifuging and washing the pellet twice with TBS, the THD was added to the beads and left for binding overnight at 4°C. Following the incubation, the pellet was washed twice with TBS. Then the bound protein was eluted from the beads by means of 50 µl TBS plus 300 mM immidazol (Figure 42b). Control samples consisted of beads that were not incubated with β3 fragment or with the THD, respectively (Figure 42, a and c). Finally, the samples were prepared for SDS-PAGE.

4.8.3. Actin Filament-based Pull-Down Assay

In pull-down assays involving actin filaments no beads are necessary as the actin binding proteins will co-sediment with actin filaments during centrifugation and will be separated from the unbound material. In this regard, actin was polymerized (10 µM) as described in Section 4.6.1.1. The actin filament solution (100 µl each) was incubated with THD, α-actinin, or BSA (final concentration 2 µM) as shown in Figure 43. To test the combined integrin-THD-actin binding all three proteins were mixed accordingly. After incubation over night at 4°C, the samples were centrifuged at 150 000 g for 1.5 h at 4 °C (Tabletop ultracentrifuge (Beckman) with TLA-100 rotor).

The supernatant was removed and the pellet dissolved in 50 µl of actin polymerization buffer. Both, supernatant and pellet, were then prepared for SDS PAGE, followed by Western Blot analysis (see Section 4.8.4).

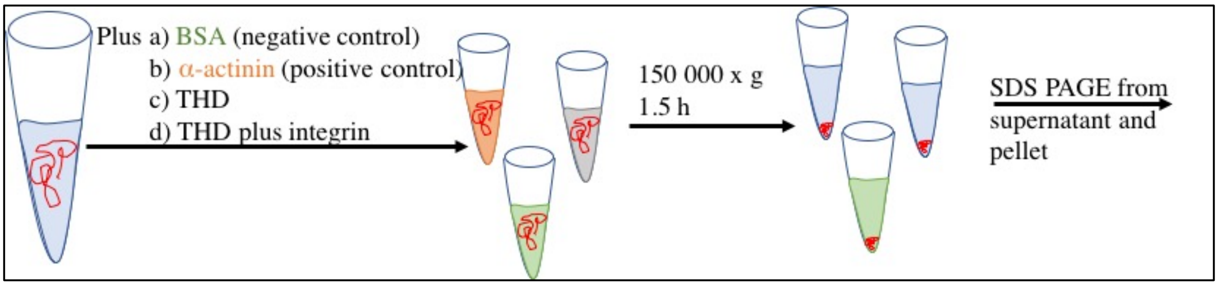

Figure 43: Sketch of procedure for actin pull-down assay. Actin filaments were incubated with a) BSA, b) α-actinin, c) THD, or d) THD and integrin together. After centrifuging / "pull-down" the presence of the according binding proteins in the supernatant or the pellet was analyzed.

4.8.4. SDS PAGE and Western Blot

To prepare samples for SDS PAGE, 3 µl of 6x loading buffer was pipetted to 15 µl of the samples, followed by incubating them for 5 min at 95 °C and then allowed to cool on ice. A SDS gel containing 8% polyacrylamid was mounted in the electrophoresis apparatus followed by the addition of the Tris-glycine electrophoresis running buffer (see Section 3.5.). Then the gel was loaded with 12 µl of the samples and a protein marker (MagicMark™ XP Western Protein Standard, Thermo Fisher Scientific, Germany). Next, the electrophoresis apparatus was attached to an electric power supply (Bio-rad, USA) and a voltage of 200 V was applied for 45-60 min. Afterwards the gel was removed from the cassette and incubated in the Western blot transfer buffer for 10 min to remove the SDS or stained with Coomassie dye (Simply Blue, Thermo Fisher).

In the meantime, the Western blot membranes (Whatman Optitran nitrocellulose membranes, Sigma Aldrich) and filter papers were cut to the dimensions of the gel followed by the soaking of the membrane, filter paper and fiber pads in the transfer buffer. To prepare the gel sandwich, the Western blot cassette was prepared as shown in Figure 44, then closed and mounted into the reservoir equipped with an ice pad and filled with the blotting buffer. An electric power supply was attached and the transfer of the proteins from the gel into the membrane was performed for 1 h at 100 V. After the transfer the membrane was removed blocked with TBS containing 1 mg/ml BSA for 1 h with shaking and washed subsequently with TBS containing 0.1% Tween20 three times for 10 min each. The membrane was incubated in TBS containing 1 mg/ml BSA for 1 h plus either an anti-His antibody (1:500, H1029 IgG mouse, Sigma Aldrich Germany) for β_3 integrin tail detection, or an anti-THD antibody (1:500, mouse, TL1 MAB1676, Millipore, Germany). Accordingly, for actin detection in the experiment of Section 4.8.3 an anti-actin antibody was used (A4700, IgG mouse, Sigma Aldrich Germany). Afterwards, membranes were washed three times with TBS containing 0.1% Tween20, 10 min each time. A horseradish peroxidase (HRP)-conjugated anti-IgG mouse antibody (1:500, goat, AB6789 Abcam, Germany) was added onto the membranes as secondary antibody for 1h at RT, followed by three washing steps with TBS with 0.1% Tween20, 10 min each time. Finally, the detection of the bands was performed by means of a chemiluminescent substrate for HRP (Pierce™ ECL Western Blotting Substrate, Thermo Fisher Scientific) in a luminescent image analyzer (LAS-3000 Imager, Fuji, Japan).

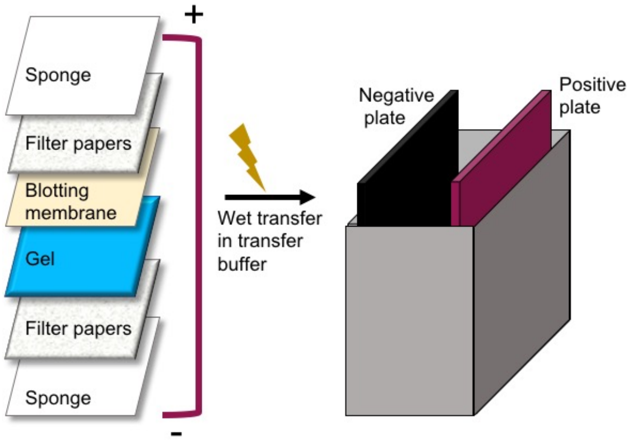

Figure 44: Assembly of the cassette containing the SDS gel and the Western Blot membrane for Western Blot Transfer.

Results and Discussion

5. Results and Discussion

After explaining the materials and methods, I will now present the results of my thesis. In this regard, I structured the section in three parts. In the first part I will show within the water-in-oil droplets the formation of lipid membrane-enclosed compartment systems – including intracellular structures – towards mimicking a eukaryotic architecture. I will further elucidate the mechanism behind the on-demand creation of these lipid structures and further I will show the release of the assembled lipid compartment systems out of the oil phase into a physiological environment.

In the second Part – towards mimicking eukaryotic cell motility – I will present the reconstitution of the functional module of actin-based dynamic networks. Thereby I will explain the mechanisms behind elongation and contraction of the cell body during locomotion.

In the third and last part I will show the reconstitution of transmembrane adhesion proteins within lipid compartment systems. Adhesion is – certainly not limited to – one of the crucial steps in cellular motility and another important functional module in the here presented synthetic cell approach towards mimicking eukaryotic cell motility.

Furthermore, I will present protein binding studies that revealed a single protein fragment as a potential linker between integrin and actin. Thus, this linker may resemble the regulatory and mechanical connection between transmembrane adhesion proteins and actin cytoskeleton, which in a living cell is provided by recruiting several proteins to the adhesion site.

Finally, I want to combine my results by creating a lipid-based compartment system with reconstituted transmembrane adhesion proteins and actin cytoskeleton. This combination of adhesion-based and cytoskeletal functional modules has never been shown in synthetic cell systems before and thus, provide major progress towards creation of cell-mimetic motility.

Part I

5.1. Water-in-Oil Droplets for Lipid-based Compartment Systems

The most fundamental module for the establishment of a synthetic cell system, is a cell-sized compartment, where biochemical reactions can take place in a defined space. Water-in-oil emulsion droplets stabilized by fluorosurfactants were chosen here as stable outer containers for the stepwise reconstruction of cellular modules. These water-in-oil droplets are created by a droplet-based microfluidic technology. This technology offers versatile strategies to manipulate the encapsulated content, either through sequential injection of building blocks or through the functional surfactants in an oil phase. Following the assembly of the surfactants at the water-oil interface, the surfactants deliver different functionalities to the encapsulated content, and by this, inhibit or trigger interaction between the surfactant shell and the encapsulated biomolecules, e.g. as presented in the following, the interaction with lipid vesicles. This results in the masking of the surfactants with a lipid bilayer, the formation of the so-called droplet-stabilized GUVs (dsGUVs), or multicompartment systems, where the lipid vesicles do not interact with the periphery and stay homogeneously distributed within the aqueous phase. To prevent or trigger lipid interactions with the periphery in this thesis, three different types of surfactants were used. An inert PEG-based, a negatively charged (Krytox) and a positively charged amine fluorosurfactant. In the following sections, the analysis and the role of the polymer-based surfactants in the assembly of lipid-based compartment systems will be described.

Note that some results of this part have been published. Thus, some figures and parts of the text in the following sections were adapted with permission from Haller *et al.*, 2018.[86]

5.1.1. Surfactant Analysis

In this part of the thesis I mainly used the commercial PEG-based surfactant from RANbiotechnology, USA. However, as the company do not provide much information about the chemical structure and its purity – which is crucial for the synthetic cell approach – I first want to start this section with the qualitative and quantitative analysis of this surfactant based on FTIR, MALDI-TOF, partitioning experiments and interfacial tension measurements (IFT).

5.1.1.1. Fourier-Transform Infrared Spectroscopy (FTIR)

In order to investigate the chemical structure of the commercial PEG-based surfactant, a FTIR spectrum were obtained from the PEG-based fluorosurfactant by Dr. Jan-Willi Janiesch. The spectrum (Figure 45) showed a typical fingerprint of a PFPE-PEG block-copolymer which was characterized already elsewhere.[241]

To control the purity of the block-copolymer, the surfactant was checked especially for the presence of its educt Krytox, since the negatively charged Krytox can interfere with encapsulated bio-content. The interaction of encapsulated content with the surfactant shell is only in specific applications required. Thus, the band at 1777 cm^{-1}, which is attributed to a stretching mode of the (C=O) bond of the Krytox[27] was examined with special care. In this regard, a tiny band at 1777 cm^{-1} could be observed revealing the presence of Krytox traces within the surfactant.

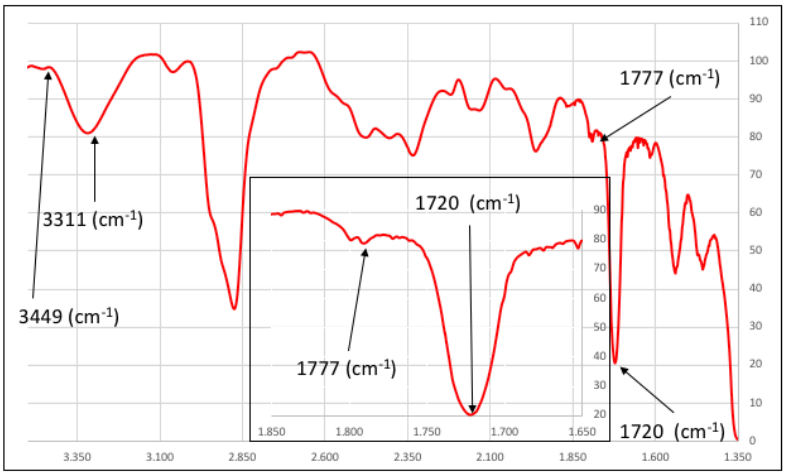

Figure 45: FTIR spectrum of perflouro-polyether-polyethylene glycol (PFPE-PEG) block-copolymer fluorosurfactants (commercial PEG-based fluorosurfactant). Absorption peaks at 3449 cm^{-1} and 3311 cm^{-1}correspond to the symmetrical and unsymmetrical stretching vibration of primary amines. The band at 1720 cm^{-1} is attributed to a stretching mode of the (C=O) band of the amid group, which connects the PEG-diamine with the Krytox.[241] A tiny band is visible at 1777 cm^{-1} representing the stretching mode of the (C=O) band of the carboxylic acid group of the Krytox educt. Reprinted from with permission from Haller et al.*, 2018.*[86]

5.1.1.2. MALDI-TOF

A further characterization of the commercial PEG-based fluorosurfactant was performed by Martin Schröter by means of MS measurements to reveal information regarding the purity and molecular weight of the chemical components. In Figure 46B the region around 2000 m/z is increased showing a series of peaks with the mass difference of 166 (region 1, shown in blue in Figure 46A). This mass difference correlates exactly to the molecular weight of PFPE monomers. Thus, the presence of Krytox molecules with a molecular weight of around 2000 Da could be confirmed. In m/z regions II and III (Figure 46C and D) a series of peaks with the mass difference of a PEG- (44 Da) plus PFPE- (166 Da) monomers was observed, referring to a brought size range of PFPE-PEG block-copolymers between 3500 Da and 6500 Da. Based on the Krytox pattern in region I of around 2000 Da, it can be assumed that the fluorosurfactant consists of a mixture of diblock- and triblock-copolymer, with an average molecular weight of around 4000 Da and 6000 Da, respectively. This means that depending on the ratio between di- and triblock-polymer, a 1.4 wt% solution of the surfactant in HFE-7500 (ρ = 1.61 g/ml) has a molar concentration between 3.8 mM (100% triblock-polymer) and 5.7 mM (100% diblock-polymer). Note, in the calculation of surfactant concentration, the amount of Krytox was ignored.

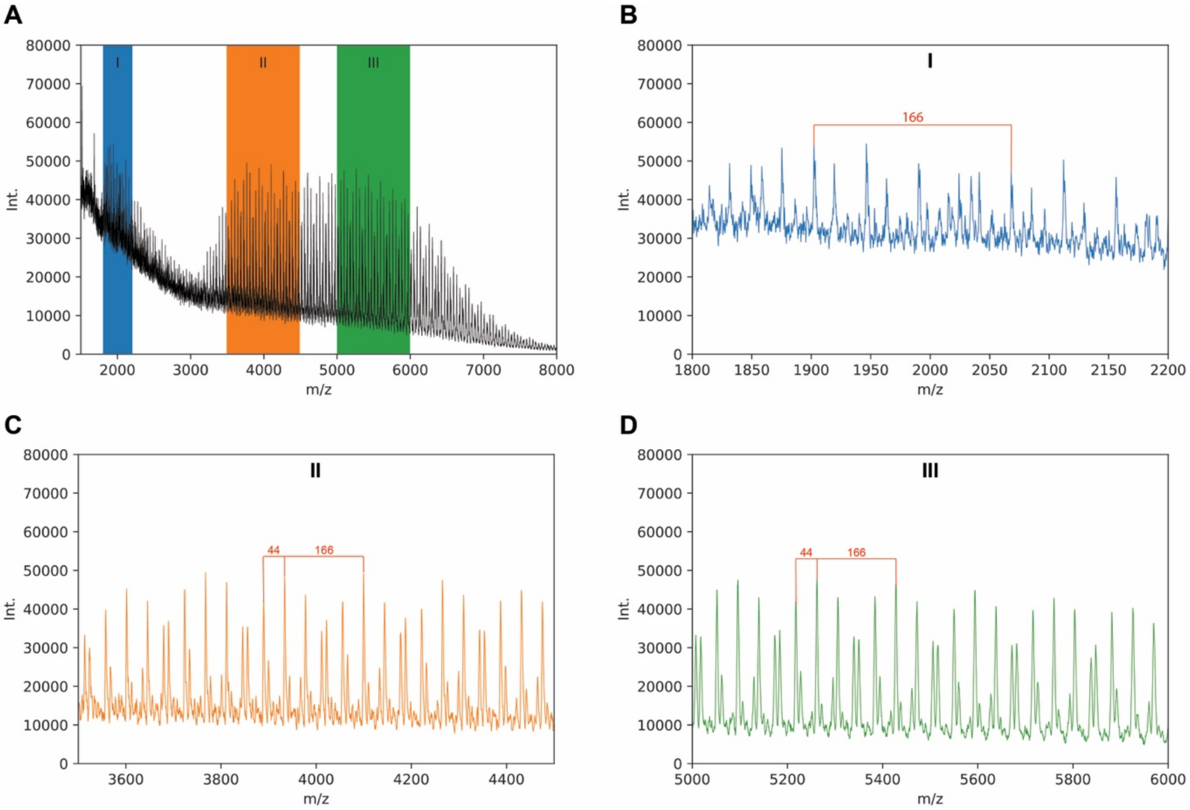

Figure 46: MS (MALDI-TOF) measurement of PEG-based fluorosurfactant. (A) Complete spectrum in m/z range of 1500 to 8000. (B) Spectrum of region I with a mass pattern of PFPE polymer (OCF(CF3)CF2, Δm = 166) referring to Krytox molecules of around 2000 Da. (C) Spectrum of region II showing the MW of diblock-polymers with mass differences of PFPE/PEG monomers (OCF(CF3)CF2, Δm = 166 + OCH2CH2, Δm = 44). D: Spectrum of region III showing the MW of triblock-polymers with mass differences of PFPE/PEG monomers. Reprinted from with permission from Haller et al., *2018.*[86]

5.1.1.3. Partitioning Experiment

As no quantitative statement can be made about the Krytox concentration by means of FTIR or MALDI-TOF measurements, partitioning experiments were performed. Towards this end, a Rhodamine 6G (Rho6G) solution was transferred onto HFE-7500 oil that contained Krytox concentrations between 0 and 1 mM and 1.4 wt% or no PEG-based fluorosurfactant. Due to the 1:1 chemical interaction between the Krytox molecules and Rho6G[250], and the adsorption and desorption of Krytox molecules at the interface, a partitioning of Rho6G molecules to the oil phase was observed (Figure 47A). Following 48 h of incubation, Rho6G content in the oil and the aqueous phases was determined by measuring the absorbance at 500 nm (Figure 47B). The values of samples containing 1.4 wt% PEG-based fluorosurfactant were compared to the values of samples on which Krytox was dissolved in pure HFE-7500 oil. Based on this analysis a concentration of approximately 0.04 mM free Krytox in 1.4 wt% PEG-based fluorosurfactants was interpolated. This concentration is order of magnitudes lower (around 1%) than the 3.8 – 5.7 mM of the PEG-based fluorosurfactants, which was estimated to correspond to 1.4 wt% by MS.

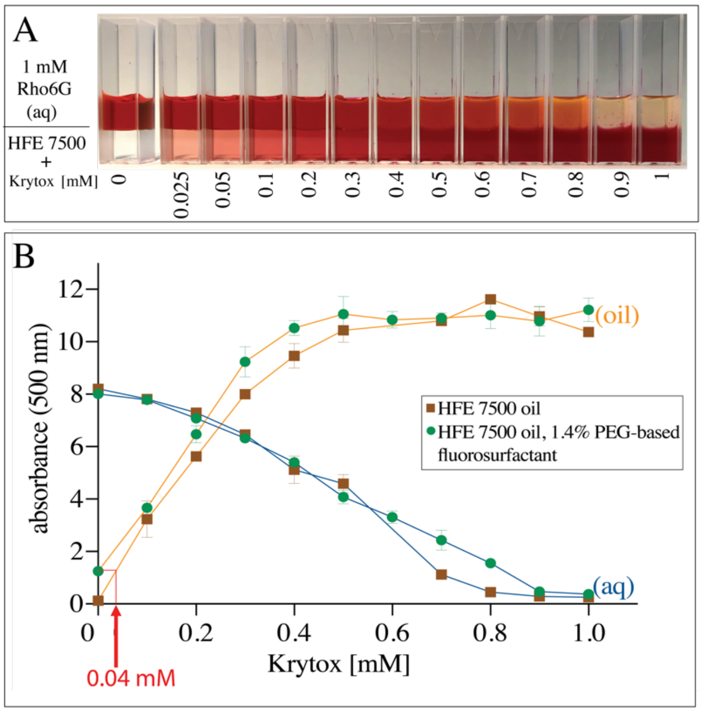

Figure 47: Representative image of the partitioning experiments (standard curves) and its analysis. (A) Aqueous solutions of 1 mM Rho6G (upper phase) are exposed to the HFE-7500 oil phase containing Krytox at different concentrations (indicated at the bottom of the images) in a 3.5 ml cuvette. (B) Spectrometric analysis (absorbance at 500nm) of Rho6G in aqueous (blue) and oil phases (yellow) after 48 h incubation. The Y-axis intercept of the samples containing 1.4 wt% PEG-based fluorosurfactants corresponds to Krytox traces in the PEG-based fluorosurfactant (in 1.4 wt% ~0.04 mM). Reprinted from with permission from Haller et al.*, 2018.*[86]

Note that partitioning experiments of the custom-made triblock and amine surfactant were performed as well, revealing partly much higher amounts of free Krytox (see Appendix, Figure SI 1).

In the synthetic cell approaches as developed in this research, the purity of the PEG-based surfactant is of major importance. Krytox is a negatively charged surfactant and therefore actively assembles at the droplets interface. The charge at the inner droplets interface is not per se desired, but might be advantageous in several applications as the formation of dsGUVs (see following sections) or, later, for the recruitment of actin filaments to the droplets periphery. Therefore, control over the charge at the droplets interface is of particular importance and, therefore should be controlled and tuned on-demand.

The here implemented approach in this concern, is to create mixtures of the inert PEG-based surfactant with Krytox or the positively charged amine surfactant. To characterize the interfacial activity of the surfactant mixtures pendant drop measurements have been performed that will be discussed in the following.

5.1.1.4. Interfacial Tension (IFT) Measurements of Surfactant Mixtures

Pendant drop measurements were performed to evaluate the assembly of surfactant mixtures at the oil-water interface and their influence on surface tension. In this regard, IFT of HFE-7500 oil (Figure 48 green) containing PEG-based fluorosurfactant with different amounts of Krytox (Figure 48 red) or amine surfactant (Figure 48 blue) was measured against water without (Figure 48A) or with (Figure 48B) 1 mM $MgCl_2$. In pure water HFE-7500 oil had an IFT of around 38 mN/m, which decreased to around 4 mN/m upon the addition of 1.4 wt% PEG-based fluorosurfactant. This indicates the assembly of the PEG-based surfactant with a high interfacial coverage.[193]

In contrast to that, by the addition of Krytox to the HFE-7500 oil the IFT decreased only until a value of around 20 mN/m. A denser packing of Krytox molecules at the interface is prevented due to the repulsion forces of the charged head group of Krytox.[196] Similarly, when Krytox was mixed to the 1.4 wt% PEG-based fluorosurfactant the IFT increased until reaching a similar plateau value of around 20 mN/m. Thus, it seemed that the 1.4 wt% (according to 3.8 – 5.7 mM, see previous Section 5.1.1.2) PEG-based surfactant did not have a significant effect on IFT when mixed with Krytox concentrations greater than 6 mM.

By the addition of amine surfactant to the 1.4 wt% PEG-based fluorosurfactant the IFT values did not increase, but slightly decrease. This shows that there is probably an increase in interfacial surfactant coverage due to the higher concentration of surfactants in the bulk (see Section 1.4.3 for theoretical details) and due to a possible denser packing of diblock surfactants in comparison to triblock surfactants.[258] Further, this indicates that probably the lateral repulsive charge effect of the amine group between the surfactant molecules is annulled by the PEG-PEG interaction.

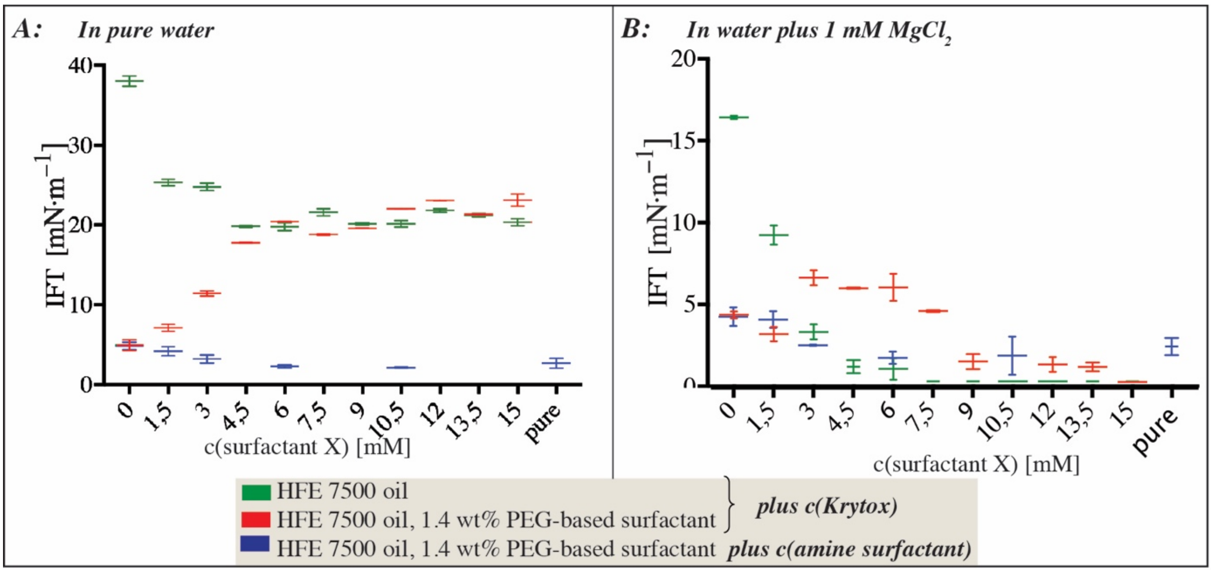

Figure 48: Interfacial tension measurements based on pendant drop analysis. Drop phase: HFE-7500 oil with and without (green) 1.4 wt% PEG-based surfactant and different amounts of x=Krytox (red) or x=amine surfactant (blue) against an ambient phase of pure water (A) or water containing 1 mM $MgCl_2$ (B).

The addition of $MgCl_2$ into the aqueous phase (Figure 48B) leads to a change in IFT values. This is due to the fact that Mg^{2+} can screen the negative charge of Krytox[196] and thus, leads to a denser packing at the interface. Interstingly, the mixture of PEG-based surfactant with increasing amounts of Krytox (red) showed a non-linear behavior. When 3 to 6 mM Krytox was added the IFT increased, however, with increasing amounts of Krytox the IFT dropped again to values of around 1 mN/m. The peak is indicating a less dense packing of surfactant molecules at the oil-water interface in these Krytox-to-PEG surfactant ratios. This is, however, probably not due to electrostatic repulsion but rather due to a steric hindrance or due to interactions of the PEG-based surfactant and Krytox, which can lead to a micellar exclusion of surfactant molecules.[182,186]

For exact IFT values of the surfactant mixtures see Appendix, Table SI 1.

Different IFT values due to different PEG-based fluorosurfactant to charged surfactant ratios revealed a very important outcome – one can tune the charge at the droplet interface in a controlled manner. This ability is of particular importance in the assembly of the single compartments (dsGUVs) that will be presented in Section 5.1.3.

In this regard, I will now, after the analysis of the surfactant, present the formation of the lipid-based compartment systems.

The use of differently charged or uncharged surfactants and differently charged membrane-lipids allow for the creation of two forms of lipid-based compartment system and a combination of both. In the following, I will first describe the microfluidic creation of so-called multicompartment system, followed by their transformation to single compartment systems and, finally, I will discuss the release of these systems out of the oil and surfactant environment into a physiologically relevant buffer.

5.1.2. Creation of Multicompartment Systems in Water-in-Oil droplets

To generate lipid-based compartment systems, small unilamellar vesicles (SUVs) were produced and encapsulated into water-in-oil droplets stabilized by different surfactant combinations as described in Section 4.5.1.

Besides the existence of a large outer compartment, an eukaryotic cell, in particular, is characterized by segregated internal reaction volumes that enable spatial and temporal assembly of biological processes.[11,259] A way to mimic the crowded environment inside a living cell, in which membrane-enclosed compartments make up nearly half of the cell volume,[11] is the development of a multicompartment system that is based on small lipid vesicles encapsulated within the microfluidic polymer-stabilized water-in-oil droplet.

Formation of multicompartment systems requires strategies to inhibit the interaction between the inner shell of the surrounding compartment and the encapsulated SUVs, so that the latter remain randomly distributed within the compartment volume. To obtain this, I set out to create droplets with an inert inner surface and encapsulated SUVs within their lumen. Towards this end, fluorescently labeled neutral, negatively and positively charged SUVs were encapsulated into water-in-oil droplets stabilized by pure uncharged PEG-based fluorosurfactants using a microfluidic droplet production device (see Section4.5.1).

Figure 49 A and B show a homogeneous distribution of the differently charged SUVs (DOPG are the negatively charged, DOTAP the positively charged, and DOPC/POPC the neutral phospholipids) and the combination of them (B) within the droplets, respectively. In none of the cases a bright ring at the periphery of the droplet was visible indicating that the inert and uncharged PEG on the inner droplet interface[206] inhibited the interaction between the SUVs and the droplet periphery. Note, similar results were obtained independently on the presence of ions or lipid charge.

The hereby created multicompartment system provides a confined space to observe and analyze SUV-based functional modules. The encapsulated small vesicular compartments resemble well the organelle structure in real cells. In this concern, an even more physiologically relevant cell-like architecture was achieved through an advancement of this multicompartment system approach, which will be described in Section 5.1.3.5.

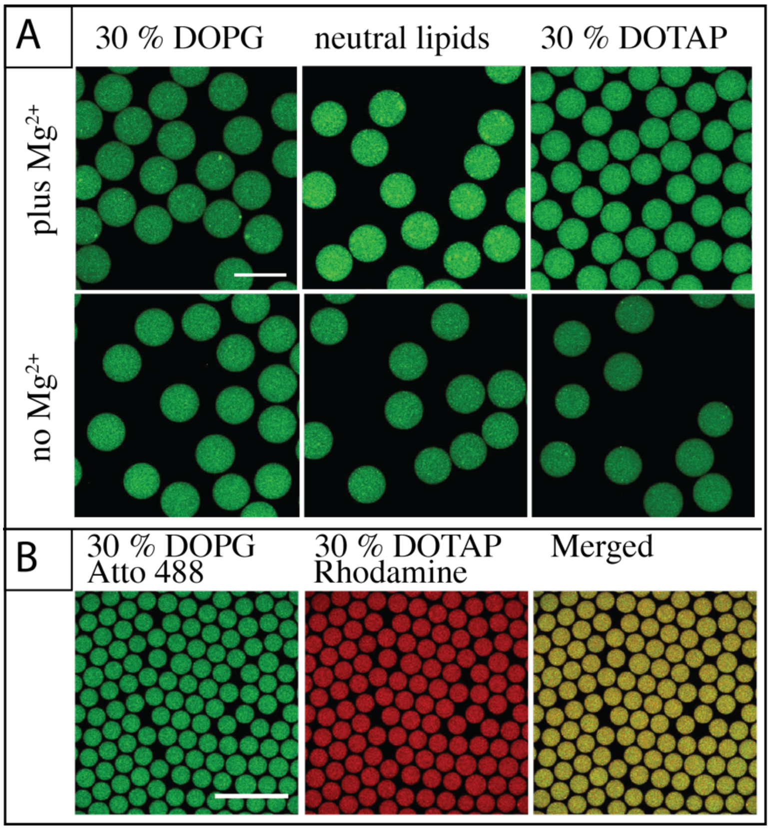

Figure 49: Representative images of homogeneously distributed fluorescence from encapsulates SUVs. A) SUVs comprised of DOPC 42.25 or 27.25% (neutral), POPC 42.25 or 27.25% (neutral), ATTO 488-labeled DOPE 0.5%, cholesterol 15%, DOPG 0% or 30% (negatively charged), and DOTAP 0% or 30% (positively charged) within the droplets generated in the oil phase containing PEG-based fluorosurfactants (1.4 wt%). No interaction of SUVs with the surfactant shell is visible independent on the presence of Mg^{2+} ions. Scale bar 50 µm. B) Two kinds of SUVs were encapsulated (30% DOPG labeled with Atto 488 and 30% DOTAP labeled with Rhodamine). Scale bar 250 µm.

For future synthetic biology applications, encapsulated SUVs could be equipped with special features as functional membrane proteins or pH or temperature sensitive lipids. The latter would allow to trigger the release of the SUV content by e.g. pH[260] or temperature.[136] This offers the possibility to carry out a stepwise reaction mediated by the successive release of substrate or reaction partners and thus, allows for a multitude of sophisticated processes as energy production and transfer as well as material transport.

5.1.3. Creation of Droplet-Stabilized GUVs (dsGUVs)

Water-in-oil droplets as cell-sized compartments that exhibit stable physical properties however lack physiological membrane properties, as it is the case in lipid-based vesicles. To combine the advantages of the mechanically stable water-in-oil droplets with physiological lipid membrane properties Weiss *et al.*[16] established recently the concept of so-called droplet-stabilized GUVs (dsGUVs), which consist of a spherical lipid bilayer covering the surfactant shell. Supported lipid bilayer (SLB) formation in 2D has been studied already intensively in the past showing the influence of e.g. vesicle charge, buffer type and surface charge on vesicle fusion.[100,261,262]

In order to create dsGUVs, electrostatic interactions between surfactant shell and encapsulated SUVs have to be generated. This interaction can be tuned by means of lipid charge, the presence of salts or by the addition of charged surfactants as Krytox or amine surfactant to inert PEG-based fluorosurfactant-containing HFE-7500 oil. Through the electrostatic attraction force between the encapsulated SUVs and the periphery, SUVs fused to a 3D-supported lipid bilayer at the periphery of the droplet, resulting in the transition from a multicompartment system to one large single compartment system, a dsGUV. This effect in correlation with surfactant and lipid charge and the presence of salt is discussed in the following sections in detail.

5.1.3.1. The Effect of Negative Interface Charge on Lipid-based Compartment Systems

Time-lapse fluorescence confocal microscopy was performed to assess the effect of the negatively charged Krytox surfactant on the formation of dsGUVs (Figure 50A). For this purpose, SUV-containing droplets stabilized by inert PEG-based fluorosurfactants were trapped in a microfluidic trapping device (see Section 4.3.3) by applying a constant oil flow (200 µl/h of HFE-7500 oil containing 1.4 wt% of PEG-based fluorosurfactants). The multi-compartment systems, characterized by a homogeneous distribution of SUVs within the droplets, were observed under these conditions (Figure 50A). To transition from multicompartment system to dsGUV, 9 mM Krytox was added to the flow of PEG-based fluorosurfactant-containing oil. Upon Krytox addition, all SUVs within the droplets were attracted to the periphery within 1 min, thereby triggering the charge-driven fusion of SUVs to the surfactant shell. With the addition of Krytox to the oil, a sufficient proportion of Krytox molecules assembles at the interface to provide the necessary charge for dsGUV formation. The negatively charged inner droplet interface attracts Mg^{2+} ions from the SUV-containing buffer, which in turn, promotes SUV (lipid composition of 42.25% DOPC, 42.25% POPC, 15% cholesterol and 0.5% ATTO 488-labeled DOPE) adhesion and eventually rupture. For clarity of presentation Figure 50B and C describe schematically the process of dsGUV formation. The accumulation of lipids at the droplet periphery was detected by means of confocal fluorescence microscopy as a bright ring in the confocal plane.

Note that by fluorescence microscopy imaging only the recruitment of the lipids to the periphery could be assed, however, it could not be judged if vesicles fused to a bilayer. Thus, bilayer formation within the droplets will be confirmed in Section 5.1.3.2. by means of cryoSEM and FRAP.

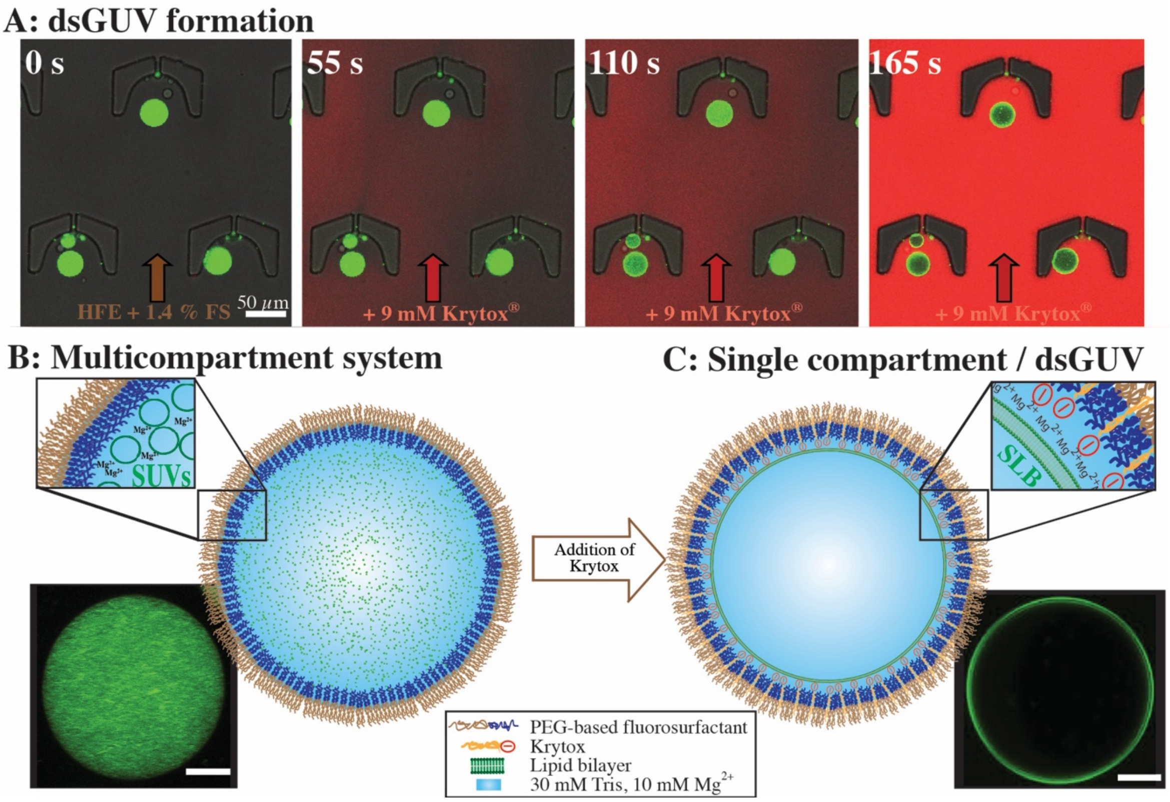

Figure 50: Controlled formation of multicompartment systems or dsGUVs depending on the surfactant charge at the interface. A) Time-lapse analysis of dsGUV formation (DOPC 42.25%, POPC 42.25%, cholesterol 15% and 0.5% ATTO 488-labeled DOPE) in a microfluidic trapping device. Time point 0 s: Droplets are trapped in PDMS cavities by applying a constant flow of HFE-7500 oil containing PEG-based fluorosurfactants ("FS"). After 55 s: Addition of HFE-7500 oil containing Krytox (9 mM). For clarity, the oil containing Krytox was labeled with 10 nM Nile red. After 110 s: Attraction of SUVs to the droplet periphery. After 165 s: The accumulation of lipids on the droplet periphery is visible as a bright ring in the confocal plane. This indicates successful dsGUV formation. Scale bar 50 µm B) Sketch and corresponding representative confocal fluorescence image (lower inset) of SUVs (in 30 mM Tris, 10 mM Mg^{2+}*) encapsulated in a water-in-oil droplet stabilized by inert PEG-based fluorosurfactants without Krytox. The confocal image shows the lipids of homogeneously distributed SUVs (DOPC 42.25%, POPC 42.25%, cholesterol 15% and 0.5% ATTO 488-labeled DOPE). C) Krytox addition (9 mM) to the surrounding oil leads to dsGUV formation. The corresponding, representative confocal image (lower inset) shows fluorescence from lipids (DOPC 42.25%, POPC 42.25%, cholesterol 15% and 0.5% ATTO 488-labeled DOPE) visible at the periphery of the droplet. Reprinted from with permission from Haller* et al.*, 2018.*[86]

To provide a more detailed understanding of how the surfactant charge influences the transition from multicompartment system to dsGUV, 1.4 wt% PEG-based fluorosurfactant was mixed with various Krytox concentrations ranging from 0.15 to 15 mM (Figure 51). The produced SUV-containing droplets were examined for lipid bilayer formation and investigated for their stability. As presented in Figure 51, no interaction between the SUVs and the interface can be observed at a Krytox concentration of only 0.15 mM (category I), therefore leaving the multicompartment systems unaltered. Attraction of the lipids to the droplet periphery, observed by the bright ring in the confocal plane, occurred at Krytox concentrations higher than 0.75 mM. However, based on FRAP measurements and cryoSEM analysis (see following Section 5.1.3.2) dsGUV formation has been approved only for Krytox concentration higher than 7.5 mM (category IV), whereas the bright ring at the droplets periphery in Krytox concentrations of 0.75 and 1.5 mM were ascribed rather to multicompartment or SUV adhesion (category II).

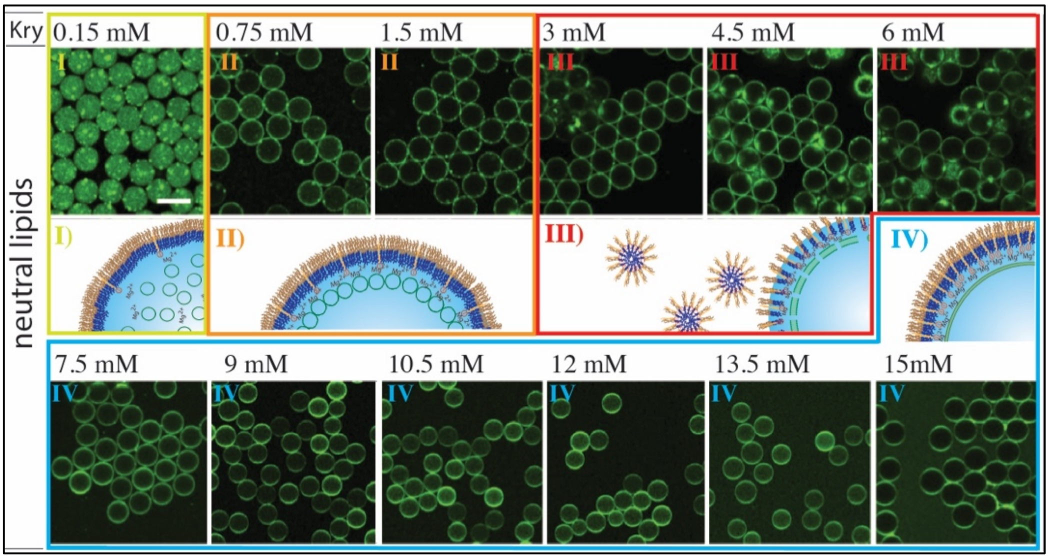

Figure 51: Effect of Krytox concentration on formation of dsGUVs. Representative confocal fluorescence images of lipid-containing microfluidic droplets at various Krytox concentrations from 0.15 mM to 15 mM. Green fluorescence from lipids (0.5% ATTO 488-labeled DOPE) encapsulated in the microfluidic droplets. Different Krytox concentrations, indicated on top of the fluorescence images, were mixed with 1.4 wt% PEG-based fluorosurfactant in the oil phase (HFE-7500 oil). Tris buffer supplemented with 10 mM Mg^{2+} *and 26.5 µM SUVs (DOPC 42.25%, POPC 42.25%, cholesterol 15% and 0.5% ATTO 488-labeled DOPE) were used as an aqueous phase for droplet formation. Based on fluorescence images and diffusion coefficients measured by FRAP (following section), lipid-containing droplets were classified into 4 categories: I) multicompartment systems, II) multicompartment adhesion, III) flocculation or fusion of the droplets and IV) to the formation of single compartments (dsGUVs). Note that the difference between compartment system II and IV can only be judged by FRAP or cryoSEM that will be described in the following section. Scale bar 50 µm. Reprinted from with permission from Haller* et al.*, 2018.*[86]

It is worth noting that partial clustering of SUVs can be observed at low Krytox concentrations, which may be attributed to Mg^{2+}-lipid interactions or Krytox domain formation at the droplet interface. Additionaly, at Krytox concentrations ranging between 3 and 6 mM flocculation of the droplets can be observed, which results in droplet fusion after few days (see Appendix, Figure SI 2) (category III). This observation correlates well with the IFT measurements (see Section 5.1.1.4), in which IFT values were increasing in the same range of PEG-surfactant-to-Krytox ratios. Flocculation is a process of destabilization of emulsion, e.g. due to low interfacial coverage.[184] In this concern a micellar exclusion due to surfactant interactions can explain this phenonema.[182,186] Interstingly, this ratio corresponds to a 1:1 ratio, considering the concentration of 3.8 – 5.7 mM for 1.4 wt% PEG-based surfactant, estimated by MS-analysis (Section 5.1.1.2).

To assess possible buffer conditions, the Mg^{2+} ion concentration for dsGUVs formation was reduced (neutral lipids) (Figure 52A) or exchanged by increased concentrations of K^+ ions (Figure 52B). A recruitment of lipids could be observed to the droplets periphery for Mg^{2+} ion concentration of 5mM and above, or in the presence of 50 and 100 mM KCl, however, no lipid accumulation at the droplet periphery was detected in lower Mg^{2+} concentration (2 mM) or in the absence of ions, independent of the Krytox concentration.

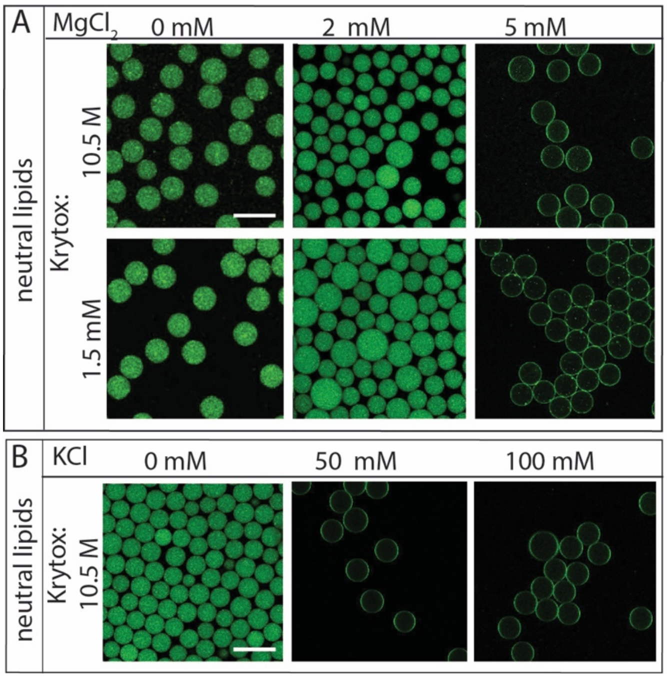

Figure 52: Representative images of fluorescence from SUVs (DOPC 42.25, POPC 42.25%, ATTO 488-labeled DOPE 0.5%, cholesterol 15%). (A) SUVs are dissolved in 30 mM Tris, pH 7.4 plus 2 mM or 5 mM $MgCl_2$ and droplets are stabilized by PEG-based fluorosurfactants (1.4 wt%) with 1.5 mM or 10.5 mM Krytox. Lipid interaction with the periphery could only be observed for neutral lipids in buffers containing 5 mM $MgCl_2$. (B) SUVs are dissolved in 30 mM Tris, pH 7.4 plus 0, 50 mM or 100 mM KCl and droplets are stabilized by PEG-based fluorosurfactants (1.4 wt%) and 10.5 mM Krytox. Lipid interaction with the periphery could be observed in buffers containing 50 mM and 100 mM. Scale bar 50 µm.

5.1.3.2. Investigation of Lipid Bilayer Formation in dsGUVs

Due to the nanoscale dimensions of the SUVs (68 nm in diameter according to DLS measurements (See Appendix, Figure SI 4), it is not possible to optically resolve whether a supported lipid bilayer has been formed (dsGUV, category IV in Figure 51) or whether SUVs are simply adhering to the surface (multicompartment adhesion, category II in Figure 51). Further in contrast to 2D, where the successful formation of a SLB can be checked by e.g. Atomic force microscopy (AFM) or monitored in real-time by means of QCM-D[262] (see Section 5.3.4.1 for assessment of 2D SLB formation by QCM-D) the methods for this 3D approach are rather limited. A possible method, however, to probe bilayer formation in 3D is via the lipid's diffusion coefficient, measured by means of fluorescence recovery after photobleaching (FRAP) (Figure 53A). In this regard, the here performed FRAP measurements revealed (see Table SI 3 in Appendix for exact values) that depending on the Krytox concentration, the measured diffusion coefficient values could be grouped into the two catgories: 1.1 ± 0.1 $\mu m^2/s$ for Krytox concentrations between 0.75 mM and 3 mM (category II, multicompartment adhesion, Figure 53C), and 5 ± 0.4 $\mu m^2/s$ for Krytox concentrations greater than 3 mM (category IV, dsGUVs, Figure 53B). The lower diffusion coefficient is ascribed to SUVs that are in active interaction with the droplet periphery and therefore exhibit slower diffusion.[263] The higher diffusion coefficient, on the other hand, correlates well with literature values for the diffusion of lipids within a fluid supported lipid bilayer in 2D.[264] This indicates that the SUVs have ruptured and a 3D supported lipid bilayer has been successfully formed.

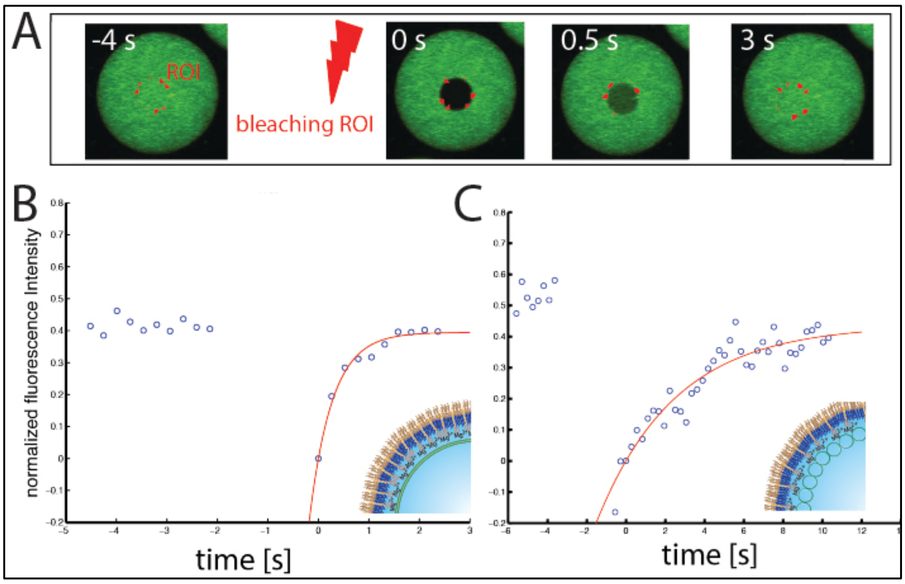

Figure 53: FRAP measurements of lipid diffusion in microfluidic droplets. A) Representative fluorescence images during FRAP measurements. B) and C) show exemplary recovery traces that makes it possible to distinguish between (B) dsGUVs (D= 5 ± 0.4 $\mu m^2/s$, n = 80)/category IV in previous section and (C) multicompartment adhesion (D= 1.1 ± 0.1 $\mu m^2/s$, n = 40)/category II in previous section. Reprinted from with permission from Haller et al.*, 2018.*[86]

Additionally, SUV-containing droplets, stabilized by 1.4 wt% PEG-based surfactant and either 0 mM, 3 mM or 10.5 mM Krytox were freeze-fractured and investigated by high-resolution cryo-SEM. As shown in Figure 54, a homogeneous distribution of SUVs, SUV adhesion and lipid bilayer formation at the periphery could be observed in presence of 0 mM, 3 mM or 10 mM Krytox, respectively. This supports the results obtained with confocal imaging and FRAP. Note that the fibrous-like connections between the SUVs can be attributed to artifacts related to cryo-SEM sample preparation and the following fracturing.

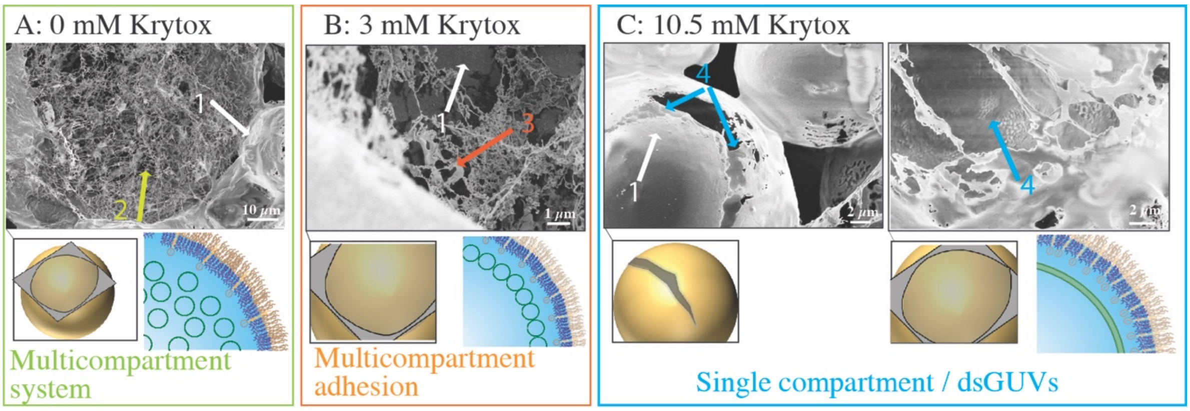

Figure 54: Representative cryo-SEM micrographs of freeze-fractured droplets. SUVs were encapsulated in droplets stabilized by 1.4 wt% PEG-based fluorosurfactant and 0 mM (A), 3 mM (B) and 10.5 mM Krytox (C). Arrows are indicating the surfactant shell (1), SUVs (2, 3) and lipid bilayer (4). Reprinted from with permission from Haller et al.*, 2018.*[86]

In various 2D studies, the formation of supported lipid bilayers, were shown to be influenced by the charge of the lipids.[262,265] Thus, in the following I will present the influence of lipid charge on dsGUV formation.

5.1.3.3. The Effect of Negative Lipid Charge on Compartment Formation

The charge density in lipid vesicles was controlled by the addition of negatively charged DOPG lipids (from 5% to 30%) to the neutral lipid composition used for SUV formation. Figure 55 shows representative confocal fluorescence images of negatively charged SUVs (from 5% to 30%) encapsulated within the droplets stabilized by 1.4 wt% PEG-based fluorosurfactants and Krytox at different concentrations (from 0.15 mM to 12 mM).

As expected, a greater amount of Krytox (3 mM) was needed to attract negatively charged SUVs to the droplet interface than if neutral lipids were used (0.75 mM). This might be due to the fact that higher attraction forces are needed to overcome the repulsion of the negatively charged SUVs.[265] Therefore, a higher density of Mg^{2+} ions was required on the inner droplet interface, which in turn corresponds to a higher Krytox concentration in the oil phase.

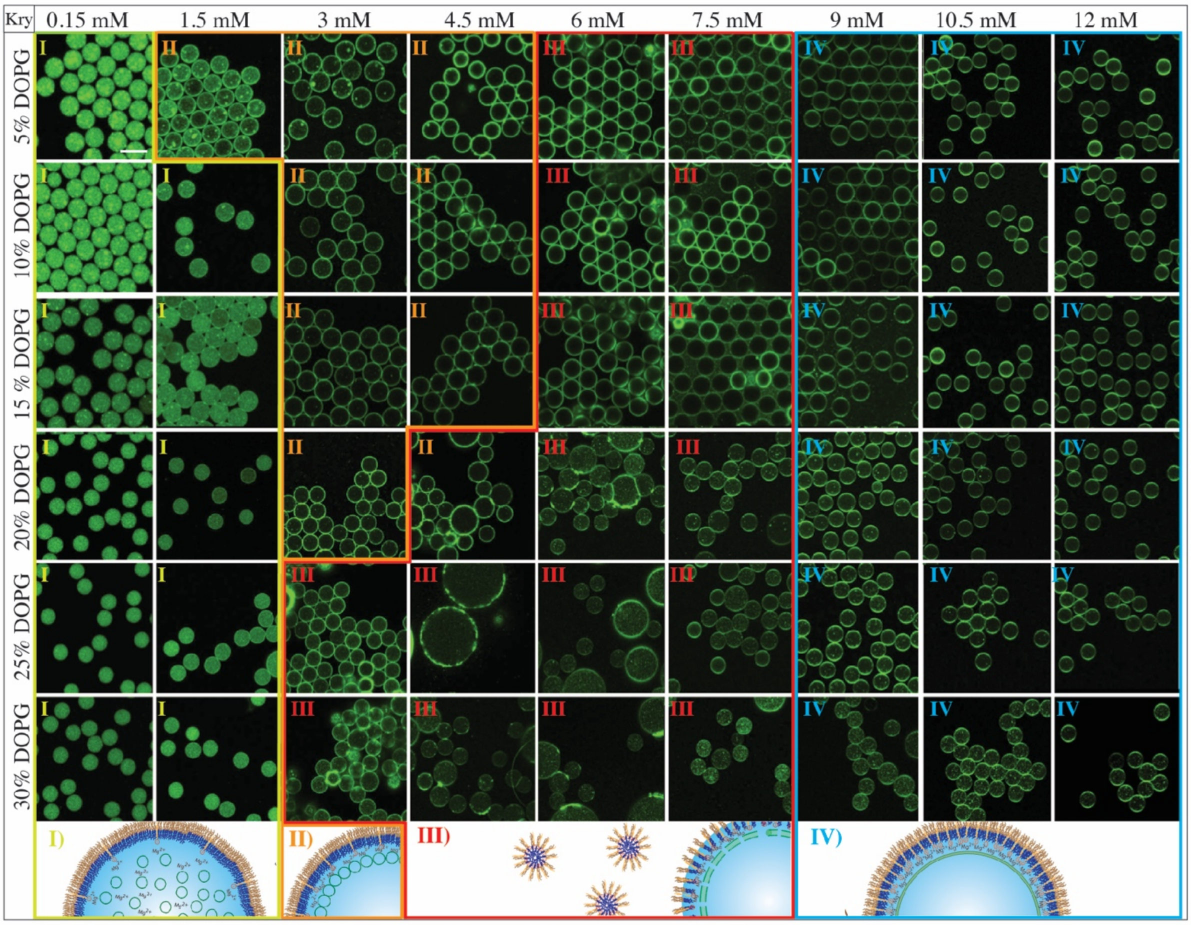

Figure 55: Phase diagram of representative confocal images showing the effect of lipid charge and Krytox concentration on the formation of a supported lipid bilayer onto the droplets shell. To evaluate the influence of negatively charged DOPG lipids on dsGUV formation, Tris buffer containing both 10 mM Mg^{2+} and SUVs with different lipid compositions (cholesterol 15%, DOPG 5% – 30%, indicated on the left, DOPC x%, POPC x%, x=rest) was encapsulated in the droplets stabilized by surfactants which contained 1.4 wt% PEG-based fluorosurfactants and various Krytox concentrations as indicated above the fluorescence images. Based on fluorescence images and diffusion coefficients measured by FRAP, lipid-containing droplets were classified into 4 categories: I) a multicompartment system II) multicompartment adhesion, III) flocculation or partial fusion of the droplets, or IV) the formation of a single compartment per droplet (dsGUV). Scale bar 50 µm. Reprinted from with permission from Haller et al.*, 2018.*[86]

FRAP measurements, performed on the lipids (30% DOPG) close to the droplet's periphery, revealed diffusion coefficients of 1 ± 0.1 and 4.2 ± 0.3 μm^2/s in the droplets stabilized by surfactants containing 1.5 and 10.5 mM Krytox, respectively (see Appendix, Table SI 3). These values refer to multicompartment adhesion and dsGUV, respectively. Just like in the case of the droplets containing neutral lipids, flocculation was observed at Krytox concentrations between 3 to 7.5 mM. Additionally, droplet coalescence occurred when the encapsulated vesicles contained more than 15% DOPG lipids.

Emulsion instability due to certain Krytox- to- PFPE–PEG–PFPE surfactant mixtures was similarly reported in a study of Matochko and colleagues, where they induced the breakage of the emulsion and the release of the content via the addition of Krytox.[266]

Further, partial leakage of lipids into the oil phase was observed at Krytox concentrations above 12 mM (See appendix Figure SI 3). This is in accordance with a work from Gruner *et al.* where they showed that the extraction of an encapsulated fluorophore into the oil phase was based on the PFPE–PEG–PFPE surfactant-to-Krytox ratio that was used to stabilize microfluidic water-in-oil droplets.[250] Note that reduced lipid leakage was detected when the lipids contained more than 20% DOPG (See appendix Figure SI 5).

For dsGUV formation with neutral and negatively charged SUVs, the presence of salt is required to screen the negative charge of Krytox by a cation layer. Thus, effectively, leading to positive charges on the surface and the an electrostatic attraction of the neutral – namely zwitterionic [261]– and negatively charged SUVs.[267] How positively charged SUVs behave in that system, will be described in the following.

5.1.3.4. The Effect of Positive Lipid Charge on Compartment Formation

A pronounced tendency towards SLB formation of positively charged lipids on negatively charged surfaces has been already shown in 2D.[267,268] Thus, DOTAP lipids (30%) were mixed with the neutral lipids to obtain positively charged lipid vesicles. Figure 56 shows representative confocal fluorescence images of 30% positively charged SUVs encapsulated within the droplets stabilized by 1.4 wt% PEG-based fluorosurfactant and Krytox at different concentrations (between 1.5 mM and 12 mM). Interaction of the lipids with the droplets periphery could be observed for Krytox concentrations above 1.5 mM.

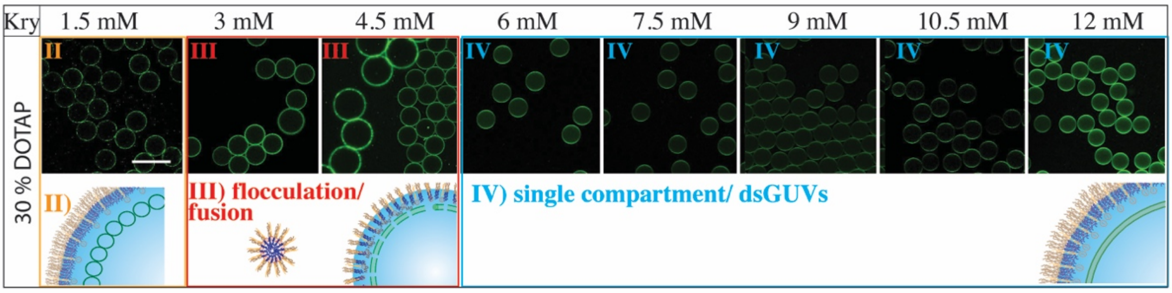

Figure 56: Representative confocal images showing the effect of Krytox concentration on positively charged SUVs (DOPC 27,25%, POPC 27,25%, cholesterol 15%, DOTAP 30%. Atto455 DOPE 0.5%), which were dissolved in Tris buffer and encapsulated in droplets stabilized by surfactants which contained 1.4 wt% PEG-based fluorosurfactants and various Krytox concentrations as indicated above the fluorescence images. Based on fluorescence images and diffusion coefficients measured by FRAP, lipid-containing droplets were categorized into II) multicompartment adhesion, III) flocculation or partial fusion of the droplets, or IV) the formation of a single compartment per droplet (dsGUV). Scale bar 50 μm.

FRAP measurements performed on the lipids in proximity to the droplet's periphery revealed diffusion coefficients of 4.5 ± 0.3 $\mu m^2/s$ for Krytox concentrations above 6 mM, indicating that the positively charged SUVs fused to create a supported lipid bilayer (see Appendix Table SI 4).[263]

Similarly, as for neutral and negatively charged lipids some flocculation and fusion of droplets can be observed in Krytox concentrations ranging from 3 to 4.5 mM Krytox due to micellar exclusion,[182,186] indicating that this effect is probably independent on encapsulated lipid vesicles. Note that positively charged SUVs were encapsulated in the absence of $MgCl_2$. Importantly, whereas negatively charged or neutral SUVs require the presence of Mg^{2+} ions, no interaction of positively charged SUVs with the periphery could be observed when Mg^{2+} was present in the buffer, independently of the Krytox concentrations. Mg^{2+} ions screen the negative charge of the Krytox and thereby prohibit electrostatic interaction of the positively charged SUVs with the surfactant shell.

5.1.3.5. The Creation of Multicompartment dsGUVs

The distinct behavior of positively and negatively charged SUVs in different buffer conditions allows to trigger a complementary response of the encapsulated SUVs. For this aim, Atto 488-labeled negatively (DOPG) and Rhodamine-labeled positively charged (DOTAP) SUVs were combined in Tris buffer without $MgCl_2$ and encapsulated into droplets stabilized by 10.5 mM Krytox.

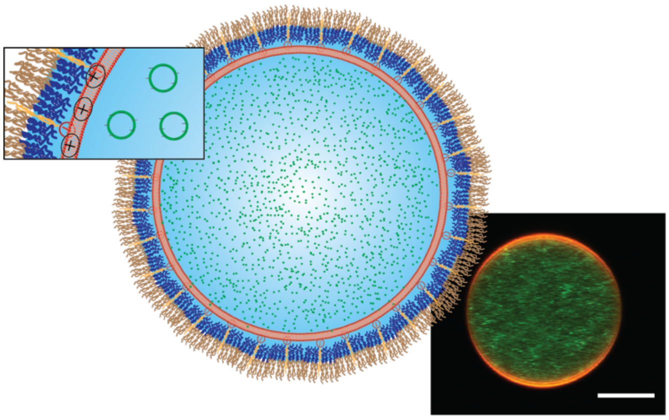

Figure 57: Sketch and confocal fluorescent image of a multicompartment dsGUV containing Atto488-labeled negatively and Rhodamine-labeled positively charged SUVs (of DOPC 27.25%, POPC 27.25%, cholesterol 15%, plus either DOPG 30% and ATTO 488-labeled DOPE 0.5%, or 30% DOTAP and Rhodamine-labeled DOPE 0.5%) in Tris buffer without $MgCl_2$, stabilized by 10.5 mM Krytox. Scale bar 10 µm.

While these conditions allowed for an interaction of positively charged SUVs with the interface, the interactions of negatively charged SUVs with the surfactants were prohibited (Figure 57).

Hence, this method allows for reconstitution of morphological lipid structures, mimicking the eukaryotic cell membrane and internal organelles.

Besides the negatively charged Krytox surfactant, a positively charged amine-terminated surfactant can be used to provide charges to the droplets' interface. In the following, the effect of this positively charged surfactant is investigated.

5.1.3.6. The Effect of a Positively Charged Interface on Lipid-Compartment Systems

To generate a positively charged droplet interface a block copolymer surfactant with a positively charged functional group (amine, NH_3) was synthesized by Dr. Jan-Willi Janiesch based on a previously published protocol (see Section 3.2.4). This surfactant comprises a PFPE hydrophobic part connected via the amid group to the hydrophilic amine-terminated PEG molecule, thus providing positive charge at the droplet's inner interface at pH of 7.4. As a first step, partitioning experiments were performed to rule out possible presence of Krytox molecules in the amine-terminated surfactants (see Appendix, Figure SI 1B). Then 5 mM of this surfactant in HFE-7500 oil was used to stabilize droplets containing neutral, negatively (30% DOPG) and positively charged (30% DOTAP) SUVs (Figure 58). Leakage of negatively charged lipids was observed in the oil phase after few minutes independently on presence or absence of $MgCl_2$.

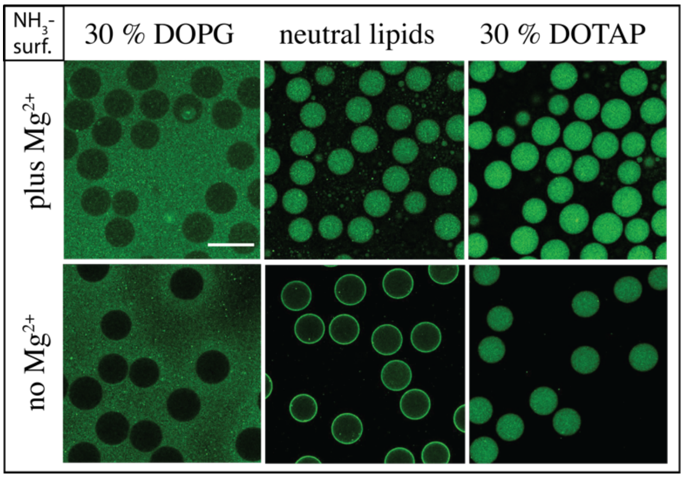

Figure 58: Confocal images showing fluorescence of Atto488-DOPE. Neutral, negatively (DOPG) and positively charged (DOTAP) SUVs (DOPC 27.25% or 42.25%, POPC 27.25% or 42.25%, cholesterol 15%, DOTAP or DOPG 30% or 0%. Atto488-DOPE 0.5%) dissolved in Tris buffer with and without $MgCl_2$ are encapsulated in droplets stabilized by 5 mM amine surfactant. Scale bar 50 μm.

This may be attributed to the strong and direct electrostatic attraction force with the surfactant molecules. Neutral and positively charged lipids were retained within the droplet. In the case of neutral lipids, adhesion of SUVs at the droplets periphery was observed only in the buffer lacking Mg^{2+} ions. This can be explained by the zwitterionic nature of neutral phospholipids[269], attracting Mg^{2+} ions, which prevent the interactions with the positively charged surface. Not surprisingly, no interactions with the periphery could be observed in case of positively charged SUVs independently on Mg^{2+} ions.

To improve retention and to tune droplet interface charge density, the interactions between the SUVs and the surfactant shell of the droplet, the amine surfactant was mixed with the inert PEG-based fluorosurfactant. Figure 59 shows representative fluorescence images of neutral and negatively charged lipids encapsulated within droplets stabilized by 1.4 wt% of inert PEG-based surfactant and different amounts of amine surfactant (from 3 mM to 10 mM). Note that for these experiments a Tris buffer without Mg^{2+} ions was used. Positively charged lipids are not presented here since they stayed unaltered in the multicompartment system independent on amine surfactant concentration or the here used buffers.

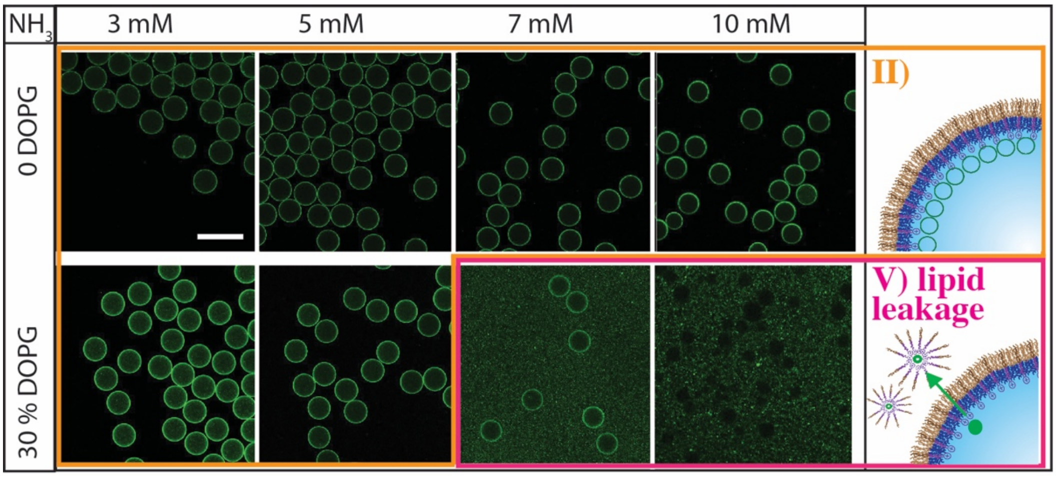

Figure 59: Confocal images showing the effect of amine surfactant concentration on encapsulated SUVs within water-in-oil droplets. SUVs (DOPC 27.25% or 42.25%, POPC 27.25% or 42.25%, cholesterol 15%, DOPG (negatively charged) 0% or 30%. Atto488-DOPE 0.5%) were dissolved in Tris buffer and encapsulated in droplets stabilized by surfactants which contained 1.4 wt% PEG-based fluorosurfactant and various concentrations of amine surfactant as indicated above the fluorescence images. Based on fluorescence images and diffusion coefficients measured by FRAP, compartment systems were categorized into II) multicompartment adhesion, V) lipid leakage. Scale bar 50 µm.

The encapsulated neutral and negatively charged SUVs were attracted to the periphery of the droplets stabilized by surfactants containing 3 mM or more amine-terminated surfactants in addition to 1.4 wt% inert PEG-based surfactant. Negatively charged lipids could be retained in the aqueous phase of the droplet, stabilized by 5 mM or less amine surfactant. For more than 5 mM amine surfactant, negatively charged lipids leaked out into the oil phase.

FRAP measurements performed on lipids close to the periphery, revealed diffusion coefficients no larger than 2.2 ± 0.2 $\mu m^2/s$ (0% DOPG, 7 mM amine surfactant) for none of the measured samples. This indicates that, probably, no fusion to a lipid bilayer took place.

The ultimate proof of the successful formation of dsGUVs is the possibility to subsequently release the assembled GUVs from the stabilizing surfactant shell into an aqueous phase. The following sections clarifies the influence of lipid and surfactant charge on GUV release.

5.1.4. GUV Release into a Physiological Environment

The continuous lipid bilayer within the dsGUVs makes the release of the GUVs from the surfactant shell and oil phase into a physiological buffer possible.[16] Towards this end, a bulk release approach (see Methods Section 4.5.5), which allows for the simultaneous generation of several hundred thousand free-standing GUVs within a few minutes, was employed (Figure 60). In this approach, the produced dsGUVs were collected in a micro tube and supplemented with an osmolarity-matched aqueous release buffer. Subsequently, a de-emulsifier (perfluoro-1-octanol) was added in order to destabilize the droplet's surfactant shell, thereby, allowing for the release of GUVs into the aqueous phase.

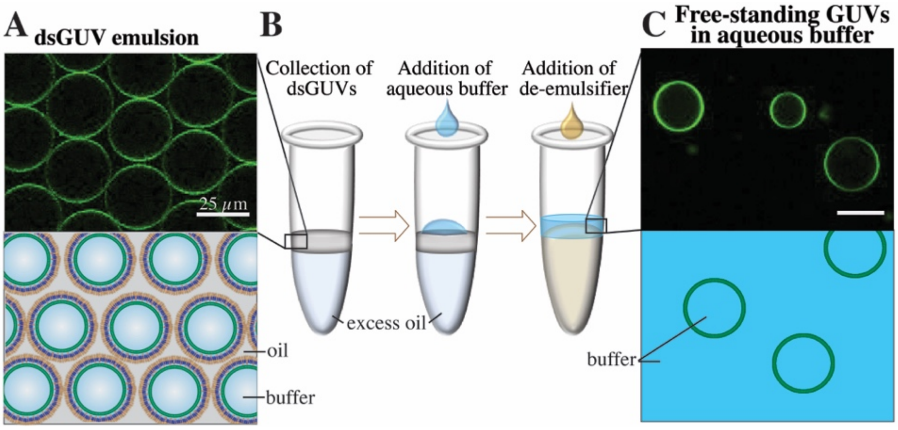

Figure 60: Bulk method to release free-standing GUVs from the stabilizing polymer shell and from the oil phase into the aqueous phase. A) Representative fluorescence image and sketch of dsGUVs (DOPC 34.75%, POPC 34.75%, cholesterol 15%, DOPG 15% and 0.5% ATTO 488-labeled DOPE, 30 mM Tris, 10 mM Mg^{2+} ions) in the oil phase (containing 1.4 wt% PEG-based fluorosurfactant and 9 mM Krytox). B) For release, droplets were collected inside a micro tube and an osmolarity-matched buffer (30 mM Tris, 10 mM Mg^{2+} ions) was pipetted onto the droplet emulsion. Upon addition of a de-emulsifier (perfluoro-1-octanol), GUVs were released from the oil phase into the aqueous phase. C) A representative fluorescence image and sketch of free-standing GUVs after release. Scale bar 25 μm. Reprinted from with permission from Haller et al.*, 2018.*[86]

The successful release of the GUVs was, however, only possible under certain conditions that correlated with the successful fusion of the vesicles to a lipid bilayer (see Section 5.1.3.2 for dsGUV investigations) but seemed to be also influenced by the retention of lipids within the droplet and the magnitude of electrostatic interactions between surfactants and lipid bilayer. These influencing factors will be discussed in more detail in the following sections.

5.1.4.1. Influence of Negative Surfactant Charge on GUV Release

In the dsGUVs assembly approach, in which Krytox molecules were used towards the attraction of SUVs to the periphery, the release efficiencies of the assembled GUVs reached values of up to 9% of the initial amount of produced dsGUVs were obtained. This is significant given the kHz production rates of dsGUVs (i.e., 2.5 x 10^6 dsGUVs are produced within 10 min) that, in turn, lead to the overall yield of approximately 2.25 x 10^5 GUVs within few minutes.

A successful release is, however, only possible upon the formation of a continuous bilayer. This, in turn, depends on Krytox concentration in the oil phase and on lipid charge (see Figure 61) as discussed in previous sections. If the attraction force between SUVs and surfactants are too low, SUVs only attach, but not rupture to form a lipid bilayer (multicompartment adhesion). On the other side, if the adhesion strength is too high, the lipid bilayer may form, however, lipid leakage into the oil phase may appear or GUVs may rupture during release.

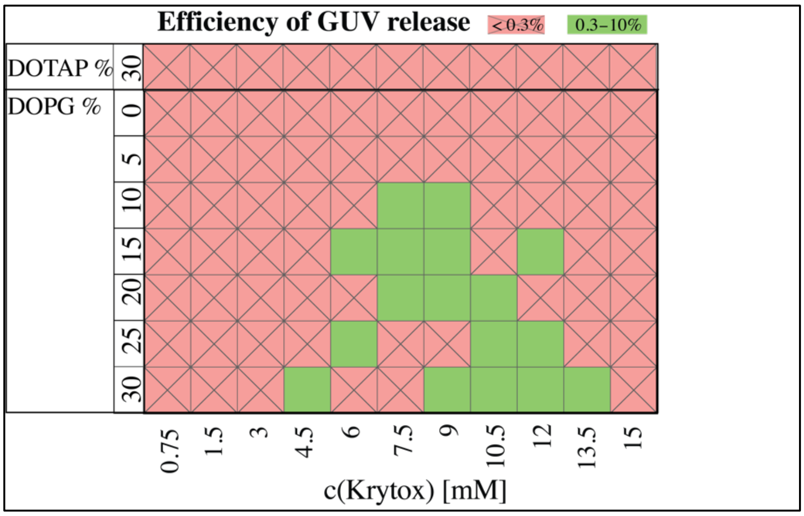

Efficiency of GUV release 🟥 <0.3% 🟩 0.3–10%

		0.75	1.5	3	4.5	6	7.5	9	10.5	12	13.5	15
DOTAP %	30	🟥	🟥	🟥	🟥	🟥	🟥	🟥	🟥	🟥	🟥	🟥
DOPG %	0	🟥	🟥	🟥	🟥	🟥	🟥	🟥	🟥	🟥	🟥	🟥
	5	🟥	🟥	🟥	🟥	🟥	🟥	🟥	🟥	🟥	🟥	🟥
	10	🟥	🟥	🟥	🟥	🟥	🟩	🟩	🟥	🟥	🟥	🟥
	15	🟥	🟥	🟥	🟥	🟩	🟩	🟩	🟥	🟩	🟥	🟥
	20	🟥	🟥	🟥	🟥	🟥	🟩	🟩	🟩	🟥	🟥	🟥
	25	🟥	🟥	🟥	🟥	🟩	🟥	🟥	🟩	🟩	🟥	🟥
	30	🟥	🟥	🟥	🟩	🟥	🟥	🟩	🟩	🟩	🟩	🟥

Figure 61: Efficiency of GUV (only size >20 µm) release from dsGUVs depends on the Krytox concentration in the oil phase (HFE-7500 plus 1.4% PEG-based fluorosurfactants) and the type and concentration of lipid charge (negatively charged DOPG and positively charged DOTAP) in the lipid composition. GUVs < 20 µm were not taken into account. Reprinted from with permission from Haller et al.*, 2018.*[86]

Efficient GUVs release was observed from the dsGUVs containing more than 10% negatively charged lipids and at Krytox concentrations between 6 mM to 13.5 mM. Higher Krytox concentrations were necessary when GUVs contained more negatively charged lipids. As expected, release was not obtained from droplets stabilized by a surfactant solution containing less than 3 mM Krytox, because no continuous supported lipid bilayer could form under these conditions (multicompartment adhesion, see Section 5.1.3.2 for dsGUV investigations). Unfortunately, release efficiency of GUVs consisting of positively charged and neutral lipids was significantly lower (below 0.3%) even though diffusion coefficients correlated with the presence of a lipid bilayer. In the case of neutral lipids, this might be attributed to the partial leakage of lipids into the oil phase predominantly observed for neutral lipids (See Appendix,

Figure SI 5). Whereas lipid leakage and release efficiency of neutral GUVs could be improved by replacing the 10 mM $MgCl_2$ with 50 – 100 mM KCl, positively charged lipids could not be released in any of the tested buffer conditions (water, KCl (data not shown)). The explanation for this could be, in my opinion, the strong and direct interaction with the charged Krytox, causing GUV rupture during the release process. However, since the release processes depends critically on counter ions present in the buffers, salt and buffer conditions may have to be investigated and adjusted further towards successful release of positively charged GUVs.

The release of the GUVs from the surfactant shell and the oil phase into a physiological environment paves the way towards future applications in which synthetic cell interactions with a physiological environment are crucial. Further the here presented method is a great benefit for the scientific community as it describes a simple way to create GUVs in high yield in a variety of possible buffers and lipid compositions, that are not allowed in case of standard GUV preparation methods as electroformation.

5.1.4.2. Influence of Positive Surfactant Charge on GUV Release

In the context of dsGUVs formation, positively charged amine-terminated surfactants have a strong potential and provide flexibility in applications since no addition of ions would be necessary (see Section 5.1.3.6, Figure 59). However, no release of GUVs has been achieved with a positively charged surfactant. This is in agreement with the relatively low diffusion coefficients (see Appendix, Table SI 5) obtained by FRAP measurements. Thus, one can assume that the interactions between the surfactants and the SUVs might have been too weak preventing the successful formation of continuous bilayers. Note that more experimental conditions should be tested in future as a change in buffer conditions may lead to successful formation of dsGUVs.

5.1.4.3. Release of Multicompartment Systems

The multicompartment systems described in Section 5.1.2 (Figure 50A) are solely confined by the droplet polymer shell; thus, their observation and analysis are performed directly in the oil/surfactant environment.

In fact, the presented approach also allows for the transfer of a multicompartment system into a physiological environment. Therefore, however, the internal aqueous volume requires to be additionally enclosed by an outer lipid bilayer (multicompartment dsGUV, see Figure 62A). To obtain this, I encapsulated a SUV-based multicompartment system inside a dsGUV using experimental conditions similar to those for single-compartment dsGUV formation (described in 4.5.1) (Figure 62). However, an excess amount of encapsulated SUVs (greater than that required for just the formation of a continuous bilayer) was necessary to obtain a spherical lipid bilayer and additional free-floating SUVs. Due to the continuous lipid bilayer, this lipid structure can be released from the surfactant shell and the oil phase into an aqueous buffer.

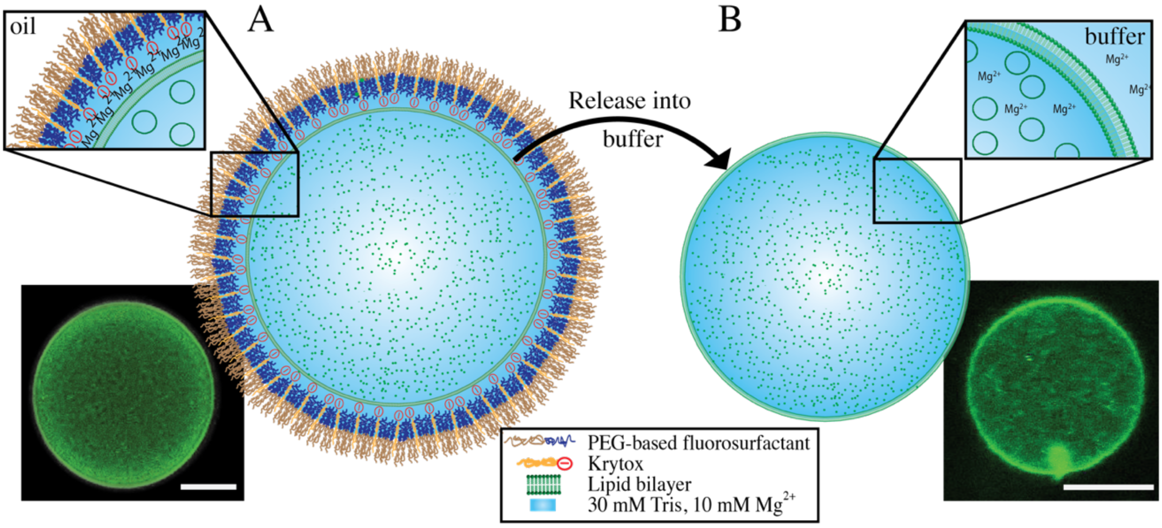

Figure 62: Schematic representation and confocal fluorescent images of multicompartment systems enclosed by a dsGUV (left) or a free-standing GUV (right). Lipid composition: DOPC 27.25%, POPC 27.25%, DOPG 30%, cholesterol 15%, Atto488-DOPE 0,5% in Tris buffer, 10 mM Mg^{2+} *A) An excess of SUVs (53 µM) was encapsulated in a water-in-oil droplet stabilized by PEG-based fluorosurfactants with 9 mM Krytox. This led to the formation of a lipid bilayer inside the surfactant shell. Excess SUVs stayed in the droplet volume, resulting in a multicompartment dsGUV. The lower inset shows a representative confocal fluorescence image of green fluorescence emitted by labeled lipids. B) Released GUV-enclosed multicompartment system in an osmolarity-matched aqueous buffer. The lower inset shows a representative confocal fluorescence image of green fluorescence emitted by labeled lipids. Scale bar 20 µm. Reprinted from with permission from Haller* et al.*, 2018.*[86]

Once the multicompartment GUV is released into a physiological buffer, it resembles greatly the architecture of a eukaryotic cell that has a similar sized outer lipid bilayer and within this cell body organelle structures. When aiming to mimic a living cell, this compartment system sets the first morphological step towards the combination of distinct reaction spaces within an outer larger confinement. In this regard, a similar system has been seen by Bolinger *et al.* In this study, SUVs were encapsulated inside larger lipid vesicles by hydrating a dried lipid film with an SUV mixture. Remarkably, it was possible to perform distinct and successive chemical reactions within this multicompartment system through the rupture of encapsulated SUVs comprising different phase transition temperatures.[136]

In the approach presented in my thesis, this could be feasible as well by picoinjecting a distinct SUV mixture into preformed dsGUVs or by selectively recruiting distinct SUVs to the periphery based on the different lipid charge (see Section 5.1.3.5). This highlights the great and versatile potential of the lipid-based compartment system in oil or in physiological buffers for future experiments.

5.1.4.4. Investigation of Released GUVs

In the following, I will characterize the released GUVs in respect to their size distribution, purity and unilamellarity.

5.1.4.4.1. Size Distribution of Released GUVs

Using droplet-based microfluidic a very monodisperse production of dsGUV can be achieved (size 29.1 ± 0.1 µm, see Figure 63 grey bar). The released GUVs, however, show a wider size distribution range, depicted in the histogram of Figure 63. This means that during the bulk release fusion and splitting of destabilized dsGUVs may happen. Splitting and fusion can be minimized by increasing the emulsion-aqueous phase interface during the release process in the micro tube (Figure 60). Alternatively, a microfluidic release device, where GUVs are released one by one can be used.[16]

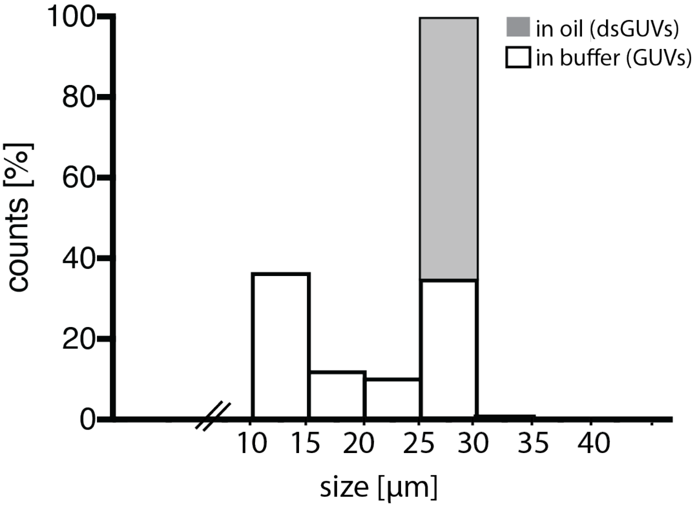

Figure 63: Size distribution of dsGUVs in the oil phase (grey column, n =187) and after the release into the water phase (GUVs, white columns, n = 190). The lipid composition comprises DOPC 27.25%, POPC 27.25%, ATTO 488-labeled DOPE 0.5%, cholesterol 15% and DOPG 30%. Note that GUVs smaller than 10 µm were not taken into account. Reprinted from with permission from Haller et al., *2018.*[86]

5.1.4.4.2. Purity Investigation of Released GUVs

To check the released GUVs for contaminations of oil or surfactant molecules, FRAP measurements and Raman analysis were implemented.

FRAP measurements performed on released GUVs consisting of 30% negatively charged lipids revealed diffusion coefficients of 3.5 ± 1 μm²/s. This diffusion coefficient is in good accordance to GUVs created by electroformation,[16] suggesting that no contaminations affecting bilayer fluidity are present in the samples.

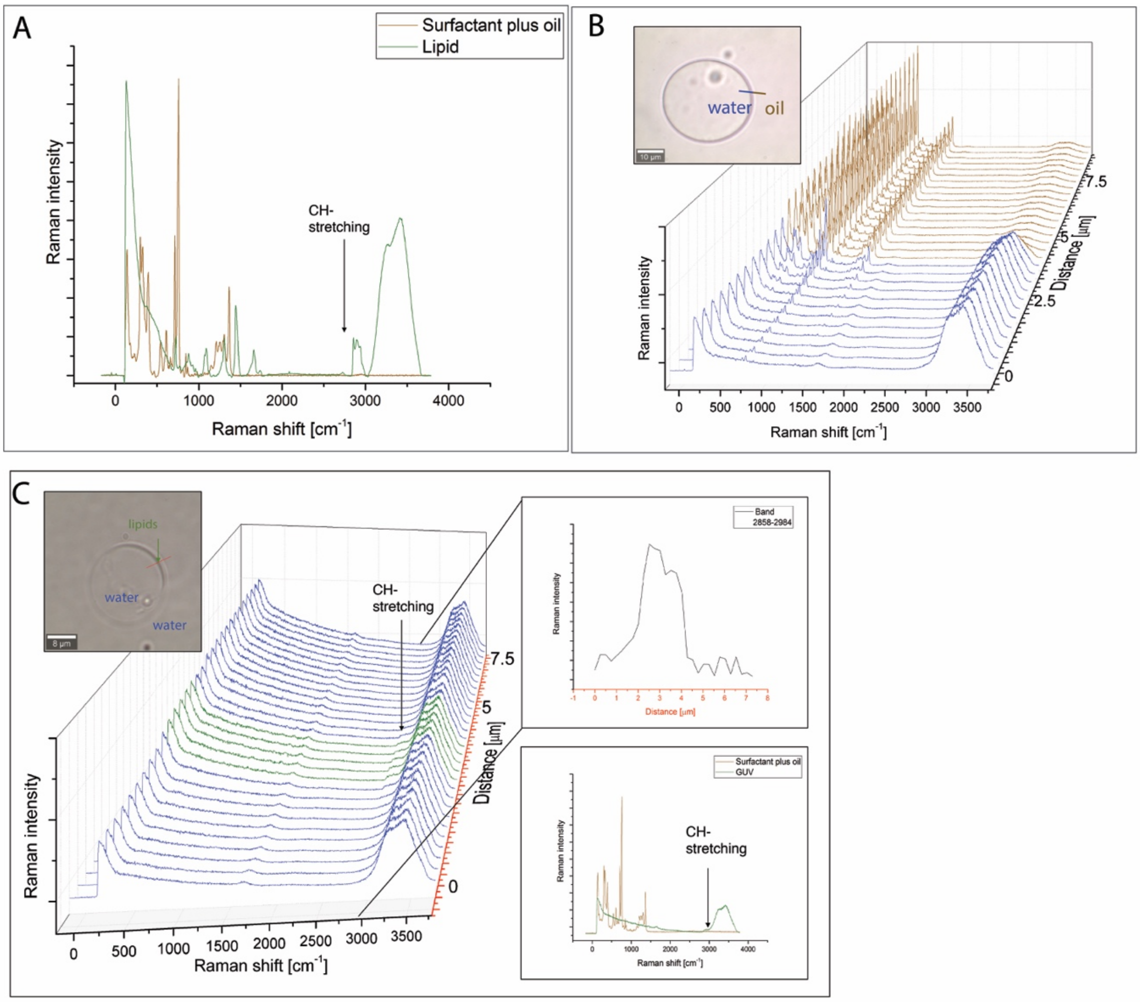

Figure 64: Raman spectra performed to investigate the purity of released GUVs. (A) Raman spectra collected from the solution of custom-made triblock surfactants in FC40 oil (brown) and from the SUVs (green), consisting of 40% DOPC, 40% POPC and 20% cholesterol. (B) Raman spectra collected across the water-oil interphase of the single dsGUV (see insert bright-field image) show characteristic water and oil peaks. In sake of clarity of presentation, the spectra collected from the oil and water phases were brown and blue colored, respectively. (C) Representative Raman spectra collected across the water-lipid interphase of the released GUV (insert bright-field image). In sake of clarity of presentation, the spectra collected from the water phases and the lipid bilayer were blue and green colored, respectively. Importantly, no characteristic peaks of the oil/surfactant were detected. Reprinted with permission from [16].Copyright © 2017, Springer Nature.

Furthermore, Raman spectra were collected from the surfactants in the oil, the SUV solution, as well as line scans were performed across the boundary layer of dsGUVs and of the released GUVs (Figure 64).

The collected Raman spectra from the SUV and from the surfactant solution showed both characteristic footprint structures (Figure 64A): SUV spectrum revealed a carbon- hydrogen stretching vibration of lipid tails (between 2800 and 3000 cm^{-1})[270] and the spectrum for the surfactants in FC40 oil, revealed similar peaks as published before.[271] These spectra were then compared to the Raman spectra collected across the interface boundary of the dsGUVs (Figure 64B) and the released GUVs (Figure 64C). In case of dsGUVs Raman spectra collected from the aqueous phase showed a large water peak between 3000 and 3500 cm^{-1} whereas the oil phase showed the characteristic spectrum of the surfactant and oil measured before. Spectra collected from the released GUVs show a large water peak and at the interface boundary of the GUV a CH-stretching peak referring to the lipid bilayer.[270] No peaks of surfactant or oil residues could be detected.

5.1.4.4.3. Assessment of Unilamellarity of Released GUVs

Giant vesicles produced by methods as e.g. gentle hydration are mainly found to possess multilamellar lipid membranes.[272] This can be disadvantageous [126] and can limit their application when it comes to e.g. transmembrane proteins in adhesion studies or other membrane-dependent functions.

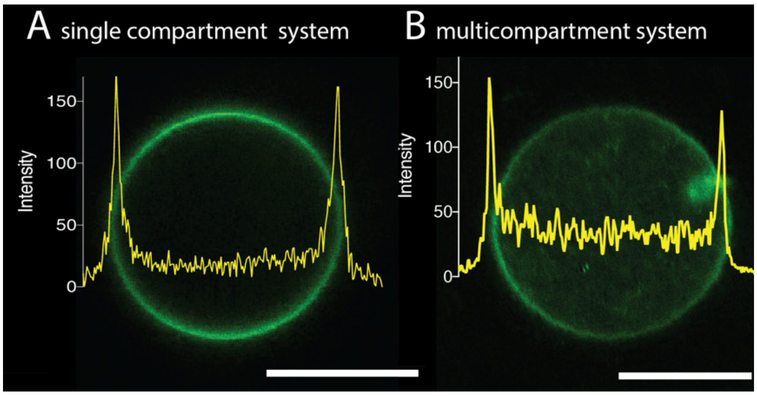

Figure 65: Representative confocal fluorescence images of (A) a single and (B) a multicompartment system released into the water phase. Images were taken under the same acquisition conditions. Fluorescent intensity profiles along the cross section of the GUVs are plotted in yellow. Fluorescence signal of 0.5% Alexa 488-labeled DOPE lipids in the lipid compositions (DOPC 27.25%, POPC 27.25%, ATTO 488-labeled DOPE 0.5%, cholesterol 15% and DOPG 30%). Scale bars, 10 µm. Reprinted from with permission from Haller et al.*, 2018.*[86]

In the approach presented in this thesis, a multilamellarity can be excluded, as the amount of encapsulated lipids is calculated and precisely adjusted to cover the inner surface of a 30 μm droplet with one bilayer. However, in case of the multicompartment GUVs presented in Section 5.1.4.3 there is an excess amount of lipids, thus, a multilamellar structure cannot be ruled out per se.

Thus, the lamellarity of the lipid structure was further investigated. In this concern, a time-lapse microscopy analysis (2 h) of the multicompartment system was performed. Here no accumulation of lipids on the periphery was observed. This indicates that the SUVs remain stable within the GUV lumen. Moreover, to exclude possible multilamellar structures the fluorescence intensity profiles of free-standing multicompartment- and single -GUVs, which were prepared and released the same way, were compared. The measurements revealed similar fluorescence intensity profiles at the boundaries of the released multicompartment GUV and the single GUVs, indicating unilamellarity also in case of the multicompartment system (Figure 65).

5.1.4.4.4. Manipulation of Released GUVs by Unbalanced Ionic Conditions

Even though, multilamellar structures have been excluded in the previous section, when investigating the released GUVs via fluorescence microscopy, it appears that, occasionally, released GUVs reveal some localized lipid accumulations. This may be due to lipids from ruptured GUVs that stick to the outer leaflet of the lipid bilayer. These excess lipids can be seen as agglomerates or as tentacle-like structures at the surface of the GUV. In equilibrated ion conditions these GUV structures are rare, however these tubular structures appear more often when increasing the mismatch between ionic conditions inside and outside GUVs, e.g. decreasing or increasing $MgCl_2$ in the ambient buffer. Figure 66 shows representative fluorescent images from released GUVs in hypotonic (A) and hypertonic (B) conditions.

It appeared that lower $MgCl_2$ concentrations in the external GUV space (pure water as release buffer) lead to more prevalent tubular structures at the outer lipid leaflet whereas higher $MgCl_2$ concentrations (15 mM $MgCl_2$ in release buffer) lead to tubular structures inside the GUVs.

GUVs with an excess membrane area and non-spherical shapes have already been reported earlier, as a result of osmotic deflation[26] or based on the depletion effect of encapsulated macromolecules (depletion effect is described in respect to actin filament bundling in Section 1.3.9.1).[121,139] Also tubular structures have been reported in GUV morphology studies based on the mismatch of the expansions of the two bilayer leaflets. This could be due to asymmetry of the lipid composition of the two membrane leaflets,[26] local pH changes[24] or asymmetric insertion of membrane proteins.[273] A lateral tension in one of the leaflets was also shown to be generated through mismatching buffer conditions between the GUV interior and exterior and thus, through a different ion adsorption on the two surfaces.[274] In this regard, simulations showed that ion binding to phospholipids leads to a tighter packing of the membrane.[275,276]

Moreover, it was estimated that an increase of Ca^{2+} ions could lead to a decrease in area per lipid of 3 – 10%.[276]

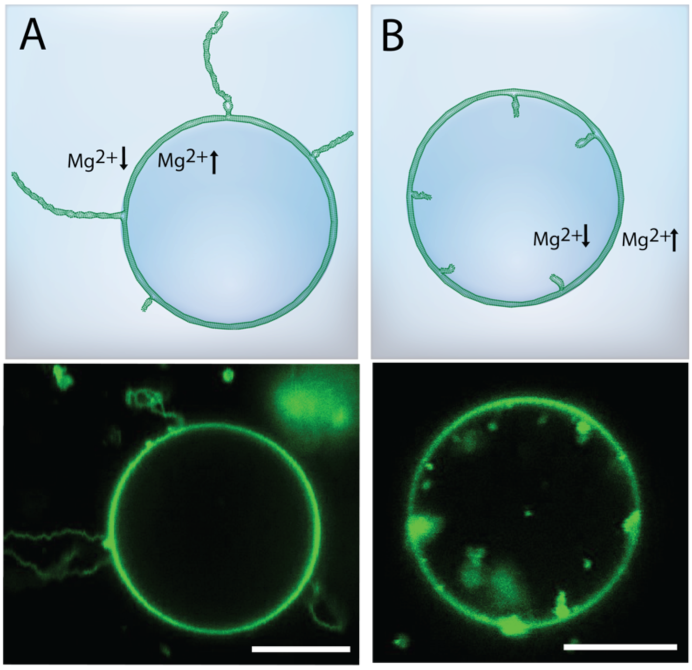

Figure 66: Representative fluorescence images from released GUVs in unbalanced ionic conditions. (A) hypotonic conditions lead to increase in tubular structures at the outer bilayer leaflet. (B) hypertonic conditions lead to tubular structures reaching into the droplets interior. Scale bar 10 µm.

For GUVs with a size of 20 µm, as presented in this thesis, this theoretically means that when there is a decrease in one of the leaflet areas of e.g. 3%, the mismatch would provide an excess membrane area of ≈ 37 μm^2. This could theoretically form tubular structures of around 235 µm in length, assuming a tube diameter of 50 nm (for calculations see Appendix, Figure SI 6).[277] This may be in agreement with the observations shown in Figure 66.

Note that such tubular structures has been also seen as a result of trans-bilayer asymmetry of the lipid composition evolving due to negatively charged ITO glasses during electroformation.[26] In case of released GUVs, an asymmetry of the leaflets can neither be excluded, since the charged droplet interface may as well lead to a biased arrangement of lipids in the two leaflets during dsGUV formation. This may need to be further investigated in future.

The GUVs with tubular structures are an excellent model to resemble eukaryotic organelle morphology like the membrane of mitochondria, the Golgi apparatus or of the smooth endoplasmic reticulum where the membrane is similarly folded.

Part I: Summary

In part I of the results I showed the creation of multicompartment and single compartment (dsGUV) systems within water-in-oil droplets as well as their subsequent release into a physiologically relevant aqueous buffer.

Further I elucidated the mechanism behind the on-demand production of either multicompartment systems or dsGUVs and showed that it is dependent on surfactant charge, SUV charge and on the presence of certain ions. The repertoire of inert, negatively and positively charged surfactants allowed for a versatile combination of lipids and salt conditions.

The multi- and single compartment systems could serve as a good cell model system, as they resemble the internal eukaryotic organelle structures and the outer cellular membrane. Remarkably, production conditions can be adjusted to generate a combination of both, a multicompartment system enclosed in the spherical lipid bilayer of a dsGUVs.

The release of these lipid-based systems into aqueous buffers increases the physiologically relevance of the approach and allows for further manipulation of the GUVs. In this concern released GUVs were used to study membrane tube formation that could model membrane folds as present in e.g. the mitochondria's inner membrane.

To sum up, I presented here the capability of this purely lipid-based systems to model the eukaryotic architecture.

Part II

5.2. Reconstitution of Cytoskeletal Networks towards Artificial Motility

Cellular motility governs many fundamental processes including, but not limited to, embryonic development, immune response, tissue formation and wound healing. In the context of a living cell, the machinery of cellular locomotion is highly complex and not fully understood as it involves many cell signaling processes. Towards elucidating cellular motility, it is important to first dissect the mechanism into its basic features. Therefore, I present a bottom-up approach in which cell motility will be broken down to three steps: a) the generation of a pushing force and an extension force at the leading edge; b) the adhesion of the leading edge to the substrate; and c) the detachment and the contraction of the cell body at the rear. Key players in these steps are 1) actin networks, creating a pushing force against the membrane in the front; 2) myosin motors leading to a contractile force at the rear; and 3) integrin transmembrane proteins responsible for adhesion and detachment of the cell body on the extracellular substrate.

In the following part I will demonstrate the assembly of these key players within the here presented synthetic cell approach. Primarily, however, I will start with the investigation of actin networks in 2D and will continue with the reconstitution of actin cytoskeletal networks within water-in-oil droplets. In this regard, I created actin-based pushing forces by the reconstitution of crosslinked and rigid actin filaments. To reconstitute the corresponding counter force, in a next step, the motor protein myosin II was introduced leading to a contractile actomyosin network. Similarly, this was investigated first in 2D and then within the synthetic cell approach. Moreover, towards the creation of an actomyosin cortex, I linked the actomyosin network to the droplet by tuning the electrostatic interaction between the network and the droplet's interface.

A highlight of this part is the observation of spontaneous motion of cytoskeletal network-containing droplets. In contrast to motility in a living eukaryotic cell, this spontaneous motion, however, was shown to be independent of pushing and contractile forces. In this regard, I will characterize multiple aspects of this spontaneous motion and finally raise a hypothesis to explain the observed artificial motion.

Some of the experiments of the following sections have been done in cooperation with Dr. Marian Weiss (postdoc, MPI, Department Prof. Spatz).

5.2.1. Actin-Generated Pushing Forces

Actin filaments have a plus and a minus end. They disassemble at the minus end or grow at the plus end upon exposure of actin monomers below or above a critical concentration, respectively.[40] Through this actin polymerization a pushing force against the cell membrane can be generated.[278] In a living cell this so-called treadmilling of actin filaments is besides actomyosin contraction one of the key aspects in cell locomotion.[11]

In a synthetic cell approach, the actin concentration is supposed to stay the same over time. Thus, the creation of treadmilling conditions is challenging.[28] Nevertheless, several previous studies have described that actin – in a steady state and without motor proteins – can indeed exert a force on the confinement.[162,163,165] In this regard, by the encapsulation of rigid actin filaments (with a persistence length larger than their confinement dimension) a deformation of the membrane has been reported. This pushing force is supposed to be mediated by the energy costs related to actin filament bending[162,163] and can resemble the stretching of the leading edge in a migrating cell. Towards this aim, I reached out to implement this pushing force within my synthetic cell approach as a key step towards reconstitution of cellular motility.

5.2.1.1. Actin Bundling to Rigid Filaments in 2D

While single actin filaments possess a persistence length of around 12 µm[168] and can generate a maximal polymerization force per monomer of around 1.5 pN,[165] actin can reach much higher persistence lengths and forces by the addition of crosslinkers e.g. a persistence length of 150 µm and much higher forces for an actin to fascin ratio of 1:2.[35,279]

In a synthetic cell actin bundling is mainly achieved by the crosslinker fascin[165] or by macromolecules,[166] as PEG or methylcellulose. Macromolecules bundle actin filaments based on the depletion effect that leads to entropy-driven interaction of larger objects (e.g. actin filaments).[168]

In this thesis, actin was purified from skeletal rabbit muscle by Christine Mollenhauer (see Section 3.4.1). To characterize the actin cytoskeleton *in vitro*, prior to the assembly in water-in-oil droplets, the activity of actin and its crosslinkers was tested in bulk on PLL-PEG coated glass slides. In low salt conditions (G-buffer, see Section 3.5) actin stayed in its globular monomeric form. Upon increasing the ionic strength of the buffer by adding the actin polymerization buffer monomers assembled to form actin filaments (1% of actin is labeled with Alexa Fluor 568) as shown in Figure 67A. Further the crosslinker fascin in a molar ratio of 1:20 or 0.4 wt% methylcellulose was added to the polymerization buffer and mixed with the actin monomers in bulk. In comparison to actin filaments without crosslinkers actin filaments formed much thicker and more rigid bundles in the presence of fascin (Figure 67B) and methylcellulose (Figure 67C), whereby the effect of methylcellulose was most prevalent.

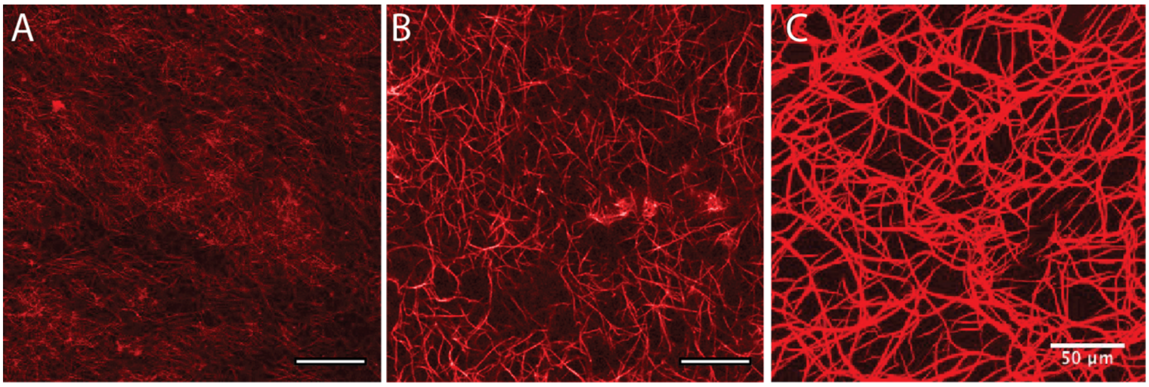

Figure 67: Representative fluorescence images of actin filaments (1% Alexa Fluor 568 conjugated actin) in polymerization buffer containing (A) no crosslinker, (B) fascin (molar ratio 1:20), or (C) 0.4 wt% methylcellulose. Scale bar 50 µm.

After showing that actin filament rigidity can be tuned in bulk, I included these crosslinked actin networks within cell-sized microfluidic water-in-oil droplets. This will be presented in the next section.

5.2.1.2. Actin-Generated Pushing Forces within Water-in-Oil Droplets

Geometric constraints alter the cytoskeletal assembly and its dynamics as it provides barriers and interfaces to apply forces on.[168,280] Therefore, actin networks were reconstituted within microfluidic water-in-oil droplets by means of a droplet production device with two aqueous inlets (see Section 4.3.1). In order to prevent polymerization prior to the droplets formation one aqueous phase contained the actin monomers (1% of actin is fluorescently labeled with Alexa fluor 568) and the other aqueous phase the polymerization buffer. A microfluidic zick-zack mixing unit ensured the mixing of the two phases following droplet formation. To test the influence of actin filament rigidity on the network assembly, actin was encapsulated in the presence of fascin (molar ratio 1:20) or in presence of 0.4 wt% methylcellulose into the droplets.

The actin network crosslinked by fascin (Figure 68A) assembled mainly in the center of the droplet without prevalent interactions with the periphery. This crosslinked actin filament network is in accordance with other studies showing comparable network arrangements in similar-sized confinements.[281,282] Distinct to that, highly ordered actin network structures were generated when actin filaments were crosslinked by methylcellulose (Figure 68B). The inset on the right of Figure 68B shows that the filaments all assembled at the periphery of the droplet into a cage-like structure, leaving the droplet's center empty. Similar actin ring structures have been seen in a previous study by Miyazaki *et al.*[166] In that study, the authors demonstrated that ring formation is dependent on the diameter of the droplet that need to be equal to or smaller than the persistence length of the filaments. This is in accordance with our observations. Whereas fascin-crosslinked actin filaments have an persistence length smaller than the confinement size,[279] thus can stretch out; the filaments in the presence of methylcellulose are much more rigid and thus cannot stretch out completely. To minimize curvature and bending energy costs, filaments assemble at the droplet's equator.[166]

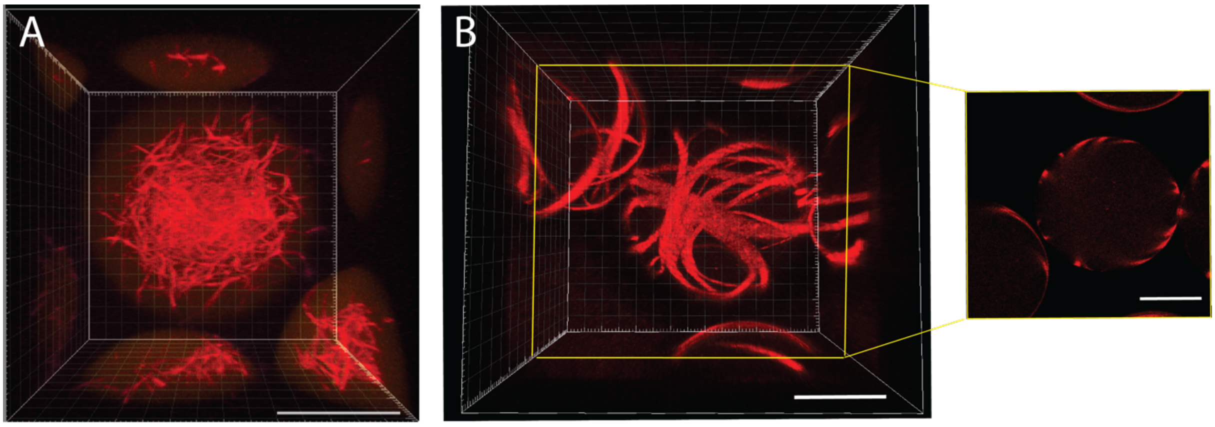

Figure 68: Z-stack projections of actin networks within water-in-oil droplets (1% of actin is labeled with Alexa Fluor 568). A) In the presence of the crosslinker fascin (1:20) Scale bar 30 µm. B) The presence of 0.4% methylcellulose leads to a cage-like actin network assembly. Insets on the right shows a confocal image of the middle of the droplet reveалling that all fibers assembled at the periphery of the droplets. Scale bar 10 µm.

Note that in other studies the encapsulation of rigid actin bundles deformed lipid-based compartments.[162,163] In the here presented system, the water-in-oil droplets comprise a much higher membrane rigidity.[165,166] Therefore, the force that the actin bundles apply on the droplets interface cannot be evidenced by droplet deformation but through the filament arrangement tightly aligned against the droplet wall.

In fact, the pushing force in a living cell are mainly based on actin treadmilling.[28] To generate such treadmilling conditions in an artificial cell is as mentioned before challenging, since it includes many signaling molecules.[28] However, in order to investigate and observe the initial actin polymerization dynamics, the polymerization process of encapsulated actin monomers to actin filaments, was slowed down. This was achieved by keeping the droplets and the buffers on ice before the droplets were imaged. Further, the increased viscosity of buffers containing methylcellulose additionally slowed down diffusion[283] and thus, the polymerization. Representative fluorescence images in Figure 69A show that at time point 0 min the fluorescence signal was still spread within the droplets, however, first polymerization sites could be observed. After 10 min the fluorescence signal was detected mainly from the actin filaments, and not from distributed actin monomers, indicating that actin polymerization was mainly completed. Anyway, network rearrangement proceeded leading to a further bundling of the filaments as presented at time point 20 min and in Figure 68 of the previous section. This dynamic arrangement is further shown in Figure 69B. Here the fluorescence intensity was converted into a color-code representing the z-position of the confocal stacks. Due to the depletion effect, thinner and shorter adjacent filaments got dynamically arranged into thicker and longer filaments. These, in turn, assembled at the periphery and created these highly ordered structures to decrease bending energy costs.

This shows that actin networks in the presence of methylcellulose are not static but are within the first 20 min dynamically arranged even though polymerization has been completed.

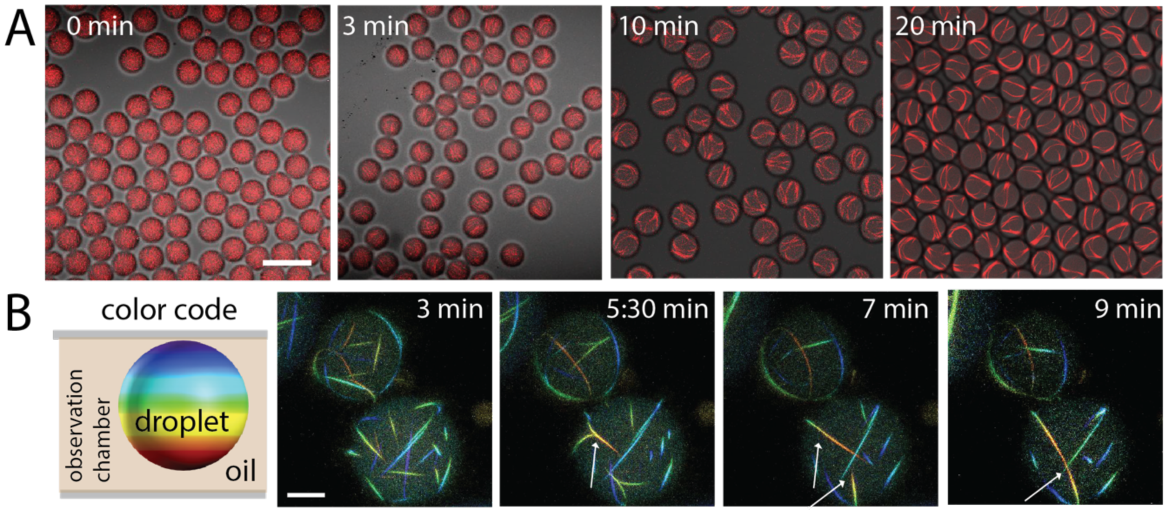

Figure 69: Representative fluorescence images of droplets containing actin in a polymerization buffer substituted with 0.4 wt% methylcellulose to different timepoint.(A) Observation of actin polymerisation: After around 3 min, fluorescent signal was still distributed within the droplets, however, first polmerization events were obvious. After 10 min fluorescence signal was localized on the polymerized actin network. Scale bar 50 µm.(B) Dynamical actin filaments arrangent due to depletion effect. Fluorescence of actin filaments (10 µM, 1% Alexa Fluor 568-conjugated actin) was converted into a color-code representing the position in the Z-plane. Arrows indicate movement of fibers. Scale bar 10 µm.

Taken together, the here presented results show the reconstitution of actin networks that, in presence of methylcellulose, exert a pushing force onto the compartment and a dynamical arrangement of the network.

With this, a key feature of cellular motility could be implemented within my artificial cell approach. Another important key feature in cellular motility is the myosin motor-driven network contraction. Towards the reconstitution of such contractile networks, actomyosin networks were first studied in bulk and then in water-in-oil droplets. This will be described in the following section.

5.2.2. Actomyosin Networks in Bulk

After the reconstitution of cytoskeletal pushing forces, I want to address next the associated – and not less important – counter force in cellular motility: the myosin motor-based contractile force.

Towards this, the motor protein myosin II was purified from skeletal rabbit muscle by Christine Mollenhauer, and combined with actin (1% of actin is fluorescently labeled with Alexa Fluor 568). To achieve polymerization conditions, actin and myosin (ratio of actin monomers : myosin 20:1) were mixed with the actomyosin polymerization buffer containing 1.1 mM ATP, resulting in an actomyosin network, whose actin filaments were crosslinked by myosin motor bundles (see Introduction Section 1.2.1.1). After around 10 min incubation time, the network was observed on a PLL-PEG coated cover slip (Figure 70B). In comparison to the network in absence of myosin (Figure 70A), the assembly of actomyosin structures showed a denser network and thicker actin bundles. This observation is expected since myosin II crosslinks actin filaments and contracts the network upon conversion of ATP to ADP.[45]

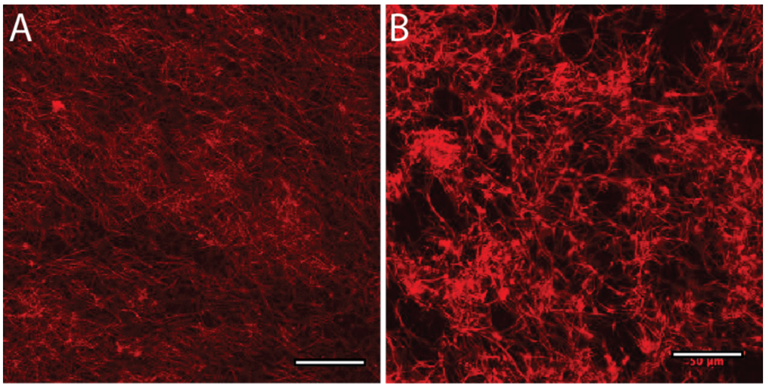

Figure 70: A and B show representative fluorescence images of polymerized actin (1% Alexa Fluor-568 conjugated) and actomyosin (20:1 molar ratio, 1.1 mM ATP) networks, respectively, on a PLL-PEG coated cover slide. The images were recorded after 10 min of incubation time at RT in actin or actomyosin polymerization buffer, respectively. Scale bar 50 µm.

The activity of the myosin motor can be seen by the cluster formation of contracted actin networks in bulk (Figure 70B). However, to further control and monitor the activity of myosin, a ATP sensor, expressed in *E.coli* and purified by Dr. Amelie Benk, was implemented, as I will show next.

5.2.2.1. ATP Sensor to Monitor Actomyosin Activity in Bulk

The ATP sensor is based on a fluorescent dye, whose excitation maxima depend on the binding of either ATP or ADP (see Section 3.4.6).[249] To test the actomyosin activity based on the hydrolysis of ATP, the sensor was mixed with ATP and actomyosin-containing buffer. Excitation spectra were collected after 25 min, 1h and 1.5 h (Figure 71). In samples containing actomyosin a clear decrease in ATP and an increase of ADP could be observed by a change in fluorescence intensity at 420 and 500 nm excitation. The change in excitation maxima indicated that after 1 h, 0.5 µM myosin had consumed 100 µM ATP, which corresponds to 0.055 ATPs per second per myosin. This consumption is significantly lower than previously described for myosin II from skeletal muscle.[284]

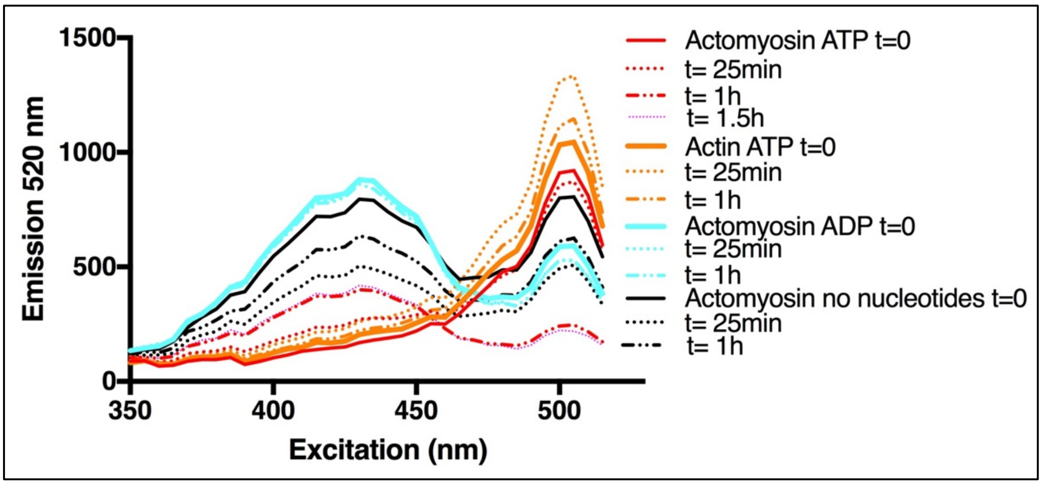

Figure 71: Analysis of ATP / ADP ratios by means of distinct excitation spectra of a ATP/ADP sensitive fluorescent dye. In presence of ADP or ATP, the fluorescent dye has a strong fluorescence emission (520nm) when excited with 420 nm or 500 nm, respectively.[249] Sample composition described on the right (myosin II: 0.5 µM, actin 10 µM, ATP or ADP: 100 µM ATP).

A reason for the reduced activity could be the fact that actomyosin buffers had to be adjusted to be compatible with the ATP sensor (see Section 3.5.2). Supposedly, this did not match the conditions for efficient myosin performance. Therefore, the myosin activity was controlled with a second method, an actin sliding or so-called motility assay, as presented in the next section.

5.2.2.2. Motility Assay to Monitor Actomyosin Activity in Bulk

A motility assay is a common approach to quantify myosin activity.[285] Towards this end, myosin was immobilized on nitrocellulose-coated glass slips in a flow chamber (see Section 4.6.1.6). Upon introduction of actin filaments into the flow chamber, the filaments bound to the myosin heads and upon addition of ATP, a sliding of the filaments could be observed. Figure 72A shows a representative fluorescence image of fluorescently labeled actin filaments bound to the myosin that was immobilized on the cover slide of the flow chamber. Actin filament movement was recorded and tracked with Image-J (trajectories are shown in Figure 72B).

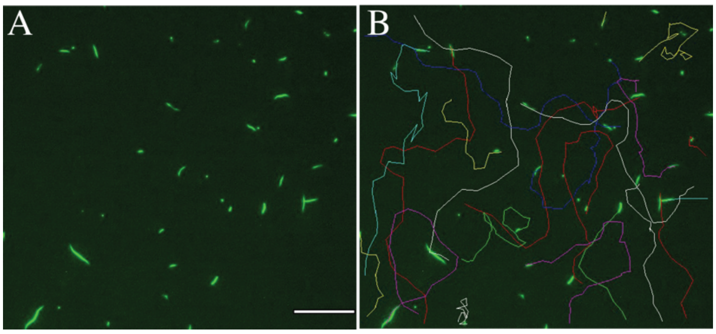

Figure 72: Actomyosin motility assay to verify myosin motor activity. (A) Atto 488 Phalloidin-labeled actin filament fragments on myosin II (bound on the cover slip of a flow chamber). (B) Upon introduction of ATP, myosin motors translocated actin filaments across the coverslip. Trajectories of filament movement were analyzed with Image-J. Scale bar 10 µm.

The calculated velocity (based on the Image-J plugin) of actin filaments of 3.39 ± 0.05 µm/s is in good agreement with previously published actin sliding performance[164] and confirmed the activity of the here used myosin II motors.

To move one step further, towards reconstitution of cellular motility, I included these contractive actomyosin networks within cell-sized microfluidic water-in-oil droplets.

5.2.3. Encapsulation of Actomyosin Network into Water-in-Oil Droplets

After proofing the myosin motor activity in bulk, I reached out to encapsulate actomyosin networks into the cell-sized water-in-oil droplets by means of a droplet production device with two aqueous inlets (see Section 4.3.1).

Figure 73 shows a merged bright-field and fluorescence z-stack projection of a droplet containing an actomyosin network shortly after the production (actin 10 µM, 1% Alexa 568-labeled actin, myosin 0.5 µM, fascin 0.5 µM). The actomyosin filaments assembled into a dense network partly agglomerated due to myosin contraction, similar to what could be observed in bulk (Figure 70B).

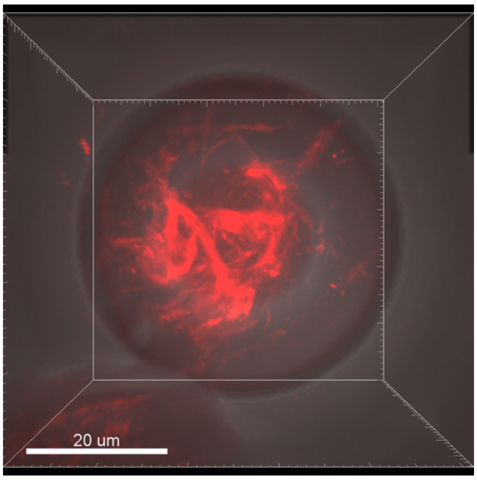

Figure 73: A merged confocal fluorescence and bright-field z-stack projection of fluorescently labeled actomyosin network (10 µM actin, 1% Alexa Fluor 568 labeled, 0.5 µM myosin, 0.5 µM fascin, in actomyosin polymerization buffer) within a water-in-oil droplet, stabilized by PEG-based surfactant. Scale bar 20 µm.

To analyze myosin activity in more detail within water-in-oil droplets, the actomyosin network contraction was studied in a myosin concentration dependent manner. This will be presented in the following section.

5.2.3.1. Analysis of Actomyosin Contraction within Water-in-Oil Droplets

In the following, I set out to study actomyosin contraction as a function of myosin motor concentration within water-in-oil droplets. In this regard, actomyosin networks with different actin-to-myosin ratios were encapsulated into droplets, stabilized by PEG-based surfactant and observed by means of confocal fluorescence microscopy (Figure 74). An increased myosin-to-actin ratio of 1/10 already lead to an enhancement in network contraction, resulting in a completely collapsed network when a myosin-actin ratio of 1:5 was used. By introducing the myosin-inhinitor blebbistatin to the actomyosin network, a reverse effect could be observed. This is an expected behavior of actomyosin activity seen already in many 2D studies.[172,286] With this I could show the activity of actomyosin networks within the droplets and further, the possibility to tune contractile forces in a controlled way within the water-in-oil droplets based on the myosin-to-actin ratio.

Note that the process of actomyosin contraction could not be observed in real-time. This indicates that the process of actomyosin contraction happened instantly right after actin polymerization and droplet formation.

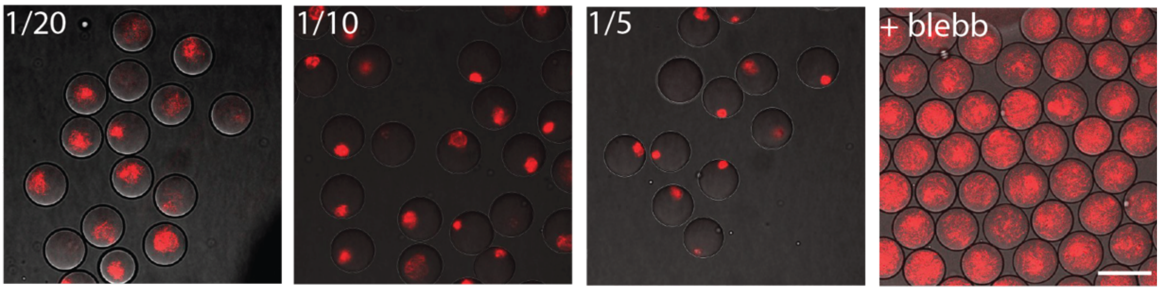

Figure 74: Representative merged fluorescence and bright-field images of actomyosin networks within water-in-oil droplets, encapsulated into droplets with different actin (1% Alexa Fluor 568 labeled actin)-to-myosin ratios. A myosin-to-actin ratio of 1:20 (left) leads to the formation of a partly contracted network. A myosin-to-actin ratio of 1:10 (right)leads to a completely collapsed network. The addition of blebbistatin inhibits myosin activity (myosin-actin ratio 1:10). Scale bar 50 µm.

In a living cell, the actomyosin network forms a membrane-connected cortex at the cell periphery. This allows to apply contractile force onto the cell body and to move the cell body forward during migration over a substrate.[41] In this regard, I reached out to implement a similar transmission of actomyosin contractile force onto the confinement in an artificial cell. The approach to mimic the protein complexes that connect the actin network to transmembrane proteins in a living cell is challenging and will be investigated separately in Section 5.3. Here, I first will present a more direct link between actin and the periphery: a linkage based on electrostatic interactions. Towards this, a negatively charged surfactant, named Krytox, was mixed with the PEG-based surfactant to stabilize the actomyosin-containing droplets.

5.2.3.2. Linkage of Actomyosin Networks to the Periphery via Electrostatic Interaction

In order to link the actomyosin network to the periphery via an electrostatic attraction force a custom-made triblock surfactant was used that contained the negatively charged surfactant molecule Krytox. Following droplet production, Krytox molecules assembled at the interface and introduced their negatively charged carboxylic group towards the aqueous phase. This allows the carboxylic group to attract counter ions from the buffer[181] and that in turn, promotes attraction of negatively charged actin molecules.

To check the adsorption of actin to the periphery, fluorescently labeled actomyosin was encapsulated into droplets stabilized by this custom-made triblock surfactant containing Krytox (see Appendix, Figure SI 1) or by Krytox-free PEG-based surfactant. Figure 75 shows fluorescence images of actomyosin networks within droplets and the fluorescence intensity profile of their cross section. The fluorescence intensity within the droplets stabilized by Krytox-containing surfactants (Figure 75A) was most prevalent at the periphery whereas in Krytox-free droplets (Figure 75B) fluorescence was mainly in the droplet's center. This shows that due to the negatively charged droplet interface, actin can be successfully recruited to the periphery, leading to an actomyosin cortex.

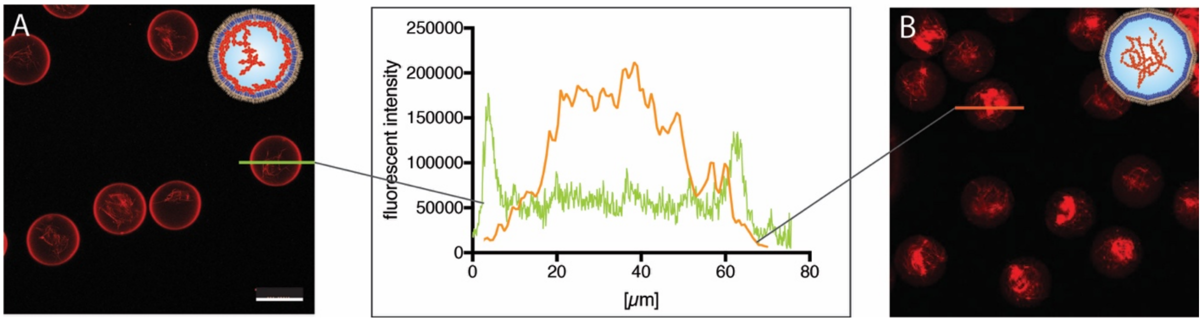

Figure 75: Representative fluorescence images of droplets containing actin (10 µM) in polymerization buffer stabilized by custom-made triblock surfactant containing Krytox (A) or stabilized by Krytox-free PEG-based surfactant (B). Scale bar 50 µm. Graph in the middle shows average fluorescence intensities of droplets cross section (n= 15). green relates to A, orange relates to B.

Similar actin cortex formation has been seen in other studies that linked the actin filaments to the periphery e.g. via positively charged lipids in the membrane,[87,171] via biotin-streptavidin-interactions[174] or via an amphiphilic protein assembled at the oil-water interface.[89]

Note that a second approach with custom-made gold-functionalized surfactants (Section 3.2.3) was tested to create an actomyosin cortex, leading to a similar but not as prominent effect (see Appendix, Figure SI 8), thus, it is not further discussed in this thesis.

As a next step, I wanted to check in what time-scales this cytoskeletal cortex is assembled at the interface. This was expected to happen within very short time-scales. Thus, I checked the actin adsorption kinetics to the droplets' interface within the droplet production device. These measurements were done in cooperation with Dr. Eli Zamir (Senior Postdoc, MPI, Prof. Spatz Department) and will be presented in the following section.

5.2.3.3. Actin Adsorption

To check the adsorption of fluorescently labeled actin to the periphery via electrostatic interactions actin-containing droplets were recorded within the microfluidic droplet production device. Towards this aim, a droplet production device was mounted on a LSM 880 confocal microscope and the distribution of encapsulated actin was analyzed by screening the fluorescence intensity profile (with an open pinhole) of flowing droplets at different distances after production, corresponding to different time points: shortly after production at the droplet-producing nozzle, before and after the microfluidic zick-zack-mixing unit, and shortly before the channel ends at the droplet outlet. In this regard, droplets were screened at each of these positions for 10s resulting in around 1200 recorded intensity profiles.

Figure 76A shows the droplet production device and color-coded fluorescence intensity profiles of the droplets' cross sections, collected at the indicated spots of the production device.

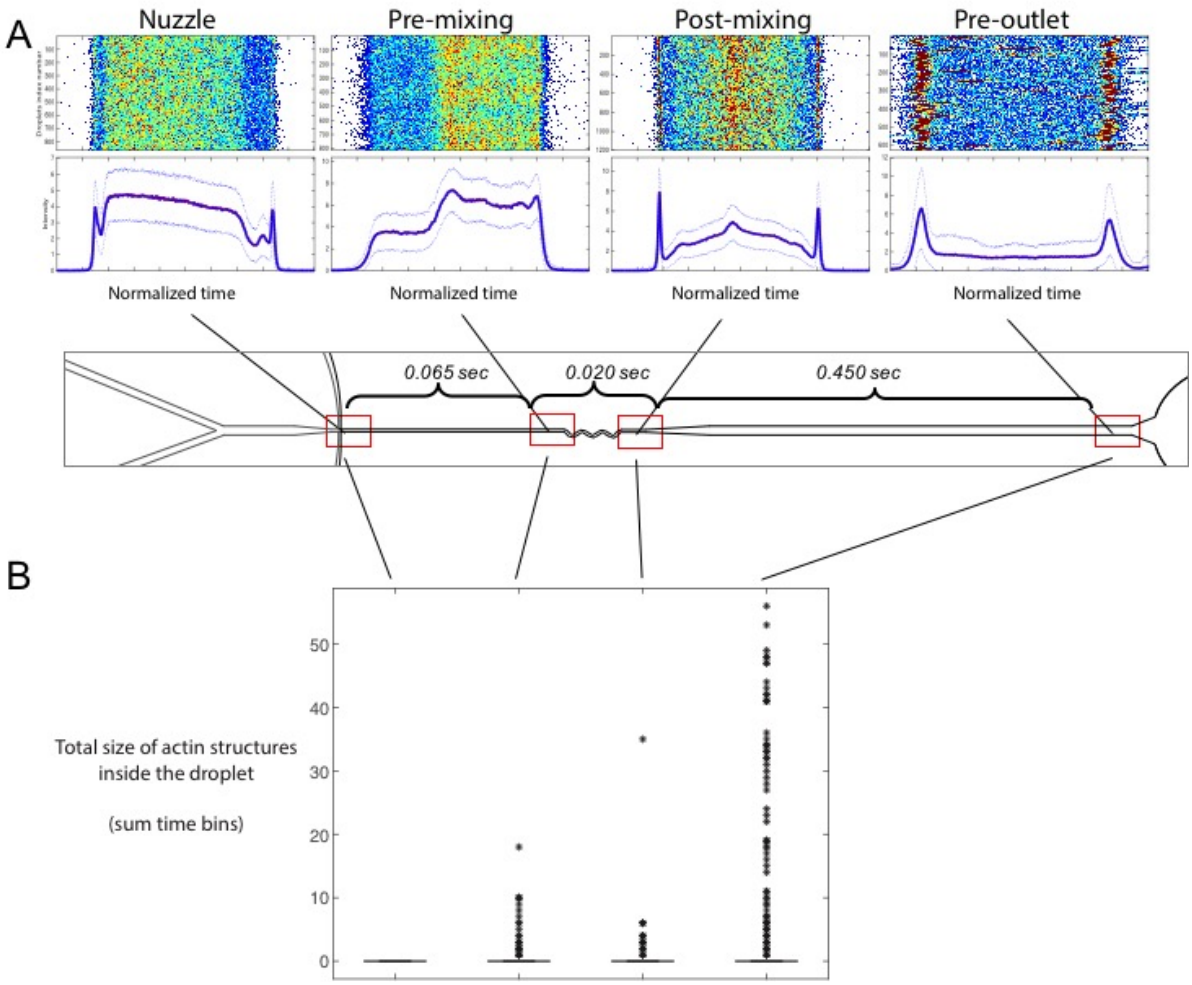

Figure 76: Fluorescence intensity screening of droplets in four positions within the production device. (A) Color-coded fluorescence intensity lines of 1200 passing droplets and the corresponding plotted means. (B) Counts of intensity peaks in the droplet centers, indicating the formation of polymerized actin filaments.

Before the mixing unit the fluorescence intensity of the droplets was located only in one part of the droplets. After the mixing unit two sharp intensity peaks indicated a clear localization of actin at the periphery of the droplets. Further, this profile shows an actin-depleted zone close to the peripheral peaks. This indicates that the recruitment of actin to the surfactant interface happened faster than the diffusion of that actin-depleted zone. These diffusion-limited adsorption kinetics would be generally not expected in such length scales.[203] However, it can be explained by the electrostatic attraction forces that seem to be mediating the adsorption process.

At the outlet, individual droplets showed in the center red spots of high intensities. This may indicate the presence of actin filaments. To quantify the polymerization events, based on the intensity peaks in the droplets center, the counts of these high intensity values were plotted

(Figure 76B). Not surprisingly, most polymerized actin filaments were found after 0.45 s at the outlet.

These results show that actin was instantly recruited to the periphery by electrostatic interactions. Moreover, these results indicate that first actin polymerization events happened also very fast within less than half a second after production.

Having investigated the time scale of initial adsorption process of actin to the periphery, I wanted to investigate next, how this linkage influence actomyosin contraction within longer time scales.

In this regard, previous studies reported that by connecting the actomyosin network to the confinement, the contractile force could be transmitted onto the confinement. This was observable by means of e.g. membrane oscillation,[171] membrane blebbing,[175] deformation,[89] or even by a collapse[171] of the compartment membrane.

Thus, I set out to assess how the linkage between the actomyosin network and the droplets' surfactant shell may impact the actomyosin network contraction in the here presented system. Towards this, I will present time-lapse studies in the following section.

5.2.3.4. Influence of Negatively Charged Surfactant on Actomyosin Networks within Droplets

To test the actomyosin contraction when the network is electrostatically linked to Krytox molecules at the droplets periphery, droplets were observed over a time period of 30 minutes. Figure 77 shows representative time-lapse images of actomyosin-containing droplets stabilized by Krytox-containing surfactants. Similarly, as seen already in the previous section, an actin recruitment based on electrostatic interaction was visible as a bright ring in the confocal plane at the periphery of the droplet.

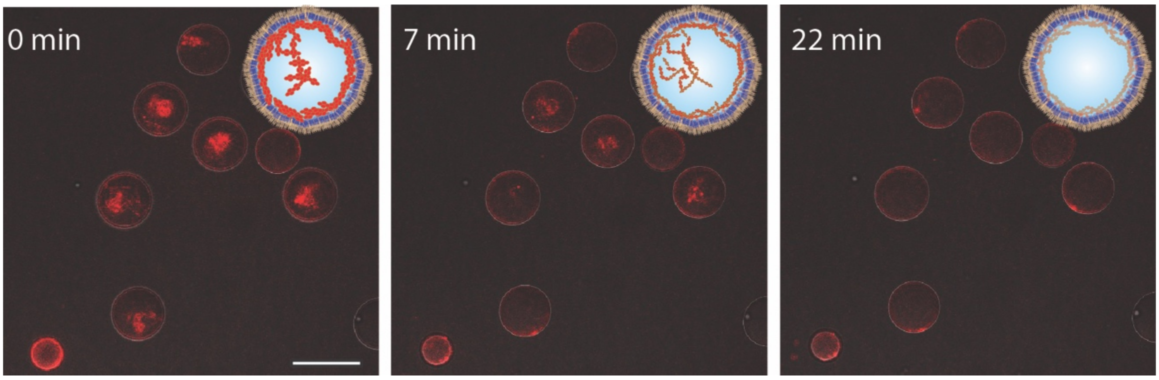

Figure 77: Representative fluorescence images of time-lapse analysis and schematic representations of actomyosin-containing droplets, stabilized by a custom-made triblock surfactant containing Krytox at different time points showing a loss of fluorescence signal with the time. Scale bar 50 µm.

However, it appeared that after few minutes the encapsulated actomyosin network started to disintegrate, resulting in a nearly vanished fluorescence signal after 22 min. This indicated that the conditions within the droplets were not stable over the time. This could be explained by the dynamic nature of the surfactant shell that goes along with a constant desorption and adsorption of new surfactant molecules[181] what may lead to the extraction of encapsulated molecules.[250] The interaction of proteins from the aqueous phase as well as the leakage of molecules out of the droplets due to Krytox has been reported before.[206,250] These effects have been explained by the carboxylic acid group of Krytox at the interface (see IFT measurements Results part I Section 5.1.1.1) that exchanges a proton by binding a counter ion from the aqueous solution. This leads to a decrease in ionic strength and a drop in pH.[181]

The decrease in ionic strength and the drop of pH can both explain the depolymerization of actin filaments, seen in Figure 77. Moreover, actin may denature when interacting with the carboxylic group of Krytox leading to a tight actin-Krytox linkage.[287] The subsequent desorption of this complex form the interface into the oil phase may then explain the overall loss of fluorescence intensity. Note that in some cases fluorescent agglomerates were found in the oil phase indicating the transport of material out of the droplet.

Especially when water-in oil droplets are used as microreactors, the retention of encapsulated content is crucial. As shown in this section, this is not always the case. The leakage of encapsulated content could be due to direct diffusion into the oil phase in case of amphiphilic molecules,[258] the formation of surfactant micelles, or the transfer of content from one droplet to another across a surfactant bilayer of the two adjacent droplets.[288]

To compromise between stable biochemical conditions and an actomyosin linkage to the interface different Krytox concentrations were tested in a next step.

5.2.3.5. Impact of Charged Surfactants on Actomyosin Networks and Droplet Dynamics

To tune the interaction of actomyosin networks with the droplets periphery, a Krytox-free, PEG-based surfactant was used and mixed additionally with Krytox. Figure 78 presents fluorescence images of droplets containing actomyosin networks stabilized by a purified PEG-based surfactant with 0, 1 and 2 mM of Krytox. While without the addition of Krytox no actomyosin cortex formation was obtained (Figure 78, left image), for 1 mM and 2 mM Krytox actomyosin networks were recruited to the periphery.

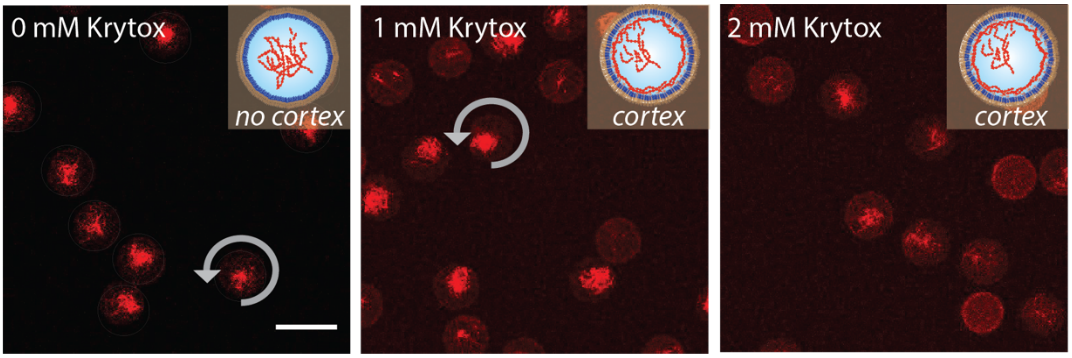

Figure 78: Representative fluorescence images of time-lapse videos and schematic representations, demonstrating actomyosin network location and droplet dynamics in the absence and presence of Krytox. Actomyosin cortex formation was observable for 1 mM and 2 mM Krytox. Droplet dynamics, indicating through the circular arrow, were observed for 1 mM and below. Scale bar 50 µm.

In contrast to previous studies where actomyosin contraction lead to a deformation of the compartment or to a cortex detachment from the compartment,[89] no such phenomena could be observed here. Not less remarkable, however, the time-lapse studies in Figure 78 revealed a rotational self-propulsion of some of the droplets. Interestingly, this happened only in droplets that were stabilized by PEG-based surfactant with no or only 1 mM Krytox. This indicates that an actomyosin cortex may be redundant for droplet rotation or, moreover, may even impair droplet motility.

Creating a controllable and directed movement is indeed an ultimate goal in artificial cell motility approaches. Thus, this observed phenomenon of self-propulsion of water-in-oil droplets was investigated further in order to elucidate the mechanism behind it.

Since the addition of higher (> 1mM) amounts of Krytox seemed to have a rather negative effect on droplet dynamics, the following experiments have been performed with pure PEG-based surfactant. In these cases, no actin-surfactant interactions were visible by confocal fluorescence microscopy.

Note, however, that on a molecular level an interaction of actin with Krytox molecules cannot be ruled out, as even the purified surfactant (that was mainly used in this thesis) contained still some Krytox traces (1% Krytox, see Section 5.1.1.3).

5.2.4. Self-Propulsion of Actomyosin-containing Water-in-Oil Droplets

During the investigation of cytoskeletal networks within water-in-oil droplets, time-lapse videos revealed a rotational self-propulsion of some of the droplets. This rotation of water-in-oil droplets has first been observed in droplets containing actomyosin networks. Figure 79 presents a representative fluorescence time-lapse analysis of a droplet showing one rotation in 25 min.

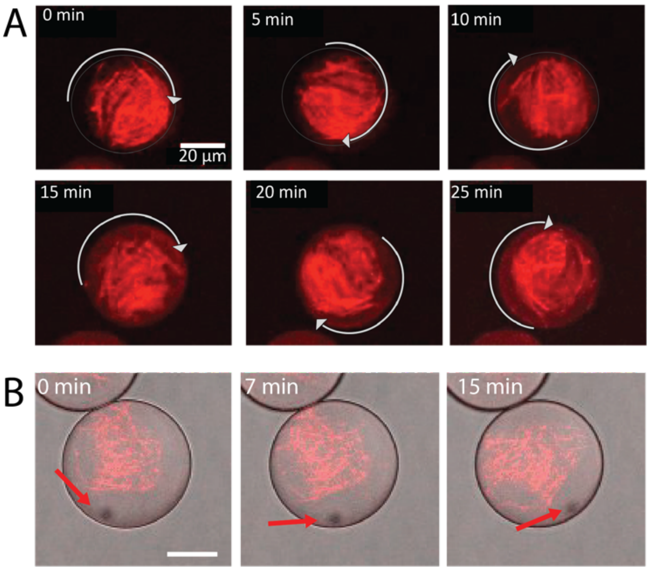

Figure 79: Representative time-lapse analysis of a rotating droplets containing actomyosin networks. (A) Fluorescence images (1% of actin is fluorescently labeled). Scale bar 20 µm (B) Merged fluorescence and bright-field images of a rotating droplet with a hydrophobic bead at the outside of the droplet that rotates along with the cytoskeleton, indicated by the arrow. Scale bar 10 µm.

To further check if the whole droplet or only the network within the droplet was rotating, hydrophobic polystyrene beads were used to break the symmetry of the droplet for observation. The arrow in Figure 79B points to the bead that rotates along with the actomyosin network, thus providing the evidence that the whole droplet was rotating and not only the network inside the droplet.

Moreover, to control if the rotation is governed by an external linearly directional flow of the oil phase, rotation speed and the direction of rotation was investigated. By incorporating fluorescent beads into the actomyosin networks of water-in-oil droplets and performing time-lapse z-stack confocal microscopy, droplet rotation could be tracked automatically by means of an Image-J plugin. The trajectories of the beads within the droplets are shown in Figure 80.

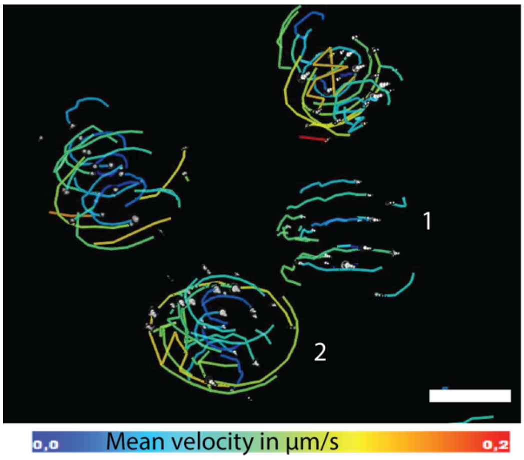

Figure 80: Trajectories of beads encapsulated within actomyosin-containing droplets. By means of confocal z-stack time-lapse microscopy, fluorescence of beads was imaged for 8 min, the fluorescence of beads was tracked and analyzed by Image-J. Scale bar 10 µm.

The color-coding represents the velocity of the beads revealing logically a faster velocity the closer the beads were located at the periphery of the droplet. Further, this analysis revealed that the rotation of the droplets was independent from each other. Whereas the droplet on the very right (droplet 1) performed a quarter turn in the tracked time (8 min), the droplet at the bottom (droplet 2) rotated around half a turn. Further, all droplets rotated in a different direction. This shows that droplet rotation is probably not accelerated by a large scale external oil flow. For future experiments, it will be great to use hydrophobic micrometer-sized beads with the density similar to the oil. These beads will be the best solution to track the oil flow.

Next, I wanted to check which kind of internal forces could initiate the observed rotation. Towards this, the two major forces of cellular locomotion - pushing and contractile forces that are described in Section 5.2.1 and 5.2.3, respectively - were investigated on their influence on droplet rotation. This will be discussed critically in the following.

5.2.5. Impact of Cytoskeletal Forces on Self-Propulsion of Water-in-Oil Droplets

In Section 5.2.3.5, I could show that no visible connection of the actomyosin network was needed to create the observed droplet rotation. Consequently, questions arise on how the actomyosin network applies contractile force onto the droplet to initiate rotation, or whether it plays a role in rotation at all.

In this regard, further investigations showed that myosin motor proteins were redundant for droplet rotation and that droplets containing pure actin filaments similarly perform droplet rotation (see Figure 81). With this, I can conclude that the myosin contractile force is not a major mediator in droplet rotation.

In order to elucidate the mechanism behind the self-propulsion, I next checked the influence on the actin pushing force, discussed already in Section 5.2.1, on droplet rotation. In this regard, time-lapse videos were performed of actin filaments encapsulated in water-in-oil droplets. Figure 81 shows fluorescence z-stack projections of the actin-containing droplets with (C) and without (B) 0.4 wt% methylcellulose to different time points. The fluorescence signal was transformed into a color-code (A) representing the z-plane within the droplets. These time-lapse videos confirmed that droplet rotation happens in absence of myosin, whereby the rotation in droplets containing the rigid actin bundles was most prevalent.

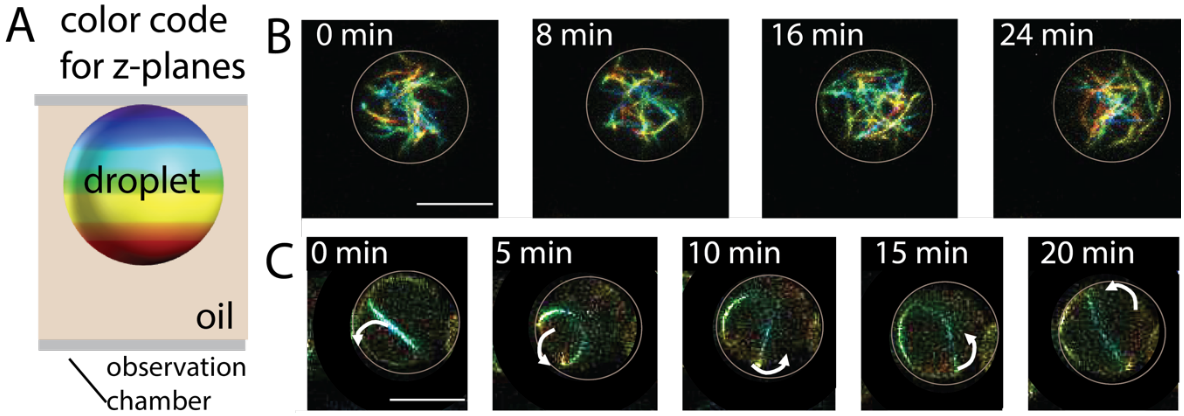

Figure 81: Influence of actin filament rigidity on droplet dynamics. (A) The fluorescence signal of the droplets is transformed into a color-code representing z-plane position. (B) Droplet containing actin filaments and no methylcellulose shows only minor dynamics. (C) Droplet containing actin filaments and 0.4 wt% methylcellulose shows rotational dynamics indicated by the arrows. Scale bar 25 µm.

In a previously published study by Miyazaki *et al.* actin filaments, which were similarly bundled by methylcellulose, were encapsulated into water-in-oil droplets. In this study similar ring structures of actin filament bundles could be observed,[166] however, no rotation of the droplets has been reported.

The only study to my knowledge showing similar rotational movement of cell-sized compartments based on encapsulated cytoskeletal networks was done by Suzuki *et al.*[289] In this study the rotation was achieved by reconstitution of microtubules and kinesin motors and was explained by the pushing force of microtubules against the membrane and by an internal fluid flow, generated by a kinesin-driven microtubule dynamics.[289]

This study has some similarities with the synthetic cell system presented in my thesis. The stiffness of the microtubules for example could be comparable to the stiffness of thick actin bundles in the presence of methylcellulose. Also, a pushing force was shown in Section 5.2.1 in my system. However, when considering symmetry breaking of forces conflicts arise. In the study of Suzuki *et al.* the kinesin motor was hold responsible for symmetry breaking.[289] In the rotation observed in my thesis it is not conclusive how the pushing force of rigid actin filaments alone could break the symmetry and initiate the rotation.

In case of methylcellulose-mediated actin bundling, time-lapse studies revealed that the actin network is not static but is dynamically arranged also without motor proteins (see Figure 69). This dynamic arrangement of actin bundles aligned closely to the periphery can cause friction with the surfactant shell and may be an explanation for symmetry breaking and the droplet rotation. However, this does not explain the observed rotation in absence of methylcellulose. Thus, a further mechanism for droplet rotation need to be identified.

In this regard, I next raise a hypothesis explaining droplet rotation based on a physico-chemical effect. This is the so-called Marangoni effect. In the following section, this effect will be explained and further underpinned with additional experiments testing self-propulsion of water-in-oil droplets.

5.2.6. The Marangoni Effect as a Driving Force for Self-Propulsion

In the previous sections of this results part I showed the reconstitution of two different cytoskeletal forces within water-in-oil droplets. The myosin-dependent contractile force and the pushing force of rigid actin bundles. Both are key players in locomotion of a living cell. However, in the observed spontaneous droplet propulsion none of these forces seem to be decisive.

Towards artificial and autonomous motion, several groups have studied self-propulsion of water-in-oil droplets based on the Marangoni effect.[216,290] This effect is governed by local inhomogeneities of the interfacial tension (IFT) around a droplet's interface that creates then a net force and due to viscous stresses an Marangoni flow.[212] This flow can, in turn, lead to a motion of a droplet (for more details see Introduction, Section 1.4.5).

In the following section, the Marangoni effect will be explained based on an experiment on macro scale.

5.2.6.1. Marangoni Effect in a Millifluidic Approach

The Marangoni effect has been investigated intensively in different fluidic systems.[212,214] It describes the creation of liquid flows at interfaces due to gradients in the IFT as a result of heterogeneous surfactant mixtures, local chemical reactions, gradients in temperature or surfactant concentrations (see Section 1.4.5 in Introduction).[193] In this regard, Thutupalli *et al.* showed a Marangoni-driven self-propulsion of water-in-oil droplets on top of a surfactant containing oil phase.[216] Here, the effect was mediated by bromine in the aqueous phase that reacted with the surfactants at the interface. This reaction lead to a local increase in IFT, what resulted in the induction of the Marangoni flow and a propulsion of the droplet.

To test if a similar effect can be achieved based on the system I studied in my thesis, I performed the millifluidic approach as described in Thutupalli *et al.* by placing water droplets containing either actin filaments in actin polymerization buffer (see Section 3.5) or the buffer alone on a petri dish filled with HFE-7500 oil plus 1.4 wt% PEG-based surfactant and 0 mM, 1.5 mM or 10.5 mM Krytox. Droplet movement was recorded for 2 min and the trajectories were tracked with Image-J. Figure 82A presents images of aqueous droplets containing only buffer or additional pre-polymerized actin filaments and the trajectories of their movement on top of the surfactant-containing oil phase. For sake of clarity aqueous droplets were labeled with red ink. Whereas all droplets showed some minor motion the motion at 10.5 mM Krytox was more prevalent. Here also a significant difference in velocity could be seen between droplets containing actin filaments and droplets containing only buffer.

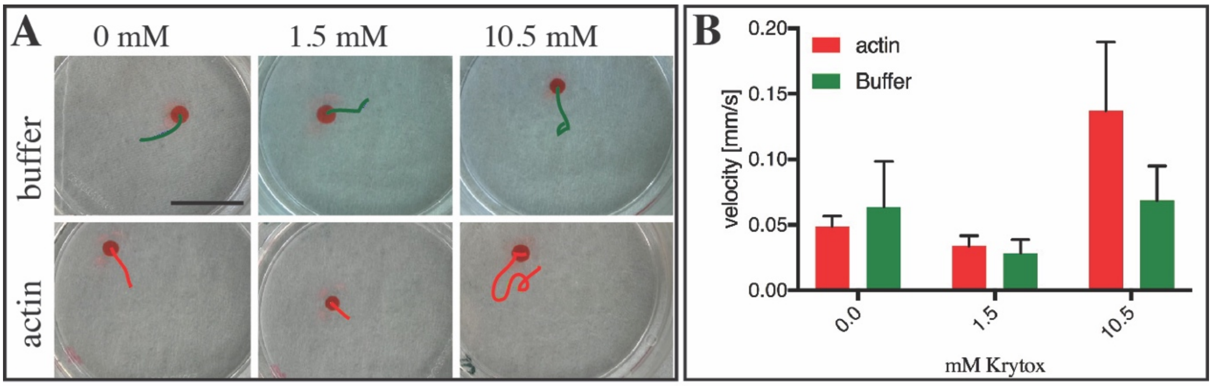

Figure 82: Self-propulsion of millifluidic droplets containing actin polymerization buffer with and without actin filaments (10 µM). (A) Images plus trajectory (2 min) of ink-labeled droplets swimming in a petri dish filled with HFE-7500 oil plus 1.4 wt% PEG-based fluorosurfactant plus 0 mM, 1.5 mM or 10.5 mM Krytox. Scale bar 1 cm. (B) Calculated velocities of protein-free (green) and actin-containing (red) droplets on oil phases containing different amounts of Krytox as indicated below.

Note that a time period of 2 min recording time was chosen, as the droplets ended up eventually at the edge of the petri dish. Thus, based on this experiment no conclusion can be drawn on how long the droplets potentially can perform the observed motion.

The here presented results indicate that actin filaments in combination with Krytox have an effect on self-propulsion of the aqueous droplets on an oil interface. Sincerely, this effect cannot be attributed to pushing forces generated by actin filament polymerization or by actin's bending rigidity, as droplet dimensions are too large to force actin to bend.

Moreover, in my opinion, the here observed droplet motion fits quite well in the theorem of Marangoni. In this concern, actin filaments, located at the droplet's interface, could create local contact points with the interface. Thereby, actin filaments allow for interaction with Krytox molecules from the oil phase. The interaction of Krytox with proteins can lead to an increase in interfacial tension [206] and thus, to a inhomogeneous IFT of the droplet. This inhomogeneity is maintained by the attraction of actin filaments to Krytox and by the constant desorption and adsorption of new Krytox molecules to that contact point forming thereby a "stagnant cap". These Krytox patches lead to an inhomogeneous interfacial tension of the droplet's interface, thus, can induce the Marangoni flow and the motion of the droplet. Figure

83 shows a schematic representation of the described mechanism. The large arrow at the right side indicate the motion of the droplet in the case that there is no friction with the glass and only one stagnation point of actin-interface interaction. When there is friction with the glass, this motion will be turned into a rotation as observed in case of microfluidic droplets in an observation chamber.

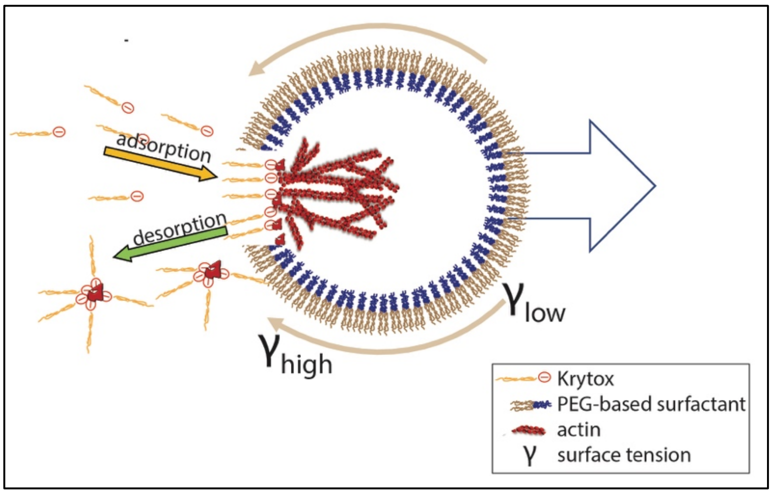

Figure 83: Schematic representation of self-propulsion of actin-containing water-in-oil droplets based on the Marangoni effect.

Clearly, the Marangoni experiment presented here is only in a limited way comparable to the rotation observed in the microfluidic droplets. The 10.5 mM Krytox necessary for droplet motion in the Marangoni experiment seems at first glance not in accordance with the rotation observed in the microfluidic system, where rotation failed by the addition of high amounts of Krytox. However, when considering the 1000 x difference in dimensions and the according difference in surface-to-volume ratios, it is feasible that for microfluidic droplets Krytox traces in the surfactant (1% Krytox) may be enough to generate the above described scenario.

The drop in ionic strength and pH in the presence of high amounts of Krytox and large surface-to-volume ratios – as in microfluidic droplets – can lead to a fast depolymerization of the filaments (see Section 5.2.3.4). This allows the monomers to interact homogeneously with the interface. In this case, a Marangoni effect cannot be expected.

Further, it can be speculated about why the methylcellulose-driven bundling of actin fibers lead to a more prevalent droplet rotation: Through the described depletion effect actin filaments are less diffusive and actin filaments are localized within few bundles. Moreover, as they assemble at the periphery to minimize the bending energy costs Krytox molecules have easy access to interact with the filaments. This may favor the Marangoni effect and thus, droplet rotation.

In a recently published paper within our group, the same microfluidic water-in-oil system has been used to create microtubule networks within droplets.[291] Here no rotation of the filament-containing droplets could be observed. This may be explained by the fact that microtubules' polymerization happens much slower (observable by eye) than the actin polymerization in the here presented approach, which happened already in the channel of the production device (see Section 5.2.3.3). Thus, initially the tubulin (microtubule monomers) is distributed in the whole droplet and may interact homogenously with the periphery. Consequently, no Marangoni effect evolves.

Towards the creation of autonomous motion, I tested the Marangoni flow in microfluidic protein-free droplets. In this regard, I encapsulated positively charged $CaCO_3$ beads[292] into droplets in order to generate a local interaction with the interface. This will be presented in the following.

5.2.6.2. Self-Propulsion in Protein-Free Droplets

The here used porous $CaCO_3$ beads shown in Figure 84 were developed by Dr. Rongcong Luo (Postdoc, MPI, Prof. Spatz Department) and produced by Dr. Ilia Platzman (Group leader, MPI, Prof. Spatz Department) by means of colloidal crystallization and encapsulation of FITC-dextran molecules.

To test the here presented hypothesis that a Marangoni flow can be induced by a local interaction of encapsulated content with the Krytox-containing surfactant interface, I encapsulated these $CaCO_3$ beads into the water-in-oil droplets stabilized by 1.4 wt% PEG-based surfactant with 10.5 mM Krytox through a simple shaking approach (see Section 4.6.2.1).

Figure 84 shows merged bright-field and fluorescence images of droplets containing a $CaCO_3$ bead localized at the periphery of the droplet. Note that the green fluorescence comes from the release of the FITC-Dextran from the beads.

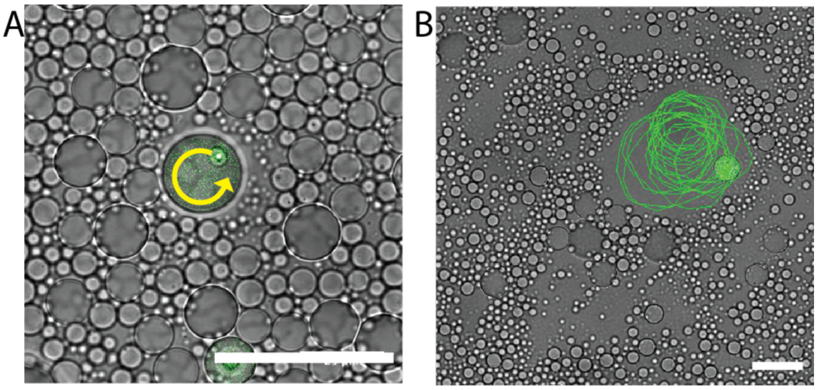

Figure 84: Merged bright-field and fluorescence images of $CaCO_3$ beads containing fluorescently labeled dextran (FITC) encapsulated in water-in-oil droplets, stabilized by 1.4 wt% PEG-based surfactant and 10.5 mM Krytox. (A) Droplet with a $CaCO_3$ bead localized at the periphery of the droplet shows rotation indicated by the arrow (1 rotation in ≈50 sec) (B) Trajectories of a second $CaCO_3$ bead-containing droplet that performs an orbital movement at velocities of 32.2 +/- 0.5 µm/s. Scale bar 50 µm.

In accordance to the here presented hypothesis time-lapse analysis revealed a rotation of the droplet (around 1 rotation in 50 sec). Even more remarkable was the phenomenon observed in another droplet. Here, the bead-containing droplet showed an orbital movement with a significant velocity of around 32.2 +/- 0.5 µm/s (trajectories in Figure 84B). These observations are in accordance with the above mentioned hypothesis that a local interaction of encapsulated content (here a positively charged $CaCO_3$ bead) can lead to self-propulsion of the droplets.

However, importantly, further investigations need to clarify if the observed self-propulsion in this case is not based on a different effect due to the dissociation of the $CaCO_3$ beads into Ca^{2+} and CO_2.

By writing the last sections I raised and discussed critically a hypothesis explaining the observed rotational movement in actin-containing as well as in protein-free water-in-oil droplets. This hypothesis is based on the Marangoni flow an effect that evolves at interfaces, which comprise local heterogeneities in interfacial tension.

The locomotion of a living cell clearly involves contractile and pushing forces of the actin network. Both of these forces I could reconstitute in the here presented artificial cell approach, but none of these were decisive for the observed self-propulsion.

Besides the cytoskeleton, the complex machinery of cellular locomotion includes also many other factors as signaling molecules and interaction with the extracellular environment. Moreover, the cell membrane is supposed to contribute to the migration process, since it needs to be enlarged when the cell body is protruded.[61] The additional membrane surface is supposed to be provided by exocytosis of internal vesicles at the front of the cell body and the according endocytosis at the rear of the cell[62] resulting in a lateral membrane flow (see Introduction Section 1.2.1.3).[61] Interestingly, in amoebas it was observed that this membrane flow flows in the same velocity as the forward movement of the cell. Thus, it is feasible that it is directly involved in the propulsion mechanism of this cell.[64] Moreover, a theoretical model showed that tangential travelling surface waves could cause a translational movement in spherical micro-sized objects.[293] Anyway, the exact contribution of this membrane flow is not well understood and require further investigations.[62] In this regard, the presented self-propulsion of the water-in oil droplets in my thesis could serve as an adequate model system since it mimics similar membrane flows as described in living cells.

The fact that such a phenomenon of membrane flow is still seen in today's living cells allows for the assumption that this mechanism may have also generated cellular motion in early evolutionary life.

Part II: Summary

In Part II of the results, I investigated in a bottom-up synthetic cell approach the major forces involved in cellular motility: an actin-based pushing and an actomyosin-based contractile force.

In this regard, I reconstituted actin and actomyosin cytoskeleton networks within water-in-oil droplets. Pushing forces were generated by tuning the rigidity of the filaments through crosslinking them based on the depletion effect. Contractile forces could be generated by combining actin cytoskeleton with myosin motor II.

Moreover, I could show a self-propulsion of the actin filament-containing droplets and I presented a hypothesis about the mechanism behind the droplet rotation that is – in contrast to motility in today's eukaryotic cells – mainly independent of pushing and contractile forces, but based on the Marangoni flow.

Part III

5.3. The Reconstitution of Adhesion-associated Proteins within dsGUVs

Besides the cytoskeletal machinery, the other key feature in cell motility is the adhesion of the cell body to the extracellular substrate. The adhesion is mainly mediated by transmembrane integrin receptors, which balance the applied forces and build together with associated proteins a mechanosensitive linkage to the actin cytoskeleton.

In this regard, I set out to reconstitute adhesion receptors, more specifically the transmembrane protein, $\alpha_{IIb}\beta_3$ integrin, in droplet-stabilized GUVs (dsGUVs). Moreover, after studying the actin cytoskeleton within the surfactant shell in the previous section, I want to move towards a more physiological compartment interface and reconstitute also the cytoskeletal network with dsGUVs. These resemble the eukaryotic cell much better than the surfactant shell itself. After assembling the actin network and the integrin transmembrane receptors individually within dsGUVs, I combined both functional modules, and thereby created an artificial cell featuring the key structures, adhesion receptors and cytoskeleton, of cellular motility combined.

In a living cell, integrin proteins are connected to the actin cytoskeleton via a dynamically interacting and mechanosensitive protein machinery. The reconstitution of the entire adhesion machinery in an artificial cell would be far too complex, thus, I reached out to identify a minimal set of purified proteins, linking the integrin to the actin cytoskeleton, in order to create a minimal adhesion complex. To assess the success, I performed protein binding assays in bulk and QCM-D studies. Thereby, I identified a protein fragment of talin, the talin head domain (THD) as a potential linker between integrin and actin.

Importantly, an artificial cell comprising these major building blocks for cellular motility as reconstituted in this thesis has never been reported. Therefore, the outcomes of this thesis might pave the way towards better understanding of the fundamental function of cellular motility and its assembly.

5.3.1. Actin Networks within dsGUVs

The dsGUVs provide a physiologically more relevant compartment interface than the surfactant shell itself. Thus, I reached out to reconstitute an actin cytoskeletal network within dsGUVs. Towards this end, two approaches were used. The first approach involved an automated microfluidic picoinjection device (see Section 4.3.1) allowing step by step assembly of functional modules in water-in-oil droplets. For these experiments the dsGUVs were produced with 1.4 wt% inert PEG-based surfactant and 10.5 mM Krytox and afterwards introduced into the picoinjection device (shown in Figure 85 and in Section 4.3.4) and actin monomers were injected into these dsGUVs containing as an aqueous phase the actin polymerization buffer.

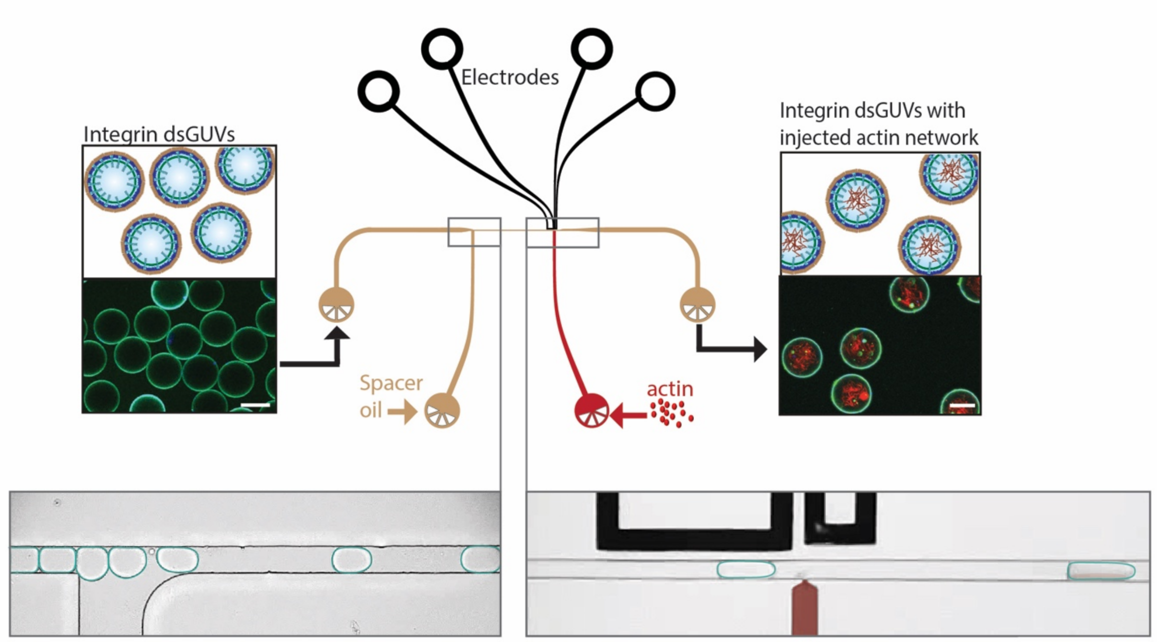

Figure 85 Assembly of an actin cytoskeleton within dsGUVs by microfluidic picoinjection. Following the formation, dsGUVs (insets upper left) were introduced into a high throughput picoinjection device (draft in the middle). Entering dsGUVs are laterally separated by an incoming oil stream (inset lower left) before approaching an electric field that leads to a poration of the surfactant shell. This allows the injection of actin monomers into the dsGUVs, when passing the injection channel (inset lower right). Insets on upper right show dsGUVs containing polymerized actin network. Scale bar 25 µm.

The second approach for the assembly of actin networks within dsGUVs is a one-step approach based on the production device with two aqueous inlets (see Section 4.3.1). Figure 86A shows two aqueous inlets: the first inlet delivers actin solution and the other provides SUVs for dsGUV formation and the actin polymerization buffer. Similarly, to the assembly of actin networks in lipid-free droplets, the actin monomers were mixed with the polymerization buffer only upon droplet formation. The droplets were stabilized by 1.4 wt% inert PEG-based surfactant and 10.5 mM Krytox.

Note that agglomeration of actin networks with the SUVs were observed for neutral and positively charged lipids. In these cases, the formation of a continuous lipid bilayer was hampered. To prevent these interactions between actin and SUVs, SUVs needed to comprise at least 10% negatively charged DOPG lipids. In this regard, the $MgCl_2$ concentration needed to be adjusted depending on the concentration of negatively charged lipids as Mg^{2+} ions interact with the lipids and hence are not available for actin polymerization.

Figure 86B shows fluorescence images of actin-containing dsGUVs produced by a microfluidic two-inlet production device.

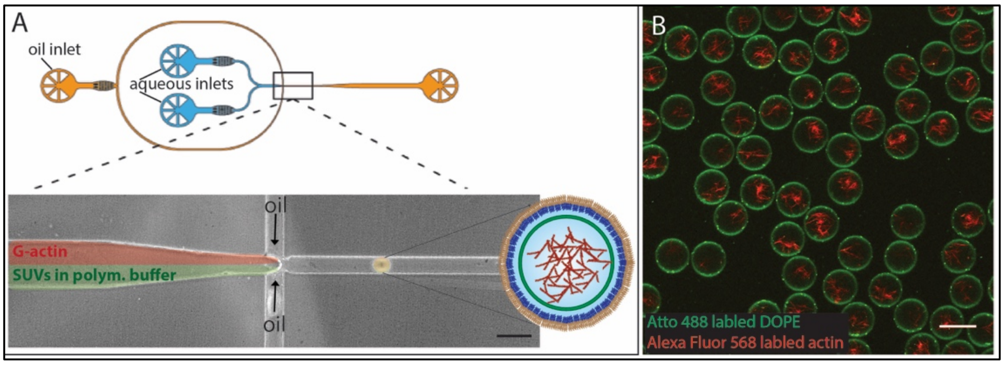

Figure 86: One-step production of dsGUVs containing actin networks by means of a droplet production device with two aqueous inlets. (A) Sketch of the production device. One aqueous phase with actin monomers (20 µM, 1% actin is Alexa Fluor 568 –labeled) in its storage buffer. Other aqueous phase with SUVs (34.75% DOPC, 34.75% POPC, 30% DOPG, 0.5% Atto488-DOPE) and double concentrated polymerization buffer. (B) Fluorescence images of dsGUVs containing actin networks. Scale bars 50 µm.

5.3.1.1. Release of Actin-Containing GUVs into an Aqueous Buffer

As shown in Section 5.1.4, protein-free dsGUVs can be released efficiently out of the surfactant shell and oil phase into aqueous buffers. The release of actin-containing GUVs could be achieved here as well (see Figure 87), however, in a much lower efficiency.

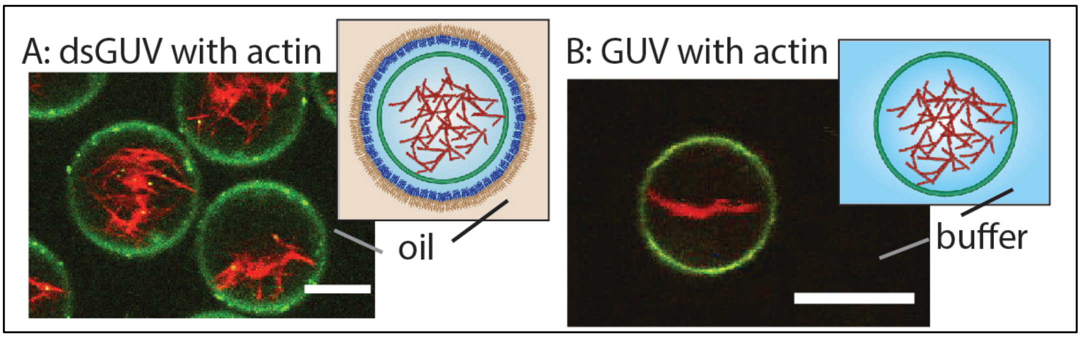

Figure 87: Representative fluorescence images of dsGUVs containing actin networks before release (A) and the corresponding released actin-containing GUV in aqueous buffer (B). Scale bar 10 µm.

A reason for the low efficiency could be that the negatively charged actin molecules interact similarly like the lipids with the charged surfactant shell and thereby interfere with the formation of a continuous lipid bilayer. To overcome this condition, the picoinjection, in which the actin is introduced into preformed dsGUVs, is advantageous in comparison to the one-step assembly.

The assembly of actin networks within GUVs has been reported in several studies in the last decades.[294] The encapsulation of actin into GUVs were mainly based on the method of gentle hydration.[162,163] This approach has a similar pitfall in yield, however, is less flexible than the here presented dsGUV approach, where GUVs can be equipped with further molecules before released into the aqueous phase.

In the next section, I will describe the reconstitution of additional biomolecules into the dsGUVs –towards the creation of a membrane-bound actin cortex – and its limitations.

5.3.1.2. Actin-dsGUV Linkage via Biotin-Streptavidin Chemistry

Whereas in a living cell, the actin network is connected to the lipid membrane by a complex of anchoring proteins, in synthetic cell approaches, much simpler connections of actin networks with the lipid membrane have been reported e.g. via biotin streptavidin interactions.[174]

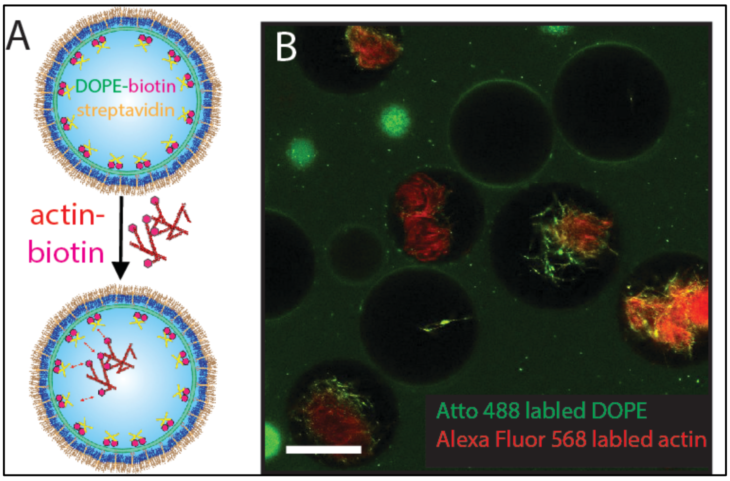

Figure 88: Streptavidin-biotin-approach to link actin to the lipid membrane of dsGUVs. (A) Sketch of SUVs (59.5% DOPC, 20% DOPG, 20% biotinylated DOPE, 0.5% Atto488-DOPE) in actin polymerization buffer plus 50 µM streptavidin (in yellow) are used to produce dsGUVs. Actin monomers (1% biotinylated, 1% Alexa Fluor 568 labeled) were subsequently picoinjected. (B) Fluorescence images of the streptavidin-biotin-approach to link actin filaments to the lipid membrane of dsGUVs. Biotin-streptavidin interactions lead to the destruction of lipid bilayer and agglomeration of lipids within the actin network. Scale bar 50 µm.

Streptavidin has four binding sites for biotin.[295] Thus biotinylated lipids are supposed to attract the streptavidin from the solution, which provide, in turn, thereby binding sites for biotinylated actin filaments (see Figure 88A). Towards this end, in my thesis, SUVs containing 20% of biotinylated DOPE lipids and a buffer containing 50 µM streptavidin were used for dsGUV production. In a second step actin monomers (1% biotinylated, 1% Alexa Fluor 568 labeled) were picoinjected into the dsGUVs.

However, this approach did not succeed as no actin cortex has been formed at the membrane as shown in Figure 88B. Moreover, the lipids detached from the surfactant shell and accumulated within the actin network or leaked into oil phase. Note that lipid leakage into the oil phase could be attributed to shearing forces within the picoinjection device.

Other studies showed linkage of actin networks to positively charged lipid membranes via electrostatic interactions.[87,171] However, such an approach lead in the here presented system to a similar agglomeration of the lipids within the actin network as seen in the biotin-streptavidin approach.

Therefore, I focused on the reconstitution of a nature-inspired connection. Towards this end, I reached out to connect the actin network to the membrane via the transmembrane protein $\alpha_{IIb}\beta_3$ integrin. This connection is of major importance in cellular motility, since it forms the mechanosensitive linkage responsible for the coordinated attachments at the front and the breakage of old attachment sites at the rear of the cell and further initiate many signaling pathways.[296] Before combining both building blocks, I first reconstituted the $\alpha_{IIb}\beta_3$ integrin within the membrane of dsGUVs alone. This approach will be presented in the next section.

5.3.2. Reconstitution of Integrin in dsGUVs

$\alpha_{IIb}\beta_3$ integrin. was purified by Christine Mollenhauer from outdated human blood platelets (Katharinenhospital Stuttgart) (see Section3.4.3).

In order to create integrin-reconstituted dsGUVs, $\alpha_{IIb}\beta_3$ integrin was in a first step reconstituted into liposomes composed of 50/50 (n/n)% eggPC and eggPG as previously described (see Section 4.7.3). In a second step these proteoliposomes were mixed 1:10 with SUVs (34.75% DOPC, 34.75% POPC, 30% DOPG, 0.5% Atto488-DOPE) and were subsequently used for dsGUV formation in a droplet production device. Figure 89A shows a merged fluorescence image of the successful reconstitution of fluorescently labeled α_{IIb}ß$_3$ integrin (Alexa Fluor 568, here shown in blue) within the lipid bilayer (labeled with Atto 488, in green) of a dsGUV.

Remarkably, the release of the integrin-GUVs into an aqueous buffer was successful. Thus, integrin-GUVs can be used for adhesion studies in parallel projects in our group.

The here presented approach of reconstitution of integrins into dsGUVs and releasing such GUVs into the aqueous phase was recently published in Weiss and colleagues.[16] Only one other study reported the reconstitution of integrin receptors into GUVs.[297] This indicates that the reconstitution of integrins into GUVs by standard methods is quite challenging.

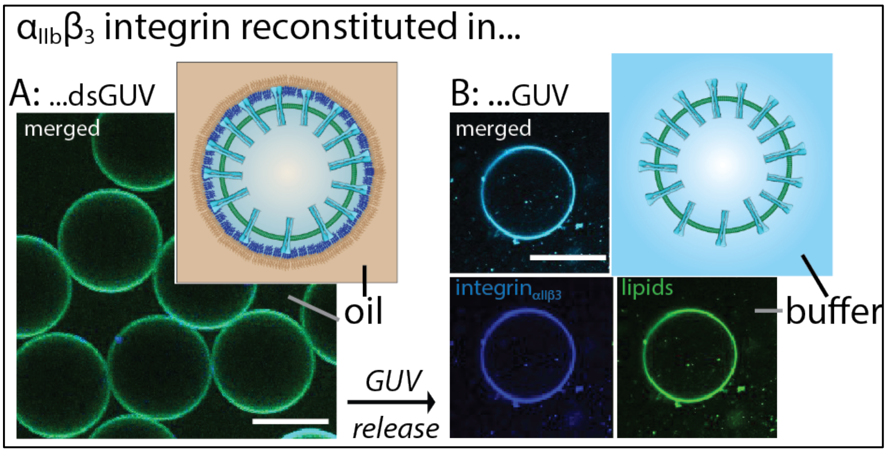

Figure 89: Representative fluorescence images of $\alpha_{IIb}\beta_3$ integrin in the bilayer of dsGUVs (A) and in GUVs after their release from the surfactant shell and oil phase into an aqueous buffer (B). $\alpha_{IIb}\beta_3$ integrin is labeled with Alexa Fluor 568 (here in blue) and lipids are labeled with Atto488 (here in green). Scale bar 25 µm

Generally, whereas the reconstitution of active membrane proteins into small liposomes is straight forward, the reconstitution into GUVs is difficult, due to the GUV's mechanical instabilities and harsh preparation conditions.[117] Therefore, I would like to emphasize the great advantage of the here presented method to reconstitute integrin proteins into GUVs. Moreover, other membrane proteins such as ATPase were shown to be functionally reconstituted by this method.[16] This success makes this approach universal for reconstitution of transmembrane proteins and allows to bypass the difficulties associated with standard preparation protocols.

5.3.3. DsGUVs with Reconstituted Integrins and Actin Networks

Next, I investigated the addition of actin networks into the integrin-reconstituted dsGUVs. This was achieved similarly as described before in Section 5.3.1: actin was either introduced after dsGUV formation via picoinjection or the one-step approach with a two-inlet production device was used. Here, one of the aqueous channel contained the SUVs (34.75% DOPC, 34.75% POPC, 30% DOPG, 0.5% Atto488-DOPE) together with the proteoliposomes and the actin polymerization buffer and the other inlet contained the actin monomers (20 µM in actin storage buffer). Figure 90 shows the successful reconstitution of $\alpha_{IIb}\beta_3$ integrin and actin networks within a dsGUV. In this experiment, the $\alpha_{IIb}\beta_3$ integrin was fluorescently labeled with Alexa Fluor 568 (shown in blue), 1% of the actin was labeled with Phalloidin Alexa Fluor 647 (shown in red) and 0.5% of the lipids were labeled with Atto488 (shown in green).

The successful reconstitution of integrin and actin network within an artificial cell has never been shown before and thus, need to be highlighted as a great achievement of this thesis and an important step towards the construction and understanding of fundamental functional modules of a living cell.

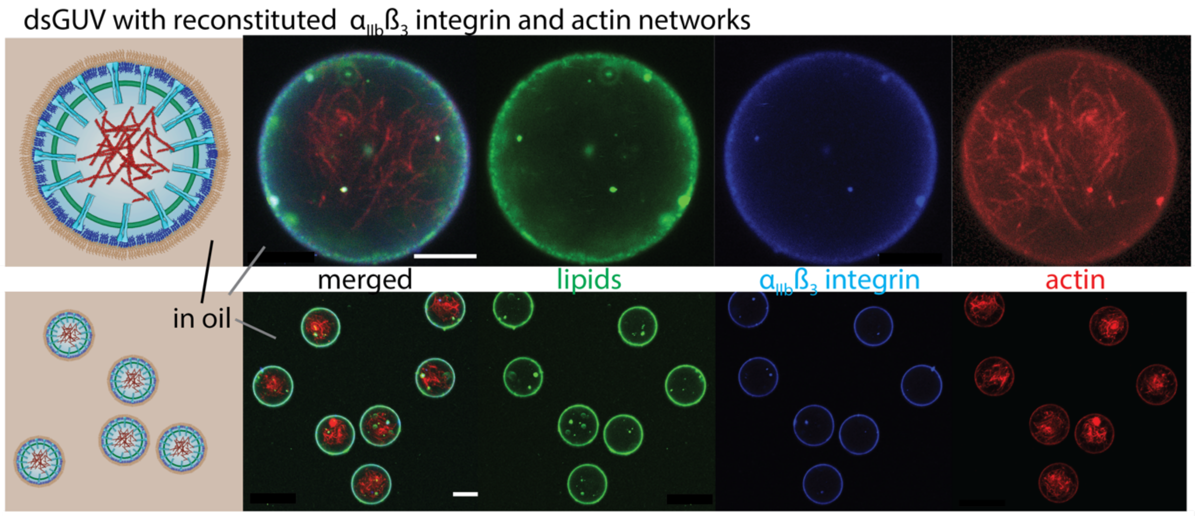

Figure 90: Representative fluorescence images of dsGUVs containing lipids (34.75% DOPC, 34.75% POPC, 30% DOPG, 0.5% Atto488-DOPE (shown in green)), $\alpha_{IIb}\beta_3$ integrin (Alexa Fluor 568 labeled (shown in blue)) and actin networks (1% of the actin is labeled with Phalloidin Alexa Fluor 647 (shown in red). Scale bar 10 µm.

5.3.4. Assembly of Minimal Adhesion Complexes

In a living cell the integrin transmembrane receptors bind with their extracellular part to proteins of the extracellular matrix and with their intracellular part to the actin cytoskeleton. This integrin - actin connection is not direct and involves several anchoring proteins (see Section 1.2.1.2 in Introduction).[53] In order to reconstitute such a adhesion complex in a synthetic cell, the protein complex has to be dissected to its very basic structure and a minimal set of purified proteins that connects the integrin to the actin network has to be identified. In this regard protein binding studies by means of QCM-D measurements and pull-down binding assays have been performed in bulk.

5.3.4.1. Binding Studies to Identify a Linker Between Actin and Integrin

In the following section, I reached out to identify anchoring proteins for the assembly of a minimal adhesion complex. In close cooperation with the protein expression and purification facility at the Weizmann Institute in Israel relevant actin or integrin binding proteins were selected to be expressed and tested for their integrin and actin binding (see Figure 91). These included focal adhesion kinase (FAK), integrin linked kinase (ILK), full length talin and talin head domain (THD). Other proteins as α-actinin were purchased from cytoskeleton.

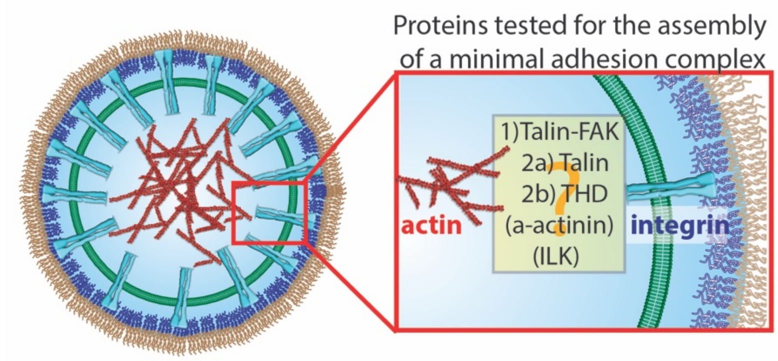

Figure 91: Sketch of possible protein linkers, to assemble a minimal adhesion complex.

The binding affinities of FAK, full length talin and THD to integrin /actin are investigated in the following.

5.3.4.1.1. Integrin - Focal adhesion kinase (FAK) interaction

The adhesion-associated protein FAK is supposed to be closely involved in the connection of integrins to the actin network. It comprises binding sites for integrin, as well as for talin, which, in turn, binds to the actin network.[298] Thus, as a first step the binding of FAK to $\alpha_{IIb}\beta_3$ integrin was tested using QCM-D. Figure 92A shows the sketch of the sequential application of the used proteins onto the QCM-D crystal, and Figure 92B the according frequency and dissipation change of the QCM-D sensor.

First, the QCM-D crystal was functionalized with the extracellular matrix protein fibrinogen which is a natural binding partner for $\alpha_{IIb}\beta_3$ integrin[51] (for further details see Section 4.8.1). Following the functionalization, $\alpha_{IIb}\beta_3$ integrin was introduced. The binding of fibrinogen and integrin could be observed in the QCM-D as an increase in dissipation and a decrease in frequency. Upon introduction of FAK, a similar dissipation and frequency change could be observed, indicating a FAK-integrin interaction.

It is worth to mention that further proteins, integrin-linked kinase (ILK) and α-actinin, was tested for integrin binding (see Appendix, Figure SI 7E, F). In this case, no affinity for integrin could be detected.

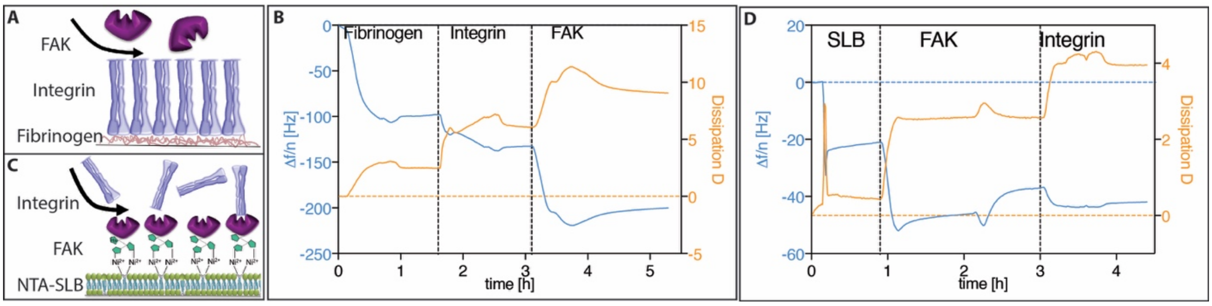

Figure 92: QCM-D measurements to study the binding of FAK to $\alpha_{IIb}\beta_3$ *integrin. A) and C): sketches of the sequential introduction of proteins onto the QCM-D crystal to test FAK integrin binding. B) and D): QCM-D data including dissipation and frequency changes upon protein binding on the crystal.*

To confirm FAK-integrin binding a second approach was applied (Figure 92C and D). Here a supported lipid bilayer (SLB) was formed on top of the QCM-D crystal by introducing SUVs (eggPC) onto the oxygen plasma treated silica surface (for further details about 2D SLB see Introduction Section 1.3.3). SLB formation could be nicely observed in a sharp dissipation peak which represents the adhesion of SUVs (high dissipation) on the crystal and the following transformation of the SUVs to a thin rigid bilayer (drastic decrease in dissipation). These observations are in accordance with SLB formation on QCM-D crystals in other studies.[262,299,300] The SLB comprised 5% NTA-Ni^{2+} labeled lipids on which FAK via its His-tag could be immobilized. Following the introduction of $\alpha_{IIb}\beta_3$ integrin, the binding of integrin to FAK could be observed in an increase in dissipation and a decrease in frequency. (see Appendix for estimated adsorbed mass, see Sauerbrey and Voigt model estimations Table SI 6 and for controls Figure SI 7A, B). This interaction is also in agreement with other studies that showed a FAK-integrin binding *in vitro* in a pull-down assay.[301]

Besides FAK, talin is a major anchoring proteins of actin to integrin.[302] While it is controversially discussed,[298] which of the two proteins is recruited first during the cellular adhesion to the substrate, they mainly appear together, suggesting that they have some binding affinity to each other.[59] However, based on a similar QCM-D approach as depicted in Figure 92A, no binding of talin to FAK could be observed (see Appendix, Figure SI 7D).

However, talin is supposed to comprise also potential binding sites for integrin and further for actin.[303,304] Thus, talin may link integrin to actin without assistance of other proteins. Therefore, next, talin-integrin interactions were tested.

5.3.4.1.2. Talin and Talin Head Domain (THD)

Talin protein was extracted and purified from chicken gizzards by Christine Mollenhauer. As a first step, talin-integrin binding was investigated by means of QCM-D measurements (Figure 93). In this regard, $\alpha_{IIb}\beta_3$ integrin was immobilized on fibrinogen-functionalized QCM-D crystals as described before in Section 4.8.1. When talin was applied on top, no significant change in dissipation and frequency could be observed, indicating that talin was not binding to $\alpha_{IIb}\beta_3$ integrin.

This result might be attributed to the fact that talin can exhibit an autoinhibited alternative structure, in which the talin tail folds up and blocks the integrin binding site.[305] To improve talin-integrin binding performance talin was preincubated with PIP_2-lipids which should bring talin in an active conformation for integrin binding.[306] Contrary to this assumption, a strong signal of unspecific binding of PIP_2 to $\alpha_{IIb}\beta_3$ integrin could be observed independently on the presence of talin (see Appendix, Figure SI 7C). Thus, a recombinant and supposedly active talin fragment, the THD, was used for further binding studies. As it is lacking the tail, autoinhibition is supposed to be eliminated, what should render the integrin binding site freely accessible.[57] To test this, the THD was introduced instead of the full length talin on top of the immobilized $\alpha_{IIb}\beta_3$ integrin on a QCM-D crystal (Figure 93C and D). In that case, a significant decrease in frequency could be observed, indicating the integrin-THD binding. These results are in agreement with previous studies showing the *in vitro* binding of THD with the intracellular part of the β_3 integrin subdomain.[306,307]

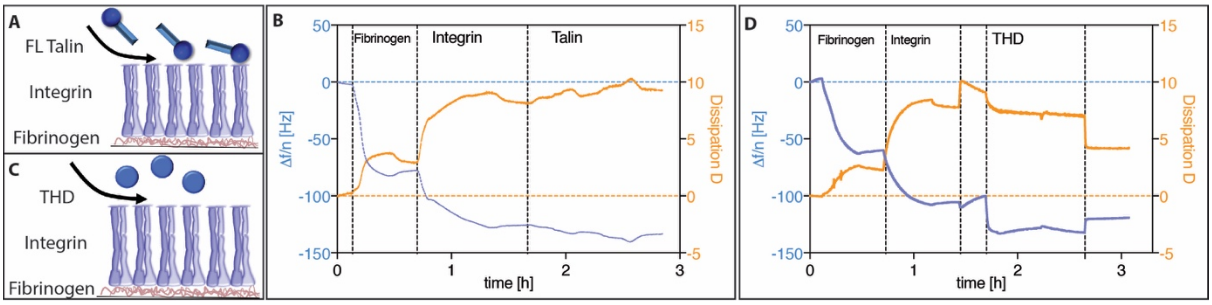

Figure 93: QCM-D measurements to study the binding of full length talin and THD to $\alpha_{IIb}\beta_3$ integrin. A) and C): schematic representation of the sequential introduction of the proteins onto the QCM-D crystal. B) and D) show representative experimental QCM-D data of dissipation and frequency changes upon protein binding on the crystal.

Further a pull-down assay (see Section 4.8.2) was performed to verify THD-integrin interactions. Therefor the recombinant β_3 intracellular integrin domain was attached via its His-tag to NTA-Ni^{2+} beads. Before the THD peptide was introduced to test its binding to the β_3 domain, all free NTA-Ni^{2+} binding sites were blocked with His-tagged ubiquitin. After several washing steps the bound proteins were eluted by imidazole and used for Western blot analysis

(Figure 94). An anti-THD and an anti-His tag antibody were used to detect the THD and the His-tagged β_3-tail, respectively, in the elution fractions. Even though a small amount of THD bound to the beads without β_3 integrin tail, the amount of THD was significantly higher on beads that were beforehand incubated with β_3-integrin. Thus, the binding of THD to $\alpha_{IIb}\beta_3$ integrin measured by means of QCM-D could be confirmed.

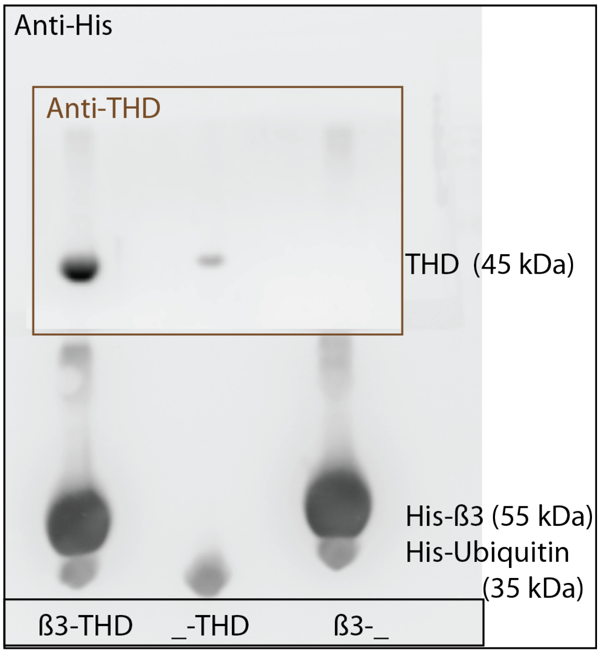

Figure 94: Representative image of a Western blot membrane showing the analysis of THD-β_3 integrin-binding by means of a pull-down assay. 1st band: sample in which THD binds to beads that were preincubated with β_3-integrin tails. 2nd and 3rd band: show control samples of beads without the incubation step of β_3-tails or THD, respectively. Free binding sites were blocked with His-Ubiquitin.

In a next experiment, THD binding to actin filaments was tested by incubating the THD with actin filaments in a micro tube. The unbound molecules were then separated from the actin filaments by a centrifugation step (pull-down). Fractions of the supernatant and the pellet were analyzed by means of SDS-PAGE (Figure 95A) and Western blot analysis (Figure 95B). Besides testing the binding affinity of THD to the actin filaments, a positive and a negative control was performed using the actin binding protein α-actinin and a non-binding protein BSA, respectively. As actin and THD have similar molecular weights and thus, were not distinguishable in SDS-PAGE, a Western blot was performed with an anti-THD antibody and an anti-actin antibody. The blot revealed that THD was partly present in the actin pellet (Row 5) and thus, proved THD-binding to actin.

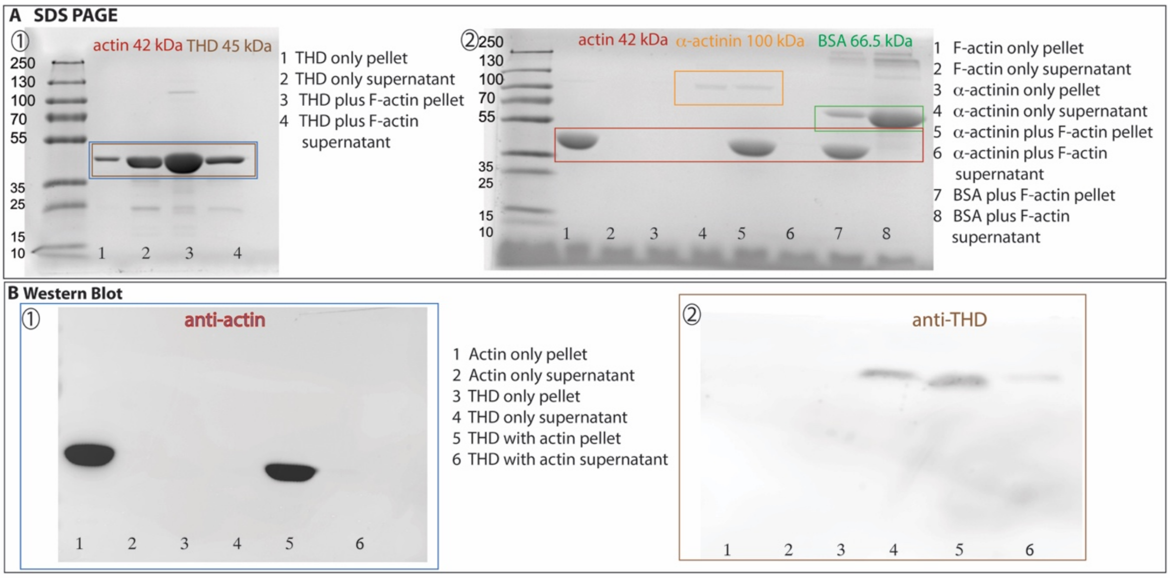

Figure 95: Representative images of SDS-PAGE and a Western blot membrane showing the analysis of a actin filament pull-down assay. (A) SDS-PAGE of pull-down assay: actin incubated with THD (1) and α-actinin and BSA (2). Samples are then centrifuged and pellet and supernatant fractions are used separately for SDS-PAGE analysis. (B) Western blot analysis of pull-down assay. Actin incubated with THD (1) anti-actin antibody and anti-THD antibody (2) showing the presence of these proteins in different pellet /supernatant fractions.

Based on these experiments the THD seems to be a promising candidate to connect integrin to the actin network. This is in accordance with other *in vitro* studies testing THD binding to actin and integrin.[57,308]

To check this further, a combined actin pull-down assay with integrin and THD was performed. In this respect, if THD connected the actin to integrin all three proteins would be found cosedimented after centrifugation. Contrary to this assumption, neither THD nor integrin was found cosemdimented with the actin filaments (see Figure 96).

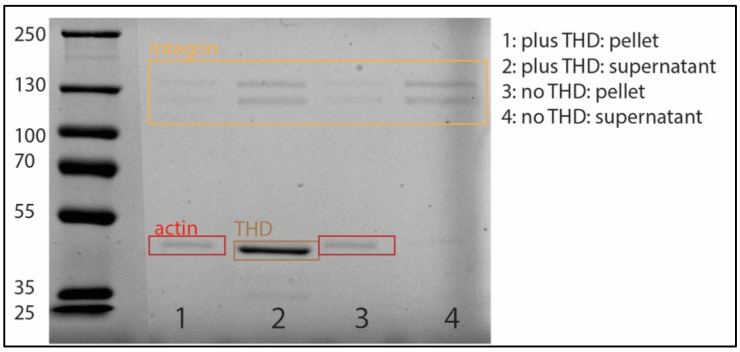

Figure 96: Representative image of SDS-PAGE showing the analysis of a F-actin pull-down assay where actin filaments are incubated with/without THD and integrin in actin polymerization buffer. Samples are then centrifuged and pellet and supernatant fractions are used separately for SDS-PAGE.

This means that the THD has probably a stronger binding affinity to integrin than to actin. In this regard, binding conditions need to be adjusted in future experiments to improve THD binding to actin, which is supposed to be optimal in low ionic strength and at pH of 6.4.[304] Thus, in future experiments the focus should be especially dedicated to testing a variety of buffers to improve the THD binding affinity to actin.

These results show that the more complex an artificial cell gets, the more difficult it is to find buffer conditions that meet all the requirements of implicated building blocks.

Generally, this may even get more difficult when building blocks of different functional modules are supposed to be combined. In some of these cases, compartmentalization like the presented multicompartment system (Section 5.1.2) can be used for the successful assembly of different functional modules in parallel.[97] Alternatively, synthetic building blocks e.g. DNA nanotechnology[98] or protein engineering[309] can be used to create more robust and adaptable building blocks.[97]

Part III: Summary

In Part III of the results, I combined the key building blocks of cellular motility within the synthetic cell approach.

First, integrin receptors and actin cytoskeleton were reconstituted within the dsGUVs separately. Then both functional modules where combined, thereby creating a synthetic cell comprising cytoskeletal and adhesion functional modules within in a physiological lipid membrane-based compartment.

Remarkably, this has never been shown before somewhere else.

Moreover, to resemble the mechanosensitive protein complex between actin and integrin that mediates cellular motility in a living cell, protein binding studies have been performed. Thereby a linker has been identified that may be used in this sense in future synthetic cell experiments.

Summary and Outlook

6. Summary and Outlook

6.1. Summary

In this thesis, the concept of bottom-up synthetic biology has been implemented to reconstitute structural and functional modules of a eukaryotic cell in an artificial and minimal system. In this regard, major achievements have been reached that will pave the way towards the understanding of cellular functions such as cytoskeletal forces and network arrangements, cytoskeletal interaction with integrin transmembrane receptors, as well as cell motility. The concept of minimal cell systems with distinct functionalities and structures allows for the better understanding of how the first form of life – probably similarly simple – has evolved on Earth.

The technological aspect in my thesis needs to be particularly emphasized. I used automated microfluidic technology to create cell-sized water-in-oil droplets as a basic model for synthetic cells. This microfluidic technology allowed for high throughput production of stable and, therefore, manipulatable synthetic cell systems with a well-defined chemical and biophysical microenvironment. The enhanced stability of the developed compartments enabled their loading with lipids, transmembrane proteins and cytoskeleton actin proteins without compromising the functionality of the synthetic cells.

The stability of the water-in oil droplets is governed by polymer-based surfactants. In my thesis, I showed that these surfactants can not only passively stabilize the water-in-oil droplets, but can be also used to manipulate the encapsulated droplet content depending on the choice of surfactant molecules in the oil. In this vein, I provided a detailed characterization of how the physico-chemical properties of the droplet's interface can be tuned by the use of differently charged surfactant molecules. The physico-chemical properties of the interface were then shown to govern the assembly of cellular modules within the droplet.

I then utilized this newly found knowledge of the surfactant's role in the droplet's interface for the reconstitution of cellular membrane structures that mimic their presentation in a eukaryotic cell, namely an outer phospholipid membrane and multiple internal compartments. Towards this aim, lipid vesicles were encapsulated into the droplets and, depending on the lipid's charge, interactions between the lipids and the droplet interface could be either permitted or inhibited. Successful implementation of this approach allowed for on-demand production of the following synthetic cell structures:

1) Spherically supported lipid bilayers, called droplet-stabilized giant unilamellar vesicles (dsGUVs) that resemble the outer lipid membrane of a eukaryotic cell;

2) Multicompartment systems, in which encapsulated vesicles are randomly distributed in the droplet volume, resembling organelles of a living cell;

3) A combination of these two membrane structures, thereby creating a synthetic cell with an outer lipid membrane as well as internal organelle-like structures.

The presented approach is extremely versatile in that after the assembly of such membrane structures within the water-in-oil droplets, free-standing GUVs can be released out of the surfactant shell into a physiological aqueous environment. Hence, this approach combines the advantages of both the initial mechanical stability provided by the water-in-oil droplet and the physiological relevance of free-standing GUVs.

The release process of GUVs based on lipid and surfactant charge was analyzed in great detail in this thesis. The released GUVs were also characterized based on their size, purity and unilamellarity. Furthermore, the released GUVs were shown to be receptive to further manipulation, allowing for the generation of vesicles with high surface-to-volume ratio as is seen in some eukaryotic organelle structures, e.g. mitochondria.

In the second part of my thesis, I focused on recapitulating cellular motility within water-in-oil droplets. Towards this aim, I broke down the complex machinery mediating cellular motility into three major elements and reconstituted these elements within water-in-oil droplets:

1) The elongation of the cell body at the front was implemented by rigid actin filaments that, upon minimizing their bending energy, pushed against the droplet wall.

2) The contraction of the cell rear was achieved by the addition of myosin motors to the actin cytoskeleton, thereby creating a contractile cytoskeletal network.

3) The attachment of the cell body to the substrate was represented by the integration of integrin transmembrane receptors within the lipid membrane of the dsGUVs.

Expanding on the achievement of reconstituting each of these three key elements in a synthetic cell separately, I then worked to combine all of these processes in one compartment. This resulted in a synthetic cell featuring cytoskeletal as well as adhesion-associated functional modules, which has never been accomplished before.

In a living cell, elongation and contraction of the cell body interplays with substrate attachment and detachment. This dynamic feedback mechanism is based on many proteins and signaling molecules connecting the actin cytoskeleton to integrins in the membrane. The reconstitution of such complex machinery in a synthetic cell has, to-date, proven too complex to achieve in the laboratory. Thus, in my thesis, I focused on determining a minimal linkage between actin and integrins in bulk binding assays. To do this, I implemented the highly sensitive and label-free QCM-D technique, as well as pull-down assays, SDS-PAGE and Western blot. Based on these techniques, I identified the THD protein fragment comprising binding sites for actin and integrins, and which could be used in future synthetic cell approaches.

When investigating cellular motility in a synthetic system, the ultimate goal is the generation of synthetic motion. In the last part of my thesis, this goal was accomplished. Surprisingly, the most obvious mechanisms in cellular motility, i.e. actomyosin-based, were shown to not be the driving force for the motility of the synthetic cells presented here. In contrast, the self-propulsion was explained by a physico-chemical effect that evolves on an interface with local changes in interfacial tension, the so-called Marangoni effect. In the case of actin-containing water-in-oil droplets, heterogeneous interfacial tension is caused by the interaction of the encapsulated actin filaments with the interface. The mismatch of interfacial tension results in a force that creates, due to viscous stresses, a flow along the interface. This flow in turn propels the droplet. Interestingly, such flows along the membrane have also been reported in cells, however, the precise mechanism has yet to be elucidated. In amoebae, these flows have shown to be directly linked to locomotion, thus, a parallel can be drawn between this semi-simple system of an amoebae and our simple synthetic cell, thereby leading to the assumption that such membrane flows may have been essential in early evolutionary life.

Taken together, the results presented here show that microfluidic water-in-oil droplets provide a powerful platform for synthetic biology with wide-ranging possibilities to study functional cellular modules.

6.2. Outlook

In this section I would like to present my view over the future perspective of the scientific achievements developed in this thesis.

Charged-mediated formation of droplet-stabilized biostructures. In the first part of my thesis I showed that the physico-chemical properties of polymer-based membranes can be precisely controlled. I presented that by a proper selection of charged and inert polymer-based surfactant molecules for the water-in-oil droplets production, the encapsulated SUVs with different lipid charge can be recruited to the surfactant shell forming droplet-stabilized GUVs. This charge-mediated approach might be extended for the recruitment of proteins to the periphery, thereby creating droplet-stabilized protein capsules. First experiments in the group showed that when the proteins are crosslinked at the periphery of the droplet, the resulting protein capsules can be released into a physiological buffer. By an intelligent design cells could be potentially encapsulated within the preformed ECM-based protein capsules. In such a way cell-containing ECM-based capsules might be generated for various biophysical and biomedical applications such as 3D printing of tissues or organoids.

Functional multicompartment systems. In this thesis, I showed that the precisely controlled phyico-chemical properties of the droplet's interface allow for the creation of multicompartment systems enclosed in a dsGUV. This was achieved by the selective, charge-mediated recruitment of encapsulated SUVs with certain lipid charge to the surfactant shell, and at the same time leaving SUVs with a different charge unaltered as organelle-like structures within the dsGUV lumen. To elevate this approach to a next level, functional modules can be included within the encapsulated SUVs. By doing so, multiple isolated reactions might be initiated in one artificial cell. Moreover, for sequestered reactions, functionalized phospholipids, e.g. pH-sensitive lipids or phospholipids with distinct phase transition temperatures could be used to create the internal SUVs. By the subsequent manipulation of the compartment systems – changing pH or temperature – encapsulated SUVs can be triggered to release their content. Very interesting will be to encapsulate protein expression or PCR machinery into the internal SUVs. These internal SUVs could then nicely resemble the ribosomes or the nucleus of a living cell.

Reconstitution of an energy module. Based on the multicompartment system, another interesting follow-up experiment would be to encapsulate ATP into the SUVs or to reconstitute ATP-Synthases and bacteriorhodopsin within the SUVs in order to fuel ATP-dependent functional modules in the cell e.g. the actin polymerization or actomyosin contraction (see

Figure 97). The reconstitution of ATP Synthases into SUVs was already successfully achieved.[310] Thus, a next obvious and probably not too complicated step would be to combine the functional modules of actin cytoskeleton and ATP producing SUVs in water-in-oil droplets.

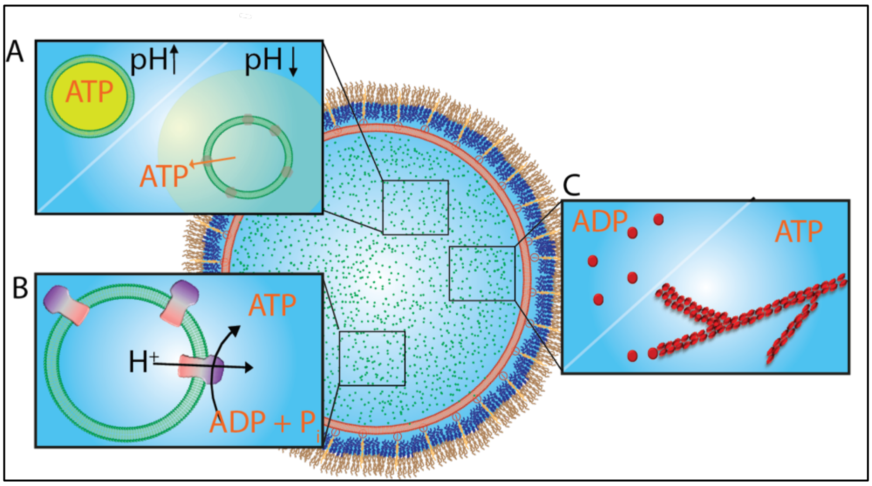

Figure 97: Schematic representation of controlled delivery of ATP into the water-in-oil droplets based on multicompartment systems. A) ATP is encapsulated in vesicles comprising pH sensitive lipids. Upon a decrease of pH, vesicles lose their integrity and ATP can leak out into the droplets continuous aqueous phase. B) ATP Synthase could be reconstituted into lipid vesicles and encapsulated into the water-in-oil droplets. Thereby having an in-situ production of ATP. C) The released or produced ATP could trigger ATP dependent reactions as e.g. actin polymerization.

Cell division model. In this thesis, I have shown successful reconstitution and characterization of several functional cellular modules in a droplet-based artificial cell. In this regard, my next idea addresses the rigid actin filament bundles that are presented in Section 5.2.1.2. These bundles align at the equator of the droplet and thus, resemble contractile ring structures (see Figure 98). Similar contractile ring structures are seen in the natural cells, shorty before the cell is dividing based on myosin-mediated contraction of these ring structures.[166] For follow up experiments, it would be interesting to figure out, if myosin motors could contract the rigid fibers and lead to network dynamics similarly seen in cell division. Next, towards the generation of a dividing droplet (Figure 98) the actomyosin network needs to be linked to the periphery. This could be for example done by a DNA linker, developed in our group. This DNA linker comprises a cholesterol tag, which attaches to the surfactant layer, and a NTA-tag, which could bind to His-tagged actin filaments in the contractile ring structures. Thereby the myosin contractile force could be applied onto the droplet compartment and a deformation or even a droplet splitting may be obtained.

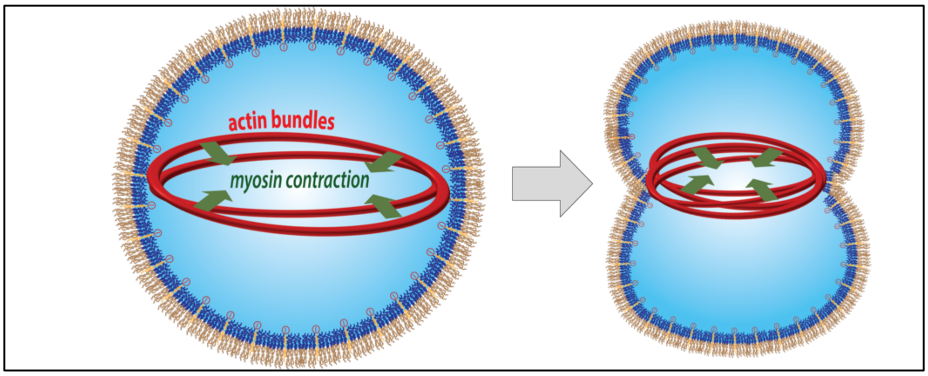

Figure 98: Schematic representation of rigid actin bundles that are encapsulated together with myosin motor proteins into water-in-oil droplets to mimic cell division dynamics. When the actin fibers are linked to the droplets wall, a deformation of the droplet due to actomyosin contraction could be obtained.

Adhesion module. Further work has to be done in the reconstitution of an adhesion complex within the artificial cell as addressed in Section 5.3.4. I showed a successful assembly of an artificial cell, comprising an outer lipid bilayer with reconstituted integrins and an actin cytoskeleton. Moreover, I showed that the talin head domain "THD" has binding sites for actin and integrin. However, THD did not bind in parallel to integrin and actin. To continue, a more robust linker has to be found or – based on further protein binding studies – binding conditions for the THD linker has to be optimized. Another solution would be to use an artificial linker. In this regard, a parallel project in our group is addressing the construction of so-called DARpins.[311] These DARpins are genetically engineered antibody mimetics that consist of two binding domains connected via a spacer of ankyrin repeats.[309] In this regard, DARpins can be engineered comprising an integrin and an actin binding domain. This approach provides a promising solution to build an adhesion complex within the described artificial cell.

The adhesion module in a living cell is involved in many signaling pathways in addition to the coordination of ECM attachment and detachment during cell locomotion.[50] This adhesion module is mechanosensitive, that means that intra- and extracellular mechanical cues can trigger its assembly and disassembly.[60] Thus, to resemble this mechanosensitive module of a living cell, it would be especially interesting to include contractile actomyosin networks into this adhesion complex model within the synthetic cells.[312] However, to test the assembled adhesion complex in subsequent binding studies on ECM substrate, the artificial cell has to be released out of the surfactant shell and oil phase into a physiological environment. This requires another set of experiments. Even though it was possible to release GUVs containing integrin alone, the addition of actin makes the release poorly efficient. The reason could be that actin is interfering with the assembly of the lipid bilayer when introduced in one step into the droplet. The sequential introduction of lipids and actin via picoinjection improves this to some extent, however, the applied electrical field creates as well distortion of the lipid bilayer that allows the injected actin to disturb the reassembly of a continuous lipid bilayer. An idea to solve this problem is by using a new picoinjection device developed in our group. This microfluidic picoinjection device is not relied on an electric field but is based on a rapid mechanical deformation of the droplets. This may lead to less distortion of the lipid bilayer and may maintain the passivation of the droplet's periphery through the lipid bilayer in order to prevent injected actin molecules to interact with the periphery.

Autonomous motility model. The fascinating field of self-propulsion of artificial systems, which was elucidated in my thesis, needs to be investigated a bit further. To study the effect of the described liquid flows a protein-free system should be used. Possible candidates are positively charged beads. I would not recommend to use $CaCO_3$ beads due to side-effects from the dissociation of the beads. Positively charged stable beads will allow higher flexibility with the buffer conditions and Krytox concentration in comparison to actin filaments that depolymerize in unphysiological pH ranges or in high Krytox concentrations. Besides the addition of internal beads, also the external flow around the droplets should be characterized by the addition of fluorescent hydrophobic beads with the same density as the surrounding oil phase.

Further it would be interesting to deeply investigate the influence of the friction effect with the cover-glass. Therefore, patterned surfaces (Figure 99) could be generated to create droplet rotation and droplet translation on surfaces with higher and lower friction, respectively.

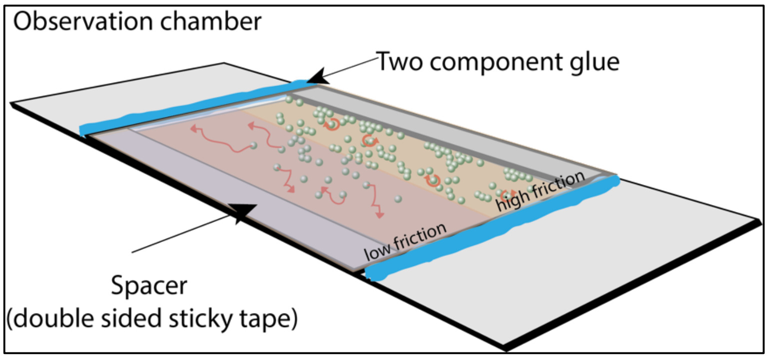

Figure 99: Schematic representation of an observation chamber containing droplets with autonomous motion due to encapsulated beads or actin filaments and the resulting Marangoni flow. Depending on the glass-droplet interaction droplets may perform a rotational or a translational motion for higher and lower friction, respectively.

The presented approaches will be possible due to the deep understanding and precise control of interfacial droplet properties as achieved in this thesis. The presented ideas for further projects show that the approach of water-in-oil droplets with tunable interface properties is highly versatile in application and paves the way for biomedical studies as well as for fundamental understanding of cellular function and life in general.

Appendix

7. Appendix

7.1. Supplementary Figures and Tables

7.1.1. Krytox Concentrations in Custom-Made triblock Surfactants

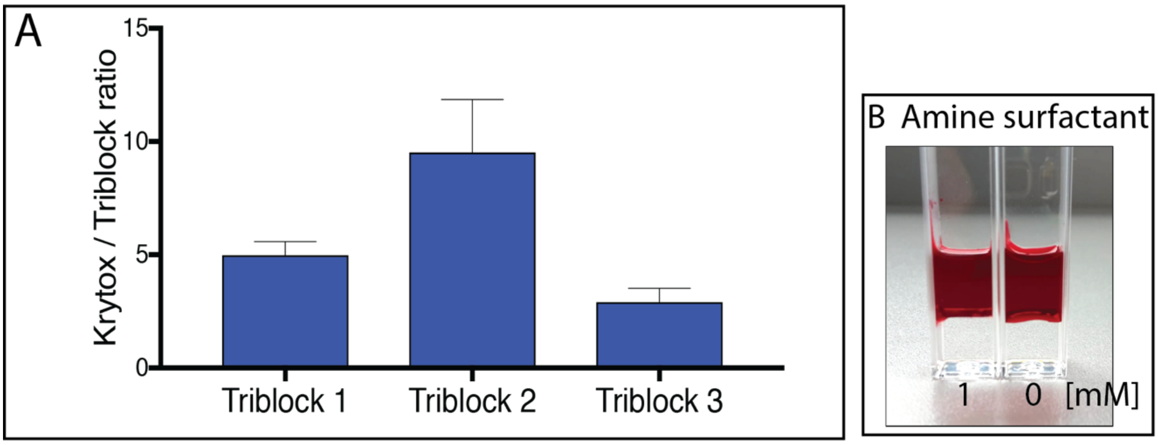

Figure SI 1: Krytox content in custom-made surfactants based on partitioning experiments. (A) Molecular ratio of Krytox per triblock surfactant of three different custom-made surfactants. Means calculated from Rhodamine6G concentrations in oil and water phase. (For more information see Methods) (B) Images of partitioning experiment to test Krytox concentration in the amine surfactant. 1 and 0 mM amine surfactant in the oil phase and 1 mM Rho6G in the aqueous phase on top after 48 h incubation. No extraction into the oil phase indicates absence of Krytox.

7.1.2. IFT measurements of surfactant mixtures

Table SI 1: IFT values of the surfactant mixtures (PEG-based surfactant and Krytox).

Krytox [mM]	0	1.5	3	4.5	6	7.5	9	10.50	12	13.5	15
plus 1 mM MgCl2											
w/o PEG-based surfactant											
Mean [mN/m]		9.23	3.30	1.21	1.07	< 1	< 1	< 1	< 1	< 1	< 1
Std. Dev		0.54	0.23	0.41	0.66	X	X	X	X	X	X
with 1.4 wt% PEG-based surfactant											
Mean [mN/m]	4.4	3.23	6.68	6.859	6.08	4.64	1.55	X	1.38	1.24	X
Std. Dev	0.21	0.44	0.47	0.72	0.83	0.06	0.46	X	0.44	0.23	X
Krytox [mM]	0	1.5	3	4.5	6	7.5	9	10.50	12	13.5	15
pure water											
w/o PEG-based surfactant											

Mean [mN/m]	38.04	25.34	24.77	19.84	19.79	21.61	21.14	20.14	21.84	21.26	20.35
Std. Dev	0.65	0.41	0.46	0.12	0.48	0.46	0.15	0.40	0.21	0.23	0.44
with 1.4 wt% PEG-based surfactant											
Mean [mN/m]	4.95	7.12	11.44	17.78	20.41	18.8	19.59	22.04	23.07	21.34	22.92
Std. Dev	0.68	0.44	0.32	0.04	0.03	0.09	0.02	0.01	0.02	0.06	0.76

Table SI 2: IFT values of the surfactant mixtures (PEG-based surfactant and amine surfactant).

NH3 surfactant [mM]	0	1	3	6	10	pure NH3
with 1.4 wt% PEG-based surfactant						
plus 1 mM MgCl2						
Mean [mN/m]	4.34	4.17	2.64	1.83	2.37	2.58
Std. Dev	0.56	0.51	0.13	0.38	1.63	0.67
pure water						
Mean [mN/m]	4.86	4.19	3.39	2.28	2.11	2.78
Std. Dev	0.54	0.57	0.76	0.19	0.06	0.88

7.1.3. Lipids in droplets after 7 days

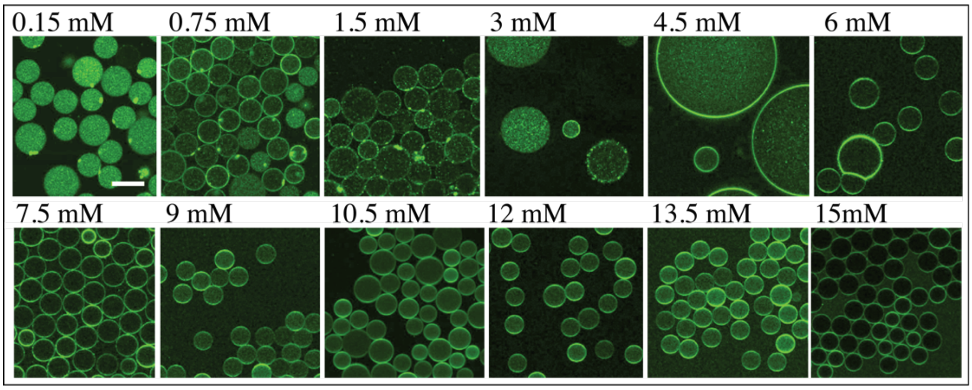

Figure SI 2: Representative images of fluorescence from lipids (0.5% ATTO 488-labeled DOPE) in the microfluidic droplets at day 7 after production. To evaluate the influence of Krytox on dsGUV formation and stability, different Krytox concentrations, indicated on top of the fluorescence images, were mixed with 1.4 wt% PEG-based fluorosurfactants in the oil phase. 10mM Mg^{2+} and SUVs comprised of 42.25% DOPC, 42.25% POPC and 15% cholesterol were used as an aqueous phase for droplets formation. Scale bar 50 µm.

7.1.4. Compartments stabilized by high Krytox concentrations

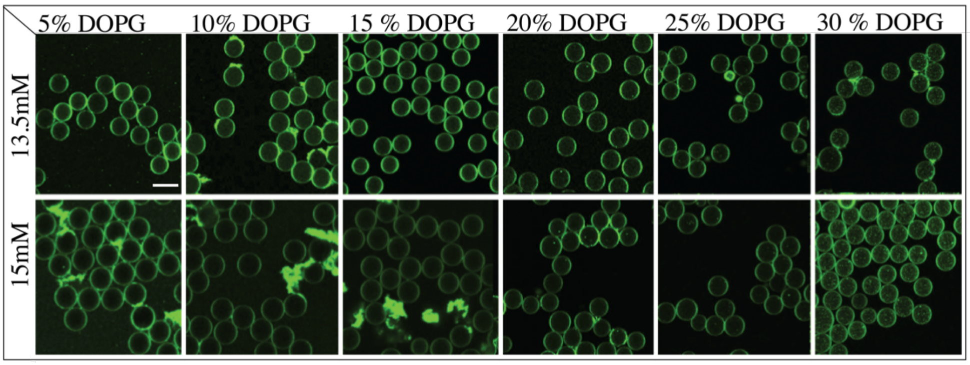

Figure SI 3: Representative images of fluorescence from lipids (0.5% ATTO 488-labeled DOPE) in the microfluidic droplets. To evaluate the influence of Krytox on dsGUV formation, different Krytox concentrations, indicated on top of the fluorescence images, were mixed with 1.4 wt% PEG-based fluorosurfactants in the oil phase. To evaluate the influence of negatively charged lipids on dsGUV formation, the Tris buffer including 10 mM Mg^{2+} *and SUVs comprised of different ratios of negatively charged DOPG lipids (DOPC x%, POPC x%, DOPG 0% – 30%, cholesterol 15%) was used as an aqueous phase for droplets formation. Scale bar 50 µm.*

7.1.5. DLS

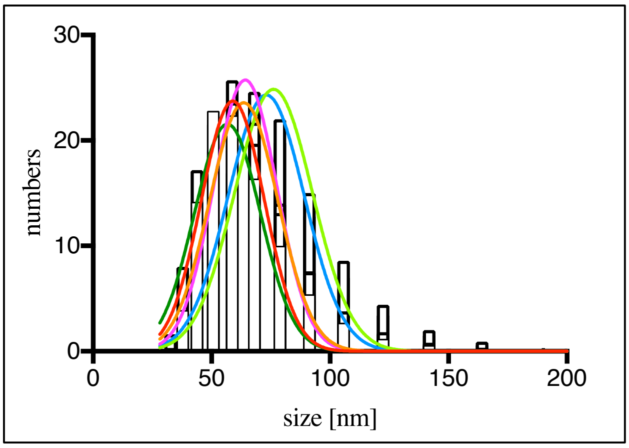

Figure SI 4: Size distribution of SUVs measured by DLS. Histogram indicates the mean distribution of 6 measurements (mean diameter: 68 ± 15 nm).

7.1.6. FRAP

Table SI 3: Diffusion coefficients of neutral and negatively charged lipids within water-in-oil droplets stabilized by different Krytox-to-PEG-based surfactant ratios

DOPG in%	c(Krytox) [mM]	Diffusion coefficient [µm^2/s]	
0	1.5	1.1 ± 0.1	n=20
0	3.0	1.3 ± 0.2	n=20
0	7.5	4.8 ± 0.4	n=20
0	10.5	5.1 ± 0.5	n=40
0	15	5.1 ± 0.3	n=20
30	1.5	1.0 ± 0.1	n=20
30	7.5	5.4 ± 0.4	n=20
30	10.5	4.2 ± 0.3	n=40
30	15	5.5 ± 0.3	n=20

Table SI 4: Diffusion coefficients of positively charged lipids within water-in-oil droplets stabilized by different Krytox-to-PEG-based surfactant ratios.

DOTAP in%	c(Krytox) [mM]	Diffusion coefficient [µm^2/s]	
30	1.5	1.5 ± 0.7	n=10
30	3.0	1.6 ± 0.2	n=10
30	4.5	3.2 ± 0.5	n=10
30	6	4.1 ± 0.3	n=10
30	7.5	4.1 ± 0.2	n=10
30	9	5.3 ± 1.0	n=10
30	10.5	4.5 ± 0.3	n=10
30	12	5.6 ± 0.4	n=10
30	13	5.2 ± 0.3	n=10
30	15	5.0 ± 0.3	n=10

Table SI 5: Diffusion coefficients of lipids within water-in-oil droplets stabilized by different amine surfactant-to-PEG-based surfactant ratios.

DOPG in%	c(amine surf) [mM]	Diffusion coefficient [μm²/s]	
0	3	1.9 ± 0.8	n=10
0	5	1.3 ± 0.2	n=10
0	7	2.2 ± 0.4	n=10
0	10	1.7 ± 0.4	n=10
30	3	1.8 ± 0.3	n=10
30	5	1.7 ± 0.5	n=10
30	7	leakage	
30	10		
Plus $MgCl_2$	3 – 10	No interaction with the periphery	
DOTAP	3 – 10		

7.1.7. Lipid leakage depending on lipid charge

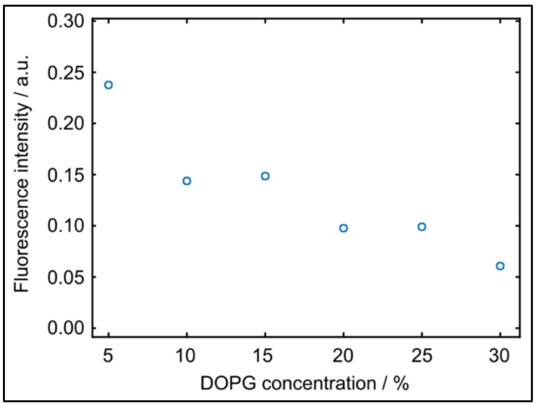

Figure SI 5: Quantification of lipid leakage from the water phase inside the droplet into the surrounding oil phase as a function of lipid charge. The fluorescence intensity from the lipids (0.5% DOPE-Atto488) in the oil phase was normalized to the intensity in the water phase. Less lipid leakage is observed at higher concentrations of negatively charged lipids (DOPG) within the lipid mixture.

7.1.8. Manipulation of Released GUVs

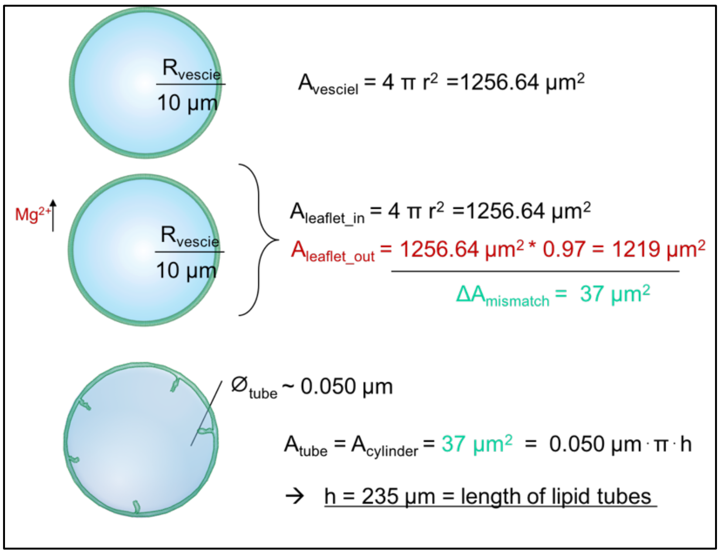

Figure SI 6: Calculation of the theoretically possible length of lipid tubes in released GUVs due to mismatching of bilayer leaflet areas (3%) in presence of higher $MgCl_2$ concentration in the surrounding aqueous phase.

7.1.1. Mass estimation of adsorbed protein on QCM-D crystal

Table SI 6: Mass estimation of adsorbed protein on QCM-D crystal based on two models: Sauerbrey (only frequency-mass relation) and viscoelastic Voigt model.

Figure 92A	[ng/cm2]	fibrinogen	Integrin	FAK
	Sauerbrey	1743.3	602	1296.9
	Voigt	2226.3	707	1412.5
Figure 92B	[ng/cm2]	SLB	FAK	integrin
	Sauerbrey	335.5	491.7	156.1
	Voigt	622.7	1164	653.1
Figure 93A	[ng/cm2]	fibrinogen	Integrin	talin
	Sauerbrey	1417.6	935.1	163.4
	Voigt	1608.1	676.4	319.7
Figure 93B	[ng/cm2]	fibrinogen	Integrin	THD
	Sauerbrey	1121.4	584.6	78.1
	Voigt	1472.2	865.1	XX

7.1.2. QCM-D Controls

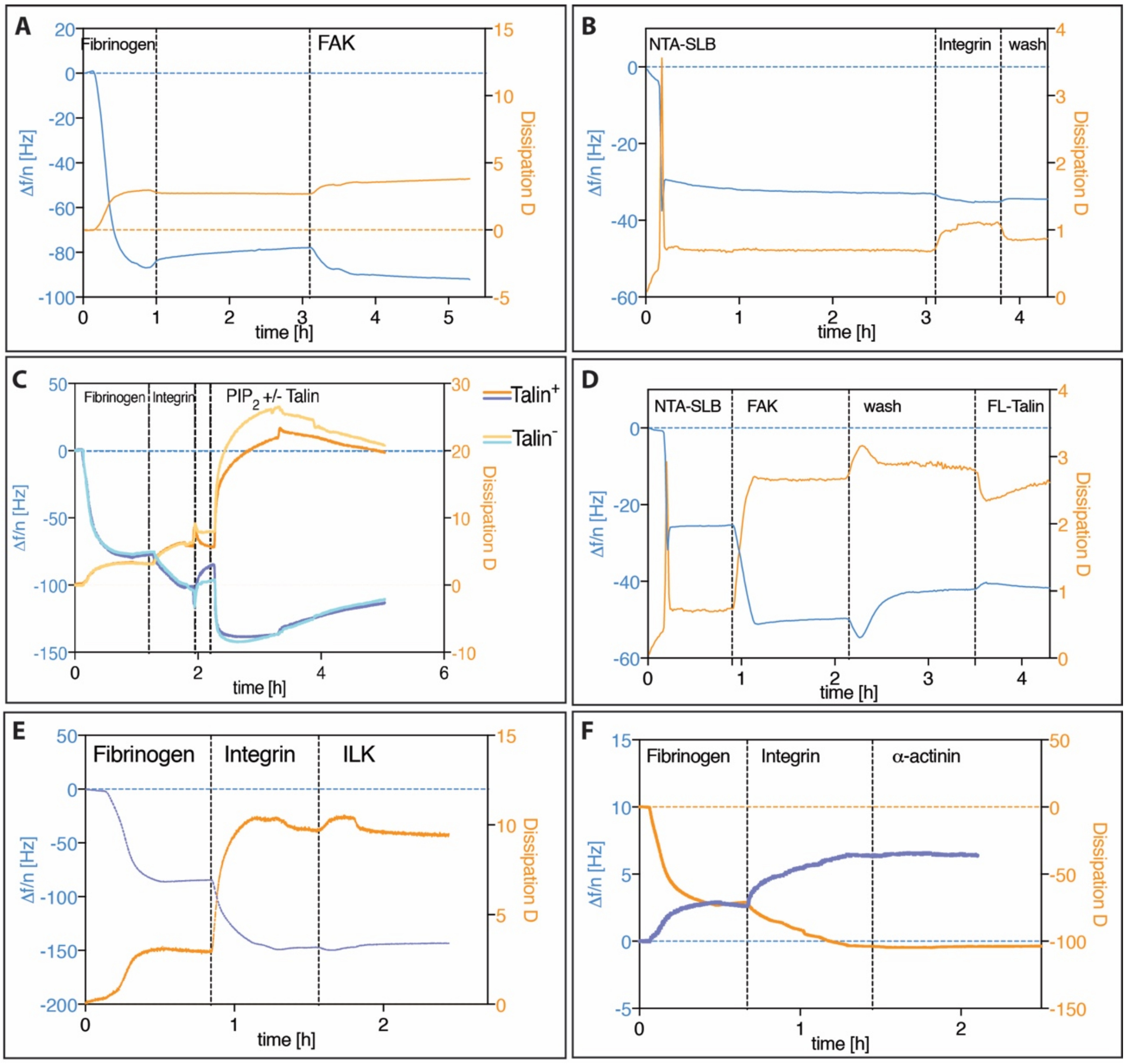

Figure SI 7: Frequency and dissipation shifts of QCM-D control measurements.

7.1.3. Linkage of Actomyosin Networks to the Periphery via Gold-linked Surfactants

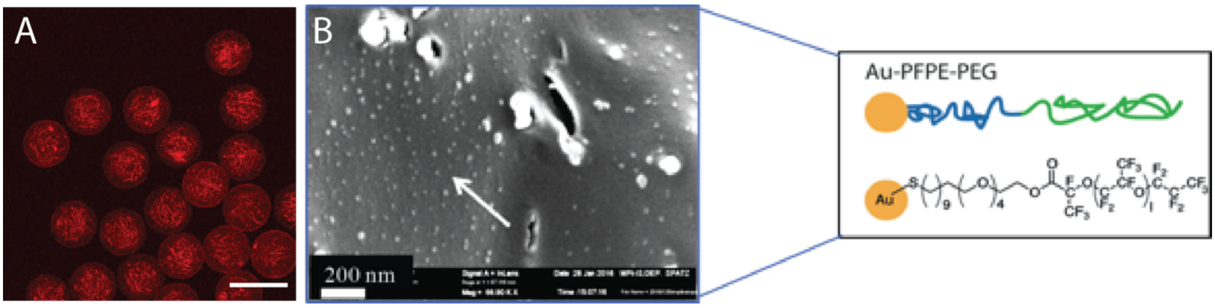

Figure SI 8: Droplets stabilized by the addition of gold-linked surfactants. A: Representative fluorescence image of actomyosin networks (1% of actin labelled with Alexa Fluor 568) within droplets stabilized by triblock surfactant and 1.2 µM gold surfactant. Scale bar 50 µm. B: cryo-SEM micrograph of the droplet's inner interface and the chemical structure of gold-linked surfactants in the inset. Arrow points to the bright spots, which are gold nanoparticles (5-10 nm) at the droplets interface.

7.2. List of Publications

Published:

Barbara Haller, Kerstin Göpfrich, Martin Schröter, Jan-Willi Janiesch, Ilia Platzman and Joachim P. Spatz, Charge-controlled microfluidic formation of lipid- based single- and multicompartment systems, Lab on a Chip 2018

M. Weiss*, J. P. Frohnmayer*, L. T. Benk, B. Haller, J.-W. Janiesch, T. Heitkamp, M. Börsch, R. Dimova, R. Lipowsky, E. Bodenschatz, J.-C. Baret, I. Platzman, and J. P. Spatz, Sequential bottom-up assembly of mechanically stabilized synthetic cells by microfluidic, Nature Materials. 2017

Accepted:

J. P. Frohnmayer*, M. Weiss*, B. Haller, J.-W. Janiesch, L. T. Benk, R. B. Lira, R. Dimova, I. Platzman, and J. P. Spatz, “Droplet-Supported Giant Vesicles as Cell-Like Compartments for Synthetic Biology,” in The Giant Vesicle Book, R. Dimova and R. Lipowski, Eds. CRC Taylor & Francis, 2017.

To be submitted:

Kerstin Göpfrich, Barbara Haller, Oskar Staufer, I. Platzman, and J. P. Spatz, Rapid assembly of complex multi-component lipid bilayer-enclosed synthetic cells, to be submitted, 2018

In preparation:

Barbara Haller*, Marian Weiss*, Jan-Willi Janiesch, I. Platzman, and J. P. Spatz, The assembly of dynamic actin cytoskeletal networks within water-in-oil droplets, in preparation, to be submitted 2019

Barbara Haller, Marian Weiss, I. Platzman, and J. P. Spatz, Self-propulsion in droplet-based synthetic cells, in preparation, to be submitted 2019

7.3. Bibliography

1. Oro, J., Miller, S. L. & Lazcano, A. The Origin and Early Evolution of Life on Earth. *Annu. Rev. Earth Planet. Sci.* 18, 317–356 (1990).
2. Ruiz-Mirazo, K., Peretó, J. & Moreno, A. A universal definition of life: Autonomy and open-ended evolution. *Nat. Life Class. Contemp. Perspect. from Philos. Sci.* 310–325 (2010). doi:10.1017/CBO9780511730191.031
3. Peretó, J. Controversies on the origin of life. *Int. Microbiol.* 8, 23–31 (2005).
4. Walde, P., Monnard, P. A., Wessicken, M., Goto, A. & Luisi, P. L. Oparin's Reactions Revisited: Enzymatic Synthesis of Poly (adenylic acid) in Micelles and Self-Reproducing Vesicles. *J. Am. Chem. Soc.* 116, 7541–7547 (1994).
5. Miller, S. L. A Production of Amino Acids Under Possible Primitive Earth Conditions. *Science (80-.).* 117, 528–529 (1953).
6. Martin, W., Baross, J., Kelley, D. & Russell, M. J. Hydrothermal vents and the origin of life. *Nat. Rev. Microbiol.* 6, 805–814 (2008).
7. Dodd, M. S. *et al.* Evidence for early life in Earth's oldest hydrothermal vent precipitates. *Nature* 543, 60–64 (2017).
8. Mulla, Y., Aufderhorst-Roberts, A. & Koenderink, G. H. Shaping up synthetic cells. *Phys. Biol.* 15, aab923 (2018).
9. Dowhan, W. Molecular basus for membrane phospholipid diversity:Why Are There So Many Lipids? *Annu. Rev. Biochem.* 66, 199–232 (1997).
10. Harayama, T. & Riezman, H. Understanding the diversity of membrane lipid composition. *Nat. Rev. Mol. Cell Biol.* 19, 281–296 (2018).
11. Bruce Alberts, Alexander Johnson, Peter Walter, Julian Lewis, Martin Raff, Keith Roberts, N. O. *Molecular Biology of The Cell.* (2008).
12. Van Meer, G., Voelker, D. R. & Feigenson, G. W. Membrane lipids: Where they are and how they behave. *Nat. Rev. Mol. Cell Biol.* 9, 112–124 (2008).
13. Owen, D. M. *Methods in Molecular Biology: Springer Protocol.* (2015). doi:10.1007/978-1-61779-527-5
14. Balla, T., Szentpetery, Z. & Yeun, J. K. Phosphoinositide signaling: new tools and insights. P. *Physiol.* 24, 231–244 (2009).
15. Erb, E. M. & Engel, J. Reconstitution of functional integrin into phospholipid vesicles and planar lipid bilayers. *Methods Mol. Biol.* 139, 71–82 (2000).
16. Weiss, M. *et al.* Sequential bottom-up assembly of mechanically stabilized synthetic cells by microfluidics. *Nat. Mater.* 17, 89–95 (2018).
17. Marquardt, D., Geier, B. & Pabst, G. Asymmetric lipid membranes: Towards more realistic model systems. *Membranes (Basel).* 5, 180–196 (2015).
18. Paulson, J. C. Glycoproteins: what are the sugar chains for? *Trends Biochem. Sci.* 14, 272–276 (1989).
19. Lodish H, Berk A, Zipursky SL, et al. *Molecular Cell Biology. 4th edition.* (2000).
20. Martin, W. F., Garg, S. & Zimorski, V. Endosymbiotic theories for eukaryote origin. *Philos. Trans. R. Soc. B Biol. Sci.* 370, (2015).
21. Gabaldón, T. & Pittis, A. A. Origin and evolution of metabolic sub-cellular compartmentalization in eukaryotes. *Biochimie* 119, 262–268 (2015).
22. Schwarz, D. S. & Blower, M. D. The endoplasmic reticulum: Structure, function and response to cellular signaling. *Cell. Mol. Life Sci.* 73, 79–94 (2016).
23. Picard, M. *et al.* Mitochondrial structure and function are disrupted by standard Isolation methods. *PLoS One* 6, 1–12 (2011).

24. Khalifat, N., Puff, N., Bonneau, S., Fournier, J. B. & Angelova, M. I. Membrane deformation under local pH gradient: Mimicking mitochondrial cristae dynamics. *Biophys. J.* 95, 4924–4933 (2008).
25. Liu, Y., Agudo-Canalejo, J., Grafmüller, A., Dimova, R. & Lipowsky, R. Patterns of flexible nanotubes formed by liquid-ordered and liquid-disordered membranes. *ACS Nano* 10, 463–474 (2016).
26. Steinkühler, J., De Tillieux, P., Knorr, R. L., Lipowsky, R. & Dimova, R. Charged giant unilamellar vesicles prepared by electroformation exhibit nanotubes and transbilayer lipid asymmetry. *Sci. Rep.* 8, 1–9 (2018).
27. Almeida, J. G., Preto, A. J., Koukos, P. I., Bonvin, A. M. J. J. & Moreira, I. S. Membrane proteins structures: A review on computational modeling tools. *Biochim. Biophys. Acta - Biomembr.* 1859, 2021–2039 (2017).
28. Siton-Mendelson, O. & Bernheim-Groswasser, A. Toward the reconstitution of synthetic cell motility. *Cell Adhes. Migr.* 10, 461–474 (2016).
29. Hassinger, J. Cell dynamics and the actin cytoskeleton. 170–203 (2014).
30. Fletcher, D. A. & Mullins, R. D. Cell mechanics and the cytoskeleton. *Nature* 463, 485–492 (2010).
31. Mofrad, M. R. K. Rheology of the Cytoskeleton. *Annu. Rev. Fluid Mech.* 41, 433–453 (2009).
32. Kamm, R. D. & Mofrad, M. R. K. Introduction, with the biological basis for cell mechanics. *Cell. Mechanotransduction* (2006).
33. Parry, D. A. D. & Steinert, P. M. Intermediate filament structure. *Curr. Opin. Cell Biol.* 4, 94–98 (1992).
34. Nogales, E. Structural insights into microtubule function. *Annu. Rev. Biochem* 69, 277–302 (2000).
35. Ehrlicher, A. J. The Forces Behind Cell Movement The Forces Behind Cell Movement. 3, 303–317 (2017).
36. Dominguez, R. & Holmes, K. C. Actin Structure and Function. *Annu. Rev. Biophys.* 40, 169–186 (2011).
37. Insall, R. H. & Machesky, L. M. Actin Dynamics at the Leading Edge: From Simple Machinery to Complex Networks. *Dev. Cell* 17, 310–322 (2009).
38. Carlier, M. F., Pantaloni, D. & Korn, E. D. Polymerization of ADP-actin and ATP-actin under sonication and characteristics of the ATP-actin equilibrium polymer. *J. Biol. Chem.* 260, 6565–6571 (1985).
39. Bugyi, B. & Carlier, M.-F. Control of Actin Filament Treadmilling in Cell Motility. *Annu. Rev. Biophys.* 39, 449–470 (2010).
40. Waterman-Storer, C. M. & Salmon, E. D. Microtubule dynamics: Treadmilling comes around again. *Curr. Biol.* 7, R369–R372 (1997).
41. Chugh, P. & Paluch, E. K. The actin cortex at a glance. *J. Cell Sci.* 131, jcs186254 (2018).
42. Hoyt, M. A., Hyman, A. A. & Bähler, M. Motor proteins of the eukaryotic cytoskeleton. *Proc. Natl. Acad. Sci. U. S. A.* 94, 12747–12748 (1997).
43. Vicente-Manzanares, M., Ma, X., Adelstein, R. S. & Horwitz, a. R. Non-muscle myosin II takes centre stage in cell adhesion and migration. *Nat. Rev. Mol. Cell Biol.* 10, 778–790 (2009).
44. Hartman, M. A. & Spudich, J. A. The myosin superfamily at a glance. *J. Cell Sci.* 125, 1627–1632 (2012).
45. O'Connell, C. B., Tyska, M. J. & Mooseker, M. S. Myosin at work: Motor adaptations for a variety of cellular functions. *Biochim. Biophys. Acta - Mol. Cell Res.* 1773, 615–630 (2007).
46. Tsuda, Y., Yasutake, H., Ishijima, A. & Yanagida, T. Torsional rigidity of single actin filaments and actin-actin bond breaking force under torsion measured directly by in vitro micromanipulation. *Proc. Natl. Acad. Sci. U. S. A.* 93, 12937–42 (1996).

47. Geiger, B., Bershadsky, A., Pankov, R., Yamada, K. M. & Correspondence, B. G. Transmembrane extracellular matrix– cytoskeleton crosstalk. *Nat. Rev. Mol. Cell Biol.* 2, 793–805 (2001).

48. Frantz, C., Stewart, K. M. & Weaver, V. M. The extracellular matrix at a glance. *J. Cell Sci.* 123, 4195–200 (2010).

49. Harburger, D. S. & Calderwood, D. A. Integrin signalling at a glance. *J. Cell Sci.* 122, 1472–1472 (2009).

50. Geiger, B., Spatz, J. P. & Bershadsky, A. D. Environmental sensing through focal adhesions. *Nat. Rev. Mol. Cell Biol.* 10, 21–33 (2009).

51. Humphries, J. D., Byron, A. & Humphries, M. J. Integrin ligands at a glance. *J. Cell Sci.* 119, 3901–3 (2006).

52. Lafoya, B. *et al.* Beyond the matrix: The many non-ECM ligands for integrins. *Int. J. Mol. Sci.* 19, 1–33 (2018).

53. Zaidel-Bar, R., Itzkovitz, S., Ma'ayan Avi, Iyengar, R. & Geiger, B. Functional atlas of the integrin adhesome Ronen. *Nat Cell Biol.* 9, 858–867 (2007).

54. Calderwood, D. A. Integrin activation. *J. Cell Sci.* 117, 657–666 (2004).

55. Liu, S., Calderwood, D. a & Ginsberg, M. H. Integrin cytoplasmic domain-binding proteins. *J. Cell Sci.* 113 (Pt 2, 3563–3571 (2000).

56. Critchley, D. R. & Gingras, A. R. Talin at a glance. *J. Cell Sci.* 121, 1345–1347 (2008).

57. Calderwood, D. A. *et al.* The Talin Head Domain Binds to Integrin β Subunit Cytoplasmic Tails and Regulates Integrin Activation. *J. Biol. Chem.* 274, 28071–28074 (1999).

58. Moser, M., Legate, K. R., Zent, R. & Fassler, R. The tail of integrins, talins, and kindlins. *Science (80-.).* 324, 895–899 (2009).

59. Lawson, C. *et al.* FAK promotes recruitment of talin to nascent adhesions to control cell motility. *J. Cell Biol.* 196, 223–232 (2012).

60. Katsumi, A., Orr, a W., Tzima, E. & Schwartz, M. A. Integrins in mechanotransduction. *J. Biol. Chem.* 279, 12001–4 (2004).

61. Tanaka, M. *et al.* Turnover and flow of the cell membrane for cell migration. *Sci. Rep.* 7, 1–13 (2017).

62. Bretscher, M. S. Exocytosis provides the membrane for protrusion, at least in migrating fibroblasts. *Nat. Rev. Mol. Cell Biol.* 9, 916 (2008).

63. Aguado-Velasco, C. & Bretscher, M. S. Circulation of the plasma membrane in Dictyostelium. *Mol. Biol. Cell* 10, 4419–4427 (1999).

64. Bailey, G. B., Diane, D. & McCoomer, N. Entamoeba Motility: Dynamics of Cytoplasmic Streaming, Locomotion and Translocation of Surface Bound Particles, and Organization of the Actin Cytoskeleton in Entamoeba invadens. *J. Protozool.* 39, 267–272 (1992).

65. Bretscher, M. S. & Clotworthy, M. Using single loxP sites to enhance homologous recombination: ts mutants in Sec1 of Dictyostelium discoideum. *PLoS One* 2, 8–11 (2007).

66. Salehi-Reyhani, A., Ces, O. & Elani, Y. Artificial cell mimics as simplified models for the study of cell biology. *Exp. Biol. Med.* 242, 1309–1317 (2017).

67. Pezzulo, G. & Levin, M. Top-down models in biology: explanation and control of complex living systems above the molecular level. 13, 1–16 (2016).

68. Andrianantoandro, E., Basu, S., Karig, D. K. & Weiss, R. Synthetic biology: New engineering rules for an emerging discipline. *Mol. Syst. Biol.* 2, 1–14 (2006).

69. Brizard, A. M. & Van Esch, J. H. Self-assembly approaches for the construction of cell architecture mimics. *Soft Matter* 5, 1320–1327 (2009).

70. Pier LuiCell, P. S. *The Minimal Cell - The Biophysics of Cell Compartment and the Origin of Cell Functionality.*

71. Buddingh', B. C. & Van Hest, J. C. M. Artificial Cells: Synthetic Compartments with Life-like

Functionality and Adaptivity. *Acc. Chem. Res.* 50, 769–777 (2017).

72. Elani, Y., Law, R. V. & Ces, O. Vesicle-based artificial cells as chemical microreactors with spatially segregated reaction pathways. *Nat. Commun.* 5, 1–5 (2014).

73. Terasawa, H., Nishimura, K., Suzuki, H., Matsuura, T. & Yomo, T. Coupling of the fusion and budding of giant phospholipid vesicles containing macromolecules. *Proc. Natl. Acad. Sci.* 109, 5942–5947 (2012).

74. Vanswaay, D., Tang, T. Y. D., Mann, S. & DeMello, A. Microfluidic Formation of Membrane-Free Aqueous Coacervate Droplets in Water. *Angew. Chemie - Int. Ed.* 54, 8398–8401 (2015).

75. Peters, R. J. R. W. *et al.* Cascade reactions in multicompartmentalized polymersomes. *Angew. Chemie - Int. Ed.* 53, 146–150 (2014).

76. Liu, X. *et al.* Hierarchical Proteinosomes for Programmed Release of Multiple Components. *Angew. Chemie - Int. Ed.* 55, 7095–7100 (2016).

77. Juniper, M. P. N., Weiss, M., Platzman, I., Spatz, J. P. & Surrey, T. Spherical network contraction forms microtubule asters in confinement. *Soft Matter* 14, 901–909 (2018).

78. Brea, Roberto ; Hardy, Michael ; Devaraj, N. Towards Self-Assembled Hybrid Artificial Cells: Novel Bottom- Up Approaches to Functional Synthetic Membranes. 48, 923–930 (2015).

79. Palivan, C. G. *et al.* Bioinspired polymer vesicles and membranes for biological and medical applications. *Chem. Soc. Rev.* 45, 377–411 (2016).

80. Xu, C., Hu, S. & Chen, X. Artificial cells : from basic science to applications. *Biochem. Pharmacol.* 19, 516–532 (2016).

81. Chang, T. M. S. 1957 Report on “Method for Preparing Artificial Hemoglobin Corpuscles”. 335–354 (1957).

82. Chang, T. M. S. First Design and Clinical Use in Patients of Surface Modified Sorbent Hemoperfusion Based on Artificial Cells for Poisoning , Kidney Failure , Liver Failure and Immunology. (1965).

83. Chang TM, P. M. Semipermeable microcapsules containing catalase for enzyme replacement in acatalasaemic mice. *Nature* 218(5138),

84. Bian, Y. & Chang, T. M. S. A novel nanobiotherapeutic poly-[hemoglobin-superoxide dismutase-catalase-carbonic anhydrase] with no cardiac toxicity for the resuscitation of a rat model with 90 minutes of sustained severe hemorrhagic shock with loss of 2/3 blood volume. *Artif. Cells, Nanomedicine Biotechnol.* 43, 1–9 (2015).

85. Baumann, H. & Surrey, T. Motor-mediated cortical versus astral microtubule organization in lipid-monolayered droplets. *J. Biol. Chem.* 289, 22524–22535 (2014).

86. Haller, B. *et al.* Charge-controlled microfluidic formation of lipid-based single-and multicompartment systems †. *Lab Chip* (2018). doi:10.1039/c8lc00582f

87. Nishigami, Y., Ito, H., Sonobe, S. & Ichikawa, M. Non-periodic oscillatory deformation of an actomyosin microdroplet encapsulated within a lipid interface. *Sci. Rep.* 6, 1–11 (2016).

88. Schaerli, Y. & Hollfelder, F. The potential of microfluidic water-in-oil droplets in experimental biology. *Mol. Biosyst.* 5, 1392–1404 (2009).

89. Abu Shah, E. & Keren, K. Symmetry breaking in reconstituted actin cortices. *Elife* 2014, 1–15 (2014).

90. Meng, F., Engbers, G. H. M. & Feijen, J. Biodegradable polymersomes as a basis for artificial cells: Encapsulation, release and targeting. *J. Control. Release* 101, 187–198 (2005).

91. Zhang, X. & Zhang, P. Polymersomes in Nanomedicine - A Review. *Curr. Nanosci.* 13, 124–129 (2017).

92. Langowska, K., Palivan, C. G. & Meier, W. Polymer nanoreactors shown to produce and release antibiotics locally. *Chem. Commun.* 49, 128–130 (2013).

93. Tanner, P., Balasubramanian, V. & Palivan, C. G. Aiding Nature ’ s Organelles : Arti fi cial Peroxisomes Play Their Role. *Nano Lett.* 13, 2875–2883 (2013).

94. Kurokawa, C. *et al.* DNA cytoskeleton for stabilizing artificial cells. *Proc. Natl. Acad. Sci.* 114, 7228–7233 (2017).

95. Huang, X., Li, M. & Mann, S. Membrane-mediated cascade reactions by enzyme–polymer proteinosomes. *Chem. Commun.* 50, 6278–6280 (2014).

96. Liao, W. C. *et al.* PH-and ligand-induced release of loads from DNA-acrylamide hydrogel microcapsules. *Chem. Sci.* 8, 3362–3373 (2017).

97. Göpfrich, K., Platzman, I. & Spatz, J. P. Mastering Complexity: Towards Bottom-up Construction of Multifunctional Eukaryotic Synthetic Cells. *Trends Biotechnol.* xx, 1–14 (2018).

98. Göpfrich, K. *et al.* Ion channels made from a single membrane-spanning DNA duplex. *Nano Lett.* 16, 4665–4669 (2016).

99. Urban, M. J. *et al.* Gold nanocrystal-mediated sliding of doublet DNA origami filaments. *Nat. Commun.* 9, (2018).

100. Castellana, E. T. & Cremer, P. S. Solid supported lipid bilayers: From biophysical studies to sensor design. *Surf. Sci. Rep.* 61, 429–444 (2006).

101. Tamm, L. K. & McConnell, H. M. Supported phospholipid bilayers. *Biophys. J.* 47, 105–113 (1985).

102. Dustin, M. L. Supported bilayers at the vanguard of immune cell activation studies. *J. Struct. Biol.* 168, 152–160 (2009).

103. Pace, H. *et al.* Preserved Transmembrane Protein Mobility in Polymer-Supported Lipid Bilayers Derived from Cell Membranes. *Anal. Chem.* 87, 9194–9203 (2015).

104. Richter, R. P., Escarpit, R. R. & Cedex, P. In V ited Feature Article Formation of Solid-Supported Lipid Bilayers : An Integrated View. *Langmuir* 22, 3497–3505 (2006).

105. Richter, R. P., Bérat, R. & Brisson, A. R. Formation of solid-supported lipid bilayers: An integrated view. *Langmuir* 22, 3497–3505 (2006).

106. Lipowsky, R. & Seifert, U. Adhesion of Vesicles and Membranes. *Mol. Cryst. Liq. Cryst.* 202, 17–25 (1991).

107. Stein, H., Spindler, S., Bonakdar, N., Wang, C. & Sandoghdar, V. Production of isolated giant unilamellar vesicles under high salt concentrations. *Front. Physiol.* 8, 1–16 (2017).

108. Patil, Y. P. & Jadhav, S. Novel methods for liposome preparation. *Chem. Phys. Lipids* 177, 8–18 (2014).

109. Ciancaglini, P. *et al.* Proteoliposomes in nanobiotechnology. *Biophys. Rev.* 4, 67–81 (2012).

110. Lapinski, M. M., Castro-Forero, A., Greiner, A. J., Ofoli, R. Y. & Blanchard, G. J. Comparison of liposomes formed by sonication and extrusion: Rotational and translational diffusion of an embedded chromophore. *Langmuir* 23, 11677–11683 (2007).

111. Dua, J. S., Rana, A. C. & A.K., B. Liposome: Methods of preparation and applications. *Int. J. Pharm. Stud. Res.* III, 7 (2012).

112. Szoka, F. Comparative properties and methods pf preparation of lipid vesicles (liposomes). *Ann. Rev. Biophys. Bioeng.* 467–508 (1980). doi:10.1073/pnas.73.11.3862

113. Kimura, M. Journal of Molecular Evolution. *J. Mol. Evol.* 16, 111–120 (1980).

114. Lecat, S. & Simons, K. Protein Expression in liposomes. *Anal. Biochem.* 68, 59–68 (2000).

115. Laouini, A. *et al.* Preparation, Characterization and Applications of Liposomes: State of the Art. *J. Colloid Sci. Biotechnol.* 1, 147–168 (2012).

116. Akbarzadeh, A. *et al.* Liposome: Classification, preparation, and applications. *Nanoscale Res. Lett.* 8, 1–8 (2013).

117. Jørgensen, I. L., Kemmer, G. C. & Pomorski, T. G. Membrane protein reconstitution into giant unilamellar vesicles: a review on current techniques. *Eur. Biophys. J.* 46, 103–119 (2017).

118. Shohda, K. I. & Sugawara, T. DNA polymerization on the inner surface of a giant liposome for synthesizing an artificial cell model. *Soft Matter* 2, 402–408 (2006).

119. Angelova, M. I. & Dimitrov, D. S. Liposome Electro formation. *Faraday Discuss. Chem. SOC* 81, 303–311 (1986).

120. Reeves, J. P. & Dowben, R. M. Formation and properties of thin-waled phospholipid vesicles. *J. Cell. Physio.* 73, 49–60 (1969).

121. Dimova, R. *et al.* A practical guide to giant vesicles. Probing the membrane nanoregime via optical microscopy. *J. Phys. Condens. Matter* 18, (2006).

122. Colletier, J. P., Chaize, B., Winterhalter, M. & Fournier, D. Protein encapsulation in liposomes: Efficiency depends on interactions between protein and phospholipid bilayer. *BMC Biotechnol.* 2, 1–8 (2002).

123. Matosevic, S. Synthesizing artificial cells from giant unilamellar vesicles: State-of-the art in the development of microfluidic technology. *BioEssays* 34, 992–1001 (2012).

124. Stachowiak, J. C. *et al.* Unilamellar vesicle formation and encapsulation by microfluidic jetting. *Proc. Natl. Acad. Sci.* 105, 4697–4702 (2008).

125. Beales, P. A., Ciani, B. & Cleasby, A. J. Nature's lessons in design: nanomachines to scaffold, remodel and shape membrane compartments. *Phys. Chem. Chem. Phys.* 17, 15489–15507 (2015).

126. Walde, P., Cosentino, K., Engel, H. & Stano, P. Giant Vesicles: Preparations and Applications. *ChemBioChem* 11, 848–865 (2010).

127. Frisken, B. J. & W, D. A. Production of Unilamellar Vesicles using an Inverted Emulsion. 2870–2879 (2003).

128. Deshpande, S. & Pfohl, T. Real-time dynamics of emerging actin networks in cell-mimicking compartments. *PLoS One* 10, 1–19 (2015).

129. Elani, Y. *et al.* Constructing vesicle-based artificial cells with embedded living cells as organelle-like modules. *Sci. Rep.* 8, 1–8 (2018).

130. Abate, A. R., Hung, T., Mary, P., Agresti, J. J. & Weitz, D. A. High-throughput injection with microfluidics using picoinjectors. *Proc. Natl. Acad. Sci.* 107, 19163–19166 (2010).

131. Schoonen, L. & Van Hest, J. C. M. Compartmentalization Approaches in Soft Matter Science: From Nanoreactor Development to Organelle Mimics. *Adv. Mater.* 28, 1109–1128 (2016).

132. Paleos, C. M. & Tsiourvas, D. Interaction between complementary liposomes: A process leading to multicompartment systems formation. *J. Mol. Recognit.* 19, 60–67 (2006).

133. Deng, N.-N., Yelleswarapu, M., Zheng, L. & Huck, W. T. S. Microfluidic Assembly of Monodisperse Vesosomes as Artificial Cell Models. *J. Am. Chem. Soc.* 139, 587–590 (2017).

134. Okumura, Y., Nakaya, T., Namai, H. & Urita, K. Giant vesicles with membranous microcompartments. *Langmuir* 27, 3279–3282 (2011).

135. Walker, Scott; Kennedy, Michael; Zasadzinski, J. Encapsulation of bilayer vesicles by self-assembly. (1997).

136. Bolinger, P. Y., Stamou, D. & Vogel, H. An integrated self-assembled nanofluidic system for controlled biological chemistries. *Angew. Chemie - Int. Ed.* 47, 5544–5549 (2008).

137. Villar, G. & Bayley, H. Environments. 6, 803–808 (2012).

138. Bouvrais, H., Duelund, L. & Ipsen, J. H. Buffers affect the bending rigidity of model lipid membranes. *Langmuir* 30, 13–16 (2014).

139. Okano, T., Inoue, K., Koseki, K. & Suzuki, H. Deformation Modes of Giant Unilamellar Vesicles Encapsulating Biopolymers. *ACS Synth. Biol.* 7, 739–747 (2018).

140. Bilal, T. & Gözen, I. Formation and dynamics of endoplasmic reticulum-like lipid nanotube networks. *Biomater. Sci.* 5, 1256–1264 (2017).

141. Biology, M. C. Lipid rafts and signal transduction. 1, (2000).

142. Voorst, F. & De Kruijff, B. Role of lipids in the translocation of proteins across membranes. *Biochem. J.* 347, 601 (2000).

143. Kagawa, Y. & Racker, E. Partial resolution phosphorylation of the enzymes catalyzing oxidative

phosphorylation. *J. Biol. Chem.* 246, 5477–5487 (1971).

144. Dopico, A. *Methods in Lipid Membranes.* (2007).

145. De Lima Santos, H., Lopes, M. L., Maggio, B. & Ciancaglini, P. Na,K-ATPase reconstituted in liposomes: Effects of lipid composition on hydrolytic activity and enzyme orientation. *Colloids Surfaces B Biointerfaces* 41, 239–248 (2005).

146. Frohnmayer, J. P. *et al.* Minimal Synthetic Cells to Study Integrin-Mediated Adhesion. *Angew. Chemie - Int. Ed.* 54, 12472–12478 (2015).

147. Weinberger, A. *et al.* Gel-assisted formation of giant unilamellar vesicles. *Biophys. J.* 105, 154–164 (2013).

148. Garten, M., Aimon, S., Bassereau, P. & Toombes, G. E. S. Reconstitution of a Transmembrane Protein, the Voltage-gated Ion Channel, KvAP, into Giant Unilamellar Vesicles for Microscopy and Patch Clamp Studies. *J. Vis. Exp.* 1–16 (2015). doi:10.3791/52281

149. Yanagisawa, M., Iwamoto, M., Kato, A., Yoshikawa, K. & Oiki, S. Oriented reconstitution of a membrane protein in a giant unilamellar vesicle: Experimental verification with the potassium channel KcsA. *J. Am. Chem. Soc.* 133, 11774–11779 (2011).

150. Dezi, M., Cicco, A. Di, Bassereau, P. & Lévy, D. Physiological Contents. (2013). doi:10.1073/pnas.1303857110/-/DCSupplemental.www.pnas.org/cgi/doi/10.1073/pnas.1303857110

151. Kahya, N., Pécheur, E. I., De Boeij, W. P., Wiersma, D. A. & Hoekstra, D. Reconstitution of membrane proteins into giant unilamellar vesicles via peptide-induced fusion. *Biophys. J.* 81, 1464–1474 (2001).

152. Chan, Y.-H. M., van Lengerich, B. & Boxer, S. G. Effects of linker sequences on vesicle fusion mediated by lipid-anchored DNA oligonucleotides. *Proc. Natl. Acad. Sci.* 106, 979–984 (2009).

153. Biner, O., Schick, T., Müller, Y. & von Ballmoos, C. Delivery of membrane proteins into small and giant unilamellar vesicles by charge-mediated fusion. *FEBS Lett.* 590, 2051–2062 (2016).

154. Otrin, L. *et al.* Toward Artificial Mitochondrion: Mimicking Oxidative Phosphorylation in Polymer and Hybrid Membranes. *Nano Lett.* 17, 6816–6821 (2017).

155. Choi, H. J. & Montemagno, C. D. Artificial organelle: ATP synthesis from cellular mimetic polymersomes. *Nano Lett.* 5, 2538–2542 (2005).

156. Features, D., Microtubules, O. F. & Dark-field, B. Y. Flagella transport I ~ ~ ~ Mitotic spindle ytoskeleton Pi gment transl ocation. *Development* 26, 135–156 (1990).

157. Kaneko, T., Itoh, T. J. & Hotani, H. Morphological transformation of liposomes caused by assembly of encapsulated tubulin and determination of shape by microtubule-associated proteins (MAPs). *J. Mol. Biol.* 284, 1671–1681 (1998).

158. Keller, P. J., Pampaloni, F., Lattanzi, G. & Stelzer, E. H. K. Three-dimensional microtubule behavior in Xenopus egg extracts reveals four dynamic states and state-dependent elastic properties. *Biophys. J.* 95, 1474–1486 (2008).

159. Hayashi, M. *et al.* Reversible Morphological Control of Tubulin-Encapsulating Giant Liposomes by Hydrostatic Pressure. *Langmuir* 32, 3794–3802 (2016).

160. Kuchnir Fygenson, D., Elbaum, M., Shraiman, B. & Libchaber, A. Microtubules and vesicles under controlled tension. *Phys. Rev. E - Stat. Physics, Plasmas, Fluids, Relat. Interdiscip. Top.* 55, 850–859 (1997).

161. Sanchez, T., Chen, D. T. N., Decamp, S. J., Heymann, M. & Dogic, Z. Spontaneous motion in hierarchically assembled active matter. *Nature* 491, 431–434 (2012).

162. Cortese, J. D., Schwab Iii, B., Frieden, C. & Elson, E. L. Actin polymerization induces a shape change in actin-containing vesicles. *Biochemistry* 86, 5773–5777 (1989).

163. Bärmann, M., Käs, J., Kurzmeier, H. & Sackmann, E. A New Cell Model --- Actin Networks Encaged by Giant Vesicles. *Struct. Conform. Amphiphilic Membr.* 66, 137–143 (1992).

164. Marston, S. B., Fraser, I. D., Bing, W. & Roper, G. A simple method for automatic tracking of

actin filaments in the motility assay. *J Muscle Res Cell Motil* 17, 497–506 (1996).

165. Tsai, F.-C. & Koenderink, G. H. Shape control of lipid bilayer membranes by confined actin bundles. *Soft Matter* 11, 8834–8847 (2015).
166. Miyazaki, M., Chiba, M., Eguchi, H., Ohki, T. & Ishiwata, S. Cell-sized spherical confinement induces the spontaneous formation of contractile actomyosin rings in vitro. *Nat. Cell Biol.* 17, 480–489 (2015).
167. Nishigami, Y., Ito, H., Sonobe, S. & Ichikawa, M. Non-periodic oscillatory deformation of an actomyosin microdroplet encapsulated within a lipid interface. *Sci. Rep.* 6, 1–11 (2016).
168. Soares e Silva, M. *et al.* Self-organized patterns of actin filaments in cell-sized confinement. *Soft Matter* 7, 10631 (2011).
169. Upadhyaya, A. & Oudenaarden, A. Van. Biomimetic Systems for Studying Actin-Based Motility Actin polymerization provides a major driving force. *Curr. Biol.* 13, 734–744 (2003).
170. Cáceres, R., Abou-Ghali, M. & Plastino, J. Reconstituting the actin cytoskeleton at or near surfaces in vitro. *Biochim. Biophys. Acta - Mol. Cell Res.* 1853, 3006–3014 (2015).
171. Ito, H., Makuta, M., Nishigami, Y. & Ichikawa, M. Active materials integrated with actomyosin. *J. Phys. Soc. Japan* 86, 1–6 (2017).
172. Murrell, M. P. & Gardel, M. L. F-actin buckling coordinates contractility and severing in a biomimetic actomyosin cortex. *Proc. Natl. Acad. Sci.* 109, 20820–20825 (2012).
173. Merkle, D., Kahya, N. & Schwille, P. Reconstitution and anchoring of cytoskeleton inside giant unilamellar vesicles. *Chembiochem* 9, 2673–2681 (2008).
174. Gao, Y. *et al.* Correction for Vosler et al., Ischemia-induced calpain activation causes eukaryotic (translation) initiation factor 4G1 (eIF4GI) degradation, protein synthesis inhibition, and neuronal death. *Proc. Natl. Acad. Sci.* 110, 19968–19968 (2013).
175. Loiseau, E. *et al.* Shape remodeling and blebbing of active cytoskeletal vesicles. *Sci. Adv.* 2, (2016).
176. Goennenwein, S., Tanaka, M., Hu, B., Moroder, L. & Sackmann, E. Functional Incorporation of Intergins into Solid Supported Membrane on Ultrathin Films of Cellulose: Impact on Adhesion. *Biophys. J.* 85, 646–655 (2003).
177. Streicher, P. *et al.* Integrin reconstituted in GUVs: A biomimetic system to study initial steps of cell spreading. *Biochim. Biophys. Acta - Biomembr.* 1788, 2291–2300 (2009).
178. J Bibette, F. L. C. and P. P. Emulsions: basic principles. *Rep. Prog. Phys.* (1998). doi:10.1088/0034-4885/77/5/056502
179. Utada, A. S. *et al.* Monodisperse double emulsions generated from a microcapillary device. *Science (80-.).* 308, 537–541 (2005).
180. Peter Atkins, J. D. P. *Physical Chemistry*. (2006).
181. Riechers, B. *et al.* Surfactant adsorption kinetics in microfluidics. *Proc. Natl. Acad. Sci.* 113, 11465–11470 (2016).
182. Katepalli, H., Bose, A., Hatton, T. A. & Blankschtein, D. Destabilization of Oil-in-Water Emulsions Stabilized by Non-ionic Surfactants: Effect of Particle Hydrophilicity. *Langmuir* 32, 10694–10698 (2016).
183. Adamson, A. & Gast, A. Physical Chemistry Of Surfaces (Adamson, Gast , 6Ed, Wiley, 1997).pdf. 190 (1997). doi:10.1002/recl.19911100413
184. Hu, Y. T., Ting, Y., Hu, J. Y. & Hsieh, S. C. Techniques and methods to study functional characteristics of emulsion systems. *J. Food Drug Anal.* 25, 16–26 (2017).
185. Taylor, P. Ostwald ripening in emulsions: Estimation of solution thermodynamics of the disperse phase. *Adv. Colloid Interface Sci.* 106, 261–285 (2003).
186. Aronson, M. P. The Role of Free Surfactant in Destabilizing Oil-in-Water Emulsions. *Langmuir* 5, 494–501 (1989).
187. Particle sciences drug development services. Emulsion Stability and Testing. *Part. Sci. Drug Dev.*

Serv. 2, (2011).

188. Guo, M. T., Rotem, A., Heyman, J. A. & Weitz, D. A. Droplet microfluidics for high-throughput biological assays. *Lab Chip* 12, 2146–2155 (2012).

189. Holtze, C. *et al.* Biocompatible surfactants for water-in-fluorocarbon emulsions. *Lab Chip* 8, 1632 (2008).

190. Gruner, P. *et al.* Stabilisers for water-in-fluorinated-oil dispersions: Key properties for microfluidic applications. *Curr. Opin. Colloid Interface Sci.* 20, 183–191 (2015).

191. Dunstan, T. S. & Fletcher, P. D. I. Compartmentalization and separation of aqueous reagents in the water droplets of water-in-oil high internal phase emulsions. *Langmuir* 27, 3409–3415 (2011).

192. Dai, B. & Leal, L. G. The mechanism of surfactant effects on drop coalescence. *Phys. Fluids* 20, (2008).

193. Baret, J. C. Surfactants in droplet-based microfluidics. *Lab Chip* 12, 422–433 (2012).

194. Baret, J. C., Kleinschmidt, F., Harrak, A. El & Griffiths, A. D. Kinetic aspects of emulsion stabilization by surfactants: A microfluidic analysis. *Langmuir* 25, 6088–6093 (2009).

195. Goddard, E. D. *Surfactants and interfacial phenomena. Colloids and Surfaces* 40, (1989).

196. Diamant, H., Ariel, G. & Andelman, D. Kinetics of Surfactant Adsorption: The Free Energy Approach. 185, 23 (2000).

197. A. Bonfillon, F. Sicoli, D. L. Dynamic Surface Tension of Ionic Surfactant Solutions. *J. Colloid Interface Sci.* (1994).

198. Tadros, T. F. *Applied Surfactants: Principles and Applications*. (2006). doi:10.1002/3527604812

199. Nagarajan, R., Ruckenstein, E. & Nagarajan, R. Critical micelle concentration. A transition point for micellar size distribution. *J. Phys. Chem.* 79, 2622–2626 (1975).

200. Jonsson, L. Development of microsystem for water-in-oil droplet generation. *Master Thesis* 80 (2014).

201. Dietzel, A. *Microsystems for Pharmatechnology: Manipulation of Fluids, Particles, Droplets, and Cells*. (2016).

202. Berry, J. D., Neeson, M. J., Dagastine, R. R., Chan, D. Y. C. & Tabor, R. F. Measurement of surface and interfacial tension using pendant drop tensiometry. *J. Colloid Interface Sci.* 454, 226–237 (2015).

203. Jin, F., Balasubramaniam, R. & Stebe, K. J. Surfactant adsorption to spherical particles: The intrinsic length scale governing the shift from diffusion to kinetic-controlled mass transfer. *J. Adhes.* 80, 773–796 (2004).

204. Hansen, F. K. & Rodsrud, G. Surface Tension by Pendant Drop. *J. Colloid Interface Sci.* 141, (1991).

205. Haeberle, S., Mark, D., Von Stetten, F. & Zengerle, R. Microfluidic platforms for lab-on-a-chip applications. *Microsystems Nanotechnol.* 9783642182, 853–895 (2012).

206. Roach, L. S., Song, H. & Ismagilov, R. F. Controlling nonspecific protein adsorption in a plug-based microfluidic system by controlling interfacial chemistry using fluorous-phase surfactants. *Anal. Chem.* 77, 785–796 (2005).

207. Siqveland, L. M. & Skjæveland, S. M. Derivations of the Young-Laplace equation. 1–20 (2013). doi:10.13140/RG.2.1.4485.5768

208. Alvarez, N. J., Walker, L. M. & Anna, S. L. Diffusion-limited adsorption to a spherical geometry: The impact of curvature and competitive time scales. *Phys. Rev. E - Stat. Nonlinear, Soft Matter Phys.* 82, 1–8 (2010).

209. Ferri, J. K., Lin, S. Y. & Stebe, K. J. Curvature effects in the analysis of pendant bubble data: Comparison of numerical solutions, asymptotic arguments, and data. *J. Colloid Interface Sci.* 241, 154–168 (2001).

210. Mucic, N., Javadi, A., Karbaschi, M. & Sharipova, A. *Encyclopedia of Colloid and Interface Science*.

(2013). doi:10.1007/978-3-642-20665-8

211. Eastoe, J. U. & Dalton, J. S. Dynamic surface tension and adsorption mechanisms of surfactants at the air . water interface. (2000).

212. Schmitt, M. & Stark, H. Marangoni flow at droplet interfaces: Three-dimensional solution and applications. *Phys. Fluids* 28, 1–20 (2016).

213. Yoshinaga, N., Nagai, K. H., Sumino, Y. & Kitahata, H. Drift instability in the motion of a fluid droplet with a chemically reactive surface driven by Marangoni flow. *Phys. Rev. E - Stat. Nonlinear, Soft Matter Phys.* 86, 1–8 (2012).

214. Seemann, R., Fleury, J. B. & Maass, C. C. Self-propelled droplets. *Eur. Phys. J. Spec. Top.* 225, 2227–2240 (2016).

215. Herminghaus, S. *et al.* Interfacial mechanisms in active emulsions. *Soft Matter* 10, 7008–7022 (2014).

216. Thutupalli, S., Seemann, R. & Herminghaus, S. Swarming behavior of simple model squirmers. *New J. Phys.* 13, (2011).

217. Diguet, A. *et al.* Photomanipulation of a droplet by the chromocapillary effect. *Angew. Chemie - Int. Ed.* 48, 9281–9284 (2009).

218. Banno, T., Kuroha, R. & Toyota, T. PH-sensitive self-propelled motion of oil droplets in the presence of cationic surfactants containing hydrolyzable ester linkages. *Langmuir* 28, 1190–1195 (2012).

219. Saville, D. A. The effects of interfacial tension gradients on the motion of drops and bubbles. *Chem. Eng. J.* 5, 251–259 (1973).

220. Hanczyc, M. M., Toyota, T., Ikegami, T. & Packard, N. Fatty Acid Chemistry at the Oil - Water Interface : Self-Propelled Oil Droplets. *J. Am. Chem. Soc.* 129, 9386–9391 (2007).

221. Duncombe, T. A., Tentori, A. M. & Herr, A. E. Microfluidics: Reframing biological enquiry. *Nat. Rev. Mol. Cell Biol.* 16, 554–567 (2015).

222. Sackmann, E. K., Fulton, A. L. & Beebe, D. J. The present and future role of microfluidics in biomedical research. *Nature* 507, 181–189 (2014).

223. Whitesides, G. M. The origins and the future of microfluidics. *Nature* 442, 368–373 (2006).

224. Manz, A. *et al.* Planar Chips Technology For Miniaturization and Integration of Separation Techniques Into Monitoring Systems - Capillary Electrophoresis On a Chip. *J. Chromatogr. A* 593, 253 (1992).

225. Melinda A. Lake, Cody E. Narciso, Kyle R. Cowdrick, Thomas J. Storey, Siyuan Zhang, Jeremiah J. Zartman, and D. J. H. Microfluidic device design, fabrication, and testing protocols. 1–26 (2015). doi:10.1038/protex.2015.069

226. Figeys, D. & Pinto, D. A Revolution in Biological and Medical Sciences A look at some of the. *Anal. Chem.* 72, 330–335 (2000).

227. Paegel, B. M., Blazej, R. G. & Mathies, R. A. Microfluidic devices for DNA sequencing: Sample preparation and electrophoretic analysis. *Curr. Opin. Biotechnol.* 14, 42–50 (2003).

228. Wu, J., Dong, M., Rigatto, C., Liu, Y. & Lin, F. Lab-on-chip technology for chronic disease diagnosis. *npj Digit. Med.* 1, 7 (2018).

229. Pennathur, S., Meinhart, C. D. & Soh, H. T. How to exploit the features of microfluidics technology. *Lab Chip* 8, 20–22 (2007).

230. Vowell, S. Microfluidics: the effects of surface tension. 1–10 (2009). at <http://www.phys.washington.edu/users/sharpe/486/vowell_f.pdf>

231. Hardt, S. & Schönfeld, F. Chapter 1 Microfluidics: Fundamentals and Engineering Concepts. *Microfluid. Technol. Miniaturized Anal. Syst.* 1–58 (2007). doi:10.1007/978-0-387-68424-6_1

232. Karger, B. L., Chu, Y. H. & Foret, F. Capillary Electrophoresis of Proteins and Nucleic Acids. *Annu. Rev. Biophys. Biomol. Struct.* 24, 579–610 (1995).

233. Seemann, R., Brinkmann, M., Pfohl, T. & Herminghaus, S. Droplet based microfluidics. *Reports Prog. Phys.* 75, (2012).

234. Williams, B. J., Anand, S. V., Rajagopalan, J. & Saif, M. T. A. A self-propelled biohybrid swimmer at low Reynolds number. *Nat. Commun.* 5, 1–8 (2014).

235. Stricker, L. Numerical simulation of artificial microswimmers driven by Marangoni flow. *J. Comput. Phys.* 347, 467–489 (2017).

236. Stone, H. A., Stroock, A. D. & Ajdari, A. Engineering Flows in Small Devices. *Annu. Rev. Fluid Mech.* 36, 381–411 (2004).

237. Sharma, S., Srisa-art, M., Scott, S., Asthana, A. & Cass, A. Microfluidic Diagnostics. 949, (2013).

238. Thorsen, T., Roberts, R. W., Arnold, F. H. & Quake, S. R. Dynamic pattern formation in a vesicle-generating microfluidic device. *Phys. Rev. Lett.* 86, 4163–4166 (2001).

239. Tan, E. K. & Chan, L. L. Exploring the relationship between Parkinson's disease and hemifacial spasm. *Acta Neurol. Scand.* 113, 350–352 (2006).

240. Blow, N. Genomics: Catch me if you can. *Nat. Methods* 6, 539–544 (2009).

241. Platzman, I., Janiesch, J. W. & Spatz, J. P. Synthesis of nanostructured and biofunctionalized water-in-oil droplets as tools for homing T cells. *J. Am. Chem. Soc.* 135, 3339–3342 (2013).

242. Lee, M. *et al.* Synchronized reinjection and coalescence of droplets in microfluidics. *Lab Chip* 14, 509–513 (2014).

243. Kim, A. J., Manoharan, V. N. & Crocker, J. C. Swelling-based method for preparing stable, functionalized polymer colloids. *J. Am. Chem. Soc.* 127, 1592–1593 (2005).

244. Pardee, J. D. & Aspudich, J. [18] Purification of muscle actin. *Methods Enzymol.* 85, 164–181 (1982).

245. Fitzgerald, L. a, Leung, B. & Phillips, D. R. A method for purifying the platelet membrane glycoprotein IIb-IIIa complex. *Anal. Biochem.* 151, 169–177 (1985).

246. Halloran, T. O. & Burridge, K. SDS-gel electrophoresis and immunoblotting Cell cultures Indirect imrnunofluorescence and microscopy. 869, 337–349 (1986).

247. Sobieszek, a, Borkowski, J. & Babiychuk, V. S. Purification and characterization of a smooth muscle myosin light chain kinase-phosphatase complex. *J. Biol. Chem.* 272, 7034–7041 (1997).

248. Berg, J., Hung, Y. P. & Yellen, G. A genetically encoded fluorescent reporter of ATP:ADP ratio. *Nat. Methods* 6, 161–166 (2009).

249. Tantama, M., Martínez-françois, J. R., Mongeon, R. & Yellen, G. NIH Public Access. 1–25 (2013). doi:10.1038/ncomms3550.Imaging

250. Gruner, P. *et al.* Controlling molecular transport in minimal emulsions. *Nat. Commun.* 7, (2016).

251. Zamir, E. *et al.* Reconceptualizing fluorescence correlation spectroscopy for monitoring and analyzing periodically passing objects. *Anal. Chem.* acs.analchem.7b03108 (2017). doi:10.1021/acs.analchem.7b03108

252. Axelrod, D., Koppel, D. E., Schlessinger, J., Elson, E. & Webb, W. W. Mobility measurement by analysis of fluorescence photobleaching recovery kinetics. *Biophys. J.* 16, 1055–1069 (1976).

253. Soumpasis, D. M. Theoretical analysis of fluorescence photobleaching recovery experiments. *Biophys. J.* 41, 95–97 (1983).

254. Volodkin, D. V., Petrov, A. I., Prevot, M. & Sukhorukov, G. B. Matrix Polyelectrolyte Microcapsules: New System for Macromolecule Encapsulation. *Langmuir* 20, 3398–3406 (2004).

255. Erb, E. M., Tangemann, K., Bohrmann, B., Muller, B. & Engel, J. Integrin aIIbb3 reconstituted into lipid bilayers is noncluseted in its activated state but clusters after frbrinogen binding. *Biochem.* 36, 7395–7402 (1997).

256. Dixon, M. C. Quartz crystal microbalance with dissipation monitoring (QCM-D): enabling real-time characterization of biological materials and their interactions. *J. Biomol. Tech.* 19, 151–158 (2008).

257. Briand, E., Zäch, M., Svedhem, S., Kasemo, B. & Petronis, S. Combined QCM-D and EIS study of supported lipid bilayer formation and interaction with pore-forming peptides. *Analyst* 135, 343–350 (2010).
258. Janiesch, J. W. *et al.* Key factors for stable retention of fluorophores and labeled biomolecules in droplet-based microfluidics. *Anal. Chem.* 87, 2063–2067 (2015).
259. Szostak, J. W., Bartel, D. P. & Luisi, P. L. Synthesizing life. *Nature* 409, 387–390 (2001).
260. Drummond, D. C., Zignani, M. & Leroux, J. C. Current status of pH-sensitive liposomes in drug delivery. *Prog. Lipid Res.* 39, 409–460 (2000).
261. Cha, T. W., Guo, A. & Zhu, X. Y. Formation of supported phospholipid bilayers on molecular surfaces: Role of surface charge density and electrostatic interaction. *Biophys. J.* 90, 1270–1274 (2006).
262. Richter, R., Mukhopadhyay, A. & Brisson, A. Pathways of lipid vesicle deposition on solid surfaces: a combined QCM-D and AFM study. *Biophys. J.* 85, 3035–3047 (2003).
263. Nollert, P., Kiefer, H. & Jähnig, F. Lipid vesicle adsorption versus formation of planar bilayers on solid surfaces. *Biophys. J.* 69, 1447–1455 (1995).
264. Macháň, R. & Hof, M. Lipid diffusion in planar membranes investigated by fluorescence correlation spectroscopy. *Biochim. Biophys. Acta - Biomembr.* 1798, 1377–1391 (2010).
265. Cremer, P. S. & Boxer, S. G. Formation and Spreading of Lipid Bilayers on Planar Glass Supports. *J. Phys. Chem. B* 103, 2554–2559 (1999).
266. Matochko, W. L. *et al.* Uniform amplification of phage display libraries in monodisperse emulsions. *Methods* 58, 18–27 (2012).
267. Richter, R. P. & Brisson, A. R. Following the formation of supported lipid bilayers on mica: a study combining AFM, QCM-D, and ellipsometry. *Biophys. J.* 88, 3422–3433 (2005).
268. Choi, S.-E., Greben, K., Wördenweber, R. & Offenhäusser, A. Positively charged supported lipid bilayer formation on gold surfaces for neuronal cell culture. *Biointerphases* 11, 021003 (2016).
269. Johnsson, M. *Sterically Stabilised Liposomes and Related Lipid Aggregates*. *Physical Chemistry* (2001).
270. Cherney, D. P., Conboy, J. C. & Harris, J. M. Optical-Trapping Raman Microscopy Detection of Single Unilamellar Lipid Vesicles. *Anal. Chem.* 75, 6621–6628 (2003).
271. Kim, H. S. *et al.* Raman spectroscopy compatible PDMS droplet microfluidic culture and analysis platform towards on-chip lipidomics. *Analyst* 142, 1054–1060 (2017).
272. Bhatia, T. *et al.* Preparing giant unilamellar vesicles (GUVs) of complex lipid mixtures on demand: Mixing small unilamellar vesicles of compositionally heterogeneous mixtures. *Biochim. Biophys. Acta - Biomembr.* 1848, 3175–3180 (2015).
273. Stachowiak, J. C. *et al.* Membrane bending by protein-protein crowding. *Nat. Cell Biol.* 14, 944–949 (2012).
274. Lipowsky, R. Spontaneous tubulation of membranes and vesicles reveals membrane tension generated by spontaneous curvature. *Faraday Discuss.* 161, 305–331 (2012).
275. Melcrová, A. *et al.* The complex nature of calcium cation interactions with phospholipid bilayers. *Sci. Rep.* 6, 38035 (2016).
276. Vernier, P. T., Ziegler, M. J. & Dimova, R. Calcium Binding and Head Group Dipole Angle in Phosphatidylserine–Phosphatidylcholine Bilayers. *Langmuir* 25, 1020–1027 (2009).
277. Harmandaris, V. A. & Deserno, M. A novel method for measuring the bending rigidity of model lipid membranes by simulating tethers. *J. Chem. Phys.* 125, (2006).
278. Lee, K. C. & Liu, A. J. New proposed mechanism of actin-polymerization-driven motility. *Biophys. J.* 95, 4529–4539 (2008).
279. Takatsuki, H., Bengtsson, E. & Månsson, A. Persistence length of fascin-cross-linked actin filament bundles in solution and the in vitro motility assay. *Biochim. Biophys. Acta - Gen. Subj.* 1840, 1933–1942 (2014).

280. Pinot, M. *et al.* Confinement induces actin flow in a meiotic cytoplasm. *Proc. Natl. Acad. Sci.* 109, 11705–11710 (2012).

281. Hase, M. & Yoshikawa, K. Structural transition of actin filament in a cell-sized water droplet with a phospholipid membrane. *J. Chem. Phys.* 124, (2006).

282. Tsai, F. C., Stuhrmann, B. & Koenderink, G. H. Encapsulation of active cytoskeletal protein networks in cell-sized liposomes. *Langmuir* 27, 10061–10071 (2011).

283. Yasui, T. *et al.* Characterization of low viscosity polymer solutions for microchip electrophoresis of non-denatured proteins on plastic chips. *Biomicrofluidics* 5, 1–9 (2011).

284. Harris, D. E. & Warshaw, D. M. Smooth and skeletal muscle myosin both exhibit low duty cycles at zero load in vitro. *J. Biol. Chem.* 268, 14764–14768 (1993).

285. Kron, S. J., Drubin, D. G., Botstein, D. & Spudich, J. A. Yeast actin filaments display ATP-dependent sliding movement over surfaces coated with rabbit muscle myosin. *Proc. Natl. Acad. Sci. U. S. A.* 89, 4466–70 (1992).

286. Bendix, P. M. *et al.* A quantitative analysis of contractility in active cytoskeletal protein networks. *Biophys. J.* 94, 3126–3136 (2008).

287. Karlsson, M., Ekeroth, J., Elwing, H. & Carlsson, U. Reduction of irreversible protein adsorption on solid surfaces by protein engineering for increased stability. *J. Biol. Chem.* 280, 25558–25564 (2005).

288. Chen, Y., Wijaya Gani, A. & Tang, S. K. Y. Characterization of sensitivity and specificity in leaky droplet-based assays. *Lab Chip* 12, 5093–5103 (2012).

289. Suzuki, K., Miyazaki, M., Takagi, J., Itabashi, T. & Ishiwata, S. Spatial confinement of active microtubule networks induces large-scale rotational cytoplasmic flow. *Proc. Natl. Acad. Sci.* 114, 2922–2927 (2017).

290. Ban, T., Yamagami, T., Nakata, H. & Okano, Y. PH-dependent motion of self-propelled droplets due to marangoni effect at neutral pH. *Langmuir* 29, 2554–2561 (2013).

291. Juniper, M. P. N., Weiss, M., Platzman, I., Spatz, J. P. & Surrey, T. Spherical network contraction forms microtubule asters in confinement. *Soft Matter* 14, 901–909 (2018).

292. Luo, R., Venkatraman, S. S. & Neu, B. Layer-by-Layer Polyelectrolyte – Polyester Hybrid Microcapsules for Encapsulation and Delivery of Hydrophobic Drugs. (2013). doi:10.1021/bm4003915

293. Stone, H. A. & Samuel, A. D. T. Propulsion of Microorganisms by Surface Distortions. *Phys. Rev. Lett.* 77, 4102–4104 (1996).

294. Brüggemann, D., Frohnmayer, J. P. & Spatz, J. P. Model systems for studying cell adhesion and biomimetic actin networks. *Beilstein J. Nanotechnol.* 5, 1193–1202 (2014).

295. Gitlin, G., Bayer, E. a & Wilchek, M. Studies on the biotin-binding site of streptavidin. Tryptophan residues involved in the active site. *Biochem. J.* 256, 279–282 (1988).

296. Brakebusch, C. & Fässler, R. The integrin - actin connection, an eternal love affair. *EMBO J.* 22, (2003).

297. Streicher, P. *et al.* Integrin reconstituted in GUVs: A biomimetic system to study initial steps of cell spreading. *Biochim. Biophys. Acta - Biomembr.* 1788, 2291–2300 (2009).

298. Serrels, B. & Frame, M. C. FAK and talin: Who is taking whom to the integrin engagement party? *J. Cell Biol.* 196, 185–187 (2012).

299. Andersson, A.-S., Glasmästar, K., Sutherland, D., Lidberg, U. & Kasemo, B. Cell adhesion on supported lipid bilayers. *J. Biomed. Mater. Res. A* 64, 622–629 (2003).

300. Cho, N.-J., Frank, C. W., Kasemo, B. & Höök, F. Quartz crystal microbalance with dissipation monitoring of supported lipid bilayers on various substrates. *Nat. Protoc.* 5, 1096–1106 (2010).

301. Schaller, M. D., Otey, C. A., Hildebrand, J. D. & Parsons, J. T. Focal adhesion kinase and paxillan bind to peptides mimicking beta integrin cytoplasmic domains. *J. Cell Biol.* 130, 1181–1187 (1995).

302. Critchley, D. R. & Gingras, A. R. Talin at a glance. *J. Cell Sci.* 121, 1345–1347 (2008).

303. Calderwood, D. A. & Ginsberg, M. H. Talin forges the links between integrins and actin. *Nat. Cell Biol.* 5, 694–697 (2003).

304. Schmidt, J. M., Zhang, J., Lee, H. S., Stromer, M. H. & Robson, R. M. Interaction of talin with actin: Sensitive modulation of filament crosslinking activity. *Arch. Biochem. Biophys.* 366, 139–150 (1999).

305. Goksoy, E. *et al.* Structural Basis for the Autoinhibition of Talin in Regulating Integrin Activation. *Mol. Cell* 31, 124–133 (2008).

306. Martel, V. *et al.* Conformation, Localization, and Integrin Binding of Talin Depend on Its Interaction with Phosphoinositides. *J. Biol. Chem.* 276, 21217–21227 (2001).

307. Yan, B., Calderwood, D. a., Yaspan, B. & Ginsberg, M. H. Calpain Cleavage Promotes Talin Binding to the ??3 Integrin Cytoplasmic Domain. *Journal of Biological Chemistry* 276, 28164–28170 (2001).

308. Xing, B., Jedsadayanmata, A. & Lam, S. C. T. Localization of an Integrin Binding Site to the C Terminus of Talin. *J. Biol. Chem.* 276, 44373–44378 (2001).

309. Stumpp, M. T., Binz, H. K. & Amstutz, P. DARPins: A new generation of protein therapeutics. *Drug Discov. Today* 13, 695–701 (2008).

310. Pitard, B., Richard, P., Dunach, M., Girault, G. & Rigaud, J. L. ATP synthesis by the F0F1 ATP synthase from thermophilic Bacillus PS3 reconstituted into liposomes with bacteriorhodopsin. 1. Factors defining the optimal reconstitution of ATP synthases with bacteriorhodopsin. *Eur. J. Biochem.* 235, 769–778 (1996).

311. Plückthun, A. Designed Ankyrin Repeat Proteins (DARPins): Binding Proteins for Research, Diagnostics, and Therapy. *Annu. Rev. Pharmacol. Toxicol.* 55, 489–511 (2015).

312. Schwartz, M. A. Integrins and extracellular matrix in mechanotransduction. *Cold Spring Harb. Perspect. Biol.* 2, a005066 (2010).

7.4. List of Figures

7.5. List of Tables

8. Acknowledgement

It is worth to mention that the Max Planck Society (MPG) stands for independent basic research. Its work and principles in the area of biological & medical, chemical & physical, as well as social & live science have led to a high degree of qualification and a large number of grants and prizes. Eighteen Nobel Prizes and numerous additional prizes with very high reputation and prestige, as the Leibniz prize that was awarded to Prof. Joachim Spatz in the last year, count for it.

This acknowledgement is to appreciate the Max Planck Institute Department of Cellular Biophysics for its commitment to do research in all its aspects. Working in an atmosphere of global teams, with people from all over the world, and working in laboratories equipped with the most sophisticated instruments is a highly inspiring experience. I am very proud of having been part of MPI.

There are of course people behind this scene to make all that happen.

It is Prof. Joachim Spatz, head of the MPI Dept. for Cellular Biophysics, who offered me a position to do research in his department. I am deeply grateful for all his scientific advice and discussions and further for all the possibilities he provided me during my research: the well-equipped labs, the exchange of scientific expertise at international conferences, and of course Antholz, the annual highlight that provided room for scientific discussions as well as time for winter sports and enjoying the time with all the other colleagues. Thanks for giving us the chance to experience that every year.

Next, I want to thank Prof. Reiner Dahint and Priv.-Doz. Dr. Günter Majer for kindly accepting to review my thesis.

Specially, I want to honor Dr. Ilia Platzman, group leader of the Microfluidic subgroup, for his valuable advice and discussions. I am very grateful for his patience and encouragement. Besides his scientific advice and solutions, he always had an open ear and time to help and cheer me up with a joke.

I further want to thank Prof. Dorothea Brüggemann who supervised me in the first half year of my Ph.D. before she moved to Bremen to found her own Emmy Noether research group. The research based on protein binding studies was mainly done under her supervision. I am very grateful for her kind help and for giving me a very good start with my Ph.D. In this regard, I

want to especially thank Prof. Benjamin Geiger who provided most of the adhesion-associated proteins for my research.

I also want to thank the whole microfluidic group, especially Dr. Kerstin Göpfrich, Dr. Marian Weiss, Dr. Jan-Willi Janiesch, Dr. Roncong Luo, Dr. Eli Zamir, Christoph Frey, Silvia Antona, Sadaf Pashapour and Stojan Perisic. Dr. Kerstin Göpfrich supported me especially the last year with her positive attitude. I am very grateful for her scientific help, her great ideas and also for the nice chats on the terrace with ice cream. Dr. Jan-Willi Janiesch who introduced me into the field of synthetic biology and synthesized the custom-made surfactants I used. Dr. Marian Weiss, who worked as well in the field of synthetic biology and supported and helped me a lot during my Ph.D. with experiments and with good advice. Dr. Rongcong Luo, I want to thank for his scientific as well as for his wise life advices and nice chats. I am grateful for Dr. Eli Zamir's excellent advice regarding microscopy and image analysis. I further want to thank Christoph Frey for the wafer preparation in the clean room and his assistance in the lab and Sadaf Pashapour and Silvia Antona for proof reading parts of my thesis and for having always a good and fun time in the lab as well as outside the institute.

Further I want to thank Christine Mollenhauer, the head of the biochemistry laboratory in Stuttgart, for her excellent work in the lab in general and for the purification of the proteins. I appreciate especially all the afford for the myosin purification. Also, I want to thank Cornelia Weber, the technician in Heidelberg, for her great advice concerning actomyosin reconstitution and motility assays.

Next, I want to acknowledge my favorite colleagues Christoph Frey, Dr. Jennifer Young and Dr. Andrew Holle that turned during the last years into one of my best friends. Thanks for all the scientific and personal advice, thanks for all the chats, coffees, lunch breaks, beers, Jean Bach trips... I will miss so much not seeing you on a daily basis.

The whole Spatz group I want to thank for the nice and friendly atmosphere. Even when having a stressful time in the lab, I enjoyed being around in the institute. All of you made this place very special to me and I will never forget having been part of it.

My friends outside the laboratory, I thank for cheering me up after long days in the lab and for being very understanding when I cancelled appointments because I was too busy with experiments or with writing my thesis.

Last but not least I want to thank my family. My parents, thanks for letting me go my way with full backing from your side. Without your loving support, I would not have been able to make it so far. Then Johanna and Jens, the best siblings I can imagine. I know we will always be a good team. I am so grateful to have you.

Parts of the research leading to these results have received funding from the European Research Council/ ERC Grant Agreement no. 294852, SynAd. This work is also part of the MaxSynBio consortium, which is jointly funded by the Federal Ministry of Education and Research of Germany and the Max Planck Society. The Max Planck Society is appreciated for its general support in all aspects of the presented research.

Eidesstattliche Versicherung gemäß § 8 der Promotionsordnung der Naturwissenschaftlich-Mathematischen Gesamtfakultät der Universität Heidelberg

1. Bei der eingereichten Dissertation zu dem Thema "**Reconstitution of eukaryotic Architecture and Motility by Microfluidic Technology**" handelt es sich um meine eigenständig erbrachte Leistung.

2. Ich habe nur die angegebenen Quellen und Hilfsmittel benutzt und mich keiner unzulässigen Hilfe Dritter bedient. Insbesondere habe ich wörtlich oder sinngemäß aus anderen Werken übernommene Inhalte als solche kenntlich gemacht.

3. Die Arbeit oder Teile davon habe ich bislang nicht an einer Hochschule des In- oder Auslandes als Bestandteil einer Prüfungs- oder Qualifikationsleistung vorgelegt.

4. Die Richtigkeit der vorstehenden Erklärung bestätige ich.

5. Die Bedeutung der eidesstattlichen Versicherung und die strafrechtlichen Folgen einer unrichtigen oder unvollständigen eidesstattlichen Versicherung sind mir bekannt.

Ich versichere an Eides statt, dass ich nach bestem Wissen die reine Wahrheit erklärt und nichts verschwiegen habe.

Ort und Datum	Unterschrift